



YAHRIEL'S 4A'S: AN INDEPENDENT INTERDISCIPLINARY FIELD

1. AEROSPACE-AERONAUTICAL SYSTEMS

2. ANTHROPOLOGY-ENGINEERING

3. APPLIED SCIENCE, TECHNOLOGY, AND SOCIETY (STS)

4. ANATOMY AND ARTIFICIAL INTELLIGENCE

BY YAHRIEL SALINAS-REYES

A PROPOSED THESIS SUBMITTED TO THE GRADUATE FACULTY IN COMPLETE FULFILLMENT OF
THE REQUIREMENTS FOR THE DEGREE OF

DOCTORATE OF NEUROSCIENCE AND BIOMEDICAL
DATA-SCIENCE/INFORMATICS

THE STUDENT AUTHOR, WHOSE PRESENTATION OF THE SCHOLARSHIP HEREIN WILL BE
REVIEWED BY THE PROGRAM OF STUDY COMMITTEE, IS SOLELY RESPONSIBLE FOR THE
CONTENT OF THIS THESIS. THE GRADUATE COLLEGE WILL ENSURE THIS THESIS IS GLOBALLY
ACCESSIBLE AND WILL NOT PERMIT ALTERATIONS AFTER A DEGREE IS CONFERRED.

UNDERGRADUATE INSTITUTION: IOWA STATE UNIVERSITY OF SCIENCE AND TECHNOLOGY

AMES, IOWA

2023

BACHELOR'S: AEROSPACE AND AERONAUTICAL ENGINEERING ('23)

MASTER'S: APPLIED SCIENCE AND TECHNOLOGY ('23)

COPYRIGHT © YAHRIEL SALINAS-REYES, 2023. ALL RIGHTS RESERVED.

NATURE'S CHAOS GAME: AN EXISTENTIALIST APPROACH INFORMED BY MATHEMATICS AND NEUROBIOLOGY

INVESTIGATOR: *Yahriel Salinas-Reyes*

RESEARCH MANUSCRIPT

i.

DEDICATION

I dedicate my thesis primarily to the two most important people in my life - my nurturing mentor known as The Cyclone of Education, and my lifelong supporter, and companion, Don Yahriel Salinas-Reyes - An embodiment of Chaos, Order, Logic, and Madness. I miss you both incredibly, and I promise to make good on my word to make you both proud.

I am deeply grateful to my family in the United States, Mexico, and El Salvador for bearing with me patiently as I worked on my thesis. I dedicate this work to all of you. Your unconditional love and strong show of support are the only things that kept me going every time I wanted to give up. To my parents, Sonia Reyes-Alvarenga and Oscar Salinas-Millan, your daily phone calls and pep talks kept me grounded and pushed me closer to the finish line. To my sister Lizbeth Salinas-Reyes, who would chide me every week and guilt trip me for being away from home - your prayers and love have kept me safe here. To my family Abigail Salinas-Reyes, Samuel Salinas-Reyes, Delmy Salinas-Reyes, and La Raza - thank you for seeing the best in me. You have never failed to cheer me up.

Lastly, to my supporters - thank you for being patient, caring, understanding, and being invested in me and my thesis. I am incredibly lucky to have you all, and I couldn't have done this without you.

Yahriel Salinas-Reyes 2023

Discussion



Cite this article: Berthaume MA, Kramer PA. 2021 Anthroengineering: an independent interdisciplinary field. *Interface Focus* 11: 20200056.
<https://doi.org/10.1098/rsfs.2020.0056>

Accepted: 7 July 2021

One contribution of 12 to a theme issue
'Biological anthroengineering'.

Subject Areas:

biomechanics, biometrics, bioengineering

Keywords:

anthroengineering, transdisciplinary,
anthropology, engineering, biomechanics,
biological anthropology

Author for correspondence:

Michael A. Berthaume
e-mail: berthaume@lsbu.ac.uk

Anthroengineering: an independent interdisciplinary field

Michael A. Berthaume¹ and Patricia Ann Kramer^{2,3}

¹Division of Mechanical Engineering and Design, London South Bank University, London SE1 0AA, UK

²Department of Anthropology, and ³Department of Orthopaedics and Sports Medicine, University of Washington, Seattle, WA 98195-3100, USA

MAB, 0000-0003-1298-242X; PAK, 0000-0002-6435-9130

In recent decades, funding agencies, institutes and professional bodies have recognized the profound benefits of transdisciplinarity in tackling targeted research questions. However, once questions are answered, the previously abundant support often dissolves. As such, the long-term benefits of these transdisciplinary approaches are never fully achieved. Over the last several decades, the integration of anthropology and engineering through inter- and multidisciplinary work has led to advances in fields such as design, human evolution and medical technologies. The lack of formal recognition, however, of this transdisciplinary approach as a unique entity rather than a useful tool or a subfield makes it difficult for researchers to establish laboratories, secure permanent jobs, fund long-term research programmes and train students in this approach. To facilitate the growth and development and witness the long-term benefits of this approach, we propose the integration of anthropology and engineering be recognized as a new, independent field known as *anthroengineering*. We present a working definition for anthroengineering and examples of how anthroengineering has been used. We discuss the necessity of recognizing anthroengineering as a unique field and explore potential novel applications. Finally, we discuss the future of anthroengineering, highlighting avenues for moving the field forward.

1. Introduction

Transdisciplinarity forms a common axiom that transcends the disciplines, creating an overarching synthesis [1] (figure 1). As these syntheses combine previously isolated thoughts and ideas, the knowledge created by their integration is greater than anything that can be created by a single discipline on its own. Simply put, the whole is greater than the sum of its parts (Aristotle). Here we propose a new field that transcends existing disciplines: anthroengineering.

A recent transdisciplinary trend combining anthropology and engineering—anthroengineering—has become increasingly popular over the last few decades. It has played a crucial role in the development of fields such as biomechanics [2,3], ergonomics [4,5] and functional morphology [6–9]. Anthropology—the science and study of human and societal culture, language and biology—and engineering—the application of science to create machines and implement technologies and tangible solutions to societal problems—are unique and distinct disciplines that infrequently share curricular overlap. When the transdisciplinary approach has been applied to anthropology and engineering, it has often leveraged methods or data from one discipline to address a question from the other (figure 2). This focus on specific problem-solving rather than a united theoretical foundation limits the impact of any innovations created by the collaboration. Thus, the power of the transdisciplinary approach is not fully realized. By leveraging both disciplines to address issues that transcend each discipline (i.e. transdisciplinary issues), syntheses can be created that are of interest not only to members of both disciplines, but also to individuals outside of either.

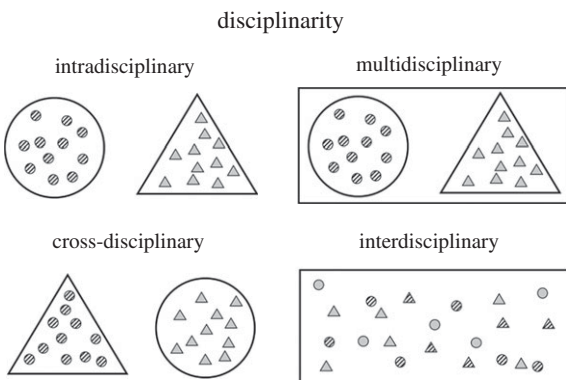


Figure 1. Types of disciplinarity that combine anthropology (circles) and engineering (triangles). Intradisciplinary: anthropologists (striped circles) and engineers (grey triangles) work within their respective fields (large circle and triangle). Multidisciplinary: anthropologists and engineers work within their respective fields to address a larger issue (rectangle). Cross-disciplinary: anthropologists investigate issues within engineering, and engineers investigate issues within anthropology. Interdisciplinary: anthropologists, engineers, anthropologists turned engineers (striped triangles) and engineers turned anthropologists (grey circles) seamlessly use both disciplines, simultaneously, to address larger issues.

The uniqueness and distinctiveness of the two disciplines means that, if a Venn diagram were to be drawn, little overlap would be apparent. Thus, it is difficult for researchers to identify issues that simultaneously leverage both disciplines. Yet, such issues exist, and many of them are crucial for the success of people and planet. Examples of such issues include the United Nations (UN) 17 Sustainable Development Goals (SDGs). These goals set forth a blueprint for how to achieve a more sustainable future for all by addressing problems ranging from poor health to inequality, environmental degradation, and peace and justice [15–17]. Because anthropologists and engineers are trained to approach these problems in discipline-unique ways, their perspectives will be distinct along a multitude of axes, and the fusion of the two disciplines will be difficult. But, ultimately, the insights gained will lead to solutions that neither discipline could achieve independently.

Despite the presence of significant overlapping issues and great benefits that could be achieved by leveraging both anthropology and engineering to address these issues, this transdisciplinary approach is rare, because no generalized framework that incorporates anthropology and engineering currently exists. Instead, frameworks are constructed for targeted projects which are often abandoned when the project is completed. Establishment of these frameworks requires an extraordinary amount of effort, and their specificity and frequent abandonment prevents them from being used for novel applications. A generalized framework is needed.

Such a framework would require, among other attributes, a common language where anthropologists and engineers can communicate effectively. It would require acknowledgement, respect and integration of expertise to develop new syntheses and a new cohort of students who are trained to think as both anthropologists and engineers simultaneously. But before a framework can be developed, this transdisciplinary approach requires a name. Without a name, the approach remains unknown, ill-defined and abstract. But with a name, this approach has identity and carries with it symbolism

beyond its meaning. We suggest, therefore, that the transdisciplinary approach, combining both anthropology and engineering, be recognized as its own, independent field called *anthroengineering*.

2. What is anthroengineering

Anthroengineering is an approach that uses theories, methods and/or data from both anthropology and engineering to address questions within and beyond both disciplines. The result is the development of new knowledge, which can take a multitude of forms (e.g. data, technologies, viewpoints, axioms, syntheses). While the true power of such an approach would lie in leveraging it to address transdisciplinary issues, anthroengineering can also be used to address questions within anthropology and engineering and to advance each field individually (figure 2).

Providing anthroengineering with a name, describing it and recognizing it as distinct entity allows for researchers to succinctly define their work and, more importantly, provides them with identity as anthroengineers. It also acts to provide a common thread and search term that can tie together all future work that uses a transdisciplinary approach to combine both anthropology and engineering. Doing so will provide those interested in anthroengineering with a direct way to learn about it and what frameworks, data and methods exist to leverage anthroengineering effectively in their own work.

3. Examples of anthroengineering

As previously discussed, examples of anthroengineering already exist, and some have existed for decades. Given our expertise, we discuss some examples largely through the lens of biological anthropology and engineering mechanics.

3.1. Classic anthropology meets classic engineering

Anthropologists have studied dental wear patterns on the micro-, meso- and macro-levels for over a century [18] to address a myriad of questions in such topics as taxonomy [19], palaeoecology [20], environmental reconstruction [21] and behaviour [22,23]. Similarly, mechanical failure analyses—and, in this situation, tribology and fracture mechanics—have been a major focus of engineering since the birth of the field as all machines experience wear [24–26]. It is, therefore, unsurprising that anthropologists and engineers have teamed up to understand better how teeth wear and fracture.

Using techniques such as nano-indentation, researchers have been able to investigate the role that microscopic particles (e.g. phytoliths, grit) play in the wear of dental enamel [27,28]. Additionally, through physical experimentation, modelling and comparative anatomy [29–32], researchers have been able to investigate the role of enamel thickness and schmelzmusters (enamel microstructure) in force and energy in failure resistance. Although researchers may not always agree on interpretations of experimental results [33–35], this research has led to advances in understanding dental wear and the factors that influence it [36], understanding functional adaptations of teeth [37,38] and the creation of bioinspired materials [39].

Similarly, principles from material science and solid mechanics (engineering) and musculoskeletal biology

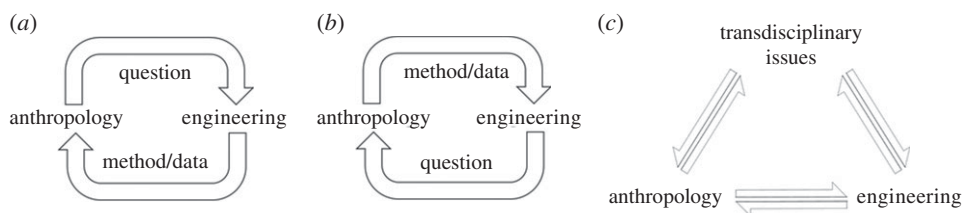


Figure 2. Transdisciplinary approaches to anthroengineering. (a) Engineering method(s)/data being leveraged to address anthropological question(s). Through an iterative process, question(s)/method(s) are refined and a synthesis is reached (e.g. the application of FE modelling to human evolution [10–13]). (b) Anthropological method(s)/data being leveraged to address engineering question(s). Through an iterative process, question(s)/method(s) are refined and a synthesis is reached (e.g. the application of ethnography to engineering design [14]). (c) Engineering and anthropological questions, methods and data are used to address transdisciplinary issues (e.g. design and/or manufacture of culturally relevant, sustainable medical devices for low- and middle-income countries).

(anthropology) have been used to understand how skeletal form (shape + size) and skeletal and ecological mechanical properties affect the way loads are transferred to the skeleton and how the skeleton responds to internal and external loads. Bone (re)models in response to mechanical strain [40–43]: this in turn affects bone's mechanical properties (remodelling) and form (modelling) (e.g. [44,45]). Bone strains have been measured experimentally using *in vivo* [46,47] and *in vitro* [48,49] techniques using strain gauges and digital image/volume correlation (DIC, DVC). However, this only delivers information on bone strain at a limited number of sites. By constructing finite-element (FE) models and validating them using experimental strains [50,51], we can obtain three-dimensional strain maps across the entire structure.

FE models require several inputs, including geometry, constraints and mechanical properties [8,52–54]. Advances in three-dimensional scanning techniques, computer science and statistical shape modelling (e.g. geometric morphometrics [55], dental topography [56]) have made it possible to not only (re)construct three-dimensional digital representations of such models [9,57–61], but also quantify complex shapes for statistical analyses [55,62–64]. Constraints come from muscles, joints and/or the external environment. Muscle force can be estimated by multiplying maximum force generation—originally estimated using physiological cross-sectional area [65–67] but now relying on muscle activation/strength [68] and often validated using electromyography [69–71]. Joint constraints are estimated using anatomical knowledge and skeletal collections. Although constraints from the external environment are often modelled as reaction forces, the mechanical properties of the environment (e.g. ground substrate composition during locomotion [72] or dietary mechanical properties during mastication [73,74]) affect the rate and manner in which the load is transmitted. Finally, mechanical properties are difficult to obtain, as bone is a hierarchical, composite structure, but techniques such as tension/compression tests, bending, indentation and ultrasound are used to estimate static and dynamic (bulk) properties [75–82]. Sensitivity studies are useful in understanding how parameter estimates affect the results, but not in validating the model [49,83–86], which requires data from empirical studies (e.g. [53,83]).

Using an extensive array of theories and methods from anthropology and engineering, we have learned more about musculoskeletal biomechanics than can be listed here. Some major findings include:

- Over a lifetime, an individual will engage in actions that will load their skeleton. In turn, their bones will generate

a set of mechanical properties and forms to properly resist the *in vivo* strains brought on by those loads [42,87–89]. But it can be difficult or impossible to determine what actions occurred in the lifetime of an individual given only a set of bone mechanical properties and forms, as multiple behaviours can yield similar loading regimes. This is further complicated with inter-populational or among-species comparisons, as genetics and neutral selection play a significant role in bone form [90].

- Skeletal morphologies particular to specific hominin species have focused attention on the relationships among form, function and behaviour [91]. For instance, the lower limb and pelvic morphology of *Australopithecus afarensis* (e.g. [92]), *Australopithecus sediba* (e.g. [93]) and *Homo neanderthalensis* (e.g. [94]) has led to long-term debates regarding their forms of terrestrial locomotion. Geometric morphometrics and other traditional statistical analyses have led to important insights (e.g. [95]), although they quantify skeletal form and not biomechanical function, and many questions remain. Inverse dynamic simulation of walking in extinct hominins offers the opportunity to expand our understanding of this critical behaviour (e.g. [92,96]), but the integration of musculoskeletal models offers the best opportunity for future insights [68].
- Masticatory loads cause mechanical strains in the skull, which significantly affect its mechanical properties and form [44,45,97]. However, the debate about the relationship between feeding mechanics and diet has led to major questions: is it possible, over an individual's lifetime, to develop a skull that is over- or under-designed for the masticatory loads it experiences [98,99]? Does a skull's ability to resist masticatory loads dictate or limit an animal's or species' diet? Does natural selection select for skull form based on its ability to resist masticatory loads [10–13,100–102]?
- Primate tooth shape is undoubtedly correlated with diet [56,103], likely because teeth have evolved to break down foods consumed more efficiently [56,104,105]. However, the interactions between multicusped teeth and food items are so complex that we lack an efficient model for describing these relationships and, thereby, predicting food item breakdown from tooth shape [64,106,107].

Although it may seem that these lines of research have created more questions than answers, the independent syntheses of anthropology and engineering have led to important insights not only for the fields of anthropology and

bioengineering but also anatomy, evolution, medicine and dentistry, to name a few. Further, the crucial questions generated would not exist if not for this transdisciplinary anthroengineering approach, and researchers would be ignorant of their ignorance.

3.2. Addressing intradisciplinary questions

Anthroengineering has also contributed in addressing more targeted questions within the disciplines of anthropology and engineering. Owing to decades of research in relatively independent fields, anthropology can provide insights into the Universe that engineering does not have, and vice versa.

Because anthropology is a discipline dominated by questions, while engineering a discipline that focuses on methods and applications, it is easy to see how the tools of engineering can be used to address anthropological questions. For example, using methods initially developed in engineering, virtual anthropology [108] has made it possible to quantitatively reconstruct palaeoarchaeological material and statistically quantify the accuracy of these reconstructions [59–61,109,110]. Two important examples of this are the reconstruction of the skull of *Ardipithecus ramidus*, which provided crucial, previously missing information about the evolution of hominin social structure, bipedalism and brain structure in hominin evolution during the Pliocene [110]. Additionally, the reconstruction of the mandible of *Homo habilis* not only showed a decoupling of brain and tooth size, but also allowed the development of a hypothesis regarding a much earlier origin of the genus *Homo* [109]. While that paper was under review, a new fossil (the Ledi-Geraru mandible) was discovered, confirming the authors' hypothesis [111].

Two additional common engineering methods—FE analysis and tension/compression tests—have been used extensively in palaeoanthropology to quantify the biomechanical performance of hard skeletal tissues and address questions concerning the evolution of primate diets [12,46,58,112–114]. The ability to print three-dimensional fossils further allows for the mechanical testing of previously inaccessible material [115–117]. These *in silico* and *in vitro* models and experiments carry with them several assumptions about the loading conditions and mechanical properties of the structure being analysed but provide valuable information about the biomechanical limits of the structure.

Given the plethora of methods in engineering, it may be more difficult to see how anthropology can benefit engineering. Nonetheless, engineering focuses on the application of science to solve problems for people, and anthropology is uniquely situated to provide the context to those problems. For instance, anthropology has improved engineering through the incorporation of anthropological methods. For example, the incorporation of ethnography into design to form the fields of design/techno-anthropology [14] and conferences like EPIC (Ethnographic Praxis in Industry Conference; www.epicpeople.org). End-user design focuses on the user's needs when designing products. By using anthropological techniques like ethnography, engineers can gather information about the wants and needs of the user that is inaccessible through focus groups developed from marketing perspectives. A classic example is in the design of the MP3 player, which was meant as an affordable

alternative to the iPod to be used in the gym. Focus groups thought they wanted a device with many options and, therefore, many buttons. The product was designed, sent to market and failed. It was only by teaming up with ethnographers that designers and engineers realized that people's hands got sweaty in gyms and that gyms were social places. Ultimately, people actually wanted devices with fewer buttons and a quick on/off switch—they just did not realize it when they were in focus groups because the questions were not asked in the proper framework [118].

Anthropologists bring with them techniques that can be used to design for the future [119] and understand the consequences of technological advances. Engineers make design decisions to help today, but rarely think about the long-term effects on societies and communities in the future: this is because many work for companies which are on a deadline and, once one project is complete, they move on to the next. A classic example of the desire to solve the problem at hand without considering the potential longer-term societal consequences has been documented [120]. Engineers working through an international development organization created a solution to a chronic water shortage by developing a 140 km gravity-driven water pipeline that supplied water taps in local settings. Before the project, local women had carried water from natural sources, at times a journey of 3 h. The water distribution system worked well, but two unintended consequences occurred: the decrease in energy expenditure due to no longer needing to carry water increased the women's fertility and, because nutritional resources remained the same, increased child malnutrition [120]. These consequences are predictable through the lens of human reproductive ecology, a key body of knowledge in biological anthropology.

Anthropologists are trained to investigate long-term societal and community trends and are in a much better position not only to understand but also to address these problems. By working together, anthropologists and engineers who are interested in finding more socially connected solutions can do more to address crippling human problems. An example of how this can work came forth at the 'Why the World Needs Anthropologists: Powering the Planet' conference at Durham University, UK, in 2018. The conference focused on the problems facing energy (e.g. production, dissemination, storage) and explored how energy professionals and anthropologists can work together to create energy innovations that change the world for the better (<https://www.dur.ac.uk/dei/events/?eventno=34503>). In many cases, applied anthropology, which focuses on the external application of anthropology to current problems, could be used to extend and/or enhance the solutions to the problems engineers are regularly faced with.

Finally, although biomimicry is a field in itself, its application often falls short of its potential. Engineers who use biomimicry often look at the biological system in isolation and with overly simplified biological theories (e.g. assuming natural selection has caused a structure to be optimal for its function, without considering the evolutionary history of that element). Biological solutions typically must solve several simultaneous problems and have evolved within a set of allometric, phylogenetic and ontogenetic constraints [121]—a core understanding in biological anthropology—and the adaptationist programme frequently employed by engineers has been rejected by biologists for decades

[122,123]. Because of this, biomimetic engineering falls short of its goals.

Anthropologists are trained to consider biological context that could lead to more effective biomimicry solutions using primates and human biological systems (e.g. the hierarchical structure of bone [124]). Take, for example, the design of the human foot, a complex structure that can be rigid in some circumstances and compliant in others. The evolutionary history of the foot is complex and filled with gaps [125], but we know it has evolved to interact with various substrates [72]. When wearing a shoe, the substrate interacting with the foot is no longer the ground, but the shoe itself [126], but shoe design does not often take foot-substrate interactions into account. Many shoe designs lead to running biomechanics that the human skeleton has not evolved to handle (e.g. high-impact forces during heel striking [127]). Similar issues can be seen in prosthetic foot design, where the impact of foot stiffness on gait biomechanics is well documented for advanced prosthetic feet (e.g. [128]). But in situations with fewer opportunities for the use of advanced medical devices, ‘one size fits all’ becomes ‘one stiffness fits all’ and the negative consequences of such choices are not appreciated. Further, even advanced medical interventions select a specified, unchanging stiffness for the prosthetic foot, when the natural foot has an adaptive, continuously changing stiffness, dependent on substrate and loading. Using anthroengineering and biomimicry approaches, answers to questions like ‘How can we use what we know about variation in Primates to make engineered products better?’ are achievable.

4. Why recognize a formal field of anthroengineering?

If anthroengineering projects already exist, why is it necessary to provide the word ‘anthroengineering’ to describe them all? It is not as if the previously discussed anthroengineering examples would cease to exist should the term ‘anthroengineering’ not be coined. More importantly, why is it necessary to recognize anthroengineering as its own field?

First, as previously mentioned, names provide identity and symbolic meaning. Should it not be given a unifying name, anthroengineering will remain elusive and ill-defined. In a well-known paper on evolutionary theory, Gould & Vrba [129] present a new word—exaptation—to describe an evolutionary phenomenon. They argue that the existing word ‘adaptation’ is defined and recognized by two criteria and biologists fail to recognize potential confusion between these criteria. Part of the reason for this confusion, they go on to say, is that one of these criteria does not have a distinctive word to describe it. They then propose that the word ‘exaptation’, which had not previously existed, be used for this criterion [129]. By providing a phenomenon with a name, Gould and Vrba took a previously undefined concept and centred it, making it tangible and real. Similarly, while anthroengineering has existed for decades, it has remained abstract and ill-defined. By providing a word to describe this line of work, anthroengineering becomes tangible and real.

Second, providing the name anthroengineering allows for the field to be recognized. This provides a thread to unite

researchers working at the intersection of anthropology and engineering, much as the word ‘anthropology’ ties together cultural, linguistic and biological anthropologists, or ‘engineering’ ties together chemical, mechanical and computer engineers. Anthropology and engineering intersect across so many areas of interest that researchers in one area are often ignorant of people working in another (e.g. design anthropologists versus palaeo-biomechanists). The word anthroengineering creates a unifying concept for these researchers and an umbrella under which those anthroengineers can meet with, learn from and work with each other.

Third, the creation of a word and field to describe this line of work creates with it a new way of thinking and new framework, but, unlike interdisciplinary projects, it also creates a permanency. This allows researchers to be trained in this novel way of thinking and apply it with a deeper understanding to new problems in the future. This will then open a new world of potential applications for anthroengineering and enable researchers to ask questions they previously would not have considered.

Once anthroengineering is established and researchers have become fully trained in the field, the questions researchers ask will change. Instead of asking how anthropology or engineering, individually, could address a problem, researchers will ask how anthroengineering can address the problem and—as such—be able to answer it in a more fully informed, comprehensive manner. New questions can be asked, such as:

- How can we leverage anthroengineering to address large problems in the world, such as the UN’s SDGs?
- How can we use anthroengineering to better understand how humans have evolved and why modern human biological variation exists in the manner it does?
- How can we leverage that information to better understand how humans are currently evolving in light of technological and societal changes and to address problems associated with racism and other identity-based biases in our technology and societies [130]?
- How can we use advanced modelling techniques to address global problems associated with healthy human ageing?

4.1. Creation of a new field

Today, many of the problems facing anthroengineering are the same as those facing interdisciplinary research in general. We recognize the issues facing research and research projects can often be distinct from those facing fields, but, at the time of writing, anthroengineering has almost solely existed at the research level, so it has not yet developed (m)any unique ‘field-level’ problems. As the plights of interdisciplinary research are much discussed, we will provide an overview of some of the main problems facing interdisciplinary research that we have witnessed within anthroengineering. We will further discuss some issues specific to anthroengineering today.

4.1.1. Publishing

Publications are currency in academia. When academics try to demonstrate their impact as researchers, they often total their number of publications, h-index, i10 index and the like for good reason. Publications foster recognition and the institutionalization of research, which in turn feeds back on the

infrastructure and capacity of centres and departments, resulting in increased support [1].

Anthroengineers are faced with several difficulties when it comes to publication that plague interdisciplinary research. When making the decision on where to publish, anthroengineers must choose between specialist and generalist journals [131]. Often, their manuscripts do not fit within the narrow remits of specialist journals and would have to change position from a truly transdisciplinary approach to one where the methods/theories from one field are being used to advance the other [132]. Until specialist anthroengineering journals are established, therefore, manuscripts must be published in generalist journals. The risk when publishing in generalist journals is that the paper will not have its desired impact, as the generalist journal may not be regularly read by anthropologists, engineers or fellow anthroengineers. The paper would then miss its target audience.

The most effective way of circumventing this issue is through publication in high-impact generalist journals with large readership bases. But herein lies two dilemmas: (i) high-impact generalist journals tend to have word/page limits, and there is often not enough space to fully explain or discuss the anthropological *and* engineering theories and methods, and (ii) these journals have many submissions and limited publication space. They are, therefore, likely only to publish material they believe will be of interest to a high percentage of their audience, meaning that they can be hesitant to accept and publish papers in untested areas that do not already have a demonstrated readership base.

Further, the editors handling the manuscripts are unlikely to be anthroengineers and are more likely to be either anthropologists or engineers, making it less likely they will be able to grasp fully the impact of the research as part of the work is outside their area of expertise. The same issue occurs when recruiting reviewers for the manuscript [133]. Often, few researchers exist with the expertise to comprehensively review the manuscript. Consequently, more reviewers must be recruited, and it is not uncommon for reviewers to provide conflicting reviews. When conflicting reviews are received by a high-impact journal, the manuscript is often rejected, as the lack of consistency among reviewers is believed to be indicative of an inferior manuscript.

As a result, researchers are required to spend years publishing high-impact research in lower impact generalist journals that may not reach their target audience, and/or moulding their research to reach the narrow remit of the specialist journals. As institutional and funding support are often hinged on the ability to publish in high-impact journals (as this is often used as a metric for the ‘quality’ of research), researchers in interdisciplinary fields must often work much harder to be recognized. Fortunately for anthroengineering, several well-respected journals have been receptive to the publication of anthroengineering manuscripts (e.g. those published by the Royal Society [106,107,134], *Proceedings of the National Academy of Sciences of the United States of America* [12] and *Nature* [58]), but more explicit definition of the field will extend this acceptance.

4.1.2. Funding bodies

Funding is almost as important as publishing in academia, but securing funding for interdisciplinary projects comes

with many of the same problems [132,135]. Instead of choosing between specialist journals, researchers are forced to choose between specialist councils (e.g. the Engineering and Physical Sciences Research Council (EPSRC), Natural Environment Research Council (NERC) and Biotechnology and Biological Sciences Research Council (BBSRC) in UK Research and Innovation (UKRI)) or specialist research areas (Biological Sciences, Engineering, International Science and Engineering, and Social, Behavioral, and Economic Sciences in the National Science Foundation (NSF)).

At a time when inter-/multidisciplinary research is heralded as the future of academia [136–138], the narrow focus of councils/research areas makes it complicated to submit interdisciplinary proposals and receive funding. When proposals are submitted to a specific research council/area, the proposal’s merit is judged within the expertise of that council/area. While submission of truly interdisciplinary proposals that transcends the boundaries of the research councils/areas can occur through cross-council submissions, councils need to be contacted prior to submission to determine if the proposal is of interest. It often takes months to answer interdisciplinary enquiries, as it requires cross-council conversations, which delay proposal submission.

Once submitted, it is consistently more difficult to be awarded funding for interdisciplinary projects [139], and it is easier to secure funding for projects that combine closely related disciplines than for disparate ones [132]. This, unfortunately, leads to a situation where the more groundbreaking the collaboration is, the harder it is to fund. Lower funding success rates are believed to originate from a bias against interdisciplinary projects. Firstly, interdisciplinary proposals are viewed as higher risk because they do not follow an established path [139]. Secondly, as with journal articles, proposals are often reviewed by reviewers and panels who are ill-equipped to evaluate all parts of the project, making it difficult for them to appreciate the scope and impact of the proposal. They instead only review the portion of the proposal for which they are an expert and are more likely to assign a mediocre or poor score to an interdisciplinary proposal than an intradisciplinary one owing to a poor understanding of the project or the foundational concepts. Having a mix of reviewers who do and do not fully appreciate or understand the project will lead to proposals being rejected, as a lack of consistency between the reviewers is viewed as a problem with the application and not the review process. Additionally, interdisciplinary proposals compete with intradisciplinary ones, which are easier to justify for the funding agent [139].

4.1.3. Institutional support

In the longer term, for anthroengineering—or any other interdisciplinary line of research—to succeed, it must have career-level institutional support. Once interdisciplinary grants are awarded, the resulting projects often include graduate students and/or postdoctoral research associates. While this training expands their knowledge in ways that we recommend, it also leads to the training of a cohort of interdisciplinary researchers who, in the case of anthroengineering, do not fit the classic definitions of anthropology or engineering. They are often not considered ‘real’ anthropologists or ‘real’ engineers. As a result, when it comes time for these individuals to obtain permanent posts, the more

interdisciplinary they are, the more difficult it is to obtain a permanent position.

During faculty searches, departments/divisions look for individuals to fill gaps in programme teaching and/or research foci, often hiring candidates who best fit the discipline(s) in which the programme awards degrees. This makes it difficult for truly interdisciplinary researchers to obtain permanent posts: an anthropologist or engineer who has spent their entire career working within the boundaries of their traditional discipline is a much stronger candidate than an anthroengineer. For the long-term success of anthroengineering, high-level institutional support is needed.

4.1.4. Anthroengineering education

In terms of education, institutions need to go a step further than the current practice. To date, all anthroengineering training has been done on an individual level in the laboratory, which requires an inordinate amount of time and effort from the laboratory's principal investigator, and from the individuals independently seeking out formal educations in both anthropology and engineering. Given how different the two disciplines are, this often requires twice the time and money to be educated in anthroengineering, limiting the ability to study anthroengineering to the privileged. Owing to the clear benefits of interdisciplinary research, and the scientific leaps that have been made by anthroengineering research already, we believe that universities should support formally training students as anthroengineers.

The majority of these students will leave academia and enter the private sector. The students trained as anthroengineers will have immediately transferable skills that make them superior on the job market to other anthropologists/engineers seeking employment. For example, a major concern among engineering companies is how to be more socially responsible, while social responsibility is a central theme in anthropology. The anthroengineers entering the job market will have the skills not only to be practising engineers, but also to be more socially responsible than engineers who have not received this training—something that is direly needed [140]. The anthroengineering cohorts will be trained in both anthropology and engineering from the start of their higher education, and, thus, taught to think using interdisciplinary approaches from the start. These anthroengineers will have the ability to see new questions and novel, innovative answers that cannot be imagined by the current generation of anthroengineering.

5. Disciplinary culture

The last issue we would like to touch upon with anthroengineering is that of disciplinary culture. In the creation of a new field, we are in the unique position to create the academic culture for the field. A focus of many disciplines, today, is to address the realities of sexism, racism, homophobia, etc., that have become engrained within these disciplines and academia in general and to take the necessary steps to solve these problems [141]. In the establishment of a new field, we can attempt to create a more inclusive academic environment from its inception [142].

When applying to hold the first symposium on anthroengineering at the American Association of Physical Anthropology (AAPA) conference in Cleveland, Ohio,

USA, 2019 (Symposium 13—Anthroengineering: a Biological Perspective), we were required to write a 300-word diversity statement. In it, we described our methods for recruiting symposium participants which reflect our vision of anthroengineering:

In recruiting participants for this symposium, we focused on early career researchers and on members of groups frequently underrepresented in research. Consequently, about half of our participants are women, and others are ethnic minorities and members of the LGBTQIA[+] community. By recruiting a diverse group of people at an early stage in their careers, we hope to foster an environment of inclusion that connects to and bolsters other such efforts at the AAPAs and in the discipline of biological anthropology generally... [Anthroengineering should value] the contributions of all people, regardless of sex, gender, ethnicity, or sexual orientation, and supports all types of research that combine anthropology and engineering.

In short, our vision for this new field is one of fairness and inclusivity, but anthroengineering will be housed in academic institutions and is born out of two fields which have their own problems. Fortunately, we are in a position where we can observe the issues present in other fields and strive to avoid those issues in this one.

6. Conclusion

In this paper, we have presented the concept of anthroengineering, provided examples of how anthroengineering has been used in the past and outline a plan for the future. Importantly, we have argued that anthroengineering should be recognized as its own, independent field: if you did not already believe this, we hope we have made converts out of you.

We cannot wait to see what the future has in store.

Data accessibility. This article has no additional data.

Authors' contributions. Both M.A.B. and P.A.K. conceived of and wrote the paper.

Competing interests. We declare we have no competing interests.

Funding. The American Association of Physical Anthropologists (now the American Association of Biological Anthropologists) provided funding for the symposium on anthroengineering.

Acknowledgements. We would first and foremost like to thank editor Tim Holt and the Royal Society for agreeing to take on these articles on anthroengineering. We would further like to thank the American Association of Physical Anthropologists for allowing us to hold the first symposium on anthroengineering in 2018 and for aiding in differing the costs of the symposium. Additionally, we extend a great gratitude for all those who took part in the symposium. There are hundreds (thousands?) of people who have helped in the development of this paper through conversations, their own research and financial support throughout our careers. We regret not being able to list all these individuals here, as such a list would add pages to the manuscript!

M.A.B. thanks his high school history teacher, Ms Brewer, for developing his interest in human history, and Jean Forward for helping him realize his love of anthropology during his freshman year at the University of Massachusetts, Amherst: they both played instrumental roles in his beginning his anthropological career. He would like to thank former Dean Kathy Rubin for playing a similar role during his freshman year in engineering. How often is it a dean regularly meets with a single first-year student just to check in and make sure they are doing ok? He would like to thank Ian Grosse, Elizabeth (Betsy) Dumont, Laurie Godfrey and Brigitte Holt for their advisory roles in his postgraduate education, and the formative conversations they had with him through the beginning of his research career. Without the opportunities they afforded him, he would never have got to where he is today.

He extends his deepest appreciation and sincerest gratitude to Sarah Elton. Through selfless support, critical insights and

constructive conversations, she helped him realize the importance of establishing the field of anthroengineering and has been instrumental to the development of anthroengineering, asking for nothing in return. Finally, he thanks Asa Barber, Robin Jones, Alessio Corso and countless others at LSBU for taking a chance on him and his dream.

P.A.K. thanks Gerald G. Eck for allowing a structural engineer to aspire to be a palaeobiomechanist. The pleasure of teaching anthropologists about statics, dynamics and mechanics of materials is based solely on the enthusiasm to explore this material that so many students over the years have exhibited. She also thanks Stephen K. Benirschke, MD for support to stay 'in the game'.

References

- Klein JT. 2008 Evaluation of interdisciplinary and transdisciplinary research: a literature review. *Am. J. Prev. Med.* **35**, S116–S123. (doi:10.1016/j.amepre.2008.05.010)
- Kramer PA. 1999 Modelling the locomotor energetics of extinct hominids. *J. Exp. Biol.* **202**, 2807–2818. (doi:10.1242/jeb.202.20.2807)
- Weber GW, Bookstein FL, Strait DS. 2011 Virtual anthropology meets biomechanics. *J. Biomed.* **44**, 1429–1432. (doi:10.1016/j.jbiomech.2011.02.079)
- Wilson JR. 2000 Fundamentals of ergonomics in theory and practice. *Appl. Ergon.* **31**, 557–567. (doi:10.1016/S0003-6870(00)00034-X)
- Hertzberg HTE. 1955 Some contributions of applied physical anthropology to human engineering. *Ann. N. Y. Acad. Sci.* **63**, 616–629. (doi:10.1111/j.1749-6632.1955.tb32114.x)
- Ruff CB, Hayes WC. 1983 Cross-sectional geometry of Pecos Pueblo femora and tibiae—a biomechanical investigation: I. Method and general patterns of variation. *Am. J. Phys. Anthropol.* **60**, 359–381. (doi:10.1002/ajpa.1330600308)
- Ruff CB, Hayes WC. 1983 Cross-sectional geometry of Pecos Pueblo femora and tibiae—a biomechanical investigation: II. Sex, age, side differences. *Am. J. Phys. Anthropol.* **60**, 383–400. (doi:10.1002/ajpa.1330600309)
- Richmond BG, Wright BW, Grosse I, Dechow PC, Ross CF, Spencer MA, Strait DS. 2005 Finite element analysis in functional morphology. *Anat. Rec.* **283**, 259–274. (doi:10.1002/ar.a.20169)
- Rayfield EJ. 2007 Finite element analysis and understanding the biomechanics and evolution of living and fossil organisms. *Annu. Rev. Earth Planet. Sci.* **35**, 541–576. (doi:10.1146/annurev.earth.35.031306.140104)
- Strait DS, DSDSDS et al. 2013 Viewpoints: diet and dietary adaptations in early hominins: the hard food perspective. *Am. J. Phys. Anthropol.* **151**, 339–355. (doi:10.1002/ajpa.22285)
- Daegling DJ, Judex S, Ozcivici E, Ravosa MJ, Taylor AB, Grine FE, Teaford MF, Ungar PS. 2013 Viewpoints: feeding mechanics, diet, and dietary adaptations in early hominins. *Am. J. Phys. Anthropol.* **151**, 356–371. (doi:10.1002/ajpa.22281)
- Strait DS et al. 2009 The feeding biomechanics and dietary ecology of *Australopithecus africanus*. *Proc. Natl Acad. Sci. USA* **106**, 2124–2129. (doi:10.1073/pnas.0808730106)
- Grine FE et al. 2010 Craniofacial biomechanics and functional and dietary inferences in hominin paleontology. *J. Hum. Evol.* **58**, 293–308. (doi:10.1016/j.jhevol.2009.12.001)
- Gunn W, Otto T, Smith RC. 2013 *Design anthropology: theory and practice*. London, UK: Bloomsbury Academic.
- Griggs D et al. 2013 Sustainable development goals for people and planet. *Nature* **495**, 305–307. (doi:10.1038/495305a)
- Sachs JD. 2012 From millennium development goals to sustainable development goals. *Lancet* **379**, 2206–2211. (doi:10.1016/S0140-6736(12)60685-0)
- UN. 2015 *Transforming our world: the 2030 agenda for sustainable development*. See <https://sdgs.un.org/2030agenda>.
- Smith HB. 2020 Foreword. In *Dental wear in evolutionary and biocultural contexts* (eds C Schmidt, JT Watson), pp. xv–xxi. Cambridge, UK: Academic Press.
- De Groot I et al. 2016 New genetic and morphological evidence suggests a single hoaxer created 'Piltdown man'. *R. Soc. Open Sci.* **3**. (doi:10.1098/rsos.160679)
- Grine FE, Sponheimer M, Ungar PS, Lee-Thorp J, Teaford MF. 2012 Dental microwear and stable isotopes inform the paleoecology of extinct hominins. *Am. J. Phys. Anthropol.* **148**, 285–317. (doi:10.1002/ajpa.22086)
- Ungar PS, Abella EF, Burgman JHE, Lazagabaster IA, Scott JR, Delezenne LK, Manthi FK, Plavcan JM, Ward CV. 2017 Dental microwear and Pliocene paleocommunity ecology of bovids, primates, rodents, and suids at Kanapoi. *J. Hum. Evol.* **140**, 102315. (doi:10.1016/j.jhevol.2017.03.005)
- Frayer DW, Clarke RJ, Fiore I, Blumenshine RJ, Pérez-Pérez A, Martinez LM, Estebaranz F, Holloway R, Bondioli L. 2016 OH-65: The earliest evidence for right-handedness in the fossil record. *J. Hum. Evol.* **100**, 65–72. (doi:10.1016/j.jhevol.2016.07.002)
- Bermúdez de Castro J, Bromage TG, Jalvo YF. 1988 Buccal striations on fossil human anterior teeth: evidence of handedness in the middle and early Upper Pleistocene. *J. Hum. Evol.* **17**, 403–412. (doi:10.1016/0047-2484(88)90029-2)
- Archard JF, Hirst W. 1956 The wear of metals under unlubricated conditions. *Proc. R. Soc. Lond. A* **236**, 397–410. (doi:10.1098/rspa.1956.0144)
- Amini S, Miserez A. 2013 Wear and abrasion resistance selection maps of biological materials. *Acta Biomater.* **9**, 7895–7907. (doi:10.1016/j.actbio.2013.04.042)
- Pödra P, Andersson S. 1999 Simulating sliding wear with finite element method. *Tribol. Int.* **32**, 71–81. (doi:10.1016/S0301-679X(99)00012-2)
- Lucas PW et al. 2013 Mechanisms and causes of wear in tooth enamel: implications for hominin diets. *J. R. Soc. Interface* **10**, 20120923. (doi:10.1098/rsif.2012.0923)
- Xia J, Zheng J, Huang D, Tian ZR, Chen L, Zhou Z, Ungar PS, Qian L. 2015 New model to explain tooth wear with implications for microwear formation and diet reconstruction. *Proc. Natl Acad. Sci. USA* **112**, 10 669–10 672. (doi:10.1073/pnas.1509491112)
- Lawn BR, Lee JJ-W, Chai H. 2010 Teeth: among nature's most durable biocomposites. *Annu. Rev. Mater. Res.* **40**, 55–75. (doi:10.1146/annurev-matsci-070909-104537)
- Chai H, Lee JJ-W, Constantino PJ, Lucas PW, Lawn BR. 2009 Remarkable resilience of teeth. *Proc. Natl. Acad. Sci. USA* **106**, 7289–7293. (doi:10.1073/pnas.0902466106)
- Ziscovici C, Lucas PW, Constantino PJ, Bromage TG, van Casteren A. 2014 Sea otter dental enamel is highly resistant to chipping due to its microstructure. *Biol. Lett.* **10**, 20140484. (doi:10.1098/rsbl.2014.0484)
- Constantino PJ, Lee JJ-W, Chai H, Zipfel B, Ziscovici C, Lawn BR, Lucas PW. 2010 Tooth chipping can reveal the diet and bite forces of fossil hominins. *Biol. Lett.* **6**, 826–829. (doi:10.1098/rsbl.2010.0304)
- van Casteren A et al. 2018 Evidence that metallic proxies are unsuitable for assessing the mechanics of microwear formation and a new theory of the meaning of microwear. *R. Soc. Open Sci.* **5**, 171699. (doi:10.1098/rsos.171699)
- Xia J, Zhou Z, Qian L, Ungar PS. 2018 Comment on van Casteren et al. (2018): softer metallic spheres do abrade harder enamel. *R. Soc. Open Sci.* **5**, 181376. (doi:10.1098/rsos.181376)
- Rabenold D, Pearson OM. 2014 Scratching the surface: a critique of Lucas et al. (2013)'s conclusion that phytoliths do not abrade enamel. *J. Hum. Evol.* **74**, 130–133. (doi:10.1016/j.jhevol.2014.02.001)
- Lucas PW et al. 2014 The role of dust, grit and phytoliths in tooth wear. *Ann. Zool. Fennici* **51**, 143–152. (doi:10.5735/086.051.0215)
- Constantino PJ, Borrero-Lopez O, Pajares A, Lawn BR. 2015 Simulation of enamel wear for reconstruction of diet and feeding behavior in fossil animals: a micromechanics approach. *Bioessays* **38**, 89–99. (doi:10.1002/bies.201500094)
- Borrero-Lopez O, Pajares A, Constantino PJ, Lawn BR. 2015 Mechanics of microwear traces in tooth enamel. *Acta Biomater.* **14**, 146–153. (doi:10.1016/j.actbio.2014.11.047)



Bleuler's Psychopathological Perspective on Schizophrenia Delusions: Towards New Tools in Psychotherapy Treatment

Filipe Arantes-Gonçalves^{1,2}, João Gama Marques^{3,4*} and Diogo Telles-Correia^{3,5}

¹ CliniPinel, Lisbon, Portugal, ² Clínica de Saúde Mental do Porto, Porto, Portugal, ³ Clínica Universitária de Psiquiatria e Psicologia Médica, Faculdade de Medicina, Universidade de Lisboa, Lisbon, Portugal, ⁴ Consulta de Esquizofrenia Resistente, Centro Hospitalar Psiquiátrico de Lisboa, Lisbon, Portugal, ⁵ Serviço de Psiquiatria e Saúde Mental, Hospital de Santa Maria, Centro Hospitalar de Lisboa Norte, Lisbon, Portugal

OPEN ACCESS

Edited by:

Drozdstoy Stoyanov Stoyanov,
Plovdiv Medical University, Bulgaria

Reviewed by:

Susana Lédo,
i3S, Instituto de Investigação e
Inovação em Saúde, Portugal
Joao Luis Freitas,
Hospital de Magalhães Lemos,
Portugal

*Correspondence:

João Gama Marques
joaogamamarques@gmail.com

Specialty section:

This article was submitted to
Psychopathology,
a section of the journal
Frontiers in Psychiatry

Received: 02 May 2018

Accepted: 19 June 2018

Published: 17 July 2018

Citation:

Arantes-Gonçalves F, Gama Marques J and Telles-Correia D (2018)
Bleuler's Psychopathological Perspective on Schizophrenia Delusions: Towards New Tools in Psychotherapy Treatment.
Front. Psychiatry 9:306.
doi: 10.3389/fpsy.2018.00306

The authors begin by addressing the historical evolution of the delusion concept and its different approaches, focusing afterwards mainly on the work of Bleuler, who stressed the proximity between delusions and the emotional life of patients with schizophrenia. Therefore, the present work intends to review the main aspects of the theory of delusion formation in schizophrenia according to Bleuler's psychopathological perspective. For that purpose, first the role of delusions in the psychopathology of schizophrenia is explored in a close relation with the Bleuler's fundamental symptoms (Alogia, Autism, Ambivalence, and Affect Blunting) nowadays known as negative symptoms. Then, persecutory, grandiosity and sexual delusions in schizophrenia are described according to the tension between logic and affects, as well as, internal conflict, schizoid features, and auto-erotism as key psychopathological pathways. Thus, with this subjective perspective, it is intended to highlight Bleuler's psychopathological contribution to the affective and meaningful causality of delusions in schizophrenia. The former might be useful in the integration with other psychopathological phenomena (hallucinations and negative symptoms) and new forms of research and therapeutic approaches in this disorder that are complementary with the contemporary tendencies in psychopathology.

Keywords: affectivity, Bleuler, delusions, schizophrenia, psychopathology

INTRODUCTION

Throughout the history of psychopathology the term delusion had several meanings distant from its current meaning of thought disorder (1). In antiquity and in the eighteenth and nineteenth centuries' French Psychiatry, the term *délire* (delusion), meant general detachment from reality that was not specific of thought impairment (1).

In eighteenth and nineteenth centuries' French Psychiatry, the term delusion included disturbances of thought, perception, emotions and affects and even psychomotoricity (2). By contrast, in the twentieth century German and British Psychiatry, the term delusion gradually became synonymous with a false belief, a disorder of the thought content (3). This tendency was generalized in the majority of the European countries and also in the United States of America, with the replacement of the old broader concept by a newer and narrower concept of delusion as a disorder of thought content.

Jaspers defined delusion as a disorder in the content of thought, separating it from other psychopathological disorders such as perception, affect and personality's. He considered primary delusion incomprehensible and in discontinuity with the individual's personality (4).

However, throughout the twentieth century, some authors such as Freud and Bleuler were not satisfied with the Jasperian definition of primary delusion as an isolated and incomprehensible phenomenon, and tried to integrate it in the general psychic life of patients.

For Freud, delusions result from a conflict between the ego and the external world that makes the former lose its contact with reality, mainly because of an intolerable frustration (5). He assumes that delusions might occupy the place left by that loss of contact with reality (6). These efforts to recapture the outside world through delusion occur in continuity with the emotional memories of the patient, previous to reality detachment (5).

Bleuler thought much about delusion in schizophrenia, namely its relation with affect, personality and the proximity with what he called the fundamental symptoms (nowadays known as negative symptoms of schizophrenia). Bleuler was the first author to gather descriptive and analytical perspectives on the psychopathology of schizophrenia. He added comprehensive and interpretative components without forgetting the importance of psychopathological description and systematization. This is an example of how it is possible to integrate different paradigms regarding the same psychopathological phenomenon.

In this article, we intend to review the main aspects related to the theory of the formation of delusion in schizophrenia, according to Bleuler's psychopathological perspective.

THE ROLE OF DELUSIONS IN SCHIZOPHRENIA PSYCHOPATHOLOGY

Bleuler systematizes the clinical presentation of schizophrenias into fundamental, accessory, primary and secondary symptoms. The fundamental symptoms, which are virtually present through all the course of the disorder (7), are also known as the famous Bleuler's four A's: Alogia, Autism, Ambivalence, and Affect blunting (8). Delusion is regarded as one of the accessory symptoms because it is episodic in the course of schizophrenia. Among the primary symptoms one can find alogia that Bleuler claimed to have a neurological etiology. All the remaining symptoms, including delusion, are considered secondary symptoms because they are an attempt of psychogenic compensation of the deficits caused by alogia. Bleuler conceptualized delusion as an accessory and secondary symptom in schizophrenia's psychopathology in very close relation with fundamental symptoms.

In alogia, as the logical thought weakens, affects become predominant and dominate the associations of the thinking processes (9). Based on this hypothesis, Bleuler described a link from alogia to delusion formation, with wishes and fears dominating the association of thoughts, bringing way to autistic thought, withdrawing the patient from external reality, predisposing him to delusion formation (7).

Regarding autism, it can be conceptualized as the predominance of inner life that distances the patient from external reality. In this sense, autism can be seen as a difficulty in contact with others (auto-erotism) but also as social isolation and negativism predisposing the patient to delusion formation (10).

Concerning affect blunting, Bleuler argues that although affects seem to be decreased at superficial psychiatric observation, they are very intense at deeper layers of the psychic life of the patient (11). Affect blunting might predispose patients with schizophrenia to delusion specifically when interpersonal conflicts bring to surface those apparently hidden emotions.

Finally, ambivalence is described as a tendency to be in the presence of contradictory feelings. Bleuler described this ambivalence as much more intense, regarding anxiety, than the one present in neurotic (not psychotic) patients (12). Considering this intense anxiety in schizophrenia's ambivalence, delusions represent a psychopathological way of dealing with these internal and emotional conflicts.

THEORY OF DELUSION FORMATION IN SCHIZOPHRENIA

According to Kraepelin (13), delusions were incorrect ideas created, not by an accidental failure of logic, but by an inner need of the patient (13). And for Bleuler and Brill (9) the most important inner needs are the affective ones. In that sense, delusions always follow a definite direction corresponding to the patients affects, and in the vast majority of cases cannot be corrected by new experience or instructions, as long as the condition which gave origin to them remains (9). Thus, delusions have their origin mainly in belief instead of logic. From Bleuler's point of view, delusions are frequently egocentric and very significant for the personality of the patient (7). By other words we can stress that the delusions thematic is mainly anchored in the patient's biography.

Bleuler acknowledges that the strength of affects (in affect blunting) combined with the weakness of logic (alogia) is the most common feature in delusions formation. When affects are present and strong, patients are more prone to logic errors, which mean that affects have a key-role in the formation of delusions (7). The latter ones might be conceptualized as stemming from unconscious thinking derived from the wide splitting of mental functions (9) where the autonomy of traumatic emotional memories becomes predominant. These traumatic emotional memories belong to the autistic way of thinking, based on the fantasies that are detached from reality. So autistic thinking and affective needs take advantage, over realistic and logical thinking, and patients become vulnerable to delusion formation (10).

PSYCHOPATHOLOGICAL MECHANISMS IN DELUSION FORMATION IN SCHIZOPHRENIA

As previously addressed, Bleuler argued that delusions were a secondary, psychogenic, kind of symptom, involving different

specific psychopathological mechanisms: internal conflict, schizoid features, and auto-erotism (12).

In internal conflict we can assume that traumatic emotional memories have influence in realistic thinking, giving rise to conflict between internal and external reality. Moreover, there is a tension because of the imbalance between pleasant and unpleasant affects and delusion formation is the only way allowing traumatic emotional memories to manifest (11).

Regarding schizoid features, Bleuler claimed that these personality traits are essential and in accordance with the autistic way of thinking (11). This kind of thinking, based on fantasies turns the patient away from reality, liberating subjective wishes, but without further adaptation (10). It always seeks pleasure and avoids pain. Freud argued that schizophrenic delusions are not only wish-fulfilling but also the attempt to recapture lost internal objects (6).

Finally, auto-erotism is as a key-feature of autism in schizophrenia as negativism has frequently an erotic side that may be pleasant as flirting, unpleasant as harassment, or both at the same time (12).

PERSECUTORIAL DELUSIONS

In this kind of delusion, Bleuler considers that there is frustration after a great ambition of the patient is not achieved (11). The patient is kept in an internal conflict between denying and accepting this frustration that may decrease his self-esteem, damaging his narcissism. Many patients in this situation cannot deal with failure and project their guilt feelings in people around them (7). Without this contradiction between ambition (wishes) and reality (possibilities) there would be no delusion of persecution (11). In other words, first patients don't have what they wish, then they don't admit their incompetency and the result is the delusion of persecution, blaming others for their failure (9). Delusion of persecution is the most common type of delusion in schizophrenia (7).

GRANDIOSITY DELUSIONS

Very frequently grandiosity delusion is secondary to persecutory delusion (6, 14, 15). When the projection of guilt (persecutory delusion) fails to balance internal wishes and external reality, delusion of grandiosity may occur as a fulfillment of the repressed wish (11). As the external reality contradicts the guilt projected into the outside world, narcissistic injury to self-esteem grows, leaving the patient with the escape of wish-fulfillment through delusion of grandiosity (7). In other words the patient justifies his persecution delusion with a grandiose explanation, feeling him as an extremely important person, thus restoring his fragile self-esteem (9). Delusion of grandiosity is the second most common type of delusions in schizophrenia (7).

SEXUAL DELUSIONS

This kind of delusions is also very common in schizophrenia. Usually, the patient believes it is forbidden for him to do what

he wishes, under threats of danger, or punishment (12). Bleuler conceptualized that sexual thematic memories have a prominent role in schizophrenia as many patients presented sexual delusions of being loved (delusional erotomania), abused (delusional rape), or pregnant (delusional gestation). According to Bleuler, sexual delusions are a combination of persecutory and grandiosity delusions (7) and can also express the traumatic emotional memories that belong to the autistic way of thinking.

DISCUSSION

Nowadays the biological paradigm has monopolized psychopathology's studies, leaving meaning and symbolic causalities behind. This approach brought a reductive and poor view of psychopathology which could and should be enriched with other lines of thought.

For Bleuler, patients' affects are extremely important in the formation of delusions in schizophrenia, and this perspective may be useful in the investigation of new forms of therapeutic approach of this disorder. It also represents humanistic and patient-centered approach regarding the patient with schizophrenia, and reflects what is actually observed in clinical practice.

Bleuler also pointed out that delusions cannot be evaluated and studied separately from the rest of psychopathology. This view is in agreement with several authors of French psychopathologists (e.g., Esquirol and Henry Ey) for whom delusions were very close to other psychopathological phenomena such as hallucinations, an interdependence that has already been approached conceptually and empirically by more recent authors (16–18).

Another important aspect of Bleuler's vision is the proximity between positive and negative symptoms. For Bleuler they are strongly linked, with the negative symptoms preceding the positive symptoms (e.g., delusions).

In sum, with Bleuler, schizophrenia deserves to be approached not only from an objective perspective but also from a subjective perspective (taking into account the affective component, and the symbolic causality) in order to grasp the real picture of what is happening inside the patients.

New research could be based on this line of thought. Namely the study of the role of psychological trauma and emotional memory in schizophrenia patients' psychopathology, trying to add complementary knowledge to genetic studies, building bridges between genetics and environment (nowadays called epigenetics); On the other hand it would be interesting to assess the effectiveness of psychotherapies (which focus on factors related to the affective and the meaningful components of symptoms), alone or in combination with psychopharmacology in the treatment of schizophrenia.

AUTHOR CONTRIBUTIONS

FA-G conceptualized and wrote the first draft of the manuscript. JG contributed with commentaries and suggestions. DT-C reviewed and supervised all the writing process.

$$\forall -\infty < x_2 < \infty, -\infty < x_3 < \infty \text{ and } -\infty < x_4 < \infty \quad (5.18)$$

$$\begin{aligned} \mathcal{V}_2^0(x_3, x_4, x_1; \xi_1, \xi_2, \xi_3, \xi_4) &= 0, \\ \forall -\infty < x_3 < \infty, -\infty < x_4 < \infty \text{ and } -\infty < x_1 < \infty \end{aligned} \quad (5.19)$$

$$\begin{aligned} \mathcal{V}_3^0(x_4, x_1, x_2; \xi_1, \xi_2, \xi_3, \xi_4) &= 0, \\ \forall -\infty < x_4 < \infty, -\infty < x_1 < \infty \text{ and } -\infty < x_2 < \infty \end{aligned} \quad (5.20)$$

$$\begin{aligned} \mathcal{V}_4^0(x_1, x_2, x_3; \xi_1, \xi_2, \xi_3, \xi_4) &= 0, \\ \forall -\infty < x_1 < \infty, -\infty < x_2 < \infty \text{ and } -\infty < x_3 < \infty \end{aligned} \quad (5.21)$$

The phase angles ξ_1, ξ_2, ξ_3 and ξ_4 are chosen such that they satisfy the prerequisites (5.18), (5.19), (5.20) and (5.21). In (C.1), (5.12), (5.13) and (5.14), the phase angles $\xi_1 = -\frac{\pi}{4}, \xi_2 = \frac{\pi}{4}, \xi_3 = \frac{\pi}{4}$ and $\xi_4 = \frac{\pi}{4}$ satisfy (5.18), (5.19), (5.20) and (5.21):

$$\frac{\mathcal{V}_1^0(x_2, x_3, x_4; -\frac{\pi}{4}, \frac{\pi}{4}, \frac{\pi}{4}, \frac{\pi}{4})}{v_r^2} = 0 \quad (5.22)$$

$$\frac{\mathcal{V}_2^0(x_3, x_4, x_1; -\frac{\pi}{4}, \frac{\pi}{4}, \frac{\pi}{4}, \frac{\pi}{4})}{v_r^2} = 0 \quad (5.23)$$

$$\frac{\mathcal{V}_3^0(x_4, x_1, x_2; -\frac{\pi}{4}, \frac{\pi}{4}, \frac{\pi}{4}, \frac{\pi}{4})}{v_r^2} = 0 \quad (5.24)$$

$$\frac{\mathcal{V}_4^0(x_1, x_2, x_3; -\frac{\pi}{4}, \frac{\pi}{4}, \frac{\pi}{4}, \frac{\pi}{4})}{v_r^2} = 0 \quad (5.25)$$

Taking note that g_i^0 equals \mathcal{V}_i^0 , the following expressions are derived for g_i^0 and

$$g^0(x_1, x_2, x_3, x_4) = \sum_{k=1}^4 \frac{\partial \mathcal{V}_k^0}{\partial x_k}:$$

$$g_1^0 = -\frac{v_r^2 \alpha}{2} \cos(2\alpha x_1) \sin(2\alpha x_3) \quad (5.26)$$

$$g_2^0 = -\frac{v_r^2 \alpha}{2} \cos(2\alpha x_2) \sin(2\alpha x_4) \quad (5.27)$$

$$g_3^0 = -\frac{v_r^2 \alpha}{2} \cos(2\alpha x_3) \sin(2\alpha x_1) \quad (5.28)$$

$$g_4^0 = -\frac{v_r^2 \alpha}{2} \cos(2\alpha x_4) \sin(2\alpha x_2) \quad (5.29)$$

$$\begin{aligned} \frac{\mathcal{G}^0(x_1, x_2, x_3, x_4)}{v_r^2} &= \alpha^2 \sin(2\alpha x_1) \sin(2\alpha x_3) \\ &\quad + \alpha^2 \sin(2\alpha x_2) \sin(2\alpha x_4) + \\ &\quad + \alpha^2 \sin(2\alpha x_3) \sin(2\alpha x_1) \\ &\quad + \alpha^2 \sin(2\alpha x_4) \sin(2\alpha x_2) \end{aligned} \quad (5.30)$$

By substituting $\mathcal{G}^0(x_1, x_2, x_3, x_4)$ from (5.30) into (5.6) and evaluating the definite integrals term by term, we can see that the results equal g_i^0 derived from (2.6); that is, $\mathcal{U}_i^0 \equiv 0, i = 1, 2, 3, 4$. We have used the integral identity (B.9) in Appendix B to perform the integrations.

Substituting for the initial condition $v_i^0, i = 1, 2, 3, 4$ from (5.1), (5.2), (5.3) and (5.4) into (3.12) with phase angles ξ_1, ξ_2, ξ_3 and ξ_4 set, respectively, to $\xi_1 = -\frac{\pi}{4}, \xi_2 = \frac{\pi}{4}, \xi_3 = \frac{\pi}{4}$ and $\xi_4 = \frac{\pi}{4}$ and performing the integrations, we arrive at the solution of the Navier-Stokes equation (2.1) in four dimensions:

$$\begin{aligned} v_1 &= v_r \left[\sin\left(\alpha x_1 - \frac{\pi}{4}\right) \cos\left(\alpha x_2 + \frac{\pi}{4}\right) \right. \\ &\quad \times \sin\left(\alpha x_3 + \frac{\pi}{4}\right) \cos\left(\alpha x_4 + \frac{\pi}{4}\right) \\ &\quad \left. - \sin\left(\alpha x_1 + \frac{\pi}{4}\right) \sin\left(\alpha x_2 + \frac{\pi}{4}\right) \right] e^{-4\alpha^2 kt} \end{aligned} \quad (5.31)$$

$$\begin{aligned} v_2 &= v_r \left[\sin\left(\alpha x_2 - \frac{\pi}{4}\right) \cos\left(\alpha x_3 + \frac{\pi}{4}\right) \right. \\ &\quad \times \sin\left(\alpha x_4 + \frac{\pi}{4}\right) \cos\left(\alpha x_1 + \frac{\pi}{4}\right) \\ &\quad - \sin\left(\alpha x_2 + \frac{\pi}{4}\right) \sin\left(\alpha x_3 + \frac{\pi}{4}\right) \\ &\quad \left. \times \cos\left(\alpha x_4 + \frac{\pi}{4}\right) \cos\left(\alpha x_1 - \frac{\pi}{4}\right) \right] e^{-4\alpha^2 kt} \end{aligned} \quad (5.32)$$

$$\begin{aligned} v_3 &= v_r \left[\sin\left(\alpha x_3 - \frac{\pi}{4}\right) \cos\left(\alpha x_4 + \frac{\pi}{4}\right) \right. \\ &\quad \times \sin\left(\alpha x_1 + \frac{\pi}{4}\right) \cos\left(\alpha x_2 + \frac{\pi}{4}\right) \\ &\quad - \sin\left(\alpha x_3 + \frac{\pi}{4}\right) \sin\left(\alpha x_4 + \frac{\pi}{4}\right) \\ &\quad \left. \times \cos\left(\alpha x_1 + \frac{\pi}{4}\right) \cos\left(\alpha x_2 - \frac{\pi}{4}\right) \right] e^{-4\alpha^2 kt} \end{aligned} \quad (5.33)$$

$$\begin{aligned} v_4 &= v_r \left[\sin\left(\alpha x_4 - \frac{\pi}{4}\right) \cos\left(\alpha x_1 + \frac{\pi}{4}\right) \right. \\ &\quad \times \sin\left(\alpha x_2 + \frac{\pi}{4}\right) \cos\left(\alpha x_3 + \frac{\pi}{4}\right) \\ &\quad - \sin\left(\alpha x_4 + \frac{\pi}{4}\right) \sin\left(\alpha x_1 + \frac{\pi}{4}\right) \\ &\quad \left. \times \cos\left(\alpha x_2 + \frac{\pi}{4}\right) \cos\left(\alpha x_3 - \frac{\pi}{4}\right) \right] e^{-4\alpha^2 kt} \end{aligned} \quad (5.34)$$

We have used the integral identities (B.1)–(B.3) given in Appendix B to perform the integrations.

Pressure is obtained from the solution of the Poisson equation (3.2). Because (3.10) is satisfied, we can express (3.5) as follows:

$$\frac{\partial p}{\partial x_i} = -\rho g_i = -\rho g_i^0 e^{-8\alpha^2 kt} \quad i = 1, 2, 3, 4 \quad (5.35)$$

This leads to straightforward integration for pressure:

$$p = \frac{\rho v_r^2}{4} [\sin(2\alpha x_1) \sin(2\alpha x_3) + \sin(2\alpha x_2) \sin(2\alpha x_4)] e^{-8\pi^2 kt} \quad (5.36)$$

6. Concluding remarks

The statement of the problem and the edifice of the proposed solution method in a space having an arbitrary number of dimensions, \mathbb{R}^n , are presented in Sections 2 and 3, respectively. The pressure field is formally obtained by taking the divergence of the Navier-Stokes equation (2.1) as a solution to the Poisson equation, yielding an expression (3.5) for pressure gradient. By inserting the pressure gradient back into (2.1) and equating the unsteady terms, $\frac{\partial v_i}{\partial t}$, to the sum of three terms that are associated, respectively, with the linear viscous force, the nonlinear inertial force and the externally applied force acting on the fluid we obtain the rephrased Navier-Stokes equation (3.7). Subject to satisfying an integral equation (3.10), (3.7) is then reduced to a non-homogeneous diffusion equation in velocity. When the externally applied force is set to zero, it is further reduced to the Cauchy diffusion equation. The nonlinearity is entirely isolated to the integral equation (3.10).

Succinctly put, subject to satisfying a certain condition (3.10), the Navier-Stokes system of equations is decomposed into two linear equations, the non-homogeneous diffusion equation and the Poisson equation, for the velocity and pressure fields respectively. The velocity and pressure fields are given by the solutions of Cauchy diffusion equation and Poisson equation respectively. The proposed solution methods belong to the class of Beltrami flows and are valid under proper regularity conditions at infinity.

Fractality of sensations and the brain health: the theory linking neurodegenerative disorder with distortion of spatial and temporal scale-invariance and fractal complexity of the visible world

Marina V. Zueva *

The Division of Clinical Physiology of Vision, Federal State Budgetary Institution "Moscow Helmholtz Research Institute of Eye Diseases" of the Ministry of Healthcare of the Russian Federation, Moscow, Russia

OPEN ACCESS

Edited by:

P. Hemachandra Reddy,
Texas Tech University, USA

Reviewed by:

Gerfried Karl Hans Nell,
NPC Nell Pharma Connect Ltd.,
Austria

Stefano Giovagnoli,
University of Perugia, Italy

*Correspondence:

Marina V. Zueva,
The Division of Clinical Physiology
of Vision, Federal State Budgetary
Institution "Moscow Helmholtz
Research Institute of Eye Diseases" of
the Ministry of Healthcare of the
Russian Federation,
14/19 Sadovaya-Chernogriazskaya
Street, Moscow 105062, Russia
visionlab@yandex.ru

Received: 12 December 2014

Accepted: 02 July 2015

Published: 15 July 2015

Citation:

Zueva MV (2015) Fractality
of sensations and the brain health:
the theory linking neurodegenerative
disorder with distortion of spatial
and temporal scale-invariance
and fractal complexity of the visible
world.

Front. Aging Neurosci. 7:135.
doi: 10.3389/fnagi.2015.00135

The theory that ties normal functioning and pathology of the brain and visual system with the spatial-temporal structure of the visual and other sensory stimuli is described for the first time in the present study. The deficit of fractal complexity of environmental influences can lead to the distortion of fractal complexity in the visual pathways of the brain and abnormalities of development or aging. The use of fractal light stimuli and fractal stimuli of other modalities can help to restore the functions of the brain, particularly in the elderly and in patients with neurodegenerative disorders or amblyopia. Non-linear dynamics of these physiological processes have a strong base of evidence, which is seen in the impaired fractal regulation of rhythmic activity in aged and diseased brains. From birth to old age, we live in a non-linear world, in which objects and processes with the properties of fractality and non-linearity surround us. Against this background, the evolution of man took place and all periods of life unfolded. Works of art created by man may also have fractal properties. The positive influence of music on cognitive functions is well-known. Insufficiency of sensory experience is believed to play a crucial role in the pathogenesis of amblyopia and age-dependent diseases. The brain is very plastic in its early development, and the plasticity decreases throughout life. However, several studies showed the possibility to reactivate the adult's neuroplasticity in a variety of ways. We propose that a non-linear structure of sensory information on many spatial and temporal scales is crucial to the brain health and fractal regulation of physiological rhythms. Theoretical substantiation of the author's theory is presented. Possible applications and the future research that can experimentally confirm or refute the theoretical concept are considered.

Keywords: fractal therapy, dynamical chaos, fractality of sensations, reactivation of brain plasticity, treatment and rehabilitation, aging, neurodegenerative diseases, amblyopia

Abbreviations: AD, Alzheimer's disease; DR, diabetic retinopathy; EE, environmental enrichment; EEG, electroencephalography; HD, Huntington's disease; PD, Parkinson's disease; PERG, pattern electroretinogram; SCN, suprachiasmatic nucleus; SR, stochastic resonance.

The Theory

Comparison of the known facts, phenomena and relationships, and logical analysis makes it possible to assume that the spatial-temporal structure of our incoming sensory information represents the key driver of the healthy development of the brain. Man is a subject and object of the dynamic chaos of nature. Natural fractals accompany us throughout our lives. Additionally, all the wealth of sensations that we receive, enjoying the results of other people's creativity and in the process of our creative thinking we can also refer to the "fractality of sensations." Distortion of the fractality of sensations may be a factor contributing to the weakening of brain's functions, distortion in cognitive performance and dynamics of gait by reducing the capacity of adaptive plasticity.

In this article, an objectively existing relationship between normal functioning or pathology of the brain and the spatial-temporal structure of the visual, auditory, and other stimuli that affect people throughout the life was proposed to exist and theoretically substantiated. The theory argues that the deficit or distortion of the fractal complexity of visual and other environmental influences may lead to anomalies of development and aging. In the same time, the use of fractal flickering and other sensory modalities of fractal stimulation helps to restore the function of the brain by acting via activation of the brain plasticity. The application of fractal therapy can provide particular benefits in the elderly, in patients with neurodegenerative disorders and amblyopia.

The following assumptions are derived directly from the theoretically established relationship:

- Fractal geometry and non-linear dynamics of complex processes are not just a characteristic property that is inherent for all natural (environmental and biological) systems. It is a sign that determines the quality of human life.
- Fractal geometry and a non-linear dynamics of physiological processes of the human body are not only typical signs of a healthy body. It is a key feature, whose preservation, maintenance, and recovery is essential to maintain physical and mental human health throughout the life, from birth to old age.

Below, we present data collected from different areas of expertise that are relevant to theoretical substantiation of the theory, including:

- Evidence of the characteristic non-linear structures in nature, of the fractal geometry and dynamics in a healthy human body and brain, and the distortion of fractality correlated to aging and pathology;
- The current understanding of the brain plasticity, dependent on the sensory experience, and neuroplasticity changes in diseases related to abnormal development and age-related conditions;
- The techniques used today to reactivate the plasticity of the adult's brain, and recent new data that may indicate a

possible usage of sensory stimuli with the non-linear temporal structure to influence the neuroplasticity.

We should note that the conclusion about the role of fractal therapy in the treatment of a variety of human diseases may be an outcome of an analysis of previously known scientific facts (i). Similarly, it can immediately follow the present theory of an objective relationship between the fractality of the environment (and our sensations) and brain health (ii).

However, the difference in logical reasoning is as follows:

- (i) In the first case, the conclusion of the possible advantages of non-linear light therapy follows from the fact that the complex dynamics of some body functions usually follow the laws of deterministic chaos. In disease, this dynamics loses its complexity. Thus, it seems logical to try to recover the complexity of rhythms by using fractal entrainment cues to synchronize the dynamics of physiological fluctuations and external rhythms.
- (ii) In the second case, the expected benefits of fractal stimuli in training and therapy follow not from typical non-linear dynamics of healthy physiological processes. Opposite, these benefits follow from an understanding of the need to preserve, maintain and restore a complex (fractal) dynamics. In certain situations, including diseases, this may need to use artificially created fractal environment.

The Non-Linear World

Characteristic Patterns of Fractal Geometry and Dynamics in Nature and Man

Natural Fractals and the Human Body

From the birth to deep old age, we live in a non-linear world, at which the scene objects and processes with the properties of fractality and non-linearity surround us. Against this background, the evolution of man took place. Against this background, all periods of our lives unfold.

The non-linear nature of physical objects is well-known today (Kirillov and Pelinovsky, 2013). Fractal geometry, which is capable to describe the natural objects, and non-linear dynamics also have been applied in the field of biology and medicine. Fractals are the irregular geometric figures or a set of points, possessing the features of self-similarity and a fractional dimensionality. Self-similarity and scale invariance are the basic properties of fractals. It means that the structure of the fractal object remains unchanged with the increase in the image regardless of the zoom (Mandelbrot, 1982; Feder, 1988; Weibel, 1991; Bassingthwaite et al., 1994; Crownover, 1995; West et al., 1999). Nature example of the simplest mathematical fractal is a treelike structure with dichotomous self-similar branching, exhibiting properties of bifurcation. Natural fractals include the relief of the sea and river coastlines, of mountain ranges, the winding river networks. The Brownian crystal growth and lightning structure – all also belong to the natural fractals (Iannaccone and Khokha, 1996).

Natural fractal structures are the result of a process of self-organization in which the communication of structural levels of different scales occurs. Resulting natural fractal objects also have a self-similar structure, that is, with zooming such structures remain the same, regardless the scaling. Natural fractals belong to a class of statistical or random fractals. The fractal dimension sets the link between fractal structures and the properties of the environment. Fractal dimension usually exceeds the object topological dimension. Physical objects are rarely self-similar at an increase of more than four orders of magnitude (West et al., 1999). West et al. (1999, p. 1677) vividly noted: "Fractal-like networks effectively endow life with an additional fourth spatial dimension, the origin of quarter-power scaling that is so pervasive in biology." We can often see new principles of self-organization in biological objects in case of an increase by two orders (Crownover, 1995).

Many complex structures of living systems exhibit fractal-like geometry. In a human body, a variety of complex anatomical structures has fractal geometry. They show the property of self-similarity at several scales (Goldberger et al., 1990, 2002; Weibel, 1991; Bassingthwaite et al., 1994; Ayers, 1997; for review see Goldberger, 2006). Examples include the blood vessel branching, networks of the tracheobronchial tree and neural networks in the brain, the folds of the intestine, choroidal plexus, etc. Treelike fractals help describing and modeling of the tracheobronchial tree. Fractal structures are supposed to be very stable, because of their redundancy and irregularity (Goldberger et al., 2002).

Non-Linear Dynamics of Physiological Processes

For the description of dynamical, unpredictably time-varying systems, the concept of deterministic chaos is applied (Mandelbrot, 1982; Stewart, 1989; Crownover, 1995). The 'chaos' implies some definite properties of the deterministic dynamical system, the most important of which are a significant dependence of such system on the initial conditions, and its internal unpredictability. Any chaotic phenomenon we can describe with its trajectory in the analysis over time. The region in the phase space, in which the path of the system's behavior is visually concentrated, is called chaotic (strange) attractor. The self-similar nature of the fractal processes can be qualitatively assessed with a graphical representation of their fluctuations at various time resolutions (Belair et al., 1995; Beuter et al., 2003). The concept of strange attractors has led to a new hypothesis of systemic properties of higher cognitive functions that depend on the dynamic interactions between parallel streams of information (Mattei, 2013).

Complex physiological processes also exhibit irregular fluctuations across multiple time scales and can be described using the theory of deterministic chaos. Fluctuations of physiological rhythms of a healthy body have the properties of fractals (Goldberger et al., 1990, 2002; Peng et al., 1993, 2002; Yamamoto and Hughson, 1994). Healthy physiological rhythms such as heart rate, respiration (Fadel et al., 2004) demonstrate complex variability that can be quantified using the fractal concept and the concept of non-linear dynamics. The self-similar nature of these fluctuations we can see when plotting at different temporal resolutions. Complex physiological

dynamics allows the body to respond rapidly to internal and external perturbations of the environment (Lipsitz, 2004).

The special edition of *Frontiers in Computational Neuroscience* has included selected articles dedicated to the applications of non-linear and fractal analyses in different research fields in neuroscience and cognitive psychology (Mattei, 2014). The topic was assigned to 'Non-linear and Fractal Analysis in Neuroscience and Cognitive Psychology.' In this issue, the selected articles demonstrate usefulness of the non-linear analysis for modeling the healthy brain dynamics, for the diagnosis of neurological and psychiatric disorders, and monitoring of the therapeutic efficiency. The results of studies confirm that the advanced non-linear analysis helps to describe the complexity of brain dynamics accurately.

The healthy heartbeat interval was found to exhibit highly irregular behavior, fluctuating in a complex manner. Scaling analysis of cardiac interbeat time series demonstrated the presence of long-range fractal correlations in variations of the healthy heartbeat (Goldberger et al., 1990, 2002; Ivanov et al., 1999). The subtle, complex fluctuations of the inter-step (stride-to-stride) interval in the healthy human walking rhythm were also shown to exhibit the scale-invariance. Walking speed had no effects on the stride interval fluctuations and long-range correlations, indicating that the fractal variability in human gait in norm is quite robust (Hausdorff et al., 1995, 1996). While the dynamics of heartbeat has a chaotic pattern with signs of self-similarity, the tachycardia is relatively periodic and possesses a vivid rhythmic nature (cited from Goldberger et al., 2002).

In the spectrum of EEG of the healthy waking human brain the alpha rhythm dominates. Lehnhertz (1999) presented an overview of studies that demonstrated a fractal dimension of alpha rhythm. Different works reported that the chaotic behavior is, likely, characteristic of the activity of the healthy brain areas, single neurons and neural networks (Babloyantz, 1989; Schiff et al., 1994; Das, 2001; Faure and Korn, 2001; Korn and Faure, 2003; Izhikevich, 2007).

The chaotic behavior is believed to make neurons able to switch quickly between different states (Schiff et al., 1994). It provides the flexibility of the central nervous system (CNS) and its resistance to external influences. The non-linear behavior of axons and excitable cells seems to have the regulatory role of inhibitory coupling once chaotic cells become members of larger neuronal assemblies (Rabinovich and Abarbanel, 1998). It has been also suggested that chaos may contribute to the neuronal code (Skarda and Freeman, 1987; van Vreeswijk and Sompolinsky, 1996; So et al., 1998).

Disruption in Fractal Dynamics of Physiological Processes

Various studies have found correlations between the aging process or disease and a loss of the complexity of many physiological processes. In pathological conditions and aging, ordered fluctuations in the parameters of physiological functions were reported (Lipsitz and Goldberger, 1992; Goldberger et al., 2002; Peng et al., 2002). Diseases tend to cause highly periodic dynamics of the process, which is dominant on the same time scale. Chaos in health allows the body to respond adequately

to rapidly and unpredictably changing circumstances. Thus, the reduction of multiscale non-linear complexity of physiological functions in pathological conditions and human aging can potentially reduce opportunities for adaptation.

The disease is not always exhibited in an increase in the regularity of fluctuations. It might also lead to the extreme irregularity of changes, which, however, do not meet the criteria for non-linear chaos (Goldberger et al., 2002). Recent clinical study verifies that increasing age is associated with a reduction in the overall heart rate variability and complexity of physiological dynamics (Takahashi et al., 2012). These data were obtained using a Shannon entropy, conditional entropy, and symbolic analysis. In the aging process, the distributions of Shannon entropy patterns remained similar to younger subjects. At the same time, the patterns were more repetitive in the old group, indicating a marked change of autonomic regulation. A decrease in complex variability in the temporal patterns of heart rate that accompany aging and disease has been attributed to a breakdown of the underlying regulatory feedback mechanisms.

The fractal scaling showed disturbance in conditions associated with the disorder of breathing and obstructive sleep apnea (Goldberger, 1997; Goldberger et al., 2002). Recently, the band-limited transfer entropy analysis revealed a reduction in the high-frequency contribution of respiration to heart rate complexity with normal aging (Nemati et al., 2013). A fractal scaling in stride interval showed a reduction in the elderly. This was also reported for patients with pathological human walking (Dingwell and Cusumano, 2000) including PD (Hausdorff et al., 1997) and HD (Bilney et al., 2005).

Electromyography reflects the activity of the spinal motoneurons. As a non-linear signal, the surface electromyogram displays chaotic behavior and has a fractal dimension (Niemenen and Takala, 1996). The non-linear parameters of surface electromyogram signal in the PD patients significantly differ from the electromyogram in the healthy control persons (Meigal et al., 2009). Recently, Meigal et al. (2013) reported that the non-linear characteristics of surface electromyogram and tremor acceleration may have a possible diagnostic and predictive value for patients with PD.

The reduction in the multiscale complexity of the background brain activity has been shown in schizophrenia (Kotini and Anninos, 2002; Takahashi et al., 2010), epilepsy (Saermark et al., 1989), AD (Besthorn et al., 1995; Stam et al., 1996; Abásolo et al., 2005; Hornero et al., 2009), and PD (Stam et al., 1995; Anninos et al., 2000).

Three major effects of AD included slowing of the EEG, decrease in the EEG complexity, and disturbances in the EEG synchrony (Dauwels et al., 2010). Strong statistical evidence was obtained for a weak non-linearity in EEG in schizophrenia. Recent advances in methodology allow assuming that the “non-linear theory” of schizophrenia may be useful for the understanding of this disorder (Breakspear, 2006).

A branched vascular network of the normal human retina showed statistical self-similarity, exhibiting the properties of fractals (Family et al., 1989; Mainster, 1990; Daxer, 1993, 1995; Avakian et al., 2002; Masters, 2004). Several research groups presented strong evidence that the fractal dimension of blood

vessels in the normal human retina is about 1.7. In many publications, the fractal analysis of the human retinal vasculature at different stages of DR showed mixed results (for review see Zueva, 2014). The contradictory results may occur because the study design was not always adequate to answer this question. The studies did not have the specific aim to determine the correlation between the fractal dimension of the retinal vasculature and the stage of retinopathy. For example, in a large cohort of diabetic patients with the early stages of DR, the fractal dimension of the retinal vasculature was analyzed in association with the presence or absence of signs of retinopathy (Cheung et al., 2009). However, these data usually were not compared with the fractal dimension of the retina in healthy individuals without diabetes. At the same time, the presence of diabetes, even in the absence of signs of DR in the fundus, can, possibly, lead to the alterations of anatomical structures, including the vascular network.

The reduction in the complexity of a dendritic branching and length in magnocellular and parvocellular layers of the lateral geniculate nucleus was recently discovered when modeling glaucoma in adult non-human primates (Ly et al., 2011). Blockade of *N*-methyl-D-aspartate receptors with memantine attenuated a decrease in the dendrite complexity and length in the relay lateral geniculate nucleus neurons in primate glaucoma (cited from Ly et al., 2011). Destruction of the dendritic branching is one of the characteristics and a potential mechanism of neurodegeneration not only for glaucoma. In AD, it may induce infringement of architecture of neural networks (Moolman et al., 2004). Disturbances to dendrite branching can disrupt the neural network organization and lead to the neural dysfunction, as in human neurological disorders including AD.

Hu et al. (2009, 2013) reported recently that in the AD patients with dementia, a parallel destruction of circadian rhythmicity and fractal patterns of activity is more pronounced in patients with greater quantity of amyloid plaques. These authors also showed in postmortem investigation that the degree of disruption in fractal activity is strongly associated with vasopressin and angiotensin-ergic neurons in the SCN. It suggests that the SCN affects the regulation of human action at multiple temporal scales and that the alterations in the fractal activity can be non-invasive biomarkers of neurodegeneration.

The Fractality of Art

Fractal Architecture

Works of art created by man may also have fractal properties. Mandelbrot (1982) was the first who tried to distinguish the architectural styles in Euclidean and fractal geometry. The basic properties of fractal structures such as a self-similarity, fractional dimension, recursiveness, and discontinuity, were used in architecture by Peter Eisenman. Jencks, Kavannagh, Johnson, and Crowe also used them in their works (cited from Oswald, 2001). Oswald (2001) focused on 20 years experience in the implementation of fractal geometry in architecture and the main trends in the development and history of acceptance and rejection of the fractal concept. He presented an overview of the rise and fall of the fractal architecture in the late 20th century, noting prominent examples of historic buildings that

exhibit fractal forms. Many historic buildings demonstrate an intuitive understanding of fractal geometry but do not constitute consciously created fractal architecture. They include medieval castles, Baroque churches, and Hindu temples. Oswald (2001) noted as an intuitive type fractal design also the works of Frank Lloyd Wright and Louis Sullivan. A project of Peter Eisenman 'House 11a' has been the first example of architectural art that uses the concept of fractal scaling.

Some examples of folk architecture, which were built by people at different times around the world, have fractal properties (Bovil, 1996; Batty, 2005). One can assume that the most beautiful cities in the world are fractals (Batty, 2005), including a plan of the city, streets, building facades and landscaping plan. The fractal approach would allow making housing that adapts naturally to the needs of residents in the growth and transport (Frankhauser, 2008; Harris, 2012; Parashar and Bandyopadhyay, 2014). Architect James Harris explicitly notes that high-rise housing and high-density architecture can lose their usefulness in the modern city and is limited to individual cells, as in a prison or in a computer that controls the world. He also noted that similar to 'as the trees spread their leaves to catch the sun, cities have to unfold to give people the air and open space' (Harris, 2012). Lu et al. (2012) reviewed recently the basic concepts of chaos theory and fractal geometry required for the architecture design, which can anticipate changes in the environment, providing adaptability and flexibility over time.

Fractal Painting

Art and musical compositions can also have a fractal dimension. An iterated function system is commonly used for generation of fractal art. However, the fractal pictures appeared long before the concept of deterministic chaos (Briggs, 1992; Barnett, 2009). These famous paintings include "The Great Wave off Kanagawa" by Katsushika Hokusai, abstract painting by Jackson Pollock "Blue Poles: Number II," an abstract landscape by the Jenifer Bacon and Gottfried Mayer-Kress "Canyons and Mesas" (cited from Barnett, 2009; see also Taylor et al., 2002, 2006). Pollock dripped paint from a can onto vast canvases. Analysis of his patterns showed that they are fractals as "fingerprint of nature" (Taylor et al., 2002, 2006). Drip painting of Pollock has been attributed to the "Fractal expressionism."

Just as is the case in architecture, paintings of many artists seem to be fractals, despite the fact that they could not know about it. When creating fractal art an artist draws fractals, but does not create them using his computer. Forsythe et al. (2011) considered the visual complexity for some time as a predictor of the significance of artistic works. This study detected the extent to which the perceived complexity of visual art can be successfully predicted using automated measurement of complexity. As the most successful predictor of visual complexity, Forsythe et al. (2011) noted GIF compression. Interestingly, the value of the fractal dimension had a larger dispersion in judgments about the perception of beauty in visual art than in the measurement of only the visual complexity, especially for abstract and natural images. Their findings also showed that the removal of color from the artistic image made observers unable to create a meaningful judgment about its beauty (Forsythe et al., 2011).

Fractal Music

As well as for the fractal painting, fractal music can be a created intuitively fractal (in fine art), or can be created artificially by various methods. Hsü and Hsü (1990, 1991) have found that the change of acoustic sound in the compositions by Bach's and Mozart's has the fractal geometry. More recently the fractal dimension of different kinds of music (rock, traditional, classical music, and others – 180 scores) Bigerelle and Iost (2000) analyzed in keeping with the time domain. They showed that the fractal dimension helps to distinguish between categories of music; i.e., music can be classified by their fractal dimensions according to its dynamic aspects. Earlier, there was revealed with the fractal motion method that the "best-sounding" music has a fractal dimension near 1.4 (Hazard et al., 1998–1999).

The Plasticity of the Brain and Sensory Experience

Brain Plasticity and Multimodal Integration

Neuronal plasticity occurring in the sensory and motor systems is the amazing ability of the brain that allows adapting to the constantly changing world during early development, and also in young and older adults. At all levels of the CNS, plasticity may be caused by the loss or excess of mono- and multimodal stimulation and injury. It can occur as the consequence of non-use or over-use, and learning new skills (cited from Mousha and Kilgard, 2006).

Neuroplasticity refers to changes in the neural circuits and synapses, including migration and integration of new neurons, neurite outgrowth, synaptogenesis, and the modulation of mature synapses. These occur in a variety of CNS levels due to changes in external and internal environment (He et al., 2006; Pascual-Leone et al., 2011; Wainwright and Galea, 2013). These changes can develop due to the injury to the brain with large-scale cortical remapping, and alterations in behavior, emotions, and thinking.

Neuroplasticity is known to play a significant role in the development, learning, memory, and in recovery from brain injury. Developmental plasticity includes changes in neural connections due to brain/environment interactions, and cellular changes induced by learning. The predominant mechanisms of plastic alterations in CNS, which occur during development, include synaptic and homeostatic plasticity, and learning. Most synapses are highly plastic, and they change their strength under the influence of its activity and other forces. Synaptic plasticity is believed to play a role in the mechanisms of learning and memory (Black, 1998; Foehring and Lorenzon, 1999). Long-term potentiation and depression (synapse-specific Hebbian forms of plasticity) are related to the processes that regulate overall levels of neuronal and network activity. The experimental research has found several mechanisms that apparently monitor the levels of activity, such as a spike-timing dependent plasticity, synaptic scaling and synaptic redistribution (Abbott and Nelson, 2000). Homeostatic plasticity modulates the neural circuit activity and changes in the synaptic strength (Wierenga et al., 2006; Butz et al., 2009). So, it regulates the destabilizing effects of developmental and learning processes.

The brain is very plastic in its early development, but previously it was assumed that plasticity decreases throughout life, and the structure of the brain is relatively unchanged over the critical period during early childhood. However, this concept has been subjected to large revisions after numerous subsequent studies that have found various manifestations of the adult brain plasticity (Dragoi et al., 2000; Chen et al., 2011). The human brain is constantly changing, being in a state of reshaping each moment of the life (Eysel, 2002, 2009; Gilbert and Li, 2012; Sur et al., 2013). Moreover, the results of recent studies suggest that the development of cortex structure is never completed but shows continuing changes, which are intelligence-dependent (Schnack et al., 2014).

Neuronal plastic changes, which never stop, are studied the visual cortex. Experimental studies in animals indicate that visual cortex exhibits considerable plasticity during development (Hebb, 1947; Hubel and Wiesel, 1970; Gordon and Stryker, 1996; Espinosa and Stryker, 2012; Nagakura et al., 2013). Plasticity is also was found in adulthood (Dragoi et al., 2001; Chen et al., 2011; Rosa et al., 2013). Plasticity in the early development and in the adult visual cortex was hypothesized to share certain universal principles although mature synapse plasticity requires additional neurotransmitter-dependent mechanisms that alter inhibition and subsequently the response gain (Sur et al., 2013).

Spontaneous network spike activity in the brain and retina plays a significant role in the initial establishment of synaptic connections during development. It may establish a basis for subsequent learning and further refinement of neural circuits and brain connectivity. For example, spontaneous network activity in the retina prior to birth has been found to cause the formation of retinogeniculate connections (Feller, 2009). During critical periods in development, changes in the structure and function of developing neuronal circuits can be experience-dependent or independent of the environmental experience but undergo the influence of endogenous or exogenous factors (Black, 1998). After the critical periods, many factors guiding brain development, such as growth factors, have been shown to be downregulated. But they can be upregulated again in adulthood in response to lesions for re-activation of neuroplasticity (cited from Eysel, 2009). The adaptive plastic changes in the adult's brain are typically space-limited to the level of axonal terminals and synapses. Therefore, the formation of new functional connections can be done by strengthening or weakening of existing synapses in the network (cited from Eysel, 2009). The neuronal reorganization will take place if the environment is modified during early stages of development, for example, following visual deprivation through eyelid suturing, or dark-rearing (Bengoetxea et al., 2012).

The ability to simultaneously use signals from several senses at the same time (in their synergy) is a fundamental aspect of the brain functioning. Multisensory integration, which synthesizes all details of the currently accessible information, provides a complete picture of the outside world. Development of multisensory integration occurs by the principles of associative learning. The ability to integrate different sensory information evolves as neurons acquire experience with the co-active cross-modal inputs (Yu et al., 2010; Xu et al., 2012; Stein et al., 2014).

As an example, in the cortex of the cat, the maturation of healthy multisensory integration has occurred over an extended period of postnatal life. An experimental study in cats reared from birth to adulthood in the dark demonstrated that sensory experience is necessary for the maturation of the cortex multisensor circuits (Carriere et al., 2007). In the absence of multimodal experience, neurons do not develop the ability to integrate their inputs although capable to respond to multiple sensory modalities. The bond of different sensory channels with each other is absent in neonates. The emergence and maturation of multisensory integration depend on the content of the early sensory experience, changing and optimizing neural networks in the brain for the adaptation of animals and humans.

There is an increasing experimental evidence that sensory deprivation is associated with cross-modal neoplastic changes in the brain. Upon visual or auditory deprivation, brain regions that typically are associated with these sensory modalities begin to involve the intact sensory modalities (Wallace et al., 2004; Wallace and Stein, 2007; Merabet and Pascual-Leone, 2010; Meredith et al., 2012). In dark-reared cats, a recent study has revealed significant modifications in temporal dynamics of the receptive field structure and the integrity of superior colliculus multisensory neurons. These modifications included discharge duration, peak and the average rate of spiking, as well as significant changes in the frequency of spontaneous activation and the degree of multisensory integration (Royal et al., 2010). These authors performed an extracellular recording of electrical activity of neurons in the multisensory deep layers of the superior colliculus in kittens reared in complete darkness until adulthood and then returned to the usual environment for an equivalent period. The results emphasized the importance of early sensory experience in the establishment of normal architecture of multisensory processing and highlight the plastic potential of adult multisensory circuits.

Cross-modal experience in the early period of animal life is likely to define the integration of stimuli of different modalities. Periodical exposure of cats reared in darkness to visual and auditory stimuli appearing randomly in space and time was insufficient to encourage maturation of the ability for cross-modal integration. At the same time, the exposure to spatiotemporally concordant cross-modal stimuli was very efficient (Xu et al., 2012). In a recent investigation, animals were also reared in the constant omnidirectional noise. Xu et al. (2014) tested whether cross-modal co-activation is sufficient for visual-auditory superior colliculus neurons integration or a covariation experience is needed. The data testify that experience with covarying stimuli is the critical factor for multisensory maturation, maybe not only in the superior colliculus, but throughout the brain. It also indicated that disturbances in one sensory modality can have an adverse impact on the ability of the brain to associate multisensory information, which was shown earlier for perturbation of visual sensitivity. In the patients deprived of early visual input by bilateral congenital cataracts the alteration in the development of multisensory functions after a period of visual deprivation has been shown (Putzar et al., 2010). In this study, the cataract patients exhibited impaired audio-visual interaction compared to normally sighted controls.

It suggests that visual input is a prerequisite in early infancy for healthy development not only of visual, but also of multisensory functions.

Original and review reports (Rapp and Heindel, 1994; Grady, 2008; for review, see Mozolic et al., 2012) and a meta-analytic review (Rhodes, 2004) have shown that widespread changes in the anatomy of the white and gray matter, neurochemistry, and functional activity occur in the aging human brain. These changes correlated to significant changes in all sensory systems. Multisensory integration also alters with age. Surprisingly, neurons retain sensitivity to cross-modal experience late in life, far after the normal developmental period for acquiring multisensory integration capabilities (Yu et al., 2010).

Studies of various design have shown that the multisensory processing provides larger improvement of performance in older than in younger adults (Helper, 1998; Sommers et al., 2005; Laurienti et al., 2006; Peiffer et al., 2007; Diederich et al., 2008; DeLoss et al., 2013). Using a two-choice audiovisual discrimination task, Laurienti et al. (2006) showed larger improvement of response time for multisensory target compared to the mono sensory purpose for the elderly than for younger adults. Diederich et al. (2008) analyzed saccadic reaction time in older and younger adults to the switch-on visual stimuli presented with and without an accessory auditory stimulus. The responses in elderly subjects were considerably slower than in the more youthful observers. However, the decrease in mean response time to bimodal stimuli compared to the single visual stimuli was more prominent in the elderly participants (Diederich et al., 2008).

Visual cortex plasticity results from a complex interplay between the individual's genetic background and the environment (Maya-Vetencourt and Origlia, 2012). Childhood environment effects, favorable or unfavorable, such as childhood neglect, interfere with all the development processes of the CNS. These events include neurogenesis, the formation and branching of neuronal processes, synaptogenesis, refinement of synaptic circuits, and myelination. The development of synaptic pathways usually occurs by the rule "use it or lose it" (Perry, 2002; Shors et al., 2012). That is, not only genetic, but also environmental aspects ("nature and nurture") influence these neural processes.

Neuroplasticity in Aging and Disease

Brain aging is believed to be reversible because the brain can re-structure itself through learning experiences, being plastic at all stages of life (Mahncke et al., 2006). Adult education and participation in different training activities are considered to be essential for the extension of the mental health (Guglielman, 2012).

Amblyopia

The insufficient multi-sensory experience is believed to play a crucial role in the pathogenesis of amblyopia. This developmental disorder occurs during a period of neural plasticity and is often considered irreversible in adults (Holmes and Clarke, 2006; Barnes et al., 2010).

Bonaccorsi et al. (2014) reviewed recently current experimental studies dedicated to the recovery of neuronal

plasticity in amblyopia. The results obtained in the rat model have hinted at a wide potential of visual perceptual learning for recovery of vision in adult amblyopic subjects.

Clinical research also found a significant degree of plasticity in the visual system of the adults with amblyopia (Levi and Polat, 1996; Polat et al., 2004; Levi, 2005). A prospective, randomized, masked, controlled study provided a high evidence that the perceptual learning lead to a twofold improvement in contrast sensitivity and visual acuity (Polat et al., 2004).

It suggests that perceptual learning reflects alterations in early neural processes localized beyond the site of convergence of the two eyes. Perceptual learning was assumed to operate via a reduction of internal neural noise and through more efficient use of the stimulus information (Levi and Li, 2009; Freiherr et al., 2013). A brief period of video-game play improved substantially various spatial vision functions of low-level and high-level visual processing, including visual acuity, spatial attention, and stereo acuity (Li et al., 2011).

Understanding the factors that predetermine the critical periods and principles of their opening and closure is expected to form the basis of new methods of therapy aimed at the improvement of visual deficits in children and adults with amblyopia. Such methods include ways for decreasing the levels of inhibition (Wong, 2012), constraint-induced therapy training (Taub, 2010; Taub et al., 2014), and many others.

The Aging Brain

Cognitive decline is accepted to be a common phenomenon during aging. There is also an alternative hypothesis that cognitive performance in old age may reflect the consequences of learning on information processing, being related to increased knowledge (Ramscar et al., 2014).

On the other hand, stereological principles of cell counting helped to reveal that changes that occurred during normal human aging were region-specific and more subtle than previously believed (reviewed by Burke and Barnes, 2006). These authors presented a systematic review of recent experimental and clinical studies on animals and human. The significant cell loss does not occur during normal aging. Plastic changes in dendritic complexity (dendritic branching and length) were even greater in aged individuals than in younger adults, and than in patients with senile dementia (Buell and Coleman, 1979; West, 1993). Burke and Barnes (2006) have reviewed functional alterations that occur during normal aging in the medial temporal lobe and the prefrontal cortex. Based on the data discussed, the authors suggest that the loss of neurons does not significantly contribute to age-related cognitive impairments. Alterations in synaptic connectivity and plasticity, Ca^{2+} homeostasis, gene expression, and network firing properties were found to contribute to the selective behavioral deficits observed in advanced age (Burke and Barnes, 2006).

Mahncke et al. (2006) define four main interrelated factors that determine the process of inevitable degradation of the brain. The authors note that reduced schedule of brain activity, noisy processing, weakened neuromodulatory control, and negative learning – all promote plastic changes in the brain and functional decline. With aging, significant changes occur in all sensory

systems and the low-level and high-level cognitive functions are involved (Mozolic et al., 2012). Progressive losses in function across multiple systems accompany the changing of multisensory integration.

Several studies have reported recently that older participants showed greater multisensory integration relative younger subjects (Mahoney et al., 2011, 2014; Freiherr et al., 2013). It occurred despite the continuing attenuation of function of the individual sensory systems. One possible mechanism that can explain this phenomenon is the principle of inverse effectiveness. This event stated that as the responsiveness to distinct stimuli (unimodal performance) decreases, the strength of multisensory integration increases (Stein and Stanford, 2008; Holmes, 2009). Mahoney et al. (2011) first proved the facilitative effect of pairing somatosensory with visual stimuli in older adults. In their investigation, younger and older adult observers responded to randomly present unimodal stimuli (auditory, visual, somatosensory) and paired multimodal stimuli (auditory-somatosensory, auditory-visual and visual-somatosensory). The reaction time was significantly smaller to multisensory than to unisensory stimuli in both groups. Nevertheless, older adults showed greater shortening of the reaction time when processing visual-somatosensory information while younger observers demonstrated a significant increase in multisensory integration for auditory-visual and auditory-somatosensory stimulation.

Age-Related Diseases

Wilbrecht et al. (2010) have shown in electrophysiological experiments in rodents that the ability of neurons to adapt in response to the impact of internal and external signals depends on their plasticity. The electrophysiological and biochemical studies performed in experimental models have found that dopamine in the basal ganglia plays a crucial role in regulating long-lasting changes in synaptic strength (cited from Calabresi et al., 2009).

In humans, different aspects of neural plasticity have been independently associated with or contribute to the disease state (Wainwright and Galea, 2013). It was assumed that disturbance of neuroplasticity played a central role in such neurological disorders as PD and AD (Lewis and González-Burgos, 2008; Hu et al., 2009; Varea et al., 2012). Understanding the mechanisms of the plasticity of the adult's brain related to multisensory experience and brain injury or degeneration may have high clinical and social relevance including the development of new ways for the reactivation of neuroplasticity.

The theory, which links cognitive changes typical of normal physiological aging to a functional distortion in the dopamine system projection to prefrontal cortex, is known (Braver and Barch, 2002). According to this theory, alterations in dopamine system function and then abnormal prefrontal cortex activation do impact on cognitive control, including working memory, attention, and inhibition. Dopamine plays a role in modulation of cell excitability and synaptic plasticity. Therefore, dopamine-dependent corticostriatal plasticity was suggested to underly the long-duration motor response to dopamine replacing therapy in the patients with PD (Zhuang et al., 2013). Patients with PD have disturbances in the perception and estimation of time (Parker et al., 2013). Dopamine deficiency in PD triggers the degenerative

process associated with adaptive changes in neuronal networks. These changes include a compensatory overactivity of remaining dopamine neurons and functional or structural remodeling in other neuronal systems (Zhuang et al., 2013). The long-term dopamine-replacing therapy can trigger adaptive phenomena or, on the contrary, the appearance of side effects. Therefore, learning the mechanisms of neuroplasticity in PD and response to the therapy is necessary for the elaboration of more effective targeted therapies.

Several studies described functional plasticity of retinal ganglion cells in glaucoma, optic neuropathy of different genesis, and other retinal pathologies (Weber and Harman, 2008; Porciatti and Ventura, 2012).

Pattern electroretinogram reflects the electrical activity of retinal ganglion cells. Clinical and experimental findings suggest that PERG may be altered long before the reduction in the retinal nerve fiber layer (Porciatti and Ventura, 2012). Porciatti and Ventura (2012) used the concept of neural plasticity to simulate the reversible/inducible changes in the PERG during the critical period (stage of retinal ganglion cell dysfunction), which precedes their death. Zhou et al. (2014) suggested that retinal glial cell activation induced by acute high intraocular pressure may cause the process of retinal synaptic plasticity through affecting the expression of synaptophysin and other synaptic proteins. In the rat model of acute ocular hypertension, the increase in expression of synaptophysin across the retina was observed from the inner to the outer plexiform layer. Therefore, glial cells can be a new target to modulate retinal synaptic plasticity after retinal injury.

Non-Drug Ways to Reactivate the Plasticity of the Adult Brain and New Prospects for the Use of Sensory Stimuli with Non-Linear Temporal Structure

An 'Active Life' and Environmental Enrichment

Numerous works have shown the ability to reactivate adult's neuroplasticity in a variety of ways (Maya-Vetencourt et al., 2008, 2011; Spolidoro et al., 2011; Prakash et al., 2014). Various studies have been developed to understand how physical activity and exercise influence the brain functioning, to identify mechanisms by which exercise can protect them, maintain and restore. Particular attention was paid to the training impact on the structure and function of the hippocampus (Shors et al., 2001, 2012). Neurons are continually born and added to the dentate gyrus throughout life (Altman and Das, 1965). However, aging causes changes in the hippocampal neurogenesis that may lead to cognitive decline with age (van Praag et al., 2002). The brain injury early in the development was shown to contribute to the emergence of health problems that manifest itself only in old age (Barnes, 1994; Grossman, 2014).

Physical activity seems to enhance the synaptic plasticity, increase vascular network complexity, and levels of neurotrophins (Shors et al., 2001). The known paradigm of training, based on the plasticity of the aging brain was designed by Mahncke et al. (2006), Merzenich (2013). The authors postulated

that in order to reactivate the brain plasticity, the older people have to be involved in the intensive complex activity. Intense activity apparently strengthens neuromodulatory systems, increases reliability and power of cortical representations, and learning management in adults. Using of training programs based on brain plasticity showed that older adults could quickly learn and significantly improve memory (Mahncke et al., 2006; Smith et al., 2009; Berry et al., 2010). The training programs also enhanced the task performance in people with schizophrenia and other mental disorders (Fisher et al., 2009; Merzenich, 2013). Chapman et al. (2013) proved that cognitive training – the complex mental activity – also induces the neuroplasticity in healthy elderly subjects.

Mora et al. (2007) suggest that physiological aging occurs asynchronously in different areas of the brain. They also hypothesized that the impact of aging on the neurons, dendrites, synapses, molecular and functional plasticity can be modulated by environmental factors even in adults (Mora et al., 2007). EE is considered to be one of the promising methods for the reactivation of the adult brain plasticity. In the EE experimental paradigm, the animals are placed in an enrichment environment. The EE allows obtaining a much greater stimulation of cognitive, motor and sensory activity than standard laboratory conditions. Recently, Alwis and Rajan (2014) critically analyzed this experimental paradigm. In an early development and adulthood, EE profoundly affects the animal brain at the functional, anatomical and molecular level (Kempermann et al., 2002; Nithianantharajah and Hannan, 2006, 2009; Butz et al., 2009; Baroncelli et al., 2010, 2012; Sale et al., 2012). Short-term exposure to the EE leads to a significant enhancement of hippocampal neurogenesis associated with a substantial improvement in cognitive performance (van Praag et al., 2000, 2005; Kempermann et al., 2002). It makes it possible to suggest that the active interaction with the outside world may mediate its positive effects on the brain function through the impact on neuroplasticity. Kempermann et al. (2002) have reported that hippocampal neurogenesis in adult mice that lived in EE for 10 months since the age of 10 months was fivefold higher than in the control mice. It was accompanied by an improvement in locomotor activity and learning efficiency, exploratory behavior. However, the authors noted that the concept of EE in studies with inbred rodents cannot be easily applied to the human conditions.

In rats and mouse models, amblyopia can be induced by monocular deprivation during early development. It has been shown that adult amblyopic rats transferred to an EE setting for 3 weeks undergo a full recovery of visual functions (Sale et al., 2007, 2012). Restoration of plasticity in enriched animals accompanied a threefold reduction in GABA release, and the beneficial effects of EE were eliminated entirely by intracortical infusion of benzodiazepine diazepam. These findings emphasize the crucial role of GABAergic transmission reduction in the manifestation of these effects of EE. Insulin-like growth factor 1 involved in neurogenesis, neuronal differentiation, and synaptogenesis, can reactivate the experience-dependent plasticity of the visual cortex in adults by reduction of local GABA levels (Maya-Vetencourt et al., 2012).

The effectiveness of physical exercise and increase of social interactions and visual stimulations in the restoration of visual function has been studied recently in adult rats with amblyopia (Baroncelli et al., 2012). The equally good result, which consisted in restoration of the ocular dominance and visual acuity, was obtained for the intensive motor activity in a running wheel. The exposure of rats to an optical EE using a rotating fluorescent lamp for maximal stimulation of the V1 neurons also showed good results. The possibility to reactivate the adult visual cortex plasticity have been demonstrated in humans with amblyopia by usage of such EE approaches, as playing video games and visual perceptual learning (Levi and Li, 2009; Astle et al., 2011; Li et al., 2011; Green and Bavelier, 2012). Mainardi et al. (2013) summarizes the current ideas about the mechanisms of the environment-induced plasticity in the arcuate nucleus of the hypothalamus.

The correct combination of appropriate pharmacotherapy with the EE strategies was suggested to be a promising therapy for certain neurological disorders to improve an internal repair capacity of the brain (review by Foster et al., 2011; Sale et al., 2012). Foster et al. (2011) focused their recent study on the different lifestyle factors and possible pharmacological therapy aimed to reduce the risk for and to improve cognitive functions in mild cognitive impairment, AD, and other age-related disorders. Special attention was paid to the fitness training, which has the largest positive impact for executive (frontal lobe) functions (Foster et al., 2011).

Noise Therapy and Stochastic Resonance

The phenomenon of SR is believed to underlie the therapeutic effects of noise for the number of pathological conditions mentioned below. It refers to the general phenomenon observed in non-linear systems when the intermediate level of activity improves detection of subthreshold signals by maximizing the signal-to-noise ratio. This phenomenon is fundamental for the physical and biological processes (Wiesenfeld and Moss, 1995; Russell et al., 1999; Pakdaman et al., 2001; Moss et al., 2004). SR occurs in any system where detection requires passing a threshold. It is described as the consequence of interactions between non-linearity, stochastic fluctuations and a periodic force (Chialvo et al., 1997; cited from Korn and Faure, 2003). Experimental studies have documented that SR can control the firing rates in crayfish mechanoreceptors, frog cochlear hair cells, and other sensory systems of animals (cited from Korn and Faure, 2003). SR was also shown to occur at the level of ion channels (Bezrukov and Vodyanoy, 1995). Different other aspects of SR role in the nervous system have been discussed (Korn and Faure, 2003; Tokuda et al., 2010).

Continuous variations in the membrane potential of neurons in the CNS are known as “synaptic noise.” It occurs due to the summation of intermittent inputs from presynaptic cells and the unreliability of synaptic transmission (Brock et al., 1952). Synaptic noise has been first assumed to be stochastic (Calvin and Stevens, 1967; Shadlen and Newsome, 1998). It was later assigned to a deterministic phenomenon that reflects the chaotic behavior of afferent inputs (see Korn and Faure, 2003 for review). During the aging, there is an increase of endogenous neuronal

noise. Its interactions with external input noise were investigated with a stochastic gain-tuning model (Faure and Korn, 2002; Li et al., 2006). With aging, the cognitive system has a larger internal neuronal noise and less plasticity. Li et al. (2006) have shown that if we stimulate the aging system, it continues to demonstrate the overall effect of SR, which requires more external noise.

We usually consider noise detrimental to cognitive performance, but the increase of knowledge about the phenomenon of SR gives reason to study the possible useful properties of the external noise in different situations. Addition of noise in non-linear systems can amplify the detection of a subthreshold signal. Therefore, the influence of the noisy environment on cognitive performance was studied with a neurocomputational model of attention deficit hyperactivity disorder (Söderlund et al., 2007). Participants were asked to perform a task to verify a mini-performance memory, verbal task to check the memory productivity, both in the presence and in the absence of auditory white noise. Authors found the positive impact of noise on cognitive function in the group with attention deficit hyperactivity disorder. This effect was explained by the phenomenon of SR, whereas the noise distorted performance in the control group (Söderlund et al., 2007). Authors proposed that the noise in the environment introduces an internal noise in the neural networks through the perception system and facilitates performance by inducing SR in the neurotransmitter systems. An important role of SR has been demonstrated earlier for dopamine signaling in the brain (Li et al., 2006).

Söderlund et al. (2007) suggested that an optimal (for different circumstances) amount of noise may be beneficial for cognitive performance, in particular in hypodopaminergic states. They suggested existence of a link between the effects of noise, dopamine regulation, and cognitive performance (Söderlund et al., 2007). Authors assumed that the noise inducing the effect of SR must be continuous and have high energy levels at all frequencies, as it takes place with white or pink noise. The computational model of the concept of SR predicted the positive impact of background noise on the attention and performance (Sikström and Söderlund, 2007). Individual differences in dopamine were supposed to handle individual differences in the noisiness effects (Sikström and Söderlund, 2007). Exposure to auditory background noise has been recently shown to improve cognitive performance in inattentive school children while it distorted the performance of attentive children (Söderlund et al., 2010). These findings suggest that there is the ability to control cognitive performance by using the background white noise stimulation (at least in children with problems of attention).

The positive effects of background noise were also found in the elderly (Priplata et al., 2003), in patients with PD (Yamamoto et al., 2005), and other neurodegenerative disorders (Priplata et al., 2003; Pan et al., 2008; Söderlund et al., 2010). These effects are consistent with the theory that links the cognitive changes characteristic of normal physiological aging with decreased function of the dopamine system projecting in the prefrontal cortex (Braver and Barch, 2002). It has been found that SR modulates neural synchronization within and between functionally relevant brain areas (Ward et al.,

2010), which may be a general mechanism of the brain functioning.

The therapeutic approaches based on the SR have been used in the treatment of gait disturbance in the patients with neurodegenerative disorders. Randomly vibrating insoles were designed to ensure coordination and gait in the elderly, patients with diabetic neuropathy, and in the period of rehabilitation after a stroke (Priplata et al., 2003; Costa et al., 2007; Ross, 2007). This treatment improved the equilibrium sense and the gait control in patients subjectively, and it caused objectively a significant increase in the fractal dimension and the complexity of the step-to-step interval fluctuations. Old participants showed greater improvement than young people. It was shown that 24-h noisy galvanic vestibular stimulation may be useful in the amelioration of akinesia symptoms in patients with central neurodegenerative disorders (Pan et al., 2008). It implies the possible mediation of the beneficial effect through the known effects of the vestibular nerve on the basal ganglia and limbic system. The 24-h noisy galvanic vestibular stimulation was apparently effective in improving the long-term heart rate dynamics in patients with multisystem atrophy and the dynamics of daytime activity in patients with PD (Yamamoto et al., 2005).

Benefits of Music

Research and experience tell us that art can heal, change human physiology and perceptions of the world. Human behavior and physiology change from the state of stress in a situation of deep relaxation, from anxiety to inspiration, so we can assume that creativity alters brain function and our lives. Staricoff (2004) reviewed studies that examined how art affects human health. Her scientific report showed the positive role of different types of art in mitigating some pathological conditions and in the training of practitioners in the field of health.

Music is known to have different psychological and physiological impacts on humans, affects brain activity and EEG (Petsche, 1996; Yuan et al., 2000; Jausovec et al., 2006). Sink et al. (2011) by using fractal analysis and data mining techniques, found strong associations between a complexity of auditory signals in the form of synthetic music and the resulting multi-channel EEG responses. They noted that psychologists believe that there is a particular fractal dimensionality in nature. "When the incoming stimuli imitate this fractal dimension, the nervous system would resonate with this fractal dimension and show a particular pattern" (Sink et al., 2011). These authors suggested a significant mathematical association between auditory stimuli in the environment and physiological processes in the human body. Confirmation of this assumption would also be another valuable proof of our theory considering the importance of the multimodal external environment to maintain human health. Improving the perception of speech-in-noise is accompanied by neural changes in the auditory processing, which indicates the plasticity of the brain (Anderson, 2013). It allows the use of auditory training for individuals who have difficulties in perceiving of useful auditory information on the background noise. There were observed effects of music on the EEG power spectrum, closely related to man's emotions (Yuan et al., 2000). Changes in the frequency components of the EEG

power spectrum from the delta to the beta-2 band were analyzed in 16 regions in silence, during noise or when listening to music. A significant decrease was seen in the power of total alpha-1 while the power of total theta increased when listening to music.

Several studies have reported an increased spatial-temporal reasoning performance after listening to Mozart for 10 min, but not in all studies this effect was observed. Also, a positive impact was unstable and depended on spatial tasks (Jenkins, 2001). Jausovec et al. (2006) investigated the influence, which Mozart's sonata for two pianos in D major (K. 448) has on brain activity in the process of solving spatial rotation tasks. The data were compared with those in participants who before and after the training listened to Brahms' Hungarian Dance number 5. Those who listened to Mozart showed a better task performance than did the respondents of the relax group and Brahms' music groups. They also displayed less complex EEG patterns and lower alpha-1 and gamma-band synchronization. Therefore, Mozart's music, by activating task-relevant brain areas, can enhance learning of the spatiotemporal rotation tasks. The results support the priming explanation of the "Mozart effect."

Earlier, Gordon Shaw suggested that if the activity of the mind may sound like music, we can use music to stimulate the brain. The music may have effect by activating the firing patterns similar to patterns of sounding music (cited from Campbell, 1997; see also Rauscher et al., 1995). Rauscher et al. (1995) hypothesized that the effect of music on intelligence can be explained by the fact that the hearing of complex music excites cortical firing patterns, which are similar to those used in spatial reasoning. Other hypotheses were also proposed for an explanation of this effect of Mozart music (Roth and Smith, 2008). For over two decades, numerous studies of "Mozart Effect" have been carried out, which confirmed or refuted increased intelligence while listening to music by Mozart. These studies reported a temporary increase in cognitive skills, or could not find a statistically significant "Mozart effect" (Allen and Blascovich, 1994; Roth and Smith, 2008). So, the high-quality evidence that would satisfy the requirements according to GRADE guidelines is not yet available (Balshem et al., 2011).

Contradictory results may be a consequence of the insufficiently adequate choice of control groups and study design. As a possible explanation, we can assume that the short-term effects of music on performance and physiology of the brain may occur because virtually all researchers used passive listening to Mozart's music. This flaw in study design might predetermine the inconsistency in published studies. Perhaps in such circumstances the effect will vary in professional musicians and non-musicians, and people that differently perceive the music. All these factors will require experimental verification of the proper design. The impact of musical training on the solution of perceptual and motor tasks is associated with structural and functional changes that occur mostly in the brains of musicians compared to non-musicians (Bhattacharya and Petsche, 2005).

The results of various studies also encourage us to pay attention to the fact that the beneficial effect of music on the perceptual learning and higher cognitive functions depends on the severity of their initial distortion. Namely, the effects in older

adults are better than in younger adults, and than in patients with neurodegenerative disorders performance improvement can be seen more frequently than in a healthy aging. Particular interest has recently attracted the impact of music on creative thinking and the role of the emotional state in our perception of the world.

The EEG data (Bhattacharya and Petsche, 2005; Fink et al., 2009; Fink and Benedek, 2014) and functional magnetic resonance imaging data (Kowatari et al., 2009; Berkowitz and Ansari, 2010; Ellamil et al., 2012) were used to characterize the creative thinking. These studies estimated the effects of musical improvisation, fine arts or other creative activity on the brain activity and functional connectivity in scientists and dancers. Creative ideation attracted an unusual pattern of neural processes that was not typical for traditional solutions (not originative) tasks (Kowatari et al., 2009; Berkowitz and Ansari, 2010; Ellamil et al., 2012). A relationship was found between the EEG alpha activity and creative thinking (Fink et al., 2009; Fink and Benedek, 2014). EEG alpha power varied depending on the creativity associated with the test requirements, and changed with the level of the individual capacity for creative thinking. The artists showed a much stronger synchronization in the short and long-delta range during the task of mentally creation of pictures, while non-artists showed improvement in the near-beta and gamma range (Bhattacharya and Petsche, 2005).

Interestingly visual perception of emotional stimuli was shown to be dependent not only on the prior knowledge, but also on the emotional state of the observer (Jolij and Meurs, 2011). Music can change the relationship between mood and visual perception. Apparently by manipulating top-down modulation of visual processing, music can ultimately alter the way we perceive the world.

The musical experience is believed to have a positive influence on the perception of speech in noise in young adults (Parbery-Clark et al., 2009; Kraus and Chandrasekaran, 2010). It was shown that compared with performance in young adults, the older musicians demonstrate an enhanced speech-in-noise perception (Parbery-Clark et al., 2011). This enhancement of speech understanding in the elderly is likely associated with a greater auditory-specific cognitive and perceptual performance. Previously, it has been also found that musical training reduces the age-related decline in hearing ability due to the enhancement of the central auditory processing (cited from Zendel and Alain, 2012). Musical experience downplays the reduction in neural precision (age-related delays in neural timing) that occurs during the natural aging process (Parbery-Clark et al., 2012).

Alain et al. (2014) analyzed recently the results of numerous investigations that describe the musical training benefits in the auditory cognition in young and elderly, including the creation of a mental representation of the auditory environment. The author paid attention to the results showing that musical training has a positive impact on neural mechanisms in young adults and exhibits long-lasting improvements in hearing and cognitive control. From these results, the assumption was made that musical training might counteract age-related changes in auditory cognition and delay the hearing decline that is commonly observed in aging.

The individualized piano instruction was reported to be an effective tool for prevention of age-related cognitive decline (Bugos et al., 2007). Many other studies testify that music training can be an effective strategy for rehabilitation of older people (Kraus and Chandrasekaran, 2010; for review see Kraus and White-Schwoch, 2014). However, the exposure to vocal or instrumental background (pleasant and arousing) music did not influence the verbal learning. It led the authors to suggest that participants ignored this background stimulation to focus on the verbal learning task (Jäncke et al., 2014). The background music was also used to distract the listener from the performance of the primary test (Salamé and Baddeley, 1989; Klatte et al., 1995; Parbery-Clark et al., 2009; Kraus and Chandrasekaran, 2010). But as we have noted above, the background white noise can improve cognitive function in inattentive subjects, but reduces the performance of attentive persons (Söderlund et al., 2010). Thus, we cannot exclude that the sign and strength of the impact of background music on cognitive function may also depend on individual characteristics, in particular, on the power of the internal neural noise. It seems important to check the probability an impact of these factors on the study result in the future research.

The healing effect of music on the auditory, visual and motor processing, cognitive and emotional state seem to be more prominent in different pathologies of the CNS than in normally aging individuals.

The observations suggest that music is likely to become a valuable tool in neurological rehabilitation. As an example, in post-stroke patients, even passive listening to music was shown to have the beneficial effect on memory and mood. Särkämö et al. (2008) demonstrated that everyday music listening during the early post-stroke stage can facilitate the recovery of cognitive functions and prevent the negative mood. Recently, Särkämö et al. (2014) found that after an acute middle cerebral artery stroke, regular listening to music can enhance cognitive recovery and improve mood. It also induces fine-grained neuroanatomical changes in the recovering brain. Authors performed a voxel-based morphometry analysis in patients with the acute stroke and after the 6-months period of rehabilitation. The patients listened to their favorite music or audio books or did not receive any material for an audition (Särkämö et al., 2014). Frontal and limbic areas in patients with the left hemisphere damage showed an increase of the gray matter volume greater in the musical group than in the verbal and in the control group. The remodeling of gray matter in the frontal areas correlated with enhanced recovery of cognitive functions. Both perceptual and motor timing showed improvement in patients with PD when using music cued gait-training (Benoit et al., 2014). This observation supports the idea that coupling gait to the rhythmic auditory cues in PD patients is based on a neural network involved in both the perceptual and motor timing.

Learning to play a musical instrument is very challenging, due to the involving of multimodal integration and higher order cognitive functions. In particular, active playing on a musical instrument can engage the sensorimotor system as well as the auditory system. Musical training involves simultaneously

the motor system and a multisensory (auditory, visual, and somatosensory) perception. Very likely, it can serve as a useful model to study the multimodal brain plasticity in humans (Zatorre et al., 2007; Lappe et al., 2008; Herholz and Zatorre, 2012).

Fractal Stimuli and Physiological Functions

One should also pay attention to the facts, which may indicate the influence of non-linear fractal factors on the fractal gait dynamics. Fractal dynamics of physiological processes, as described above, is an essential feature of a healthy organism. Destruction of fractal dynamics, including the rhythm of the gait, characterizes aging and some neurodegenerative disorders. We suggested earlier that dynamic fractal flickering may be a useful tool in the search for non-linear dynamics involvement in the activity of a visual system. And it may be a possible basis for new diagnostics and treatment of neurodegenerative diseases of the retina and brain (Zueva, 2013).

The fractal patterns of gait can be changed by synchronizing the gait dynamics with the fractal temporal structure of stimuli. Several studies have showed this ability for auditory (Hove et al., 2012; Kaipust et al., 2013; Uchitomi et al., 2013; Marmelat et al., 2014) and visual stimuli (Rhea et al., 2014a,b). Recent works (Rhea et al., 2014a,b) revealed that fractal patterns in the step-to-step intervals significantly changed during walking on a fractal visual metronome (flashing red square). However, the participants were not able to adequately reproduce the persistent fractal pattern that the stimuli exhibited. The experiment consisted of three phases: walking without the fractal stimulus, walking during entraining to a fractal visual stimulus, and walking with no stimulus. The fractal gait patterns of healthy young adults became enhanced during the synchronization phase. The effect remained after entrainment in the post-synchronization phase. The discrete fractal stimulus was noted to affect the retention better, causing a more persistent gait pattern in synchronization phase as compared to continuous fractal stimulus.

The results obtained in patients with PD can be considered as an evidence of the role that the temporal structure of the cue is essential to the sign or power of their effects on the CNS. Walking with fixed-tempo Rhythmic Auditory Stimulation can improve many aspects of the gait timing in PD patients (reviewed by Thaut and Abiru, 2010; see also Hove et al., 2012). However, this stimulation has been found to reduce rather than to increase the fractal scaling of step-to-step intervals (Hausdorff et al., 1997). Moreover, the stride variability becomes synchronized around a single frequency (Delignieres and Torre, 2009). Conversely, Hove et al. (2012) showed that the dynamic characteristics of the stride interval fluctuation in patients with PD can be improved to a healthy 1/f fluctuation level using interactive rhythmic cues. These authors emphasized that patients and healthy participants rarely synchronized the dynamics of gait with a fixed tempo Rhythmic Auditory Stimulation. When the synchronization occurs, the fractal scaling of gait patterns decreased far from healthy 1/f levels.

Uchitomi et al. (2013) recently studied the PD patients that were tested in four experimental situations: with the interactive

rhythmic cue, fixed tempo-cue, 1/f fluctuating tempo-cue, and no cues. There was a significant effect of interactive rhythmic cues – the gait fluctuations of the patients gradually returned to a healthy level reinstating 1/f fluctuation while this did not happen in other circumstances. In the condition of interactive WalkMate, the cue rhythm was changed in response to the subject's gait rhythms, that is, there was a mutual synchronization of the gait rhythms and cue rhythms via mutual entrainment. The authors suggest that mutual entrainment can facilitate gait relearning and expect a wider application of interactive rhythmic cues in the fields of rehabilitation.

In a review, 14 studies investigating whether a rhythmic auditory (music) cueing improves walking in patients with other neurological conditions than PD were analyzed (Wittwer et al., 2012). Moderate evidence of improving velocity and stride length in people with stroke due to gait training with rhythmic music were noted. Insufficient evidence for benefits of gait training using synchronization of walking to rhythmic auditory cues was found in HD, spinal cord injury, traumatic brain injury, dementia, multiple sclerosis, and normal pressure hydrocephalus. However, the authors suggest that the failure may be due to the poor methodological quality of some works (Wittwer et al., 2012).

Sejdić et al. (2012) studied the effects of different rhythmic sensory cues (aural, visual, and tactile) on the temporal dynamics of the healthy adult's gait. These authors showed the greatest auditory rhythmic signal impact on walking parameters. However, the visual cue had no statistically significant effect on the scaling exponent.

Hunt et al. (2014) conducted a special study to find out whether the temporal structure of the complex auditory cue has different effects on the temporal pattern of the target behavior. The authors showed the ability to control the auditory–motor coupling by sound signals of different colored noise, which shift the temporal structure of the fractal gait dynamics to the statistical properties of specific signals.

Music perception is a complex cognitive task that involves the integration of the various structural components of music (melody, harmony, rhythm, tempo, and others). Different neural correlates have been associated with the music perception (Platel et al., 1997; Schmithorst et al., 2005; Gomez and Danuser, 2007; Lin et al., 2014). Hadjidakimouli et al. (2010) studied the EEG signals including the Mu rhythm in groups of advanced music students and non-musicians on the movements during the sound and audiovisual stimulation. Music students showed a significantly greater sensorimotor response at the auditory stimulation compared to non-musicians. At the audiovisual stimulation, the results were similar in both groups.

It is essential to note that these findings, on the one hand, may indicate a predominant role of professionally adequate stimuli (auditory) for musicians playing on the instruments. And, on the other hand, they do not exclude a smaller role of audiovisual integration in the modulation of locomotor activity in healthy individuals. Further investigations may determine the impact of audiovisual and auditory stimulation in aging and pathological conditions involving a reduction in fractal scaling of gait patterns in musicians and non-musicians.

The Logical Substantiation of the Theory

Key Facts and Regularities Derived from the Analyzed Studies include the following Highlights

- Nature is full of non-linear fractals that surround us throughout our lives.
- Humans evolved in a non-linear world, gaining experience in a complex multisensory environment.
- Fluctuations of physiological rhythms of a healthy body have the fractal properties and can be described using the theory of deterministic chaos.
- The fractal regulation of physiological processes is impaired with age and in diseases. Aging and pathological conditions tend to cause a loss of the complexity of many physiological processes, and quite often – to strict control of their fluctuation.
- The reduction in the multiscale complexity of the brain's structure and activity characterizes the age-related neurodegenerative disorders of the brain and retina.
- Neuroplasticity plays a significant role in development, learning, memory, and in recovery from brain injury. Developmental plasticity includes changes in neural connections due to brain/environment interactions, and cellular changes induced by learning.
- The sensory deprivation that reduces or completely destroys the quality or quantity of a mono- and multisensory experience in the early brain development can alter the neural networks and functional connections that the brain continues to use in adulthood.
- At all levels of the CNS, adaptive or maladaptive plasticity may be caused by the loss or excess of mono- and multimodal stimulation and injury. It occurs as the consequence of a non-use or over-use or learning new skills.
- The brain plasticity decreases throughout the life, but the adult neuroplasticity can be reactivated in a variety of ways.
- The physical activity and exercise, cognitive training, increase in social interactions and visual stimulation, and other training programs related to the EE paradigm can re-activate the brain plasticity playing a crucial role in the improvement of cognitive function.
- Exposure to the auditory background (white) noise improves cognitive performance in inattentive people while it distorts the performance of attentive persons.
- The therapeutic approaches based on the SR improve the gait disturbance and cognitive performance in the patients with neurodegenerative disorders. Application of these approaches seems to be useful in the elderly and in the period of rehabilitation after a stroke.
- Architecture, painting, and musical compositions may have a fractal dimension.
- Listening to music and musical training have a positive impact on cognitive and motor functions, the brain activity, mood, and intelligence.
- Fractal patterns of gait can be changed by synchronizing the gait dynamics with the fractal temporal structure of

sensory cues. The more prominent effect was proven for interactive rhythmic cues, suggesting that mutual entrainment can facilitate the gait relearning effectively.

- The temporal structure of the complex auditory signal has different effects on the temporal pattern of the target behavior. Auditory-motor coupling can be controlled by sound signals of different color types of noise, which transfer the temporal pattern of the fractal gait dynamics to the statistical properties of specific signals.

Table 1 presents the summary of the current data, which are significant to the logical substantiation of the theory, and appropriate references.

Logical Conclusions that We Draw from a Comparison of Scientific Observations Gained in Various Fields of Research

The experience of human evolution in a non-linear world and the interactions of humans throughout their life with a non-linear environment permit us to assume that these factors underlie the brain plasticity resulting from this experience. These factors can underlie the management of external inputs through different modalities. We believe that not only the quality and quantity of sensory information, but its non-linear fractal structure in many spatial and temporal scales is important for the health of the brain and is involved in fractal regulation of biological rhythms.

Different studies have shown the principal ability to reactivate adult neuroplasticity in a healthy aging and age-dependent CNS pathologies in a variety of ways through learning experiences and physical exercise. So, it is logical to assume that this experience can be of greater benefit if it involves the interaction of sensory brain structures with mono- or multimodal stimuli having time-invariant fluctuations of their parameters. The fractal patterns of gait were shown to change by synchronizing the dynamics of gait with the fractal temporal structure of auditory rhythm and with interactive rhythmic cues. We assume that the fractal audio-visual and sensory-motor stimulation may involve other mechanisms of fractal regulation of body rhythms compared to the direct coupling (synchronization) of the rhythms discussed in the recent articles. More probable is that fractal audio-visual stimulation presents an effective way to improve sensory processing, cognitive and motor function through the reactivation of brain plasticity.

Art can heal, changing the human physiology and perceptions of the world. Nevertheless, the results are not the same in different studies. The short-term effects (or the absence of effects) of Mozart's music on the performance and brain physiology may be linked to the fact that all the researchers used the passive listening to Mozart's music. In other studies, the effects of musical training during the solution of perceptual and motor tasks were associated with structural and functional changes that occurred mostly in the brain of musicians when compared to non-musicians.

It is essential to note that these findings, on the one hand, may indicate a predominant role of professionally adequate stimuli (auditory) for musicians playing on the instruments. And, on the other hand, they do not exclude the smaller role of audiovisual integration in the modulation of locomotor activity

in healthy individuals. Further investigations can probably determine the effect of audio-visual and auditory stimulation in an aging musicians and non-musicians, as well as in pathological conditions associated with a reduction in the fractal scaling of the gait rhythm.

Various studies also encourage us to pay attention to the fact that the positive effect of music on the perceptual learning and higher cognitive functions depends on their initial distortion. The effect is better for the elderly than young adults and patients with neurodegenerative disorders than in normal aging. The healing effect of music on the auditory, visual and motor processing, cognitive and emotional state seems to be more prominent in different pathologies of the CNS than in normally aging individuals.

Similar to the results of musical training, we should expect the less pronounced effects of different cognitive and perceptual training in young healthy compared to the elderly or individuals suffering from age-related diseases. The capacity of homeostatic mechanisms in a healthy subject should be apparently sufficient to withstand the environmental perturbations of moderate strength. Otherwise, the detection of a significant shift in the characteristics of sensory and motor functions in young healthy individuals perhaps would be more correctly considered as an evidence of potentially damaging rather than therapeutic effect.

We can also presume that fine arts and music created by great masters may have fractal properties and potential curative impact on the person who actively perceives these works by passing them through his heart and brain. On the other hand, active participation in creative activity can alter the brain functioning, and, as a result, change the life. The results that showed the effects of music on creative thinking and emotional state, which mediate our perception of the world, may evidence this assumption.

Background noise stimulation increases arousal and performance of inattentive people but reduces the performance of attentive persons. One cannot exclude that the sign and power of the background music impact on cognitive function may also depend on individual characteristics, in particular, the strength of the internal neural noise.

Factors that may Reduce the Complexity of the World Picture Painted by the Brain

The human brain needs to obtain the complex multi-sensory experience during a lifetime. The distortion or diminishing of our sensory experience may lead to a disruption of the perfect complex structure, connectivity and functioning of the brain in the early development, or may underlie neurodegenerative disorders in the old age. The inherent complexity of the human sensory perceptions and the integration of multimodal sensory information from the individual channels in a holistic perception of the world are well-proved now. It allows to suggest that for the healthy brain, maintenance and preservation of the complexity and rich diversity of environmental stimuli that accompanies humans from birth and throughout the life are also critically important.

In the surrounding world, the linear stimuli with the ordered temporal or spatial structure are not usually effectively affecting people because they are not typical for our natural habitat.

The preservation, maintenance and recovery of the fractal temporal-spatial structure and a nonlinear dynamics of the human brain physiology are essential to maintain physical and mental human health throughout the life, from birth to old age.

The use of fractal visual, auditory and other stimuli helps restoring the function of the brain in the elderly, in neurodegenerative disorders and amblyopia by reactivating the brain plasticity.

In the experiments and clinical trials of different designs it is necessary to explore:

The efficiency of fractal visual and auditory stimulation in the improvement of cognitive functions and brain activity in pathological conditions:

The significance of the use of a fractal environment or fractal stimulation for preventive and curative purposes in neurodegenerative brain disorders

The similarities and differences in the results of impact of passive listening to music, passive exposure to the fractal stimuli and white noise to reactivate the brain plasticity and functions

The significance of the use of a fractal environment or stimulation for preventive and curative purposes in older people with cognitive decline

The significance of the use of a fractal environment or stimulation in conditions that alter the level of internal noise of the retina

The significance of the use of a fractal environment or stimulation for preventive and curative purposes in retinal ganglion cells pathologies, including glaucoma and diabetic retinopathy

The possibilities and indications for the use of the combined multimodal fractal therapy

The possibilities and indications for the use of the combined fractal stimulation and noise therapy

The significance of the use of a fractal environment or fractal stimulation for preventive and curative purposes for children and adults with amblyopia

FIGURE 1 | The directions for future studies based on the theory of ‘Fractality of sensations’ to explore benefits of non-linear stimulation and a scope of its application.

However, there are situations in which we are subjected to a more or less prolonged exposure to monotonically structured artificial environment. Formation of these conditions might be related to private life conditions of a person. For example, in a risk category one can include the residents of cities with a limited diversity of the visible landscape, people with the reduced mobility and possibility to change scene – the disabled, chronically ill, institutionalized patients. In a separate group, one should include elderly subjects suffering from not only gait disturbance, but also having visual and hearing impairment. In the old age, there is a sharp narrowing of the diversity of experiences and a decrease in the total flow of sensory information available to man. It limits the perception of the complexity of the world around them.

Deficiency or loss of complexity of sensations and images created by the brain may occur under the following conditions:

- (1) A decline in the intensity of light reaching the retina reduces or distorts the perception of geometric and dynamic fractals of nature.
- (2) A decrease in image contrast alters not only the perception of the details of the observed object, but also its geometric complexity. In amblyopia associated with the reduction of subjective brightness and contrast of the image, one can expect the positive impact of the therapeutic fractal stimulation.
- (3) In the cases of transparent optical media and standard eye refraction, the reduction of complexity of the images processed by the retina and brain, can apparently occur:

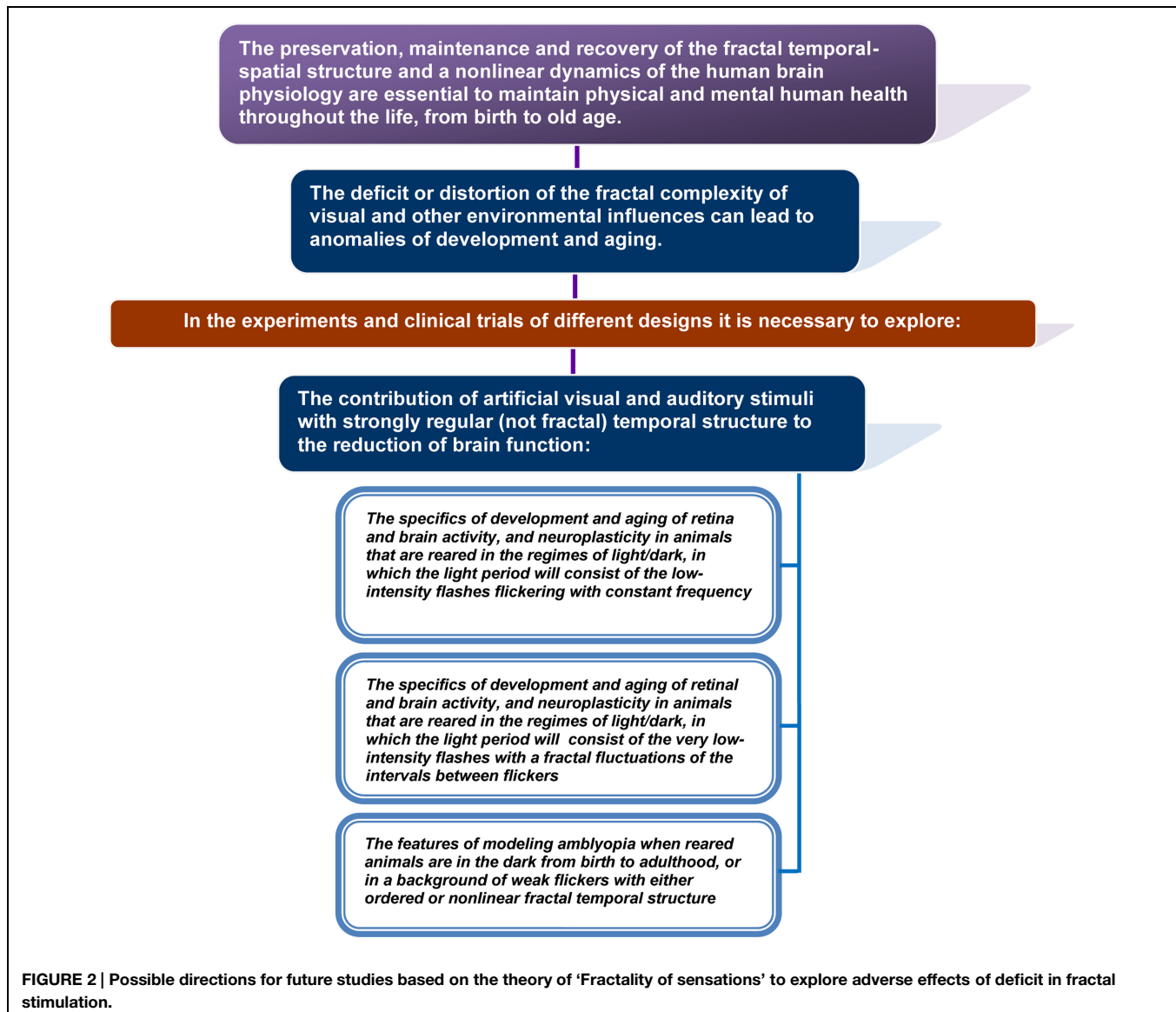


FIGURE 2 | Possible directions for future studies based on the theory of ‘Fractality of sensations’ to explore adverse effects of deficit in fractal stimulation.

- In the pathology of the retinal ganglion cells (glaucoma, optic neuritis of different etiology, etc.), when distorted information is sent by the retinal ganglion cells to the lateral geniculate nucleus and visual cortex;
- In pathological conditions, which alter the level of internal noise of the retina;
- In neurodegenerative diseases, such as glaucoma and AD, when the simplification of visual processing likely reflects the simplification of neural networks and loss of complexity in the functional activity of the brain and retina.

(4) The monotony of visual and other sensory features of the habitat:

- Low levels of life and culture: deficit of impressions and emotional experiences;
- Urbanization problems: deficit of diversity in architecture;

- Low levels of social communication: deficit of the diversity of experience;
- A monotonous work: deficit of creativity.

In all these situations, the diversity of living conditions can play an important role. The effect is expected to be greater when involving the multisensory integration.

Possible Applications and Future Research

The presented theory provides the basis to open new directions for scientific studies. These studies primarily should be designed to test the usefulness and validity of the assumptions that are closely related to and follow directly from the declared theoretical relationships. **Figures 1 and 2** indicate some directions for future studies based on the theory of ‘Fractality of sensations’ to explore benefits of non-linear stimulation and a scope of its application and adverse effects of deficit in fractal stimulation.

The efficiency of fractal visual and auditory stimulation in the improvement of cognitive functions and brain activity in pathological conditions is necessary to be estimated in the experiments and clinical trials of different designs (**Figure 1**).

One should compare the impact of mono and multisensory fractal therapy and the known effect of white noise described in the elderly, patients with PD and inattentive persons. It is desirable also to explore the possibilities of and indications for the combined use of fractal stimulation and noise therapy.

For children with amblyopia and older people with cognitive decline, it is especially important to ascertain the significance of the use of a fractal environment or fractal stimulation for preventive and curative purposes.

One should also explore another assumption related to the theory that exposure to artificial visual and auditory stimuli with strongly regular (not fractal) temporal structure may contribute to the reduction of brain function (**Figure 2**). The mechanisms of revealed adverse effects would be necessary to describe and explain.

It seems important to assess consequences of urbanization and positive impact of the new art in the architecture of the cities and their lighting to provide non-linearity of ambient human artificial environment closer to the natural conditions. The habitat change changes a man.

Future experimental and applied research in these and related areas could provide opportunities to confirm or deny the validity of the predictions contained in the theory.

Weaknesses in the Theory to Clarify in Future Studies

It is unlikely that all the wealth of sensations that a natural environment gives us is limited only to structures with the properties of temporal and spatial fractals. It is impossible to equate the world in all its diversity with a deterministic chaos in the nature. The spatiotemporal structure of various natural stimuli is diverse and may include low-dimensional rhythms, differing degrees of randomness. All the factors that accompany man in his evolution and the early periods of brain development have to play a role in the formation and self-organization of the CNS, and in the mechanisms of neuroplasticity. There is a marked difference between the passive human exposure to natural stimuli during the life and active perception of spatial-temporal stimuli. In the latter case, one should underline the significance of a dynamic behavior and creative thinking.

Existing knowledge does not yet allow us to assume how different the impact of the artificial fractal rhythms in comparison to white noise and cognitive and physical training on patients with amblyopia and neurodegenerative diseases can be. It seems most likely that the greatest potential benefit can be expected from the combination of these factors, which may vary for different pathological conditions, and this has to be substantiated and proved experimentally. One should explore how making a passive training effective for those who, for example, cannot play a musical instrument or actively enjoy music. The same problem may exist with the usage of artificial fractal stimulation that is always passive. It is interesting to investigate the similarity in the

effects of passive listening to music and passive exposure to the fractal stimuli, and the impact of white noise.

Future studies should also answer the following distinct questions. What kinds of mono or combined stimulation will help to overcome the adverse effects of the increased level of internal noise in the sensory system and the brain of patients and the elderly? What are the mechanisms and laws of interaction of intrinsic neural noise and external noise? Clarification of these issues is expected to define or limit the range of conditions that best meets the rules formulated in the theory of “fractality of sensations.”

Conclusion

We proposed for the first time in this article that temporal and spatial structures of visual and other sensory signals, which affect us throughout the life, are crucial for the normal development and aging of the brain. Conversely, the absence of fractal sensations is supposed to promote distortion of brain functioning and reduce the capacity of the adaptive plasticity.

Known facts related to different aspects of the problem have been considered. Described literature data and logical analysis allowed theoretical substantiating and formulation of a theory named “fractality of sensations.” The theory establishes relationships between the normal functioning and pathology of the brain and visual system, and the spatial-temporal structure of the visual and other sensory stimuli that affect people throughout their life. The theory argues that the deficit or distortion of the fractal complexity of visual and other environmental influences may lead to anomalies of development and aging. Application of fractal flickering and other fractal rhythms helps to restore the function of the brain and visual system, particularly in the elderly, in patients with neurodegenerative disorders, as well as with amblyopia.

We outlined here possible applications, experimental and applied research, based on the key tenets of the theory, as well as the weaknesses of the theory, which need to be clarified in future studies. Since the average life expectancy increases, the prevalence of age-related neurodegenerative diseases is also steadily increasing. Thus, the creation of new non-pharmacological methods of therapy that may slow cognitive decline, as well as weaken the manifestation of neurodegenerative diseases is an imperative. Development of new practical training paradigms based on the principles outlined in the theory may be useful in the prevention of cognitive decline, treatment, and rehabilitation of various pathologies of the brain. Also, the fundamental tenets of the theory can be used to mitigate the social problems associated with the objective limitations of the fractal complexity of sensations in particular categories of people.

Acknowledgments

I am grateful to my colleague Natalia Maglakelidze for her helpful comments on a preliminary version of this manuscript, to Stephanie Reeves for correcting English and to Pavel Balaban for the help with the manuscript.

Research



Cite this article: El-Nabulsi RA. 2022
Emergence of lump-like solitonic waves
in Heimburg–Jackson biomembranes
and nerves fractal model. *J. R. Soc. Interface*
19: 20220079.
<https://doi.org/10.1098/rsif.2022.0079>

Received: 26 January 2022

Accepted: 21 February 2022

Subject Category:

Life Sciences—Mathematics interface

Subject Areas:

biocomplexity, biomathematics

Keywords:

fractal dimensions, solitonic, Heimburg–
Jackson model, lump wave

Author for correspondence:

Rami Ahmad El-Nabulsi
e-mails: el-nabulsi@atiner.gr,
nabulsiahmadrami@yahoo.fr

Electronic supplementary material is available
online at rs.figshare.com.

Emergence of lump-like solitonic waves in Heimburg–Jackson biomembranes and nerves fractal model

Rami Ahmad El-Nabulsi^{1,2,3}

¹Research Center for Quantum Technology, Faculty of Science, and ²Department of Physics and Materials Science, Faculty of Science, Chiang Mai University, 50200, Thailand

³Athens Institute for Education and Research, Mathematics and Physics Divisions, 8 Valaoritou Street, Kolonaki, 10671 Athens, Greece

RAE-N, 0000-0001-5357-0208

The aim of this study is to extend the soliton propagation model in biomembranes and nerves constructed by Heimburg and Jackson for the case of fractal dimensions. Our analyses are based on the product-like fractal measure concept introduced by Li and Ostoja-Starzewski in their attempt to explore anisotropic fractal elastic media and electromagnetic fields. The mathematical model presented in the paper is formulated for only a part of a single nerve cell (an axon). The analytical and numerical envelop soliton of this equation are reported. The results obtained prove the emergence of lump-type solitonic waves in nerves and biomembranes. In particular, these waves decay algebraically to the background wave in space direction. This scenario is viewed as a particular class of rational localized waves which are solutions of the integrable Ishimori I equation and the (2 + 1) Kadomtsev–Petviashvili I equation. The effects of fractal dimensions are discussed and were found to be significant to some extents.

1. Introduction

In the last decades, new technological imaging devices such as FMNR (functional magnetic nuclear resonance), CAT (computed axial tomography), PET (positron emission tomography), etc., have been constructed in order to better understand the local and global morphological complexity of several biological and living processes. In particular, the topological and hierarchical neuron structures in the human brain could provide neuroscientists with an experimental and a theoretical framework within which to examine the neural bases of behaviours, together with those that are frequently described in cognitive terms [1,2]. However, these experimental studies, although based on solid theoretical backgrounds, are not sufficient to comprehend the complexity of information processing in the brain and much theoretical works are still required. Recently, it was observed that two plausible mathematical tools to analyze and describe the complexity of cellular and neural brain behaviour are fractals and multifractals [3–5]. Based on experimental evidence, most biological processes may follow fractal rules and could be depicted as fractal entities. Nowadays, modern neurosciences and behavioural brain research are based on fractals analysis and have been a major archetype move in the last decades. Neurons in the brain are characterized by a self-similarity pattern, which is one of the basic properties of fractal geometry, offering a solid mathematical tool to describe neurons and the nervous system quantitatively in all their physiopathological spectrums [4]. It is noteworthy that fractals play a leading role in biology, medicine and several aspects of neurosciences [6] including morphological embryology [7], pyramidal neurons in mammalian motor cortex [8], cortical pyramidal neurons analysis [9], neuronal and glial cellular morphology [10], nonlinear behaviour of awake and sleep stages [11], analysis of states of consciousness and unconsciousness [12]–, study of cerebral cortical surface in

schizophrenia and obsessive-compulsive disorder [13], characterization of atrophic changes in the cerebral cortex [14], cortical functional connectivity networks and severity of disorders of consciousness [15], study of exchange of local and global information processing in the brain [16], etc. (for a good review we suggest [17] and references therein). Fractal analysis is the most valuable mathematical tool for measuring dimensional, geometrical and functional parameters of biological cells, tissues and organs. It is noteworthy that fractals in fact cannot exist in biomembranes, since the scaling behaviour of normal objects is restricted when approaching the molecular size section. However, a recent study based on peridynamic model simulations and experiments performed on spreading double bilayers suggests that the emergence of a kind of fractal morphologies [18]. In this study, we are interested in fractals arising in the nervous system. In fact, the implications of fractal geometry in the neurosciences have been a chief paradigm move over the last decades as it allows for quantitative study and explanation of the geometric complexity of the brain, from axon to the neuronal networks [19].

In neuroscience, the classic theory to describe the propagation of nerve pulse across the axonal membrane with an amplitude of about 100 mV is the Hodgkin–Huxley model (HH) [20]. This model treats the transmitted impulses as pure electrical signals and aims to clarify the spread of signals across the nerve membrane using electrical circuits through explicit ion-conducting proteins (called ion channels) which leads to fleeting voltage changes. In other words, the HH model is used to typify the action potential of a squid axon and has been used successfully in describing and predicting a large number of neuronal properties. This is a dissipative isentropic process and based on the well-known Kirchhoff circuits with electrical currents introduced by the ion flux. The circuit involves a capacitor with constant capacity (the nerve membrane) and the channel proteins as resistors. This model plays a leading role in molecular biology, electrophysiology of biological membranes and dissipative hydrodynamic processes [20]. It is notable that under the HH paradigm the action potential is described as a purely electrical signal whereas the work done by Iwasa & Tasaki [21] is purely an experimental work. We stress that in the realm of the HH model, the action potential is described as an electrical signal whereas experimental observations describing mechanical swelling accompanying the electrical signal in a giant squid axon was not described in a HH model addressed in [21]. The main outcome of [21] based on the examination of the mechanical responses of crab and crayfish axons is that crustacean axons expand during the depolarizing phase of the action potential. Nevertheless, the HH model has been extended by several authors through various ways, e.g. incorporating complex geometries of dendrites and axons based on microscopy data [22], including ion channel populations based on experimental data [23], etc. (see [24] and reference therein). We stress that large-scale neurobiologically models have been used to perceive the presence of efficient brain networks for a broad assortment of tasks in which information processing takes place at the network level with rich temporal behaviour [25].

From a mathematical viewpoint, although a variety of properties of the dynamics of the HH vector field have been studied in the literature, nonetheless, we remain far from an inclusive theory on the dynamics displayed by this

vector field [26–28]. In fact, the HH model fails to explain several features of the propagating nerve pulse, including the reversible release and reabsorption of heat and the additional mechanical, fluorescence and turbidity changes. The alternative model addressed by Heimburg and Jackson in [29,30] is in fact based on some experimental observations as a Boussinesq-type equation with an uncommon nonlinear term. However, they did not deal with the physiological heat changes but only derived a pulse-shaped localized solution for their model equation. The extension of their work to deal with the associated heat exchanges was done in [31] yet heat exchanges will not be taken into account throughout this study. One nice observation by Heimburg and Jackson is that the adiabatic pulses travelling through the membranes could be electromechanical solitons. Hence, the Heimburg and Jackson (HJ) model is able to explain the effect of anaesthetics on nerve pulse conduction and some thermodynamic processes of the neurons' membrane connected with nerve pulse such as physiological heat changes. In the HJ model, solitons propagate at a minimum velocity and besides soliton profiles are stable as a function of the soliton velocity. Solitons propagate at maximum amplitude and a minimum velocity comparable to the propagation velocity in myelinated nerves. In non-myelinated nerves, propagation velocities of solitons are considerably slower. Several models may explain the deformation of the unmyelinated axon wall. One recent model introduced in [32], is inspired by the mechanics of microstructured materials. The model also explains how dissipation may influence the process. Let us recall that there are two classical definitions for a soliton: (a) a soliton can be described as a stable particle-like state in a nonlinear system [33], (b) another way is defining through its properties as a wave in the nonlinear environment that has (i) a stable form, (ii) is localized in space, (iii) restores its speed and structure after interaction with another soliton [34]. It is also worth-mentioning that using solitons to model nerve pulses is to some extent a fundamentally flawed concept because nerve pulses annihilate each other during a head-on collision, which is backed up by a large number of experimental observations in a wide range of settings, while solitons, as a rule, do not because they need to interact elastically (restoring their shape and velocity after collision) and this is a fundamental contradiction. What Heimburg, Jackson and other authors who are investigating the 'mechanical' nerve pulse aspect have shown is that such a soliton-type solution can exist in a mathematical model composed for a lipid bi-layer. However, so far there has been no experimental work that would have been able to observe a 'mechanical nerve pulse', i.e. a mechanical signal on a test system similar enough to a real axon or neuron that behaves like a real nerve signal, meaning that it has the three key properties (1) threshold for excitation, (2) annihilation during a collision, (3) a time delay before you can propagate the next pulse. The experimental works that observe a mechanical wave in nerves [21] have been able to observe a mechanical wave accompanying the electrical signal but not a stand-alone mechanical signal that behaves like a nerve pulse.

In fact, one crucial feature of lipid bilayers is that they display phase transitions from solid-ordered to liquid-disordered states. Hence, they are considered an impulse for the proliferation of solitons is the lipid melting due to the propagation of a localized density wave in the axon

membrane [35]. We stress that Heimburg *et al.* [30] proposed their model for a longitudinal mechanical density change as a Boussinesq-type equation (a wave equation with added nonlinear and dispersive effects) and determined some coefficients for their model by doing an experiment on a lipid mixture, which is not quite the same as a real nerve fibre. Experimental data were instead used to determine the nonlinear parameters for their model. It is noteworthy that the soliton model in nonlinear dispersive media arises due to a weak balance between the steepening effects of nonlinearity and the spreading effects of wave dispersion. Solitary waves are a subset of a family of coherent structures and could acquire a stable shape under some constraints [36]. It should be stressed again that the solution obtained by Heimburg *et al.* in [30] is not a ‘soliton’ since stability has not been checked if their solution is stable through the collisions with another solution. It will be better to entitle these solutions by ‘soliton-like’, or ‘solitary waves’. The question of whether the solutions described by Heimburg *et al.* are really ‘solitons’ has been addressed by Lautrup *et al.* [29] where it was concluded that ‘*in particular, if multisoliton solutions were constructed it was recognized that, in spite of the strong interaction between them, solitons ‘pass through’ one another without losing their identity*’. Hence, the solutions obtained in [30] are not solitons but are merely solitonic or soliton-type solutions, as they interact with each other inelastically, as was demonstrated in [29].

Despite the significant connections between fractals and physiology as discussed in [36], there is potentially very little research that treats the fractal aspects of the HH soliton model [37]. It is notable that some models based on fractional aspects have been introduced; nevertheless, these models are based on the concept of fractional analysis and not fractal calculus [38,39]. Moreover, it should be stressed that the fractal aspects of solitary waves were addressed in literature through dissimilar aspects but not within the HH model [40,41]. Yet, our approach will be based on a different aspect to those found in literature known as the ‘product-like fractal measure’.

In fact, this new concept was introduced recently by Li and Ostoja-Starzewski in order to describe dynamics in anisotropic and continuum media [42–44] and was motivated by Tarasov fractal calculus arguments [45,46]. It is considered a successful approach, which has proved to have several successful implications in sciences and engineering at different scales [47–58]. In the Li and Ostoja-Starzewski approach (LOSA henceforth), the dynamic equations of motion hold mathematical forms involving integer-order integrals, whereas their local forms are expressed through partial differential equations with integer-order derivatives except that they contain coefficients involving fractal dimensions. Hence, this model is suitable to describe dynamics in fractal dimensions and at all scales. We set-up in brief the basic mathematical aspects of LOSA: we assume we have a parallelepiped of different lengths x_1, x_2, x_3 , mass $m = m(x_1, x_2, x_3) \approx x_1^{\alpha_1} x_2^{\alpha_2} x_3^{\alpha_3}$ and density $\rho = \rho(x_1, x_2, x_3)$ in a medium of dimension $D = \alpha_1 + \alpha_2 + \alpha_3$ where $0 < \alpha_k \leq 1$ is the fractal dimension in the direction x_k . Mathematically, one can define the mass of the parallelepiped by the following triple integral $m = \int_V \prod_{k=1}^3 c_1^k(\alpha_k, x_k) dx_k = \int_V \rho \prod_{k=1}^3 d\mu_k(x_k)$ over the volume V . Here $d\mu_k(x_k) := \prod_{k=1}^3 c_1^k(\alpha_k, x_k) dx_k$ is the length measurement and $c_1^{(k)}(\alpha_k, x_k) = \alpha_k ((l_k - x_k)/l_{k0})^{\alpha_k - 1}$ is a coefficient function of the length l_k along axis $0 < x_k < l_k$ obtained from the Jumarie’s fractional integral and l_{k0} is a typical length

where its meaning depends on the physical problem under study. The parallelepiped is, therefore, characterized by the volume coefficient $c_3 = \prod_{i=1}^3 c_1^{(i)}$. Li and Ostoja-Starzewski has proved that for $c_2^{(k)} = c_1^{(i)} c_1^{(j)} = c_3/c_1^{(k)}, i \neq j, j \neq k$, the vector calculus identities and the following fundamental theorems of vector calculus hold accordingly:

- the Gauss theorem $\int_{\partial W} f_k n_k dS_d = \int_W f_{k,k} c_2^{(k)} c_3^{-1} V_d = \int_W f_{k,k} c_1^{-1(k)} dx_1 dx_2 dx_3$,
- the Stokes theorem $\int_A \mathbf{n} \cdot \nabla \times \mathbf{f} dS_d = \int_S \mathbf{f} \cdot d\mathbf{l}_{\alpha_1}$,
- the divergence theorem $\int_V \nabla^D \cdot \mathbf{f} dV_D = \int_V \nabla^D \cdot \mathbf{f} c_1^{(1)} c_2^{(2)} c_3^{(3)} dx dy dz = \int_S \mathbf{f} \cdot \mathbf{n} dS_d$.

Here $dS_d^{(k)} = c_2^{(k)} dS_2 = c_1^{(i)} c_1^{(j)} dS_2 = (c_3/c_1^{(k)}) dS_2, i \neq j, j \neq k$ is the planar surface element, dS_d is the infinitesimal fractal surface element and $dV_D = c_1^{(1)} c_2^{(2)} c_3^{(3)} dx dy dz$ is the infinitesimal fractal volume element. As a result, the gradient and the Laplacian operators hold respectively the unique forms $\nabla_k^D = (c_1^{(k)})^{-1} \nabla_k$, $\Delta_k^D = \nabla_k^D \cdot \nabla_k^D$ and $\nabla^D = \mathbf{e}_k \nabla_k^D$ with \mathbf{e}_k are base vectors. LOSA mathematical structures are in fact comparable to more than a few approaches discussed in literature yet based on fractional calculus [59,60]. It is noteworthy that the extended fractional HH model has been addressed in the literature [39]. Besides, it was revealed in [61] that a fractional capacitance model may overcome the following drawbacks of the HH model: ignorance of dielectric losses in the membrane and the assumption of an ideal membrane capacitance. Let us recall also that there exists a physically based connection between fractional calculus and fractal geometry [62]. Moreover, there are many indications that ion channel proteins exhibit memory and are based on a power-law self-similar function [63,64]. Hence fractal kinetics may help to understand how ion channel conductance profiles are affected by fractal dimension [65,66]. These power-law and correlation characteristics may be practical in the coding and decoding process of HH neuron [67]. These outcomes motivate the studies of HH and HJ models in fractal dimensions. It is notable that neurons possess a wide variety of shapes, sizes and electromechanical properties [68]. There exist also several observations based on experimental studies which indicate that an Action Potential (AP) is accompanied with a number of physiological changes in the nerve membrane such as, production and absorption of heat, variation of axon diameter, density, pressure and length [69]. Hence, the neurons are subject to an increase and decrease in axon diameter and density. Hence, the LOSA and its associated parameters, such as characteristic lengths and density, may be a successful attempt to describe the HH and HJ models in fractal dimensions.

Moreover, in this study we will extend the LOSA by using the Hausdorff fractal time derivative operator (HFTDO), which is derived from fractal calculus (FC). We will prove that the combination of the LOSA with HFTDO will give rise to a nonlinear partial differential equation that holds a number of particular features and will be used to describe soliton wave propagation characteristics. In fact, FC is a relatively new field introduced to deal with kinetic fractal theory where the continuous time is replaced by the fractal time [70,71]. Such a derivative substitution is effective at very low scales [72]. Based on FC, the HFTDO takes the general form $D^\beta := (T_0/\bar{\tau})^{\beta-1} D$ where $D^\beta = \partial/\partial\bar{\tau}^\beta$ and $D = \partial/\partial\bar{\tau}$, $\bar{\tau} = t - \tau$, $0 < \tau < t$, T_0 is a characteristic time and β is a real parameter close to unity and is interpreted in FC as the fractal dimension of time [73–77]. We can associate τ to the locally

recorded time and t to the final measured value of the moving body time. When t varies, the complete earlier time interval varies as well. This operator is also obtained from the fractional velocity arguments which has the mathematical form $v_{\pm}^{\beta}f(x) \triangleq \lim_{\varepsilon \rightarrow 0} v_{\beta}^{\varepsilon \pm}[f](x)$ and is defined in terms of the fractal variations operators $v_{\beta}^{\varepsilon+}[f](x) = (f(x+\varepsilon) - f(x))/\varepsilon^{\beta}$ and $v_{\beta}^{\varepsilon-}[f](x) = (f(x) - f(x-\varepsilon))/\varepsilon^{\beta}$. Two cases were discussed in [78–81]: $0 < \beta \leq 1$ and $1 \leq \beta < 2$, which proves dissimilar dynamics. Another comparable definition has been also introduced in [82–84] by using indefinite limit and L'Hospital rule such that $f^{(\beta)}(x) \triangleq \lim_{\varepsilon \rightarrow 0} \Delta^{\beta}f(x)/L^{\beta}$ where $\Delta^{\beta}f(x) = f^{\beta}(x+\varepsilon) - f^{\beta}(x)$ and $L^{\beta} = (x+\varepsilon)^{\beta} - x^{\beta}$. These approaches led to the definition of the HFTDO. Note that:

$$D^{\beta}D^{\beta} = \left(\frac{T_0}{\bar{\tau}}\right)^{\beta-1} (D^2 + \frac{1-\beta}{\bar{\tau}}D) := \left(\frac{T_0}{\bar{\tau}}\right)^{\beta-1} (B_{1-\beta})_{\bar{\tau}},$$

where $(B_{1-\beta})_{\bar{\tau}} := D^2 + \frac{1-\beta}{\bar{\tau}}D$ is the Bessel operator [85]. Several applications of HFTDO were discussed in [86–93]. However, for very large time, we can use the following asymptotic rule $(B_{1-\beta})_{\bar{\tau}} \approx D^2$. It is notable that fractal time has been used in studying nonlinear dynamics of microtubes in cells which are considered as a network for solitary waves [94]. In addition, multifractal time series has been used to study the topological properties of both experimental and simulated microtubes [95]. In fact, the implications of fractal time have been discussed in several complex systems including living cells [96–98]. There exist also several arguments which indicate that biological time is fractal [99] and in addition, fractal time has been used to study the movement activity of *Drosophila* [100]. The importance of spatial and temporal scaling to the study of biological systems and physiological processes [101] motivate us to consider fractal time in this study.

This study is organized as follows in §2, we introduce the basic set-ups of the theory; in §3, we discuss some of its main computational properties and features; finally conclusions and perspectives are given in §4.

2. Basic set-ups of the fractal Heimburg-Jackson model

In order to implement LOSA + HFTDO in HJ theory, we let $\Delta\rho^A$ be the area density change in the plane (τ, z) and we introduce the following nonlinear partial differential equation in fractal dimensions (α, β) which is derived from the Euler equations of compressible media (comparable to a variable-coefficient wave equation) [102–107]:

$$\begin{aligned} S(z) \left(\frac{T_0}{\bar{\tau}}\right)^{\beta-1} (B_{1-\beta})_{\bar{\tau}} \Delta\rho^A &\equiv S(z) \left(\frac{T_0}{\bar{\tau}}\right)^{\beta-1} \left(\frac{\partial^2}{\partial \bar{\tau}^2} + \frac{1-\beta}{\bar{\tau}} \frac{\partial}{\partial \bar{\tau}} \right) (\Delta\rho^A), \\ &= \nabla_z^{\alpha} (c^2 \nabla_z^{\alpha} (\Delta\rho^A)) \equiv \left(\frac{l_0}{l-z}\right)^{\alpha-1} \frac{\partial}{\partial z} \left(c^2 \left(\frac{l_0}{l-z}\right)^{\alpha-1} (\Delta\rho^A) \right), \end{aligned} \quad (2.1)$$

where the function $S(z) = S_0((l-z)/l_0)^m$ is, in general, associated with density [108], m is a real parameter, $S_0 > 0$, c is the celerity of sound, which usually is a function of $\Delta\rho^A = \rho^A - \rho_0^A$ in particular close to melting transitions in membranes with ρ^A being the lateral density of the membrane and ρ_0^A the equilibrium lateral density in the fluid phase of the membrane [102,109]. We recall that we are

consider a one-spatial dimensional model where τ is the time and z is the position along the nerve axon. In the HJ model, the soliton-like model considers the wave equation for area density changes $\Delta\rho^A$ that originates from the Euler equations of compressible media. In general, the celerity of sound takes the form $c^2 \approx c_0^2 + p\Delta\rho^A + q(\Delta\rho^A)^2 + \dots$ where p and q describe the reliance of the sound velocity on density in the vicinity of the melting transition and are subject to experimental statistics and $c_0 \approx 176.6 \text{ m s}^{-1}$ is the low frequency sound velocity [24]. It is noteworthy that equation (2.1) is a fractal generalization of the Euler–Poisson–Darboux equation, which is used in many problems of modern mathematics and physics [110]. Besides, the variable-coefficients (linear or nonlinear) partial differential equations supply us, in several dynamical systems or physical theories, with more plausible information on the inhomogeneities of media than analogous constant-coefficient counterparts. It is notable that neurons exhibit a kind of spatially inhomogeneity in biological bodies. The brain, for example, exhibits an inhomogeneous allocation of neurons and astrocytes throughout the diverse brain areas [111,112]. Inhomogeneities have also been observed in biomembranes and bionanocomposites [113–115] and have important implications in bioengineering.

In order to take into account the dispersion effect, a fourth-order fractal derivative term $-h\Delta_z\Delta_z(\Delta\rho^A) \equiv -h\Delta_{zz}(\Delta\rho^A)$ is added to equation (2.1) in the HJ model. $\Delta_z = \partial^2/\partial z^2$, $\Delta_{zz} = \partial^4/\partial z^4$, h in the HJ model is assumed to be a small constant describing the frequency dependence of the speed of sound. In this study, we will extend the HJ model by adding the term $-\Delta_z\Delta_z(h(z)(\Delta\rho^A))$ since in general, the medium is subject to various external constraints which may give rise to higher-order solitonic waves with variable coefficients [116–122]. Some authors added a fourth-order mixed partial derivative term to model the inertial properties of the membrane as a modification to the original model and have interpreted the dispersive term included in the original HJ model as representing the elastic properties of the membrane [123,124]. Hence, the additional element may represent physically or physiologically in the present model describing a density pulse in a biomembrane.

For very large evolution time, the HJ equation in fractal dimension $0 < \alpha \leq 1$ takes the form (fractal Boussinesq-type equation):

$$\begin{aligned} S_0 \left(\frac{Z}{l_0}\right)^m \left(\frac{T_0}{\bar{\tau}}\right)^{\beta-1} \frac{\partial^2}{\partial \bar{\tau}^2} \Delta\rho^A &= \nabla_Z^{\alpha} (c^2 \nabla_Z^{\alpha} (\Delta\rho^A)) - \Delta_Z^{\alpha} \Delta_Z^{\alpha} (h(Z) \Delta\rho^A) \\ &\equiv \nabla_Z^{\alpha} c^2 \nabla_Z^{\alpha} (\Delta\rho^A) + c^2 \Delta_Z^{\alpha} (\Delta\rho^A) - \Delta_Z^{\alpha} \Delta_Z^{\alpha} (h(Z) \Delta\rho^A), \end{aligned} \quad (2.2)$$

It is noteworthy that one is able to solve equation (2.2) numerically or using the Sonine–Poisson–Delsarte transmutation method, which are the transmutations of the hyper-Bessel operators and functions [125] keeping the Bessel operator $(B_{1-\beta})_{\bar{\tau}} := D^2 + \frac{1-\beta}{\bar{\tau}}D$, however, our aim is to give an asymptotic solution of the HJ theory of biomembranes and nerves system. Since we have:

$$\begin{aligned} \Delta_Z^{\alpha} \Delta_Z^{\alpha} (h(Z) (\Delta\rho^A)) &= h(Z) \Delta_Z^{\alpha} \Delta_Z^{\alpha} (\Delta\rho^A) + 4\nabla_Z^{\alpha} h(Z) \nabla_Z^{\alpha} \Delta_Z^{\alpha} (\Delta\rho^A) \\ &\quad + 6\Delta_Z^{\alpha} h(Z) \Delta_Z^{\alpha} (\Delta\rho^A) \\ &\quad + 4\nabla_Z^{\alpha} (\Delta\rho^A) \nabla_Z^{\alpha} \Delta_Z^{\alpha} h(Z) \\ &\quad + (\Delta\rho^A) \Delta_Z^{\alpha} \Delta_Z^{\alpha} h(Z), \end{aligned} \quad (2.3)$$

we can write equation (2.1) as:

$$\begin{aligned} S_0 \left(\frac{T_0}{\tau}\right)^{\beta-1} \frac{\partial^2}{\partial \tau^2} \Delta \rho^A &= \left(\frac{Z}{l_0}\right)^{2(1-\alpha)-m} \\ (\nabla_Z c^2 \nabla_Z (\Delta \rho^A) + c^2 (\Delta_Z + \frac{\alpha-1}{Z} \nabla_Z) (\Delta \rho^A)) \\ - \left(\frac{Z}{l_0}\right)^{4(1-\alpha)} h(Z) \left(\Delta_{ZZ} (\Delta \rho^A) + \frac{(\alpha-1)^2}{Z^2} \Delta_Z (\Delta \rho^A)\right. \\ - \frac{(1-\alpha)(2\alpha^2-\alpha+1)}{Z^3} \nabla_Z (\Delta \rho^A) \Big) - \left(\frac{Z}{l_0}\right)^{4(1-\alpha)} (\Delta \rho^A) \\ \left(\Delta_{ZZ} h(Z) + \frac{(\alpha-1)^2}{Z^2} \Delta_Z h(Z) - \frac{(1-\alpha)(2\alpha^2-\alpha+1)}{Z^3} \nabla_Z h(Z)\right) \\ - 4 \left(\frac{Z}{l_0}\right)^{4(1-\alpha)} \nabla_Z h(Z) (\nabla_{ZZZ} (\Delta \rho^A) + \frac{1-\alpha}{Z} \Delta_Z (\Delta \rho^A) \\ + \frac{(1-2\alpha)(\alpha-1)}{Z^2} \nabla_Z (\Delta \rho^A)) - 4 \left(\frac{Z}{l_0}\right)^{4(1-\alpha)} \nabla_Z (\Delta \rho^A) \\ \left(\nabla_{ZZZ} h(Z) + \frac{1-\alpha}{Z} \Delta_Z h(Z) + \frac{(1-2\alpha)(\alpha-1)}{Z^2} \nabla_Z h(Z)\right) \\ - 6 \left(\frac{Z}{l_0}\right)^{4(1-\alpha)} (\Delta_Z h(Z) + \frac{\alpha-1}{Z} \nabla_Z h(Z)) \\ (\Delta_Z (\Delta \rho^A) + \frac{\alpha-1}{Z} \nabla_Z (\Delta \rho^A)). \end{aligned} \quad (2.4)$$

The scales $c^2 := c^2(\Delta \rho^A) = \bar{c}^2(\Delta \rho^A)(Z/l_0)^{1-\alpha}$ and $h(Z) = h_0(Z/l_0)^{\alpha-1}$ (h_0 being a tiny constant) reduce equation (2.4) for very large propagation distance to:

$$\begin{aligned} S_0 \left(\frac{T_0}{\tau}\right)^{\beta-1} \frac{\partial^2}{\partial \tau^2} \Delta \rho^A &\approx \left(\frac{Z}{l_0}\right)^{3(1-\alpha)-m}. \\ \nabla_Z (\bar{c}^2 \nabla_Z) \Delta \rho^A (-h_0 (\nabla_{ZZZ} (\Delta \rho^A))) + O(\frac{1}{Z^2}) \end{aligned} \quad (2.5)$$

We let $Z = l_0^{1-n} X^n$ and $\tau = T_0^{1-\chi} \tilde{\tau}^\chi$ (n and χ are real parameters) which convert equation (2.5) for $h_0/X \ll 1$ and for very large time to:

$$\begin{aligned} \frac{S_0}{\chi^2} \left(\frac{T_0}{\tau}\right)^{\chi \beta + \chi - 2} \frac{\partial^2}{\partial \tau^2} (\Delta \rho^A) &\approx \left(\frac{X}{l_0}\right)^{2-n(m+3\alpha)} \\ \nabla_X (\bar{c}^2 \nabla_X - h_0 \nabla_{XXX}) (\Delta \rho^A). \end{aligned} \quad (2.6)$$

$$u(z, \tau) = \frac{2P}{S + N \cosh \left(\bar{c}_0 / \sqrt{h_0} \sqrt{1 - \eta^2} \left(l_0 (l - z/l_0)^{m+3\alpha-1/2} - (4\eta \bar{c}_0 / \sqrt{S_0(1+\beta)^2}) T_0 (t - \tau/T_0)^{1+\beta/2} \right) \right)}. \quad (2.11)$$

In the next section, we will analyse some of the computational properties of equation (2.11).

3. Computational aspects of the fractal Heimburg–Jackson model

For $m=0$ and $\alpha=\beta=1$, equation (2.11) is reduced to its conventional form. However, a plausible solution exists for $\alpha>1/2$. Besides, when $t \approx \tau$, the solution $u(Z)$ is roundly spatial and is plotted in figure 1 ($u_1(Z)$) and figure 2 ($u_2(Z)$) for $\eta=0.95$, $l_0=1$, $h_0 \approx 2m^4 \times s^{-2}$ and different values of m and α . In fact, $u_1(Z)$ and $u_2(Z)$ are solutions of $u(Z)$ for different values of the parameters,

Figure 1 appears to show the HJ equation solution, which is similar to the one published and analysed by Lautrup *et al.* in [29], whereas figure 2 describes the evolution for different parameters in the positive domain. These wave profiles are different from wave profiles analysed in [24]. We observe deformations or distortions in the shape of these profiles compared to the results obtained in [24] due to the fractal dimensions of the medium although the solution displays exponentially localized

Obviously, for $n=2/(m+3\alpha-1)$ and $\chi(1+\beta)=2$ equation (2.6) is considerably simplified to:

$$\frac{(1+\beta^2)S_0}{4} \frac{\partial^2}{\partial \tilde{\tau}^2} \Delta \rho^A \approx \nabla_X (\bar{c}^2 \nabla_X - h_0 \nabla_{XXX}) (\Delta \rho^A) + O\left(\frac{1}{X}\right), \quad (2.7)$$

where $\tilde{\tau} = 4\tilde{\tau}/\sqrt{S_0(1+\beta^2)}$. Again, the change of variables $u = \Delta \rho^A / \rho_0^A$, $Y = (c_0 / \sqrt{h_0}) X$, $t = (c_0^2 / \sqrt{h_0}) \tilde{\tau}$, $B_1 = (\rho_0 / \bar{c}_0^2) p$ and $B_2 = (\rho_0^2 / \bar{c}_0^2) q$ transform equation (2.7) to roughly the conventional form:

$$\frac{\partial^2 u}{\partial t^2} \approx \nabla_Y (B(u) \nabla_Y u) - \Delta_{YY} u + O\left(\frac{1}{Y}\right) \quad (2.8)$$

where $B(u) = 1 + B_1 u + B_2 u^2$ with $B_1 \approx -16.6$ and $B_2 \approx 79.5$ as determined experimentally for a synthetic lipid membrane [24]. The coordinate transformation $\xi = Y - \eta t$ (η being a dimensionless propagation velocity of the density pulse) converts equation (2.8) to:

$$\eta^2 \Delta_\xi u \approx \nabla_\xi (B(u) \nabla_\xi u) - \Delta_\xi \Delta_\xi u + O\left(\frac{1}{\xi}\right). \quad (2.9)$$

The solution of this equation is given by [23]:

$$u(\xi) = \frac{2P}{S + N \cosh(\xi \sqrt{1 - \eta^2})}. \quad (2.10)$$

Here $P = a_+$, a_- , $S = a_+ + a_-$, $N = a_+ - a_-$, $a_\pm = -(B_1/B_2)$ $(1 \pm \sqrt{(\eta^2 - \eta_0^2)/(1 - \eta_0^2)})$ with $\eta_0 = \sqrt{1 - B_1^2/6B_2} \approx 0.649851$, $1 > |\eta| > \eta_0$ and $h_0 \approx 2 m^4 \times s^{-2}$, i.e. $a_+ \approx 0.39$, $a_- \approx 0.08$, $P \approx 0.007371$, $S \approx 0.4089$ and $N \approx 0.3711$ [24]. In term of the original coordinates, the solution is given by:

$$u(z, \tau) = \frac{2P}{S + N \cosh \left(\bar{c}_0 / \sqrt{h_0} \sqrt{1 - \eta^2} \left(l_0 (l - z/l_0)^{m+3\alpha-1/2} - (4\eta \bar{c}_0 / \sqrt{S_0(1+\beta)^2}) T_0 (t - \tau/T_0)^{1+\beta/2} \right) \right)}. \quad (2.11)$$

solitary solutions for a finite range of subsonic velocities. Comparing the positive domains of figures 1 and 2, we observe the presence of long tails for lower fractal dimensions and for large scales, which represent one of the main features of fractal and fractional wave equations [126].

In figures 3–6, we plot the three-dimensional numerical variations of $u(Z)$ after fixing the numerical values of (l_0, T_0) and for different values of m , α and β to observe the physical behaviour of the system ($Z = l - z$, $T = t - \tau$ and the base of figures 3–6 correspond to (Z, T)):

These graphs describe dissimilar cone wave solitonic solutions which reveal a symmetric surface and peaks in the centre depending on the fractal dimensions of the medium. We observe how our obtained solutions change their wave structure via appropriate choices of the numerical values of (m, α, β) . These solutions illustrated graphically clarify the new features of the model in question. The novelty of our solutions is shown by comparing these numerical solutions with figure 7 obtained in the conventional HJ approach [24]. In particular, we have the emergence of a lump-like soliton wave whereas in the approach of [24], such a solution is not present (as shown in figure 7).

localized waves, which are solutions of the integrable Ishimori I equation and the (2 + 1) Kadomtsev–Petviashvili I equation, which describes small-amplitude shallow-water waves in particular when the Bond number is greater than 1/3 [128]. More explicitly, lump solutions with kink backgrounds are used to describe nonlinear patterns on a shallow water surface with dominating surface tension [129]. The lump soliton solutions have been regularly used in different fields of sciences including biology and chemistry [130–132]. It is interesting to obtain lump-type soliton solutions in the HJ model for biomembranes and nerves. In the present model, the lump-type solitonic wave is due to the fractal dimensions of the medium and the influence of the dispersion and nonlinear effects. Varying the numerical values of (l_0, T_0) can lead to a variation of the range of the lump wave but has no effect on the amplitude. Hence, the amplitude of the lump is not affected by the numerical values of (m, α, β) and (l_0, T_0) . This is comparable to the lump wave solutions for the (3 + 1) Kadomtsev–Petviashvili I equation in fluid [133]. It is notable that, in general, the origin of the lump waves is still a matter of debate even through research argues that solitons can release or swallow lump waves [134].

It will be of interest to extend this work to analyse collision phenomena among lump waves with periodic and single-, double-kink soliton solutions of the present model and to compare the outcomes with findings obtained in literature within the (2 + 1)-dimensional Kadomtsev–Petviashvili soliton model [132] and peakon model [135,136]. The solutions obtained in this study show that the proposed model is consistent and simple and so, we believe that the recommended idea could be extended for supplementary nonlinear models in neurosciences. It will also of interest to estimate fractal dimensions directly from the observed behaviour of the neuro-system.

References

- Schlinger HD. 2015 Behavior analysis and behavioral neuroscience. *Front. Hum. Neurosci.* **9**, 210. (doi:10.3389/fnhum.2015.00210)
- Johnston D, Wu SMS. 1995 *Foundations of cellular neurophysiology*. Cambridge, MA: MIT Press.
- Bernard F, Bossu JL, Gaillard S. 2001 Identification of living oligodendrocyte developmental stages by fractal analysis of cell morphology. *J. Neurosci. Res.* **65**, 439–445. (doi:10.1002/jnr.1172)
- Ieva AD, Grizzi F, Jelinek H, Pellionisz AJ, Losa GA. 2014 Fractals in the neurosciences, part I: general principles and basic neurosciences. *Neuroscientist* **20**, 403–417. (doi:10.1177/1073858413513927)
- Ieva AD, Esteban FJ, Grizzi F, Klonowski W, M. Martin-Landrove M. 2015 Fractals in the neurosciences, part II: clinical applications and future perspectives. *Neuroscientist* **21**, 30–43. (doi:10.1177/1073858413513928)
- Weibel ER. 2005 Mandelbrot's Fractals and the geometry of life:a tribute to Benoît Mandelbrot on his 80th birthday. In *Fractals in biology and medicine*. (eds GA Losa, D Merlini, TF Nonnenmacher, ER Weibel). Basel, Switzerland: Birkhäuser.
- Pirici D, Mogoașă L, Mărgăritescu O, Pirici I, Turodić V, Coconu M. 2009 Fractal analysis of astrocytes in stroke and dementia. *Rom. J. Morphol. Embryol.* **50**, 381–390.
- Porter R, Ghosh S, Lange GD, Smith TG. 1991 A fractal analysis of pyramidal neurons in mammalian motor cortex. *Neurosci. Lett.* **130**, 112–116. (doi:10.1016/0304-3940(91)90240-T)
- Schierwagen A, Costa L, Alpár A, Gártner U. 2007 Multiscale fractal analysis of cortical pyramidal neurons. In *Bildverarbeitung für die medizin 2007: Informatik aktuell* (eds A Horsch, TM Deserno, H Handels, HP Meinzer, T Tolxdorff), pp. 424–428. Berlin, Germany: Springer Verlag.
- Smith TG, Lange GD. 1995 Fractal studies of neuronal and glial cellular morphology. In *Fractal geometry in biological systems: an analytical approach* (eds PM Iannaccone, M Khokha), pp. 173–186. New York, NY: CRC Press.
- Pereda E, Gamundi A, Rial R, Gonzalez J. 1998 Non-linear behaviour of human EEG: fractal exponent versus correlation dimension in awake and sleep stages. *Neurosci. Lett.* **250**, 91–94. (doi:10.1016/S0304-3940(98)00435-2)
- Ruiz de Miras J et al. 2019 Fractal dimension analysis of states of consciousness and unconsciousness using transcranial magnetic stimulation. *Comp. Meth. Prog. Biomed. Biomedicine* **175**, 129–137. (doi:10.1016/j.cmpb.2019.04.017)
- Ha TH, Yoon U, Lee KJ, Shin YW, Lee JM, Kim IY, Ha KS, Kim SI, Kwon JS. 2005 Fractal dimension of cerebral cortical surface in schizophrenia and obsessive-compulsive disorder. *Neurosci. Lett.* **384**, 172–176. (doi:10.1016/j.neulet.2005.04.078)
- King RD, George AT, Jeon T, Hynan LS, Youn TS, Kennedy DN, Dickerson B. 2009 Characterization of atrophic changes in the cerebral cortex using fractal dimensional analysis. *Brain Imag. Behav.* **3**, 154–166. (doi:10.1007/s11682-008-9057-9)
- Varley TF, Craig M, Adapa R, Finoia P, Williams G, Allanson J, Pickard J, Menon DK, Stamatakis EA. 2020 Fractal dimension of cortical functional connectivity networks & severity of disorders of consciousness. *PLoS ONE* **15**, e0223812. (doi:10.1371/journal.pone.0223812)
- Bieberich E. 2002 Recurrent fractal neural networks: a strategy for the exchange of local and global information processing in the brain. *Biosyst.* **66**, 145–164. (doi:10.1016/S0303-2647(02)00040-0)
- Werner G. 2015 Fractals in the nervous system: conceptual implications for theoretical neuroscience. *Front. Physiol.* **1**, 15.
- Taylor M, Gozen I, Patel S, Jesorka A, Bertoldi K. 2016 Peridynamic modeling of ruptures in biomembranes. *PLoS ONE* **11**, e0165947. (doi:10.1371/journal.pone.0165947)
- Di Ieva A. 2016 Fractals in neuroanatomy and basic neurosciences: an overview. In *The fractal geometry of the brain. Springer series in computational neuroscience* (ed. A Di Ieva). New York, NY: Springer.
- Hodgkin AL, Huxley AF. 1952 A quantitative description of membrane current and its application to conduction and excitation in nerve. *J. Physiol.* **117**, 500–544. (doi:10.1113/jphysiol.1952.sp004764)
- Iwasa K, Tasaki I. 1980 Mechanical changes in squid giant-axons associated with production of action potentials. *Biochem. Biophys. Research Comm.* **95**, 1328–1331. (doi:10.1016/0006-291X(80)91619-8)
- Almog M, Korngreen A. 2016 Is realistic neuronal modeling realistic? *J. Neurophysiol.* **116**, 2180–2209. (doi:10.1152/jn.00360.2016)
- Gerstner W, Kistler WM, Naud R, Paninski L. 2014 Ion channels and the Hodgkin–Huxley model, Chapter 2. In *Nonlinear dynamics: from single neurons to networks and models of cognition*, pp. 28–57. Cambridge, UK: Cambridge University Press.
- Gogoi P, Bujarbarua SM, Roym S. 2018 Modeling a bioinspired neuron: an extension to the H–H model. In *Advanced computational and communication*

Plastic Dissipation Mechanisms in Periodic Microframe-Structured Polymers

By Lifeng Wang, Mary C. Boyce,* Cheng-Yen Wen, and Edwin L. Thomas

Novel lightweight micro- and nanostructured materials are being used as constituents in hierarchically structured composites for providing high stiffness, high strength, and energy absorbing capability at low weight. Three dimensional SU-8 periodic microframe materials with submicrometer elements exhibit unusual large plastic deformations. Here, the plastic dissipation and mechanical response of polymeric microframe structures is investigated using micromechanical modeling of large deformations. Finite element analysis shows that multiple deformation domains initiate, stabilize, and then spread plasticity through the structure; simulated deformation mechanisms and deformation progression are found to be in excellent agreement with experimental observation. Furthermore, the geometry can be used to tailor aspects of 3D behavior such as effective lateral contraction ratios (elastic and plastic) during tensile loading as well as negative normal stress during simple shear deformation. The effects of structural geometry on mechanical response are also studied to tailor and optimize mechanical performance at a given density. These quantitative investigations enable simulation-based design of optimal lightweight material microstructures for dissipating energy.

1. Introduction

New design concepts for energy absorption materials, especially for personal protection applications, have attracted great interest in material science.^[1] Novel lightweight micro- and nanostructured materials are being used as constituents in hierarchically structured composites for providing high stiffness, high strength, and energy absorbing capabilities.^[2,3] Multifunctional microframe structures appear widely in nature, examples include cork,^[4] the *Euplectella* sp. skeleton,^[5] and sea urchin exoskeleton,^[6] and possess optimized mechanical properties, which

inspire many man-made structural materials at micro- and macrolength scales. At the submicron scale, the constituent material of such porous cellular structures can present improved mechanical properties compared to that of the corresponding bulk materials.

Polymer microstructures with reduced feature size are anticipated to possess enhanced energy absorption capability over their bulk counterparts due to the size-scale dependence of the mechanical failure mode. For example, bulk scale brittle polymeric materials can exhibit highly ductile plastic deformations at small length scales;^[7,8] below a critical film thickness, the failure strain of glassy polymers and thermosetting polymers can greatly increase.^[9,10] Recently two-dimensional (2D) and three-dimensional (3D) SU-8 periodic microframe structural materials with submicrometer elements, low density, and feature sizes at the lengthscale of several hundreds of nanometers were fabricated using laser interference lithography.^[11,12] These structures exhibit unusually large plastic deformations when subjected to complex multiaxial loading conditions with local failure strains reaching up to ~300% in the thin members of 3D SU-8 microframes;^[12] in particular, the images of deformed structural elements clearly depict the classic features of cold drawing of glassy polymer bars including neck initiation, neck stabilization, and neck propagation. Although the mechanical behavior of the microframe-structured materials has not yet been quantified, the unique characteristics of plastic deformation in the thin elements, including necking and subsequent mechanical stabilization and drawing into long fibrils, indicate the potential of these structures to function as highly dissipative elements in lightweight energy absorption materials.

Here we investigate the plastic dissipation of 3D periodic SU-8 polymer microframe structures using micromechanical modeling (MM) to simulate the large deformations in tension, compression, and shear observed in these materials. MM is an efficient method to determine overall mechanical behavior of structural and composite materials based on the constituent material stress-strain behavior together with a periodic representative volume element (RVE) of the microstructure. MM also simultaneously captures details of the underlying deformation mechanisms governing the response.

[*] Prof. M. C. Boyce, Dr. L. F. Wang
Department of Mechanical Engineering
Massachusetts Institute of Technology
Cambridge, MA 02139 (USA)
E-mail: mcboyce@mit.edu
Dr. C. Y. Wen, Prof. E. L. Thomas
Institute for Soldier Nanotechnologies
Department of Materials Science and Engineering
Massachusetts Institute of Technology, Cambridge, MA 02139 (USA)

DOI: 10.1002/adfm.200801483

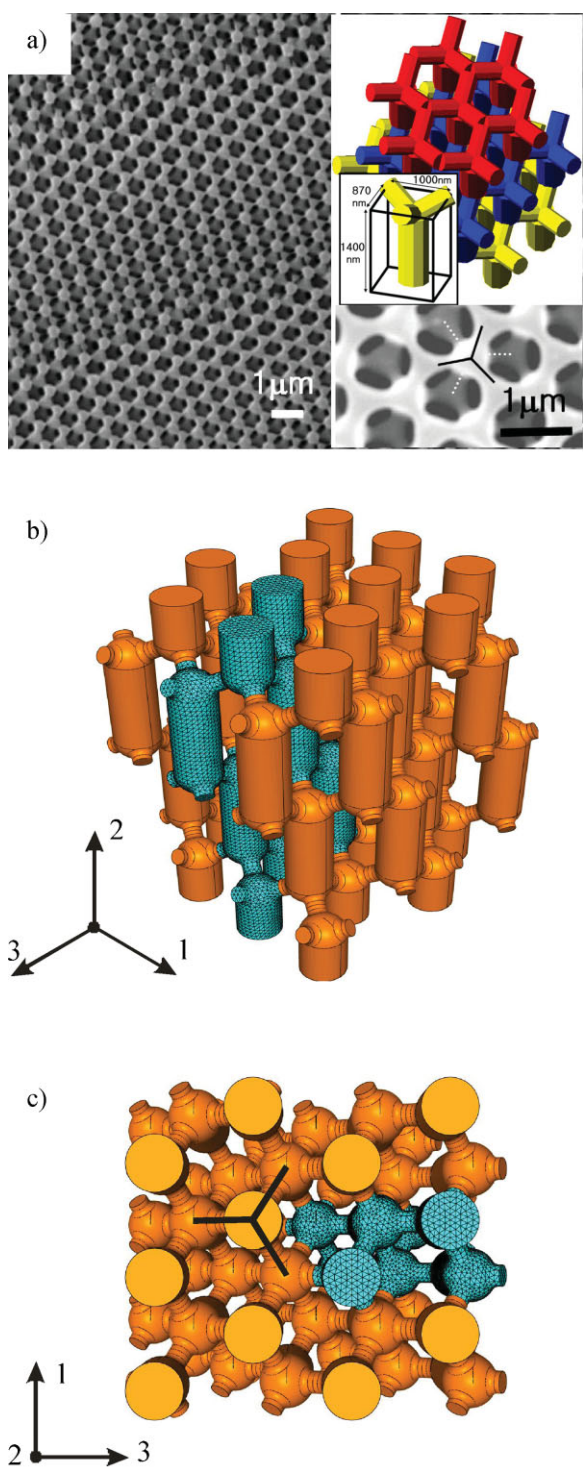


Figure 1. 3D SU-8 microframe structure fabricated using interference lithography [12]. a) Scanning electron microscopy images of the 3D SU-8 microframe structure [12]. The small inset shows a perspective view of the structure with the basic motif of the four-functional element. b,c) Finite element-based micromechanical model of microframe structure from different viewpoints; the meshed RVE consists of six motifs (shown green).

2. Results and Discussion

2.1. Computational Approach

The RVE geometry is created based on the fundamental repeat unit of the microframe structure. Figure 1a depicts micrographs and schematics of the 3D structure under consideration; the inset schematic shows the basic motif comprised of a thicker vertical post and three thinner diagonal struts and its spatial arrangement. In order to implement boundary conditions on the RVE expediently, the 3D structure motif of the microframe structure consists of one thick post and six thinner obliquely oriented struts, each of one-half the length of a full strut. In each layer there are two motifs which capture not only the macroscopic deformation but also the local deformational characteristics. The RVE consists of six motifs arranged in the unit cell. Figure 1b and c shows the finite element-based micromechanical model of the structure with the six motifs of the RVE shown in green (with mesh), surrounded by five neighboring RVEs (orange) for illustration purposes. For this structure, the initial volume

Table 1. The processing routes of the SU-8 used in Refs. [8,11,12]

SU-8	Processing history	T _g (°C)
Beams	Soft bake 65 °C, 1 min and 95 °C, 3 min Exposed: 365 nm UV light, 270 mJ cm ⁻²	155 (DMA)
Wen et al. [8]	Post-exposure bake: 65 °C, 1 min and 95 °C, 1 min Developed in PGMEA and rinsed in IPA and dried	
Beams	Same procedure as above but with an additional	277 (DMA)
Wen et al. [8]	Hard bake: 180 °C, 5 min	
3D microframes	Soft bake: 95 °C, 10 min Exposed: 532 nm Nd:YAG laser, 5–10 J cm ⁻²	100 (DSC)
Jang et al.[12]	Post-exposure bake: 65 °C, 5 min	
2D microframes	Same procedure as Ref. [12]	100 (DSC)
Choi et al.[11]		

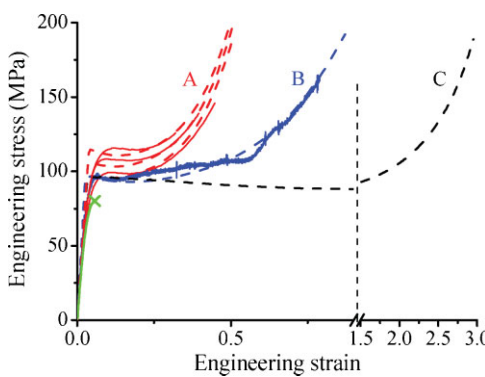


Figure 2. Engineering stress–strain behavior of SU-8 beams under uniaxial tension: experiments (solid lines) and constitutive model prediction (dashed lines). The A, B, and C curves present material properties of the material states characterized by draw ratios of 1.45, 1.75, and 3.0, respectively. Tensile tests conducted at the strain rates of 10⁻³, 10⁻², and 10⁻¹ s⁻¹ are included for the SU-8A sample; the SU-8B and SU-8C behaviors are shown for a strain rate of 10⁻³ s⁻¹. Green line presents the brittle behavior of an SU-8 film.

Table 2. Material property constants for SU-8 with different material states (these model parameters have the same meanings with those in Refs. [15–17]).

Elastic		Viscoplastic				Strain hardening			
Draw ratio	E [GPa]	ν	$\dot{\gamma}_0 [10^5 \text{ s}^{-1}]$	$\Delta G [10^{-19} \text{ J}]$	$s_0 [\text{MPa}]$	$s_{ss} [\text{MPa}]$	$h [\text{MPa}]$	$C_R [\text{MPa}]$	N
1.45	3.3	0.33	4.62	1.78	103	98	300	12.0	1.42
1.75	3.3	0.33	4.62	1.78	103	98	300	12.0	1.90
3.0	3.3	0.33	4.62	1.78	103	98	300	12.0	8.00

fraction of polymer is 26%, which is consistent with experiments ($\sim 30\%$).

The infinite periodic nature of the structure is captured through periodic boundary conditions.^[13,14] The RVE can be subjected to any arbitrary macroscopic deformation gradient. In this study, the periodic RVEs are subjected to several loading conditions, including uniaxial tension in different directions, uniaxial compression, as well as simple shear. The average macroscopic response for each case is calculated through virtual work considerations.^[13,14]

2.2. Material Properties

The stress-strain behavior of the SU-8 material inherent to the particular microframe material modeled in this study has not been measured. However, micrographs of the microframe structure after deformation clearly depict that the structural elements undergo extensive plastic deformation with elements exhibiting neck initiation, stabilization and propagation—i.e., the classic cold (below glass transition temperature) drawing process of a polymer. Hence, the SU-8 of interest exhibits elastic-plastic behavior with a clear yield stress, a regime of low strain hardening, followed by significant strain hardening at a stretch of around 3.0. Given that the stress-strain behavior for the microframe SU-8 material state was not available, the experimentally obtained stress-strain behavior of SU-8 processed into uniform cross-section beams via a different processing history^[8] is used as to provide a representative SU-8 elastic-plastic behavior; the Wen et al. data is further supplemented here with additional tests to quantify the rate dependence of SU-8 (strain rates of 10^{-3} , 10^{-2} , and 10^{-1} s^{-1}). The different processing routes of the SU-8 materials are given in Table 1. Note that the first processing route of Table 1 produces a brittle material. Figure 2 depicts the experimental stress-strain behavior of uniform cross-section beams of SU-8 produced using the second processing route of Table 1; these samples exhibit the characteristic features of the tensile behavior of ductile polymers: initial linear elasticity, fol-

lowed by a rate-dependent yield stress, strain softening, and subsequent strain hardening at larger strains. As evident in Figure 2, the Wen et al. SU-8 materials exhibited a draw ratio that depended on the cross-section of the fabricated beam (higher draw ratio for smaller cross-section beam: draw ratio of 1.45 for a $25 \times 25 \mu\text{m}^2$ and 1.75 for $1.6 \times 1.6 \mu\text{m}^2$). The yield stress does not depend on specimen size. Furthermore, the stress-strain behavior of the SU-8 material of the microframe structure clearly differs from that of the Wen et al. SU-8 as evidenced by the experimentally observed draw ratio of ~ 3.0 for the structural

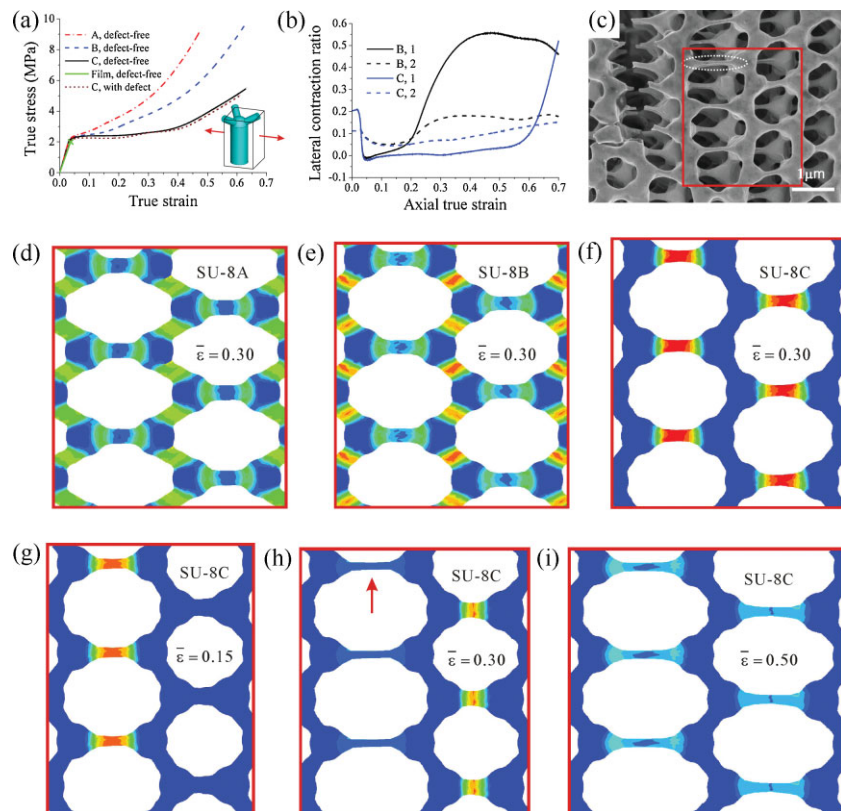


Figure 3. Mechanical response of microframe structures under macroscopic uniaxial tension in the 3-direction. a) Macroscopic true stress-strain curves of defect-free and imperfect microframe structure with various material properties. b) Lateral contraction ratios versus axial true strain using material property SU-8B and SU-8C. c) Experimental evidence of plastic deformation of structural elements with up to 300% plastic strain (e.g., circled beam) [12]. d–f) Simulated micrograph of defect-free microframe structure at a strain of 0.30 using material property SU-8A, SU-8B, and SU-8C, respectively. g–i) Simulated micrographs of microframe structure with imperfections at strains of 0.15, 0.30, and 0.5, where beam (pointed out) strain is about 280%. The progression in strain is in agreement with the experimental observations as depicted in the SEM image (Fig. 3c).

elements of the microframe compared to the 1.45 and 1.75 draw ratios of the Wen et al. materials; data on the yield stress is not available for comparison. Since the processing of the SU-8 beams^[8] is not identical to the SU-8 in the microframes,^[12] the stress-strain measurements only serve as an approximation for the SU-8 elastic-plastic stress-strain behavior to capture the plasticity experimentally observed in the deformed microframes;^[12] material draw ratios will be varied in the simulations to examine this effect on the microframe deformation mechanics.

A constitutive model^[15–17] for the large strain, rate dependent elastic-viscoplastic behavior of glassy polymers is used to capture the features of the observed stress-strain behavior for SU-8 material states. From the stress-strain curves of Figure 2, we have determined three sets of material constants for SU-8 beams which correspond to material states with draw ratios of 1.45, 1.75, and 3.0. To capture these behaviors, all properties were taken to be the same except the strain hardening properties were changed to provide the proper draw ratio for each case, including a draw ratio of 3.0 for the microframe case. Properties are listed in Table 2. Note that here the parameter N is chosen to capture the limiting chain extensibility which in turn captures the draw ratio. Initial linear elasticity, rate-dependent yield, strain softening, and hardening behaviors are all captured by the model compared to experimental data. We use “SU-8A, SU-8B, and SU-8C” to denote the material properties for material states with draw ratios of 1.45, 1.75, and 3.0, respectively. For comparison, SU-8 film properties are also plotted in Figure 1b (the green curve), which exhibits a brittle failure at a strain of about 5%.^[8] This is consistent with bulk behavior of fully cured SU-8.^[18]

2.3. Micromechanical Simulation Results and Discussions

The simulated macroscopic uniaxial tension behaviors for the microframe structured materials are shown in Figure 3 for constituent materials SU-8A, SU-8B, and SU-8C for tension in the 3-direction. Figure 3a shows the overall microframe uniaxial stress-strain behaviors for each of the materials, demonstrating the influence of constituent material behavior on the microframe behavior. The microframe structure strain hardens at lower strains for the lower draw ratio materials. The influence of the constituent material strain hardening behavior also controls the progression of deformation within the microframe as evident in the snapshot contours of plastic strain rate (regions of active plastic deformation) taken at a macroscopic strain of $\bar{\epsilon} = 0.30$ for SU-8A, SU-8B, and SU-8C in Figure 3d–f, respectively. In the case of SU-8A, the frame member axially aligned with the loading direction has plastically deformed and strain hardened such that, by $\bar{\epsilon} = 0.30$, the active straining has progressed into the connecting nodes and further progressed into the diagonal members, resulting in macroscopic strain hardening occurring soon after yield for this material (Fig. 3a). In contrast,

for the material states characterized with a higher draw ratio, deformation is observed to be localized within the structural member aligned with the loading direction with necking down to a smaller diameter prior to neck stabilization and propagation

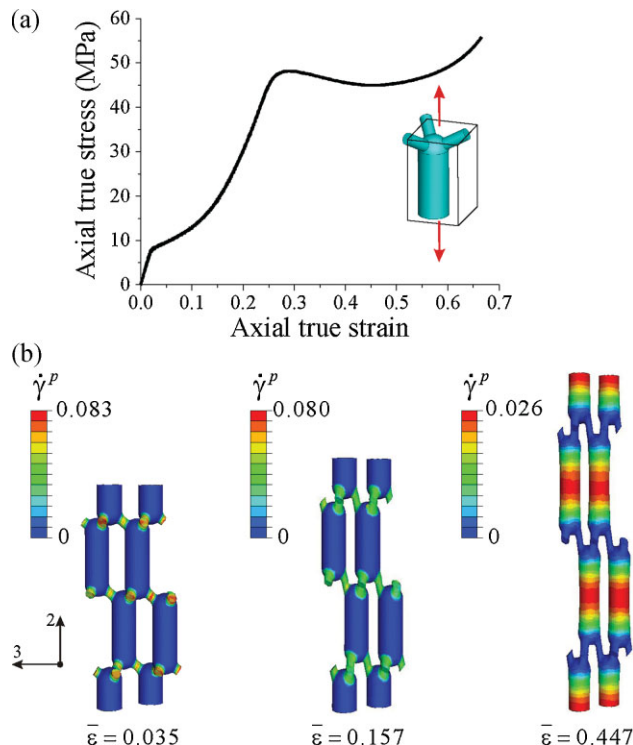


Figure 4. Mechanical response of the microframe structure under macroscopic uniaxial tension in the 2-direction. a) Simulated macroscopic stress-strain curves. b) Simulated results showing contours of plastic strain rate at increasing macroscopic tensile strain levels.

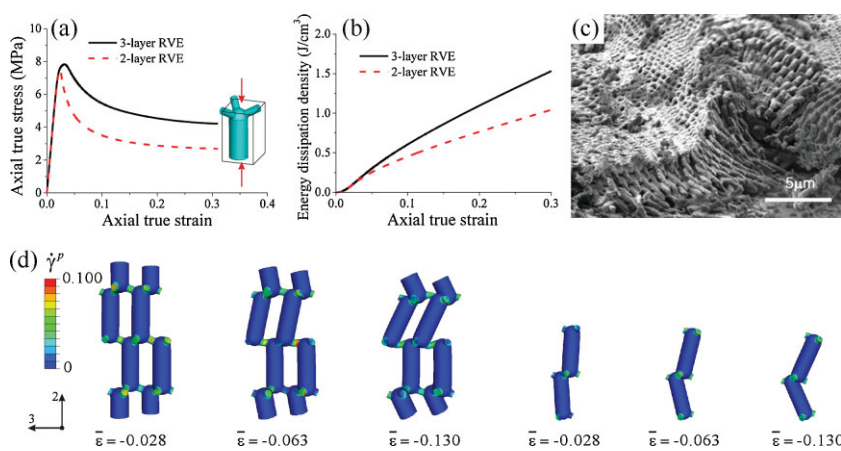


Figure 5. Mechanical response of the microframe structure under macroscopic uniaxial compression in the 2-direction. a) Simulated macroscopic stress-strain curves. b) Predictions of energy dissipation density as a function of compression strain. c) Micrograph of a portion of the film that was compressed, showing the collapsed microframe region at left [12]. d) Simulated contours of plastic strain rate for three- and two-layer RVEs at increasing macroscopic compression strains.

(Fig. 3e and f for SU-8B and SU-8C), corresponding to the delayed strain hardening behavior of the microframe structures shown in Figure 3a. (As an aside, using the macroscopic material properties in the microframe structure results in brittle failure of the microframe at a strain of 0.04 because the material locally reaches its failure strain.) Figure 3b shows the lateral contraction ratios as a function of axial true strain for the microframe structure with constituent materials SU-8B and SU-8C. The initial elastic Poisson ratios in the two directions are 0.11 and 0.20. When the struts parallel to the loading direction yield, the lateral contraction ratios become very small (approaching 0) since the macroscopic strain is accommodated by extension (with local necking and neck propagation) of the members coaxial with the applied load. Once the diagonal frame members begin to plastically deform, they rotate toward the axial direction, and the lateral contraction ratios increase; the macroscopic strain where this change in contraction behavior begins is found to depend on the draw ratio of the constituent material as seen in Figure 3b. This highly nonlinear contraction behavior under large strain (up to 1.5) has also been observed in some polymer cellular foams with an initially negative elastic Poisson's ratio.^[19]

For perfect periodic microframe structures, struts located in the same periodic positions will experience the same deformation histories during a loading process (see Fig. 3d–f). However, in the experimental investigations, as shown in Figure 3c, struts in the same periodic positions experience different levels of deformation as a result of small irregularities/imperfections in the local structure geometry or material properties. To capture this effect, imperfections are introduced into the RVE in the form of slightly thinned struts at different locations. Deformation is then found to first localize in a thinned strut with neck initiation, stabilization, and propagation localizing in one layer of struts (Fig. 3g) and then, upon strain hardening of that layer, deformation progresses to the next layer of struts (Fig. 3h and i). This deformation progression capitalizes on the strain hardening behavior of a polymer which enables the spreading of deformation during plasticity rather than the localization of deformation in one layer until reaching failure. The predicted deformation progression mechanism agrees well with the experimental observation (see SEM image Fig. 3c). This spreading mechanism can be used to further enhance the design of energy dissipative microstructures.

Figure 4 shows the mechanical response of the microframe structure under macroscopic tension in the 2-direction. Two inflection points are observed in the macroscopic tension stress-strain curve at axial strains of about 0.02 and 0.29 correlating to the yield of the thin (200 nm) diagonal struts and the yield of the thicker (500 nm) posts, respectively. Microscopic and local features of deformation are further illustrated in the contours of plastic strain rate shown in Figure 4b at different levels of macroscopic axial strain. Plastic flow in the microframe structure initiates in the central region of the thin diagonal struts. After initial yield, necking, neck propagation, and strain hardening in the thin struts, deformation spreads to the thick posts corresponding to the second inflection point in the macroscopic tensile curve.

Figure 5 shows the mechanical response of the microframe structure under compression. The macroscopic compression curve (Fig. 5a) exhibits a single yield point that corresponds to the yielding of the diagonal members and the internal “buckling”

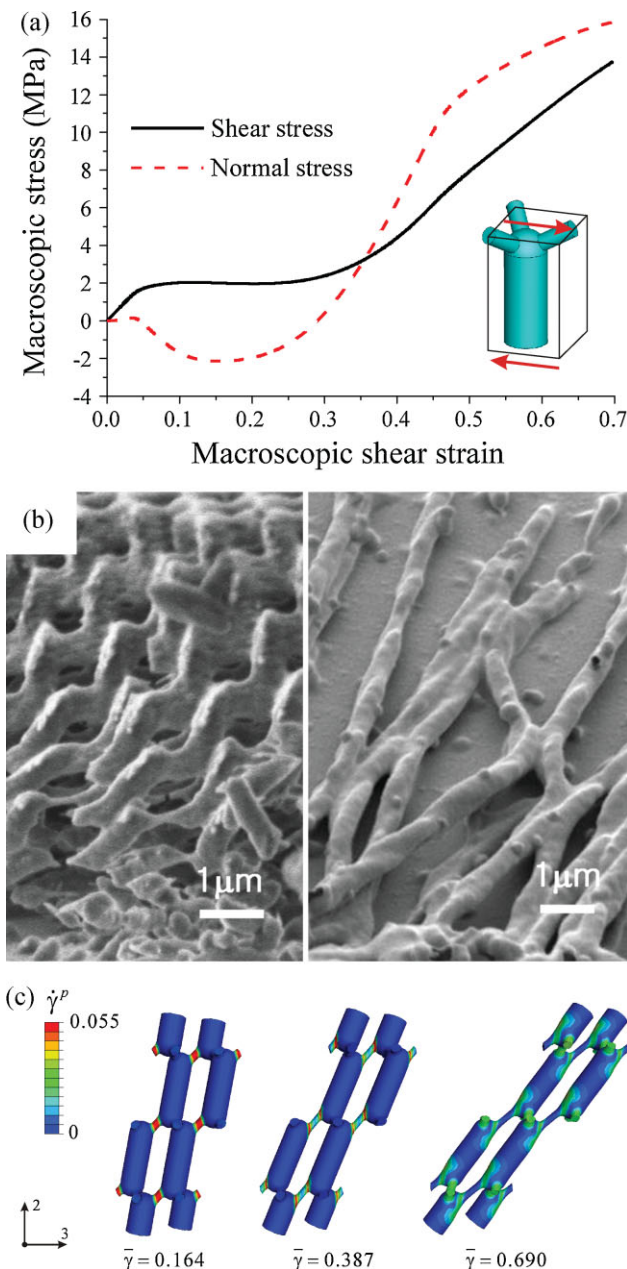


Figure 6. Simulated mechanical response of the microframe structures subjected to simple shear deformation in the 32-plane. a) Macroscopic shear stress and normal stress versus the shear strain curves. b) SEM micrograph of shear region of the microframe film and plastically deformed microfibrils [12]. c) Simulated results show contours of plastic shear strain rate at increasing levels of shear strain.

collapse of the microframe structure. Figure 5d exhibits compressed configurations of the two- and three-layer RVEs under increasing levels of macroscopic axial strain. After a critical strain, the structure collapses and the thinner struts plastically bend and rotate (also see experimental observation in Fig. 5c). The critical strains are 0.024 and 0.032 for the two- and three-layer RVEs due to the different allowable wavelength buckling

instability for each case due to the periodic boundary condition. The energy (per unit volume) absorbed during compression for these two cases are shown in Figure 5b. This result reveals the ability to also tailor and increase the energy absorption capacity of a periodic structure by forcing different buckling wavelengths (perhaps with internal structural constraints).

The mechanical response of the microframe structure during simple shear deformation is shown in Figure 6. The deformed configurations shown in Figure 6c show that the macroscopic shear strain is accommodated by plastic straining of the thin diagonal struts which then enable large scale rotation and alignment into “rows” of the entire structure. This deformation mechanism is suggested to account for the formation of the long fibrils observed in the experiments (see Fig. 6b).

The shear stress–shear strain behavior and corresponding normal stress–shear strain behavior are both shown in Figure 6a. As expected, at small strains, there is negligible normal stress. Once the first yield event occurs and larger strain ensues, the normal stress is found to be negative (over the range of macroscopic shear strains from 0.05 to 0.29). In contrast, for simple shear deformations of isotropic solids, the normal stress would be positive. The large negative normal stress is a result of the anisotropic microstructure and the deformation-induced changes and rotations in the microstructure. Similar negative normal stress has been observed in carbon nanotube-filled polymer nanocomposites^[20] and networks of semiflexible biopolymer gels.^[21] These results suggest the tailoring of microstructure to achieve prescribed normal stress evolutions during simple shear to further aid in energy absorbing mechanisms during shear deformations (where the inherent normal stress response can be used to either close up or prop open a structure during shear loading).

2.4. Beam Ratio Effects

The topology of the microstructure clearly plays a key role in the mechanical response of microframe materials.^[22,23] Here, the effect of underlying geometry on the nonlinear mechanical behavior will be discussed. The beam ratio (BR) defined as the ratio of the diameter of diagonally oriented struts to the diameter of the vertical post, is a structural parameter we define to compare different microtruss and microframe materials. The microframe structure discussed thus far has a BR = 0.4 and a volume fraction f of polymer of $f = 0.26$. For comparison purposes, five microframe structures are now simulated with BR varying from 0.4 to 1.2 while maintaining f fixed at $f = 0.26$.

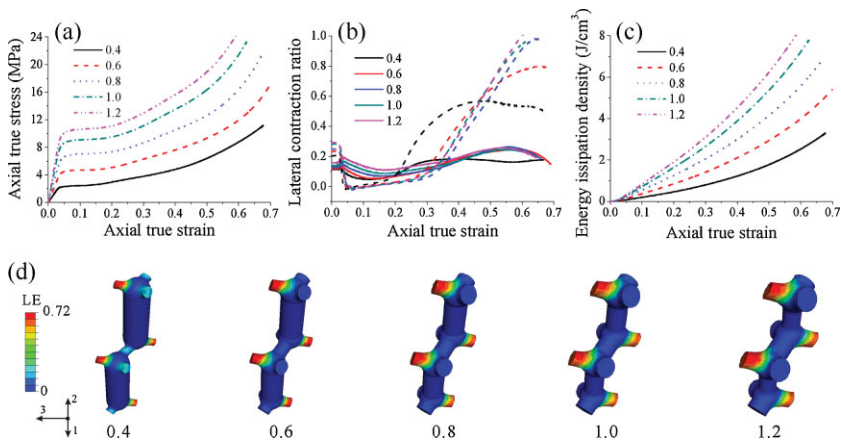


Figure 7. Micromechanical modeling results of the comparison of microframe structures with different geometries under uniaxial tension. a) Stress–strain curves in the 3-direction. b) Lateral contraction ratio relationships (1-direction: dashed lines, 2-direction: solid lines). c) Predictions of energy dissipation density as a function of microscopic tension strain. d) Contours of maximum principal true strain of the 3D RVEs with different structure ratios at a uniaxial tension strain of 0.30.

The behaviors of these structures subjected to uniaxial tension, simple shear deformation, and uniaxial compression are compared.

For the case of uniaxial tension in the 3-direction (see Fig. 7a), the Young’s modulus and yield stress are found to increase with an increase in BR while the yield strain remains the same. These dependencies are direct results of the axial behavior in the 3-direction being governed by the particular diagonal member aligned with the 3-direction; the increase in diameter of this member with increase in BR gives the increase in macroscopic modulus and yield stress; the scaling of the macroscopic yield stress with modulus gives the yield strain to be relatively independent of BR. All structures show similar lateral contraction behavior as a function of axial strain (Fig. 7b). Figure 7c provides

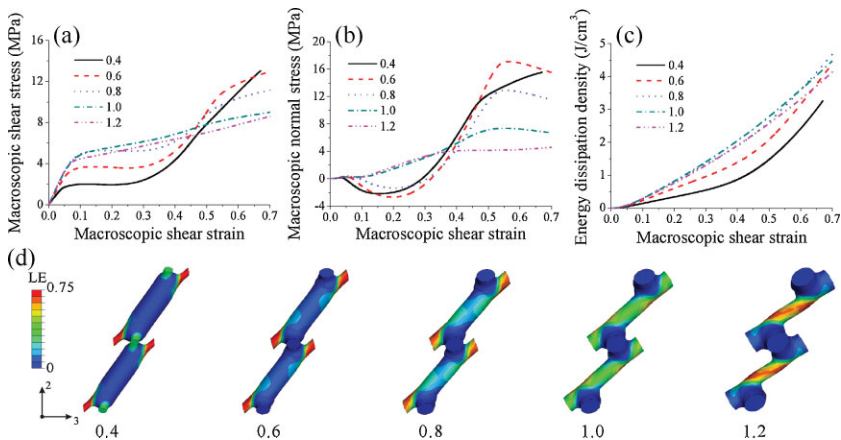


Figure 8. Micromechanical modeling results of the comparison of microframe structures with different geometries under macroscopic simple shear deformation. a,b) Shear and normal stress–strain curves under simple shear deformation in the 32-plane. c) Predictions of energy dissipation density as a function of microscopic shear strain. d) Contours of maximum principal true strain at a shear strain of 0.70.

the calculated total strain energy absorption under uniaxial tension which is shown to dramatically increase with an increase in BR at any given macroscopic strain. Contours of maximum principal true strain for the five structures at a macroscopic strain of 0.30 are shown in Figure 7d further emphasizing the dominant role of the diagonal strut aligned with the 3-direction.

For the case of simple shear, the mechanical response is dominated by the plastic stretching and rotation of various members; the members which govern this shear behavior are found to depend on BR. When $BR = 0.4, 0.6$, and 0.8 , the thin diagonal members govern the behavior; whereas for BR larger than 1.0 , yield and necking initiate in the “vertical posts” since these are now the “weaker link.” Figure 8d shows the maximum principal true strain distributions for all five structures under a shear strain of 0.70 further illustrating how the deformation mechanism depends on BR . Furthermore, the normal stress behavior is seen to transition from a negative value for small BR to a positive value at the larger BR ratios (see Fig. 8b); this dependence is related to the orientation of the diagonal members and the evolution of the net section force in these members in each structure. For this type of 3D microframe structure, the mechanical balance between vertical post and diagonal member governs the linear and nonlinear behavior. Figure 8c shows the strain dependence of the calculated energy absorption. The absorption is greater in the higher BR materials compared to the 0.4 BR , but is nearly identical for the BR cases of $0.8, 1.0$, and 1.2 as also seen in the nearly identical shear stress-strain curves.

For the case of uniaxial compression, the mechanical response is dominated by the structure stability and the plastic deformation of various members. When $BR = 0.4, 0.6$, and 0.8 , a single peak strength is observed in the stress-strain curves as shown in Figure 9a, followed by a stress drop and then a long plateau, which allows energy dissipation at near constant load. These structures

show the buckling-dominated behavior, arising from the plastic yielding of the diagonal members and subsequent hinge formation giving buckling, bending, and rotation (see Fig. 9c). When BR is larger than 1.0 , there no longer exists a thin diagonal member and yielding initiates in the vertical posts (Fig. 9c); structural “collapse” takes a different form occurring at much greater strain where a second “peak” is seen in the computed stress-strain curve. This behavior enables the structures to absorb much more energy as shown in Figure 9b. The absorbed energy per unit volume at 25% strain is up to 4 MJ m^{-3} , which is higher than many commercially available polymer foams^[4] (e.g., 3 MJ m^{-3} for a PP foam of density of 0.6 Mg m^{-3} and 1.5 MJ m^{-3} for a PU foam of density of 1.05 Mg m^{-3}), whereas the density of the microframe structure in this study is only 0.3 Mg m^{-3} . Hence, the corresponding energy absorption per unit mass at 25% strain is 13.3 MJ Mg^{-1} for our microframe compared to 5.0 and 1.4 MJ Mg^{-1} for the commercially available PP and PU foams.

In most applications, the selection and design of cellular solids for energy absorption depend on the specification of the problem. Here it is shown that, at a given density, the modulus, yield stress, and energy absorption can be further optimized by tailoring the geometry of microframe structures which can be controlled by interference lithography to meet different requirements (see Appendix for the comparison of the relative modulus and the collapse stress of a cellular solid from our simulations and existing theoretical models for idealized geometries).

3. Conclusions

In summary, fully three-dimensional micromechanical models of microframe structures have enabled the quantitative investigation of the macroscopic response and underlying plastic dissipation mechanisms in microframe-structured polymers subject to very large strain deformation histories. The simulations successfully predict the deformation mechanisms observed experimentally and provide the corresponding macroscopic stress-strain behaviors for arbitrary load histories, quantifying elastic, yield, and post-yield dissipation behavior. The results highlight important features of the inelastic behaviors of these structures including i) the ability to utilize the strain hardening plasticity of the polymer to spread deformation throughout the structure enabling dissipative pathways prior to localized failure; ii) the ability to utilize the microstructure to tailor the lateral contraction behavior, not just at small strains, but also during large inelastic deformations; iii) the ability to tailor the microstructure to achieve either positive or negative normal stress behavior during simple shear; iv) the ability to optimally structure the material (e.g., at fixed density) to achieve desired nonlinear anisotropic mechanical performance as well as maximum energy absorption.

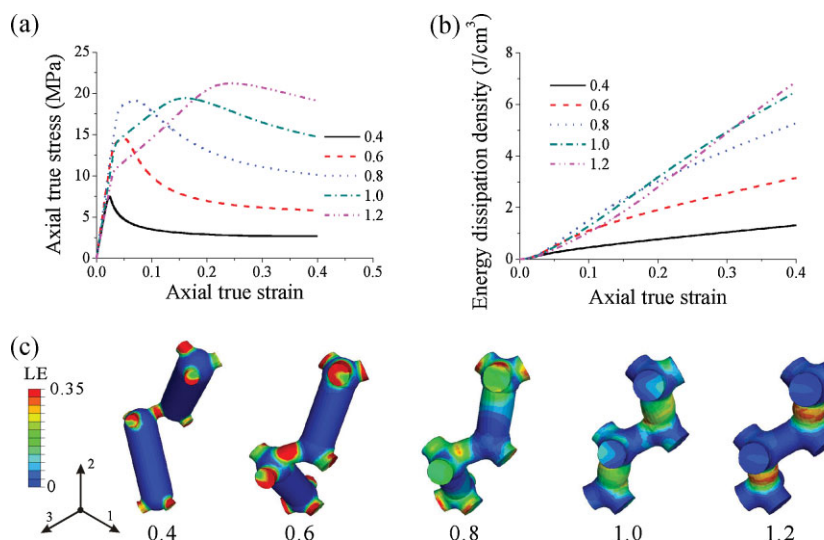


Figure 9. Micromechanical modeling results of the comparison of microframe structures with different geometries under macroscopic compression. a) Stress-strain curves under uniaxial compression in the 2-direction. b) Predictions of energy dissipation density as a function of microscropic compression strain. c) Contours of maximum principal true strain at a compression strain of -0.20 .

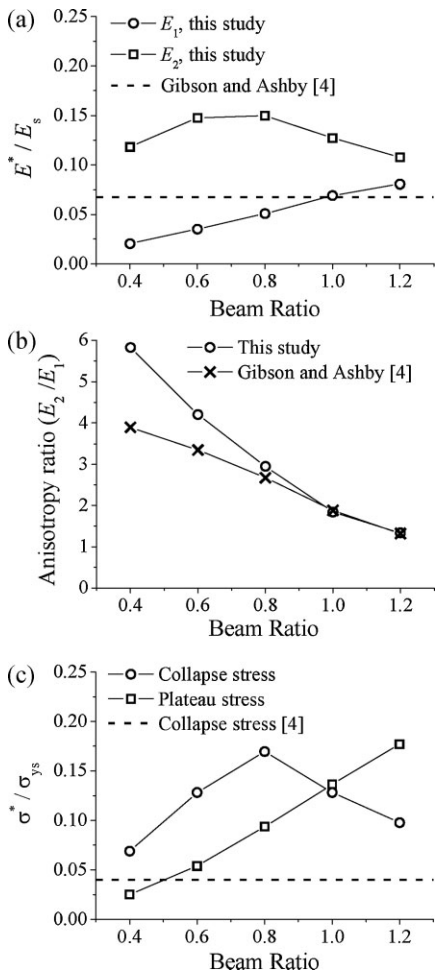


Figure 10. Comparison of the results of a cellular solid of relative density $\rho^*/\rho_s = 0.26$ as calculated for the different BR materials of this paper and as calculated from idealized open-cell cubic model [4]. a) The relative modulus normalized by the solid modulus (equiaxed cubic cell for Gibson–Ashby data). b) The modulus anisotropy ratio (elongated cubic cell for Gibson–Ashby data). c) The initial plastic collapse stress and plateau stress normalized by the yield strength of the solid (equiaxed cubic cell for Gibson–Ashby data).

Appendix

The Young's modulus, E^* , of open-cell cellular solid (with random and isotropic cellular microstructure) have been found to be related to their density, ρ^* , relative to the solid density, ρ_s , and the Young's modulus of the solid, E_s , via

$$\frac{E^*}{E_s} = C \left(\frac{\rho^*}{\rho_s} \right)^n \quad (1)$$

where C and n can be obtained by fits to experimental data. Models based on idealized microstructures have been proposed by several investiga-

tors.^[4,23–25] The Gibson–Ashby model^[4] assumes a cubic RVE of beams and finds $n=2$ and C to be close to 1 if the struts are fully dense.

For the polymer microframes reported in this paper, the relative density is fixed to be 0.26. The simulated Young's modulus varies from 67 to 266 MPa in the 1-direction and 355–495 MPa in the 2-direction, which depends on BRs. Figure 10 shows the comparison of the relative modulus and the plastic collapse stress from our simulation and the idealized cubic open-cell cellular model.^[4]

Acknowledgements

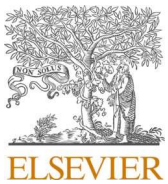
This research was supported by the US Army Research Office through the Institute for Soldier Nanotechnologies under the Contract DAAD-19-02-D0002. L. F. Wang acknowledges the partial support of the Hock Tan Postdoctoral Fellowship.

Received: October 6, 2008

Revised: November 14, 2008

Published online: March 19, 2009

- [1] P. J. Hogg, *Science* **2006**, *314*, 1100.
- [2] A. B. Dalton, S. Collins, E. Munoz, J. M. Razal, V. H. Ebron, J. P. Ferraris, J. N. Coleman, B. G. Kim, R. H. Baughman, *Nature* **2003**, *423*, 307.
- [3] A. Y. Cao, P. L. Dickrell, W. G. Sawyer, M. N. Ghasemi-Nejhad, P. M. Ajayan, *Science* **2005**, *310*, 1307.
- [4] L. J. Gibson, M. F. Ashby, *Cellular Solids: Structure and Properties*, 2nd ed., Cambridge University Press, Cambridge **1999**.
- [5] J. Aizenberg, J. C. Weaver, M. S. Thanawala, V. C. Sundar, D. E. Morse, P. Fratzl, *Science* **2005**, *309*, 275.
- [6] Y.-H. Ha, R. A. Vaia, W. F. Lynn, J. P. Costantino, J. Shin, A. B. Smith, P. T. Matsudaira, E. L. Thomas, *Adv. Mater.* **2004**, *16*, 1091.
- [7] M. C. M. Van der Sanden, H. E. H. Meijer, P. J. Lemstra, *Polymer* **1993**, *34*, 2148.
- [8] C. Y. Wen, W. S. Kim, E. L. Thomas, unpublished.
- [9] E. J. Kramer, L. L. Berger, *Adv. Polym. Sci.* **1990**, *91*–92, 1.
- [10] M. C. M. Van der Sanden, H. E. H. Meijer, *Polymer* **1993**, *34*, 5063.
- [11] T. Choi, J.-H. Jang, C. K. Ullal, M. C. LeMieux, V. V. Tsukruk, E. L. Thomas, *Adv. Funct. Mater.* **2006**, *16*, 1324.
- [12] J.-H. Jang, C. K. Ullal, T. Choi, M. C. LeMieux, V. V. Tsukruk, E. L. Thomas, *Adv. Mater.* **2006**, *18*, 2123.
- [13] M. Danielsson, D. M. Parks, M. C. Boyce, *J. Mech. Phys. Solids* **2002**, *50*, 351.
- [14] M. Danielsson, D. M. Parks, M. C. Boyce, *J. Mech. Phys. Solids* **2007**, *55*, 533.
- [15] M. C. Boyce, D. M. Parks, A. S. Argon, *Mech. Mater.* **1988**, *7*, 15.
- [16] E. M. Arruda, M. C. Boyce, *Int. J. Plasticity* **1993**, *9*, 697.
- [17] E. M. Arruda, M. C. Boyce, *J. Mech. Phys. Solids* **1993**, *41*, 389.
- [18] R. Feng, R. J. Farris, *J. Micromech. Microeng.* **2003**, *13*, 80.
- [19] J. B. Choi, R. S. Lakes, *J. Mater. Sci.* **1992**, *27*, 4678.
- [20] S. B. Kharchenko, J. F. Douglas, J. Obrzut, E. A. Grulke, K. B. Migler, *Nat. Mater.* **2004**, *3*, 564.
- [21] P. A. Janney, M. E. McCormick, S. Rammensee, J. L. Leight, P. C. Georges, F. C. Mackintosh, *Nat. Mater.* **2007**, *6*, 48.
- [22] A. G. Evans, J. W. Hutchinson, N. A. Fleck, M. F. Ashby, H. N. Wadley, *Prog. Mater. Sci.* **2001**, *46*, 309.
- [23] M. Maldovan, C. K. Ullal, J.-H. Jang, E. L. Thomas, *Adv. Mater.* **2007**, *19*, 3809.
- [24] R. M. Christensen, *J. Mech. Phys. Solids* **1986**, *34*, 563.
- [25] W. E. Warren, A. M. Kraynik, *J. Appl. Mech.* **1988**, *55*, 341.



Monte Carlo analytical-geometrical simulation of piezoresistivity and electrical conductivity of polymeric nanocomposites filled with hybrid carbon nanotubes/graphene nanoplatelets



M. Haghgoor^a, R. Ansari^{a,*}, M.K. Hassanzadeh-Aghdam^{b,*}

^a Faculty of Mechanical Engineering, University of Guilan, Rasht, Iran

^b Department of Engineering Science, Faculty of Technology and Engineering, East of Guilan, University of Guilan, Rudsar-Vajargah, Iran

ARTICLE INFO

Keywords:

- A. Multifunctional composites
- B. Nanocomposites
- C. Electrical properties
- D. Analytical modeling

ABSTRACT

Piezoresistivity and electrical conductivity of carbon nanotube (CNT)/graphene nanoplatelet (GNP)-filled polymer nanocomposites are investigated using a 3D Monte Carlo analytical-geometrical model. GNPs and CNTs are considered as randomly distributed solid thin rectangular cube and cylinder, respectively. After establishment of a random CNT/GNP network, electrical conductivity and relative resistance change with strain is calculated. Model considers effect of CNT and GNP deformation on filler separation distance as the dominant factor for percolation tunneling. Comparing model results with experimental data of hybrid nanocomposites showed a good agreement for electrical conductivity and piezoresistivity. Analytical model is developed on the basis of geometrical tunneling percolation theory to consider the effect of several parameters like height of barrier potential, GNP side length, CNT orientation and dimensions on electric behavior of nanocomposites. Results revealed that CNT dispersion state and GNP dimensions have significant effects on the percolation threshold and resistivity change ratio of nanocomposites with strain.

1. Introduction

A new class of conductive nanocomposite made by incorporation of electrically conductive fillers in a polymer matrix is used in electrochromic devices, strain-detecting sensors, supercapacitors, and electromagnetic interference shielding [1,2]. Combining conductive fillers (e.g. CNT and GNP) could improve filler network conductivity because the conductivity of filler is much higher than that of a matrix [3,4]. CNTs provide high-strength and large surface area with special 1D physical structure ideal for conductivity and GNPs offer excellent conductivity with 2D high aspect ratio structure ideal for gathering many types of contact for charge transport capability [5,6]. Hybrid nanocomposite with two or more fillers of different geometric shapes, dimensions and aspect ratios could achieve better conductivity and lower cost than those reinforced with either CNTs or GNPs alone (unary composites) [2]. Fillers with different geometries can affect the 3D network structure formation and bring various capabilities such as great strength and conductivity to nanocomposite [7,8]. Bridging of CNT network between GNPs could improve the network percolation by quantum tunneling which plays a dominant role in the electrical transport of CNT based

nanocomposite through a percolation process [9,10]. At low volume fractions, the nano-fillers are too far apart and the electrical conductivity is low. The low electrical conductivity is due to the small number of fillers linked together. Therefore, the fillers are not electrically related to each other. The isolated fillers decrease distance with the increase of the number of adjacent fillers [11]. In this situation, tunneling happens between neighboring fillers leading to gradual increase in the conductivity of nanocomposite. After that a complete electrical path is formed due to the enlarged number of fillers, the electrical conductivity of composite enhances abruptly which this rapid increment in electrical conductivity is known as percolation behavior [12]. Electrical conductivity in CNT reinforced nanocomposite is widely specified by this percolation event, which originates from the distributions of both insulating and conducting phases with hugely different electrical properties [13,14].

Addition of a small amount of CNT/GNP fillers to polymer improves the piezoresistivity by keeping interfacial bonds during strain while maintaining the light weight of composite [15]. Piezoresistive materials are able to translate stress into a convertible signal [16]. Nanocomposites whose piezoresistive behavior has been increased with CNT/

* Corresponding authors.

E-mail addresses: r_ansari@guilan.ac.ir (R. Ansari), mk.hassanzadeh@gmail.com (M.K. Hassanzadeh-Aghdam).

GNP incorporation are promising for applications such as strain sensing, health and fitness monitoring [17–19]. These high aspect ratio nano-fillers (CNT and GNP) are the most suitable conductors for highly flexible strain sensing applications [20]. The GNPs have very efficient reinforcing capability due to their 2D parallel alignment in the stretching plane, while CNT has the most robust conductive network formation during stretching due to more interactions of the 1D structures [21]. Thus, the hybrid fillers can form a structure in which the GNPs with great entanglement capability bundle CNTs in the formation of conductive network [22,23]. These local bonding are promising for piezoresistivity due to the high surface area along 2D geometry of GNP and long distance charge transmission capability of 1D CNTs [24,25]. The strain sensitive conductivity is emanated from the destruction of the CNT/GNP conductive paths. Therefore, piezoresistivity happens due to the synergistic interaction between GNP and CNT which increases load bearing capability and compensates poor strength of polymer to loads [14,21].

Analytical models including percolation theory has preference over time consuming numerical methods. Many analytical models predict electrical conductivity based on the shape of nanofillers, orientation of CNT and tunneling resistance between them. Recently, various analytical models are presented to study the electrical conductivity and piezoresistivity of polymer based carbon nanocomposites.

Rahman and Servati [26] developed a model for CNT-polymer conductivity considering the effect of inter-tube tunneling through the polymer. They investigated the statistical effects of inter-tube distance and alignment on the tunneling. They presented a numerical model for the tunneling resistance as a function of CNT concentration and polymer properties. They reported that piezoresistivity increases non-linearly with increasing strain and this enhancement diminishes with lower orientation angle. Wang and Ye [27] numerically investigated the mechanism and optimization of piezoresistive CNT-polymer composites. They introduced average junction gap as a quantitative description of the conductance variation of a CNT network to study the parameters of CNT and polymer on piezoresistivity. Their numerical results showed that the junction resistances between CNTs are a major component of the network conductance of the composite. Feng et al. [28] studied the bi-axial stretching effects on the electrical conductivity of CNT composites by a mixed micromechanics model with the consideration of the electrical conductive mechanisms. They considered the bi-axial stretching effects by volume expansion of composite, re-orientation of CNTs and change of conductive networks. They reported that bi-axial stretching decreased the electrical conductivity of composite due to dominant role of the stretching induced change in conductive networks. They found that the decreasing rate of electrical conductivity enhanced in the bi-axial stretching plane. Souri et al. [29] carried out a theoretical study of polymeric nanocomposite based on the self-consistent effective medium theory to provide physical insight into complex material systems. They adopted the effects of the interface and tunneling effects to demonstrate that the overall piezoresistive sensitivity reduces when the lower interfacial resistivity of CNTs is considered. They investigated the effects of MWCNT weight percentage, length and tunneling effects on the piezoresistivity of the nanocomposite. Xiang et al. [30] fabricated a high-performance strain sensor of CNT polymer nanocomposite. They established a conductive model to study the electro-mechanical properties of the strain sensor based on Simmons' tunneling theory. They reported that the sensor sensitivity was greatly improved with the addition of low content uniformly dispersed CNTs. Fang et al. [31] investigated an analytical model to describe the influence of mechanical deformation on the effective electrical conductivity of CNT reinforced composites. Strain-induced change of the electrical conductivity illustrated the effect of mechanical strain on the effective electrical conductivity. They treated both the strain-induced volume fraction change of inclusions and the strain-induced tunneling conductivity change of CNTs as the linear functions of the strain. They reported that the effect of the strain on the electrical conductivity diminishes with higher volume

fraction of CNTs. Tang et al. [32] predicted the electro-mechanical response of conductive CNT-based composite by considering CNT dimensions, interphase and dispersion state. They considered the stretching-induced changes in the model by the variation of CNT content, CNT orientation, and percolated conductive network. They considered the key factors including filler geometry, interphase region, filler dispersion, Poisson's ratio and barrier height in affecting the piezoresistive response of CNT-based composite sensors. They declared that the piezoresistive sensitivity of the nanocomposite increased with filler content above the percolation threshold and higher matrix barrier height.

The above-mentioned literature review demonstrates that there have been many analytical studies on the piezoresistive response of single filler nanofiller modified composites. However, very limited analytical work exists in literature to explain the piezoresistive response of hybrid nanocomposite. This work presents a Monte Carlo analytical-geometrical percolation network model to study the effect of strain on the resistivity change of hybrid CNT/GNP polymer nanocomposite. In this analytical model, the straight and uniformly dispersed CNTs interact with thin rectangular GNPs. The coupling between the electrical and structural response representing the macro-scale nanocomposite is obtained by firstly evaluating the new positions of fillers and secondly calculating the electrical resistivity between them. The predicted results are compared with previous experimental data. Results show that the current analytical model agrees well with the experimental data reflecting the capability of the model to predict the piezoresistivity of conductive network composed of many conductive paths each formed by separated conductive fillers with lots of contacts between them. At the end, the parametric studies are represented to show the changes of electrical conductivity and piezoresistive sensitivity of hybrid polymer nanocomposite providing links between nano-scale network features such as the aspect ratio, alignment, distribution and geometries of CNTs and GNPs and macro-scale electro-mechanical response.

2. Model generation

2.1. Integration of CNTs

In this section, an analytical model is prepared based on the inter-particle distance variation to predict the resistance change ratio occurred in CNT/GNP polymer nanocomposite due to a mechanical strain. Evaluation of changes in mutual position and contacts of fillers is the easiest way to establish a relationship between electrical properties of a material and its deformational state. For this, consideration of various parameters concerned with the geometrical connection configuration is needed. At first, the CNT distribution state that coincides with the geometrical contact configuration of CNTs spread in the insulating polymer is attained. For this, an RVE of the CNT dispersed in the matrix is presented.

Fig. 1 shows 3D cubic RVE with CNTs and GNPs. The dimensions of the RVE are $L_x \times L_y \times L_z (10 \times 10 \times 10 \mu\text{m}^3)$, large enough to contain many fillers but small compared to the length over which the deformation could vary [33]. RVE consist of polymer matrix, CNT and GNP in which cylindrical CNT with length of l and a diameter of d and GNPs with side length of S and thickness of t are distributed in the polymer matrix. The number of fillers in the 3D RVE is set by their assigned volume fraction ($10^{-15} \cdot V_f / \pi r^2 l$). For a newly generated CNT, if the ending point is located outside of the RVE, it is removed and will be substituted with a new one which fulfills the RVE limited space condition. In this study for the sake of simplifying the calculation, the distortion of CNT and wrinkle of GNP are ignored, and also the hard-core models for CNT and GNP lead to non-penetrating fillers.

Based on the 3D Monte Carlo model, a random distribution of CNTs is generated in the 3D RVE. Conductive 1D CNT can transport electrons by tunneling and contact. This conductive CNT is free from defect and

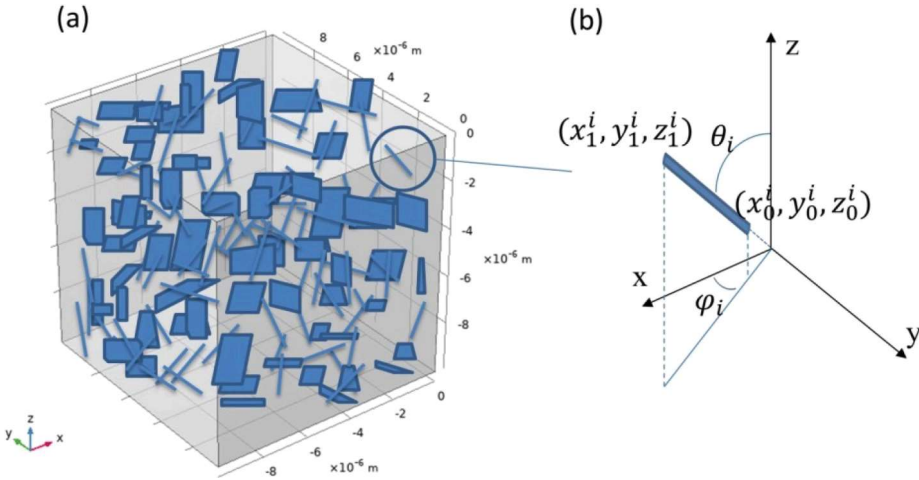


Fig. 1. Schematic of (a) a CNT/GNP hybrid nanocomposite (b) the i th randomly oriented CNT.

structurally perfect and the surrounding polymer is not affecting its electrical properties. CNT dispersion state has an important effect on its electrical properties. Every CNT added in the model can be described by a line segment with a starting point (x_0^i, y_0^i, z_0^i) and an ending point (x_1^i, y_1^i, z_1^i) such that.

$$\begin{Bmatrix} x_0^i \\ y_0^i \\ z_0^i \end{Bmatrix} = \begin{Bmatrix} x_0^i \\ y_0^i \\ z_0^i \end{Bmatrix} + \begin{Bmatrix} l_i \sin \theta_i \cos \varphi_i \\ l_i \sin \theta_i \sin \varphi_i \\ l_i \cos \theta_i \end{Bmatrix} \quad (1)$$

where l_i , φ_i and θ_i are the length, azimuthal and polar angles of the i th CNT, respectively. Here x_1^i , y_1^i , z_1^i , φ^i and θ_i follow a uniform distribution as drafted in Eq. (2).

$$\begin{Bmatrix} x_0^i \\ y_0^i \\ z_0^i \\ \varphi_i \\ \theta_i \end{Bmatrix} = \begin{Bmatrix} L \times \text{rand} \\ L \times \text{rand} \\ L \times \text{rand} \\ 2\pi \times \text{rand} \\ \cos^{-1}(2 \times \text{rand} - 1) \end{Bmatrix} \quad (2)$$

Here "rand" denotes some random number in the interval $(0,1)$ and L is the side length of RVE.

The network resistance includes both intrinsic resistance of CNT and tunneling resistance between CNTs. The intrinsic resistance of a CNT is $R_f = \frac{4l}{\sigma_f \pi d^2}$. Where d is CNT diameter and σ_f is the CNT intrinsic electrical conductivity determined experimentally.

The contact region between two CNTs is at the nanoscale, the dimension of which can be less than the Fermi wavelength $\lambda_F \approx 0.74 \text{ nm}$. As such, the electron tunneling through the contact junction is in ballistic transport range, the current-voltage characteristic is given by the Landauer-Büttiker formula [34] as depicted in Eq. (3).

$$I = \frac{2e}{h} \int \tau M [f(E - eV) - f(E)] dE \quad (3)$$

Using $f = \left\{ 1 + \exp\left(\frac{E - E_F}{k_B T}\right) \right\}^{-1}$ known as Fermi-Dirac distribution function, where E_F is the Fermi energy, Eq. (3) can be written as drafted in Eq. (4) [35].

$$I = \frac{2e}{h} \int_0^\infty \tau M \left[\frac{1}{e^{\frac{E-\mu-eV}{k_B T}} + 1} - \frac{1}{e^{\frac{E-\mu}{k_B T}} + 1} \right] dE \quad (4)$$

Here, M is the total number of conduction channels and the symbol τ denotes a transmission probability for the electron to tunnel through the polymer obstacle between a CNT and a GNP. Both of them are functions of electron energy level E . The quantities T and μ represent the respective temperature and the chemical potential of the CNT. Other constants are the electron charge $e (1.6022 \times 10^{-19} \text{ C})$, Planck's constant $h (6.6261 \times 10^{-34} \text{ Js})$, and Boltzmann constant k_B . The symbol τ is the electron transmission probability which can be estimated by solving the Schrödinger equation with rectangular potential barrier. If the minimum distance between walls of a pair of CNTs is less than the cutoff distance, the CNT pair is considered in contact. Due to the van der Waals repellent force, the walls of contacting CNTs are not separated by less than the d_{vdW} .

$$\tau = \begin{cases} \exp\left(-\frac{d_{vdW}}{d_{tunnel}}\right) & 0 \leq d_{ij} \leq D + d_{vdW} \\ \exp\left(-\frac{d_{ij} - d}{d_{tunnel}}\right) & D + d_{vdW} < d_{ij} \leq D + d_{cutoff} \end{cases} \quad (5)$$

Tunneling distance is obtained by $d_{tunnel} = h/\sqrt{(8m_e \Delta E)}$ where m_e is the mass of electron, ΔE is the height of barrier potential. By the first order Taylor expansion and using the integral $\int_0^\infty \frac{x}{e^x + 1} dx = \frac{\pi^2}{12}$, the asymptotic expression of Eq. (4) can be derived as depicted in Eq. (6).

$$\int_0^\infty \tau M \frac{1}{e^{\frac{E-\mu}{k_B T}} + 1} dE \approx \int_0^\mu \tau M dE + \frac{\pi^2}{6} (k_B T)^2 \frac{d[\tau M]}{dE} \quad (6)$$

To derive a concise formula to estimate the tunneling resistance, we consider the asymptotic behavior of Eq. (6) using Sommerfeld expansion with respect to the temperature T .

$$I = \frac{2e}{h} \left\{ \int_\mu^{\mu+eV} \tau M dE + \frac{\pi^2}{6} (k_B T)^2 \times \frac{d[\tau M]}{dE} \Big|_{\mu}^{\mu+eV} \right\} \quad (7)$$

Under low bias voltage V , it can be estimated that $\int_\mu^{\mu+eV} \tau M dE \approx eVM\tau$ and $\frac{d[\tau M]}{dE} \Big|_{\mu}^{\mu+eV} \approx eVM \frac{d\tau}{dE} \Big|_{\mu}$. Here, the channel number M is assumed to be an integer that cannot follow a continuous change of

variable E . Then Eq. (7) is reduced to an averaged 1-D tunneling model, and the contact resistance can be evaluated by Eq. (8).

$$I = \frac{2e}{h} \left\{ \int_{\mu}^{\mu+eV} \tau M dE + \frac{\pi^2}{6} (k_B T)^2 \times \frac{e V M d^2 T}{d E^2} |\mu| \right\} \approx \frac{2e}{h} \left\{ \int_{\mu}^{\mu+eV} \tau M dE \right\} \quad (8)$$

Current carried per unit energy is equal to $\frac{2e}{h}$ which is about 80 nA/meV. Wide conductors containing large number of tunneling points have very small tunneling resistance.

Using the tunneling probability formula Eq. (5), resistivity can be deduced from Eq. (9).

$$R_{ij} = \frac{h}{2e^2} \frac{1}{M \tau_{ij}} = \frac{h}{2e^2 M \exp\left(-\frac{d_{ij}\sqrt{8m_e\Delta E}}{h}\right)} \quad (9)$$

Here $m_e (9.1093829 \times 10^{-31} \text{ kg})$ is the mass of electron. Multiplying a which is the area for electrons to tunnel, equal to the cross-sectional area approximated by $\pi d^2/4$ to top and bottom of division line, tunneling resistivity between two neighboring CNTs can be achieved by Eq. (10) [35].

$$\begin{aligned} Y(s_0, t_0, s_1, t_1) &= \frac{1}{2} \|X_0(s_0, t_0) - X_1(s_1, t_1)\|^2 \\ &= \frac{1}{2} (s_0^2 + t_0^2 + s_1^2 + t_1^2) - s_0 s_1 (U_0^T \cdot U_1) - s_0 t_1 (U_0^T \cdot V_1) - t_0 s_1 (V_0^T \cdot U_1) - t_0 t_1 (V_0^T \cdot V_1) + s_0 (U_0^T \cdot \Delta) + t_0 (V_0^T \cdot \Delta) - s_1 (U_1^T \cdot \Delta) - t_1 (V_1^T \cdot \Delta) + \frac{1}{2} \|\Delta\|^2 \\ &= \frac{1}{2} p^T \begin{bmatrix} 1 & 0 & -U_0^T \cdot U_1 & -U_0^T \cdot V_1 \\ 0 & 1 & -V_0^T \cdot U_1 & -V_0^T \cdot V_1 \\ -U_0^T \cdot U_1 & -V_0^T \cdot U_1 & 1 & 0 \\ -U_0^T \cdot V_1 & -V_0^T \cdot V_1 & 0 & 1 \end{bmatrix} p + [U_0^T \cdot \Delta V_0^T \cdot \Delta - U_1^T \cdot \Delta - V_1^T \cdot \Delta] p + \frac{1}{2} \|\Delta\|^2 = \frac{1}{2} p^T Q p + f^T p + c \end{aligned} \quad (10)$$

$$R_{ij} = \frac{h^2 \cdot d_{ij} \cdot \exp\left(\frac{4\pi d_{ij}\sqrt{2m_e\Delta E}}{h}\right)}{ae^2 \sqrt{2m_e\Delta E}} \quad (11)$$

Tunneling effect happens between two CNTs when the shortest distance between them is less than the cutoff distance that is the maximum possible thickness of the polymer separating two CNTs that allows electron hopping $d_{\text{vdW}} + d < d_{ij} < d + d_{\text{cutoff}}$.

The shortest distance between each pair of straight CNTs are calculated to determine if the pair is in contact or not. The distance between two CNTs is calculated using the technique to calculate the distance between two skew lines. The calculation involves forming vectors along the directions of the lines and using both the cross product and the dot product. If i th and j th CNTs' vectors (v_i and v_j) are connected by a vector v_{ij} , the minimum distance between them is defined as $d_{ij} = \frac{\|v_{ij} \cdot (v_i \times v_j)\|}{\|v_i \times v_j\|}$.

2.2. Integration of GNPs

It is well known that the electrical conductivity of CNT/GNP composites can be represented by the resistance of CNT/GNP percolating network inside the composite. GNP is assumed as a thin rectangular cube

with side length S and thickness t which its intrinsic resistivity is $R_f = \frac{S}{t^2 \sigma_f}$. GNPs can be found in rectangular form as declared in previous experimental studies [36,37]. The i -th GNPs can be positioned through the set of coordinates of the starting point (x_0^i, y_0^i, z_0^i) and two nonzero arbitrary vectors passing through the starting point in which their cross product is the normal to the GNP surface. In the RVE, GNPs are randomly generated and uniformly dispersed with origin P_i and the two vectors from origin be U_i and V_i which sketches edges of rectangular GNP [3].

$$U_i = \begin{Bmatrix} u_x^i \\ u_y^i \\ u_z^i \end{Bmatrix}, V_i = \begin{Bmatrix} v_x^i \\ v_y^i \\ v_z^i \end{Bmatrix}, u_x^i, u_y^i, u_z^i, v_x^i, v_y^i = S. \text{"rand"}, v_z^i = \frac{-(u_x^i \cdot v_x^i + u_y^i \cdot v_y^i)}{u_z^i} \quad (12)$$

The symbol S is GNP side length. Points on the thin rectangular GNP are represented by Eq. (12) [38].

$$X_i = P_i + s_i U_i + t_i V_i \quad (13)$$

Here the parameters $0 < s_i < 1$ and $0 < t_i < 1$ are unknowns and $\|U_i\|$ and $\|V_i\|$ represents the length and width of thin rectangular GNP. GNP thickness added to half squared distance between two individual GNPs is defined as depicted in Eq. (13) [38,39].

$$\text{where } p = [s_0 t_0 s_1 t_1]^T, \Delta = C_0 - C_1, f = [U_0^T \cdot \Delta V_0^T \cdot \Delta - U_1^T \cdot \Delta - V_1^T \cdot \Delta] \text{ and } c = \frac{1}{2} \|\Delta\|^2.$$

Finding the minimum of the problem where Y is a function that returns a scalar and accepts the variables (s_0, t_0, s_1, t_1) , "fmincon" of MATLAB attempts to find a minimum of a scalar function of several variables, starting at an initial estimates. For minimizing the objective function, subject to the bound constrain, lower and upper bounds on individual components, instead of writing two files, objective function and bounding constrain, one file is written which contains both functions as local functions. Then the constrained minimization starts from starting point and local minimum function finds variables which satisfy the constraints. The minimum distance between a CNT, $X_0(s_0) = P_0 + s_0 Q_0$ and a GNP, $X_1(s_1, t_1) = P_1 + s_1 U_1 + t_1 V_1$ can be described by Eq. (14).

$$Y(s_0, s_1, t_1) = \frac{1}{2} \|X_0(s_0) - X_1(s_1, t_1)\|^2 \quad (14)$$

Fig. 2 shows the schematic representation of the hybrid CNT/GNP nano-structure with different CNT and GNP dispersion conditions. The details of the CNT maximum orientation angle and GNP dispersion

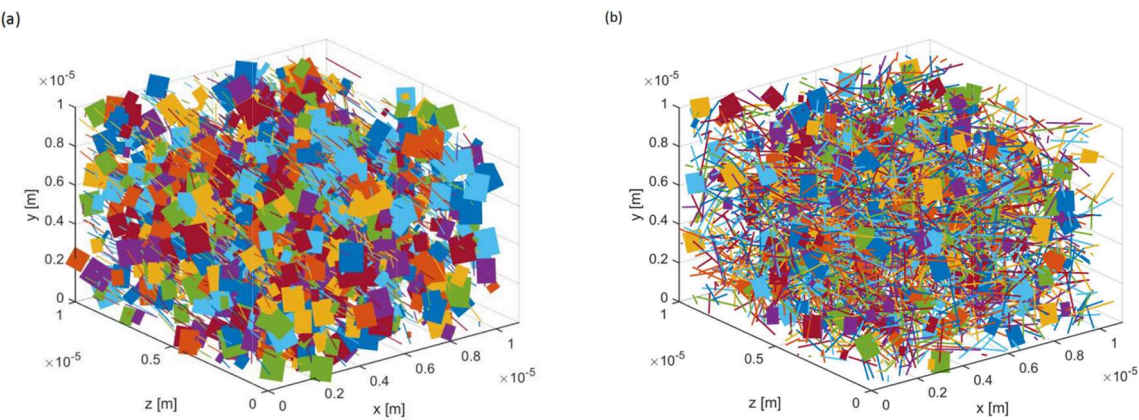


Fig. 2. Schematics of the nano-structure of nanocomposites with different CNT and GNP dispersion conditions.

Table 1
Details of the CNTs and GNPs dimensional characteristics in the RVE.

Schematic description	Max. CNT orientation angle (rad)		Volume fraction (vol.%)		Length (Side length) (μm)	
	φ	θ	CNT	GNP	CNT	GNP
2(a)	$\pi/6$	$\pi/12$	0.2	1.2	2	2
2(b)	π	$\pi/2$	0.3	0.6	3	1.5

condition are listed in [Table 1](#).

The electrical resistance of a network of randomly dispersed CNTs and GNPs is known to be dominated by the tunneling of the electrons between nearby CNTs and GNPs [\[40\]](#). Quantum phenomena of nearest-neighbor CNTs and GNPs interactions connecting two sides of the conductive network via transport of electron along fillers are dominant and several orders larger in magnitude than nanofillers intrinsic resistance, therefore, contact and tunneling resistances between CNTs and GNPs were preferred and the intrinsic resistance and CNTs and GNPs were ignored [\[41,42\]](#).

The resistivity is evaluated by recognizing the connective percolating network linking two opposite faces of RVE. Once a conductive network is found, the Dulmage-Mendelsohn decomposition method is used on the conductive network to eliminate the segments that do not participate in conducting current. Then the remaining conductive network is transformed into resistor network by calculating the resistance between the different nodes.

Passing from one CNT or GNP to another makes an increase in electrical potential. Presenting the electrical potential of the i th CNT or GNP by ϑ_i , the current flow from i th CNT or GNP to each electrode can be demonstrated with the assembly of tunneling currents from the j th CNT or GNP to other CNTs or GNPs and from j th CNT or GNP to the two electrodes. Then, the system of equations that determines the voltage distribution over the resistor network is solved based on Kirchhoff's law [\[43\]](#).

$$\sum_{i=1,2,j}^N \frac{\vartheta_i - \vartheta_j}{R_{ij}} + \sum_{i=1}^2 \frac{\vartheta - \vartheta_j}{R_{ij}} = 0, j = 3, 4, \dots, N \quad (15)$$

Here the first term is the sum of tunneling from j th CNT or GNP to other CNTs or GNPs and the second term refers to the sum of tunneling currents from j th CNT or GNP to two electrodes. A Cholesky decomposition algorithm for sparse matrices is used to solve these matrix equations and to find the potentials. The current passing through each CNT or GNP is calculated by $I_{ij} = (\vartheta_i - \vartheta_j)/R_{ij}$, using Ohm's law, the conductivity is obtained $\sigma = \sum_{\vartheta_i} I_{ij}$.

[Fig. 3](#) demonstrates a flowchart of the steps taken to identify

percolation threshold, electrical conductivity and piezoresistivity of nanocomposite considering randomly dispersed hybrid CNT/GNP fillers with different morphologies. First, a 3D RVE of size $L_x \times L_y \times L_z$ is generated. Next, CNTs as line segments and GNPs as rectangular platelets are randomly distributed in the 3D cube. The dimension and orientation of nanotubes and platelets are described based on random numbers. The shortest separation distance between neighboring fillers is evaluated and particles with inter-particle distance less than the tunneling cutoff distance are assumed electrically connected. With existence of at least one conductive path, the electrical conductivity of the RVE is computed in terms of resistance proportional to the separation distance. With the construction of other conduction paths, Kirchhoff's current and Ohm's law are used with the incomplete Cholesky conjugate gradient method to predict the overall resistance of the RVE. Later, to study the piezoresistivity of the nanocomposite, a strain is applied to the RVE and the new geometrical characteristics of the RVE and fillers updated coordinates and positions are defined. The obtained new configuration of the electronic band structure is used to detect the new percolating CNT-GNP networks in the RVE leading to calculation of the electrical resistance. The new resistance of the RVE at a fixed strain is compared to the resistance of the unstrained RVE to compute piezoresistivity. Then, Strain is incremented at each step, and the procedure is repeated.

2.3. Piezoresistivity

In this study the piezoresistivity of percolated RVE is modeled. Tensile strains were applied to the RVE and the change in electrical resistance was observed. The formulation for the 3D modeling of piezoresistivity is done by assuming a perfect mechanical coupling between the matrix, CNTs and GNPs [\[14\]](#). Therefore, any applied strain will result in the deformation of each CNT and GNP and in the change of their orientations. When the CNT/GNP polymer composite is under an incremental uniaxial strain $\Delta\varepsilon$ along the Z-axis, the coordinates of the center point of the i th CNT segment distributed in the RVE $(\bar{x}_c^i, \bar{y}_c^i, \bar{z}_c^i)$ will become [\[44,45\]](#).

$$\left(\bar{x}_c^i, \bar{y}_c^i, \bar{z}_c^i \right) = (x_c^i(1 - \nu\Delta\varepsilon), y_c^i(1 - \nu\Delta\varepsilon), z_c^i(1 + \Delta\varepsilon)) \quad (16)$$

Where $(\bar{x}_c^i, \bar{y}_c^i, \bar{z}_c^i)$ is the updated coordinates of the center point of the i th CNT segment and ν is the Poisson's ratio. After strain is applied, a new state of CNTs will happen in the RVE and more CNTs tend to be aligned along the stretching direction. The coordinated of starting and ending points of the i -th CNT after strain are expressed as drafted in Eq. [\(17\)](#).

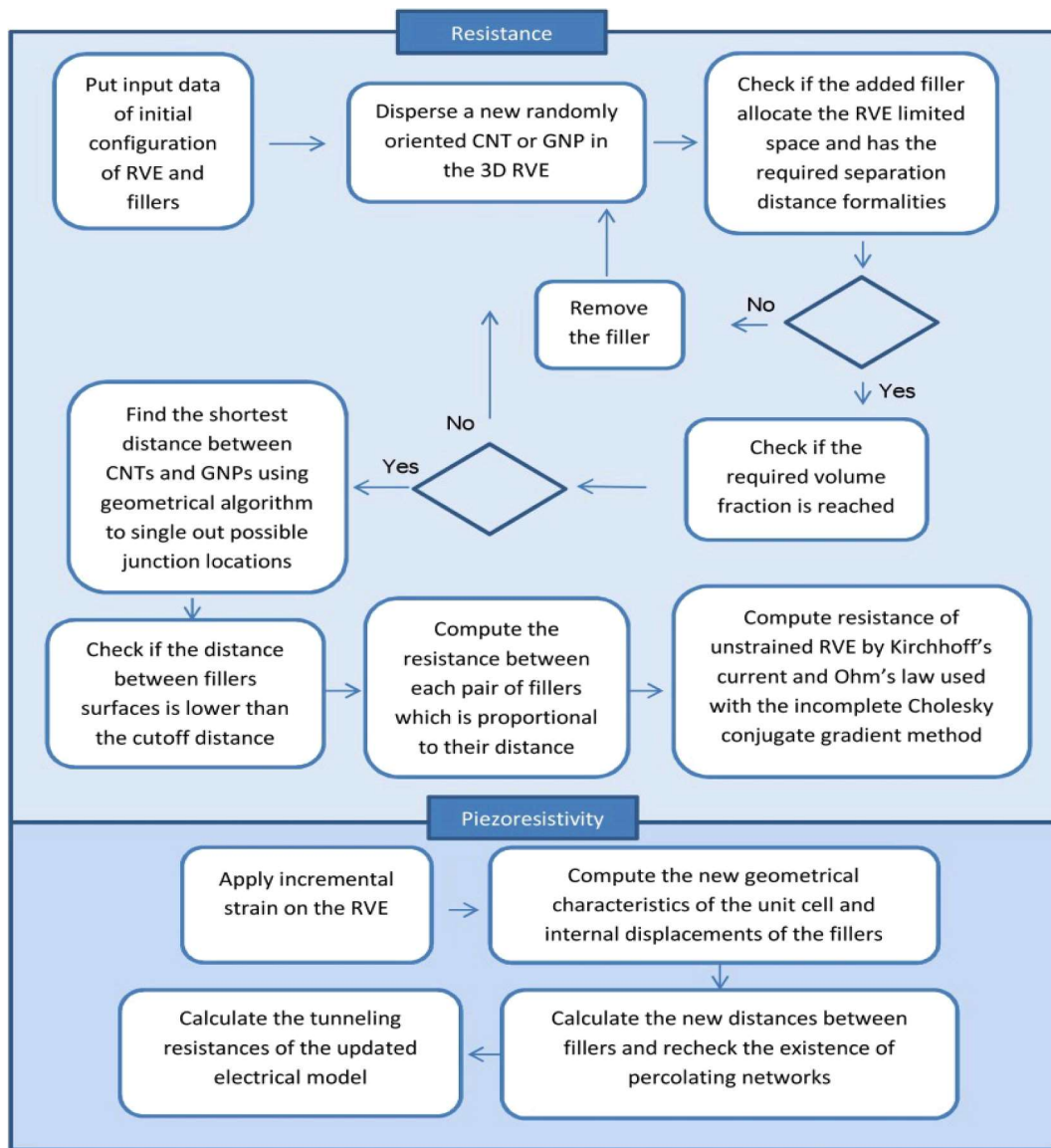


Fig. 3. Flowchart of different calculation steps of Monte Carlo simulation based on the present methodology.

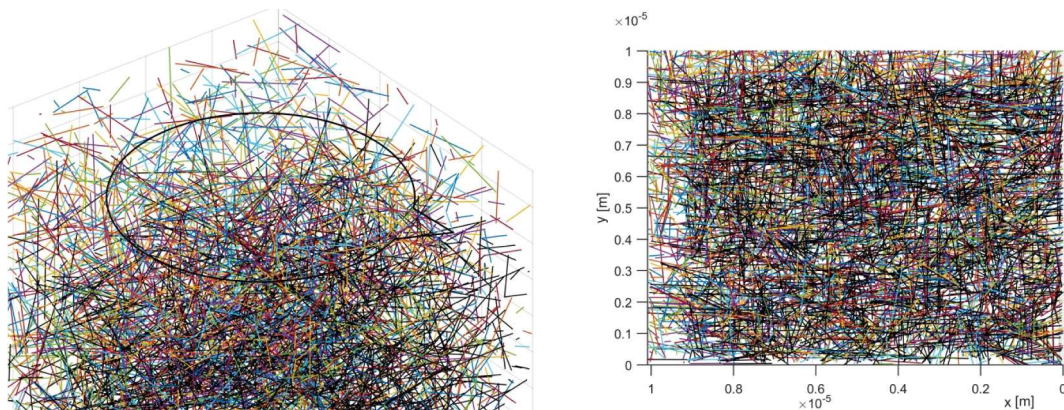


Fig. 4. Schematic of the CNT nano-structure change with the strain.

Table 2
CNT nanostructure change with the strain.

RVE Condition	Mean X position (μm)	Mean Y position (μm)	Mean Z position (μm)	Mean orientation angle (rad)
Unstrained	4.9332	4.9999	5.0209	1.5688
Strained	4.6612	4.6885	5.6553	1.4317

$$\bar{x}_0^i = \bar{x}_c^i - \left\{ \bar{x}_c^i - x_0^i(1 - \nu\Delta\varepsilon) \right\} \times \begin{pmatrix} l_i \\ \bar{l}_i \end{pmatrix},$$

$$\bar{y}_0^i = \bar{y}_c^i - \left\{ \bar{y}_c^i - y_0^i(1 - \nu\Delta\varepsilon) \right\} \times \begin{pmatrix} l_i \\ \bar{l}_i \end{pmatrix},$$

$$\bar{z}_0^i = \bar{z}_c^i - \left\{ \bar{z}_c^i - z_0^i(1 + \Delta\varepsilon) \right\} \times \begin{pmatrix} l_i \\ \bar{l}_i \end{pmatrix},$$

$$\bar{x}_1^i = \bar{x}_c^i + \left\{ x_1^i(1 - \nu\Delta\varepsilon) - \bar{x}_c^i \right\} \times \begin{pmatrix} l_i \\ \bar{l}_i \end{pmatrix},$$

$$\bar{y}_1^i = \bar{y}_c^i + \left\{ y_1^i(1 - \nu\Delta\varepsilon) - \bar{y}_c^i \right\} \times \begin{pmatrix} l_i \\ \bar{l}_i \end{pmatrix},$$

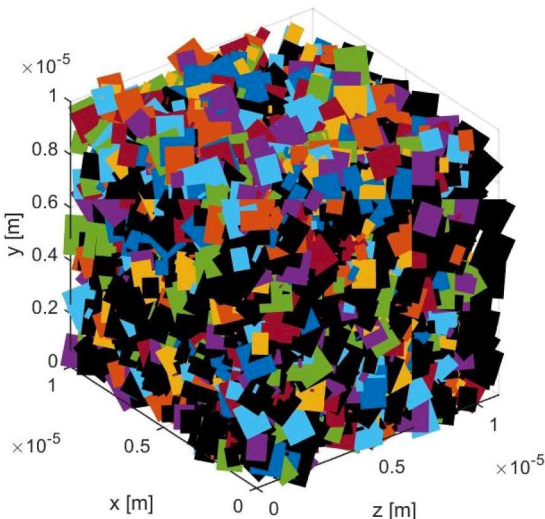
$$\bar{z}_1^i = \bar{z}_c^i + \left\{ z_1^i(1 + \Delta\varepsilon) - \bar{z}_c^i \right\} \times \begin{pmatrix} l_i \\ \bar{l}_i \end{pmatrix} \quad (17)$$

The locations of CNT intersections will transform after strain. Fig. 4 shows a schematic representation of the CNT polymer strained composite (10% of strain) in the Z-direction which CNTs in black are moved by strain. The details of CNTs' nanostructure change with strain are drafted in Table 2.

Following the re-orientation model, the change in GNP position is considered here. With tensile strain in the Z-direction, the starting point P_i of the i th GNP moves transnationally in accordance with the strain and the Poisson's ratio, as depicted in Eq. (18) [46].

$$\bar{P}_x^i = P_x^i(1 - \nu\Delta\varepsilon), \bar{P}_y^i = P_y^i(1 - \nu\Delta\varepsilon), \bar{P}_z^i = P_z^i(1 + \Delta\varepsilon) \quad (18)$$

Where i is the index of i th GNP. The updated vectors from origin are



described in Eq. (19) [47].

$$\bar{U}_i = \begin{Bmatrix} u_x^i(1 - \nu\Delta\varepsilon) \\ u_y^i(1 - \nu\Delta\varepsilon) \\ u_z^i(1 + \Delta\varepsilon) \end{Bmatrix} \quad (19)$$

$$\bar{V}_i = \begin{Bmatrix} v_x^i(1 - \nu\Delta\varepsilon) \\ v_y^i(1 - \nu\Delta\varepsilon) \\ v_z^i(1 + \Delta\varepsilon) \end{Bmatrix}$$

Eventually, the separation distance of a pair of rectangular GNPs is calculated by Eq. (13).

The change in the electrical resistance of the composite due to the mechanical deformation can be expressed as depicted in Eq. (20) [12].

$$\frac{\Delta R}{R} = \frac{R_{\text{new}} - R}{R} = \frac{R_{\text{new}}}{R} - 1 \quad (20)$$

Here R and R_{new} are the electrical resistances of the undeformed and deformed composites, respectively. And ΔR is the corresponding change of the electrical resistance of the nanocomposite caused by mechanical deformation [31]. Fig. 5 shows the schematic representation of GNP polymer strained composite (10% of strain) in the Z-direction where GNPs in black are transformed by strain.

3. Results and discussion

To demonstrate the validity of the proposed single-step Monte Carlo approach, the comparison between the calculated electrical conductivity and the experimental data of GNP composite filled with a specific CNT volume fraction is done. The experimental data was obtained from the Liu et al. [48], Al-saleh [49], Gao et al. [50], Stankovic et al. [51], and Qi et al. [52]. The composite tested by them used different volume fractions of fillers but with approximately similar GNP and CNT properties. In the calculation, the two important parameters are taken as $\Delta E = 3\text{eV}$ and $d_{\text{cutoff}} = 1.4\text{nm}$. To reduce the computational cost, the dimension of the unit cell was set to $10 \times 10 \times 10\mu\text{m}^3$, which has been estimated to be large enough for an reliable prediction. It is evident from Fig. 6(a) that there is a good agreement between the calculated and experimentally measured electrical conductivity of the composite. There are some discrepancies related to uniform dispersion state assumed in the model while most experiments cannot fabricate composite with filler uniform dispersion. Fig. 6(a) also shows that the values of the electrical conductivity of the nanocomposite increased several orders of

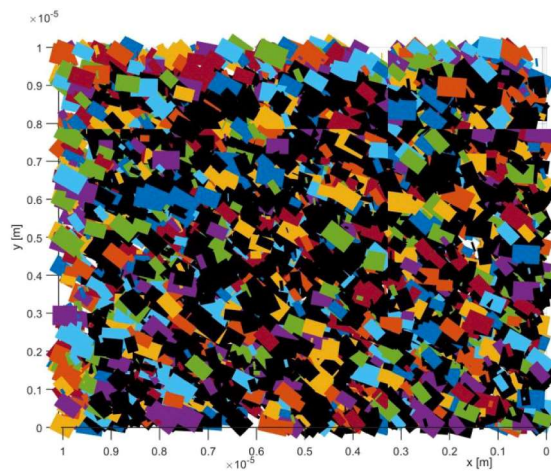


Fig. 5. Schematic of the GNP nano-structure variation with the strain.

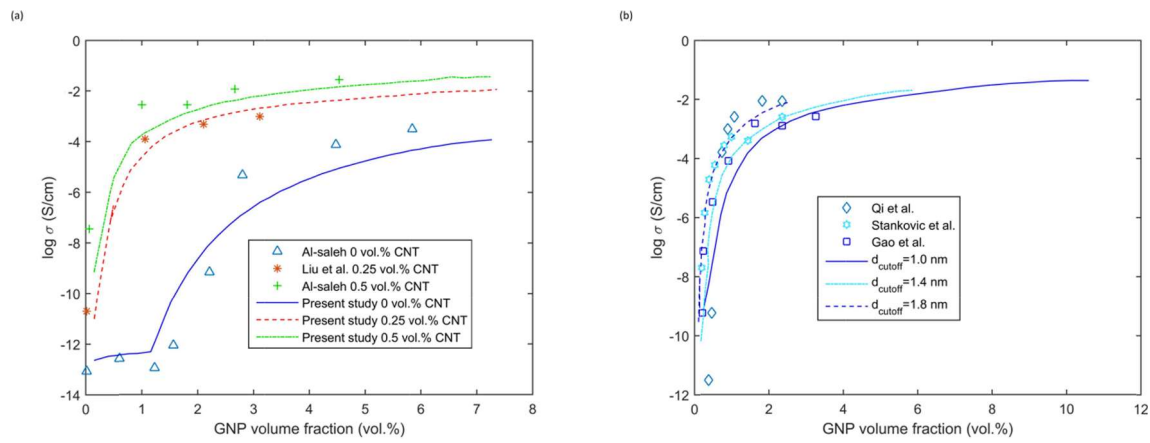


Fig. 6. Comparison of present study predictions and (a) experimental data [48,49], and (b) experimental data [50–52].

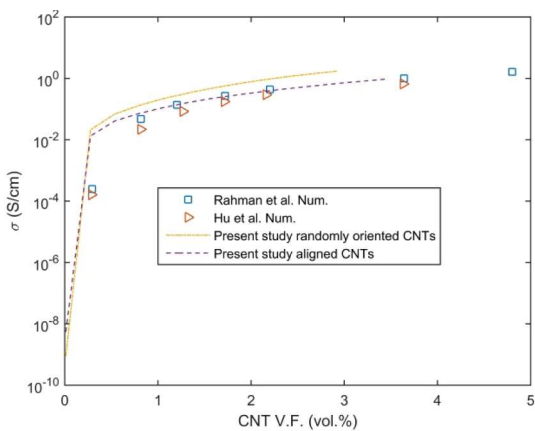


Fig. 7. Comparison between the predicted results of the analytical model and the numerical estimations [26,53].

Table 3
Dimensional and electrical properties of CNT and GNP [9,28,47,49].

Property	CNT	GNP
Intrinsic conductivity (S/m)	10,000	50,000
Length (Side length) (μm)	4	3
Diameter (Thickness) (nm)	10	30
Height of barrier potential (eV)	4	4
Cutoff distance (nm)	1.4	1.4

magnitude within a small volume fraction range of GNP. In order to see the overall electrical conductivity dependence on the value of cutoff distance, Fig. 6(b) shows predicted effective electrical conductivity of model in comparison with the experimental data of GNP composite with 0 vol% of CNT. The small discrepancy may be attributed to the assumptions made, such as cutoff distance, fixed side length and thickness of GNPs. From Fig. 6(b), it can be seen that for a composite with a fixed volume fraction, the increase in the cutoff distance marginally increases the electrical conductivity. Such small dependence may partly relate to tunneling which decays exponentially with cutoff distance and exponential behavior of τ make the compensations for large cutoff distance.

To further verify the model's electrical conductivity predictions, the model results of CNT/polymer nanocomposite are compared with Rahman et al. [26] and Hu et al. [53] numerical studies predictions. Fig. 7 demonstrates that the electrical conductivities predicted by model agree well with the numerical studies predictions.

Multiple RVEs filled with CNTs and GNPs with volume fraction

ranging from 0.1% to 15% are created to examine the effect of various parameters on the electrical conductivity and piezoresistivity. The material properties of CNT and GNP are depicted in Table 3 which are derived based on previous numerical and experimental studies.

In order to predict the effects of different parameters on the conductivity of nanocomposite, the electrical conductivity is plotted with respect to GNP volume fraction. The electrical conductivity of hybrid nanocomposite with different CNT aspect ratios is shown in Fig. 8(a) as a function of GNP volume fraction. Aspect ratio l/d is an important parameter that combines the influence of the length and diameter of CNT into one parameter attributed to effective length. Fig. 8(a) demonstrates that the conductive properties of the nanocomposite are closely related to the aspect ratio of CNT and electrical conductivity increases with aspect ratio because larger aspect ratio indicates longer conductive pathways and more interactions. Whereas, the reduction of effective length by lower aspect ratio would not be beneficial for the formation of effective conductive networks by reducing the number of inter-tube tunneling contacts along a conductive path. This reveals that larger aspect ratio is mainly beneficial for the synergy arising from the hybrid fillers which helps the average separation distance falls in the suitable theoretical range < 1.4 nm for electron hopping. Fig. 8(b) presents the effects of the GNP side length on the electrical conductivity of the hybrid nanocomposite. Obviously, the GNP side length has a significant effect of the percolation threshold while its influence on the overall electrical conductivity extenuates at higher volume fraction. This finding is understandable because the effect of side length of the GNP is prominent when GNPs are sparsely dispersed and further increasing the volume fraction can attenuate this effect. In addition, the higher probability of the formation of conductive networks related to electron hopping at higher volume fraction contributes to this decreasing trend.

Fig. 9 shows the effect of CNT orientation and heights of barrier potential on the electrical conductivity of nanocomposite as a function of GNP volume fraction. Randomly oriented CNTs relate to maximum orientation angle and aligned CNTs refer to minimum orientation angle. Results show that the percolation happens earlier in nanocomposites with randomly oriented CNTs, indicating that the electrical conductivity can be effectively enhanced by distributing CNTs in all possible directions. The extent of interactions between the nanofillers and matrix polymer in the nanocomposite is significantly controlled by the interfacial area and channel length. This means that highly aligned CNTs would not be beneficial to provide a highly conductive network due to the weak interactions between themselves. Whereas, randomly oriented CNTs lead to an exceptionally large interfacial area of nanocomposite where many conductive paths exist accompanied with huge interconnections. As shown in Fig. 9(b), the dependence of electrical conductivity on potential barrier height provides significant insights

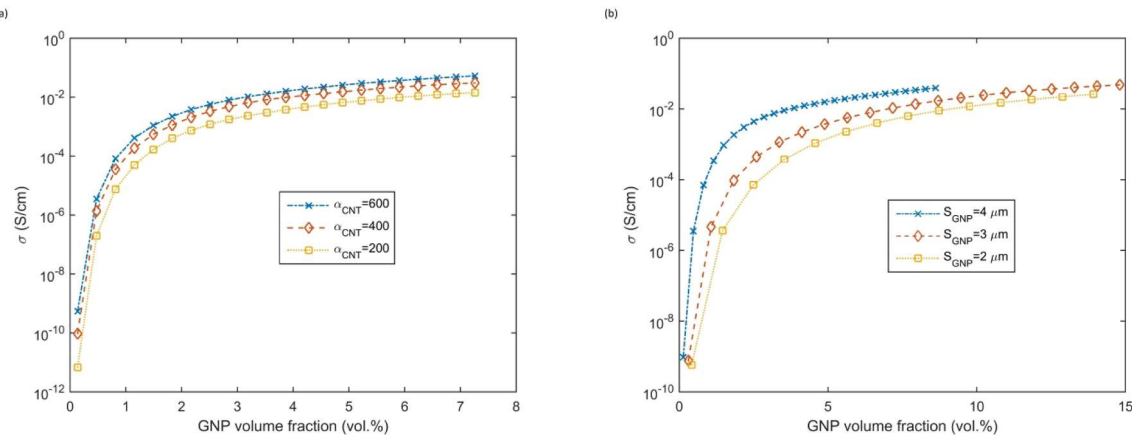


Fig. 8. Predicted electrical conductivity of hybrid nanocomposite with 0.25 vol% CNT versus the GNP volume fraction for different (a) CNT aspect ratios (b) GNP side lengths.

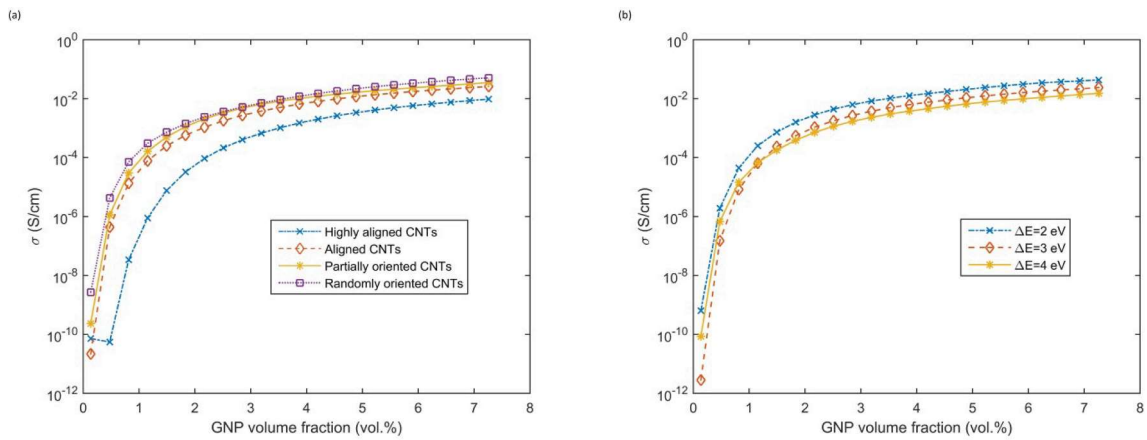


Fig. 9. Predicted electrical conductivity of hybrid nanocomposite versus the GNP volume fraction for different (a) CNT orientations (b) heights of barrier potential.

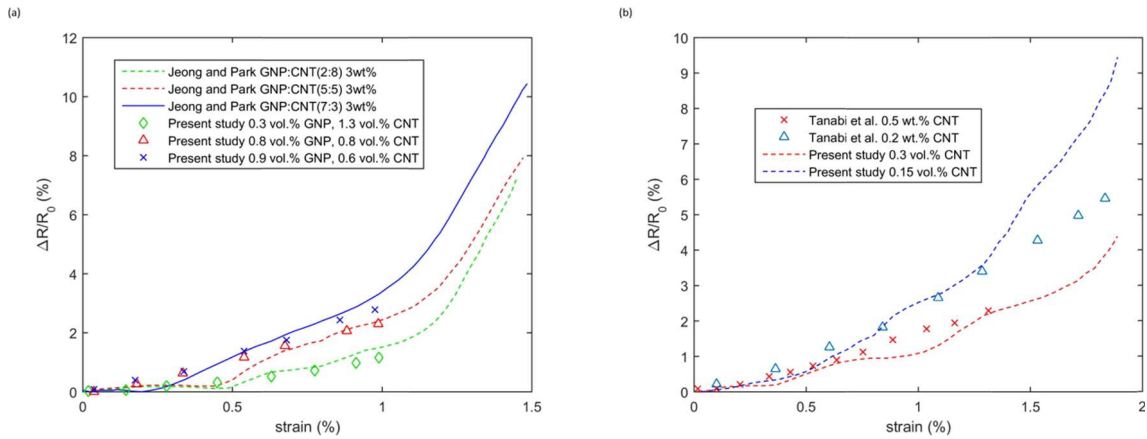


Fig. 10. Comparison of piezoresistivity predicted by the model for (a) CNT/GNP nanocomposite with experimental data [54], and (b) CNT nanocomposite with experimental data [55].

into the effect of work function difference between fillers and polymer. Based on percolation theory, formation of continuous network among fillers can be achieved if electron could transport between CNTs. Moreover, the insulating polymer thickness between crossing CNTs plays a significant role in the tunneling resistance which depends on height of barrier potential. Therefore, the decreasing height of barrier potential allows more CNTs to be connected in order to form the

conductive paths. The surface area related to the incorporation of more filler in the percolation network led to this higher electrical conductivity.

The CNT/GNP hybrid nanocomposite is employed for the purpose of theoretically predicting the piezoresistivity obtained in previous experiments. Comparisons between the analytical predictions and the experimental data of Jeong and Park [54] are shown in Fig. 10(a) with

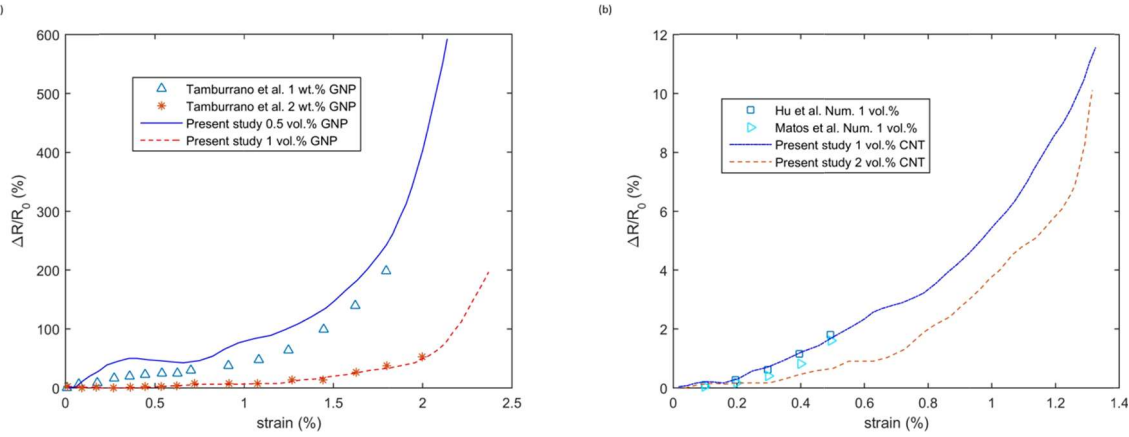


Fig. 11. Comparison of piezoresistivity predicted by the model for (a) GNP polymer nanocomposite with experimental data [56], and (b) CNT polymer nanocomposite with numerical results [58,59].

different volume fraction ratios of CNT/GNP. Referred to experimental data, the predicted response of the material is almost linear regarding relatively low strains in accordance with the model predictions. However, the model predicts an initial non-linear decrease of the resistance change ratio versus strain due to the variations of the locations of CNTs and GNPs in the strained RVE. New paths may form and existing paths may break due to the incremental strain of 0.05% at each time step inflicted on the RVE. In the beginning of the curve, it seems that the average number of distorted paths overweight the average number of formed paths. In addition, at low strain, the distances of adjacent CNTs were short and the conductive network still could keep the stable state under small deformation. Later, model predicted that the resistance exponentially increased with applied strain. This phenomenon is related to the destruction of the conductive network inside the polymer composite and the reduction of percolated CNT paths. In all cases, a very good agreement can be noted between model predictions and experimental data, indicating the capability of the model to predict the piezoresistivity behavior. Fig. 10(b) shows piezoresistivity of nanocomposite for different CNT volume fractions in comparison with experimental data of Tanabi et al. [55]. Randomly oriented CNTs had an average diameter of 10 nm and an average length of 1.5 μm . Fig. 10(b) illustrates that there is a good agreement between the model predictions and the experimental data. Fig. 10(b) also demonstrates that the change in resistance is mild with higher CNT volume fraction related to more overlaps generated among CNTs which is understandable because when the CNTs are highly populated in any direction then any change in the strain will change both the linear and angular distance between the CNT pairs.

To investigate the validity of the proposed model, the piezoresistivity predictions are compared with Tamburrano et al. [56] experimental data. The GNP's wt.% can be converted to the GNP's vol.% considering GNP's density (2.1 g/cm^3) and polymer's density (1.05 g/cm^3) [57]. Fig. 11(a) demonstrates that the present model predictions match well with the experimental data reflecting that, at the same strain, differences in scattered GNPs' volume fractions lead to different resistance change ratios. Moreover, at small strains, the mean inter-platelets separation distance varies due to the improved in-plane alignment of high aspect ratio GNPs toward better electrical conductivity. At much higher strains, the conductive pathways are broken due to increased separation distance of aligned GNPs and the nanocomposite becomes more resistive.

To further exhibit the predictability of the analytical model, another comparison between the proposed model and other numerical studies (Matos et al. [58] and Hu et al. [59]) are conducted. Fig. 11(b) shows the predicted resistance change ratio versus strain for an RVE with size of $15 \mu\text{m}$, containing 1 and 2 vol% of CNTs. CNT's average length and diameter are $5 \mu\text{m}$ and 50 nm. From Fig. 11(b) it can be noted that there is a small discrepancy between the analytical results derived from the current theoretical model and numerical studies. The discrepancy is due to the consideration of the different set-ups in model establishments such as different dispersion states and structures of CNTs. This is due to the fact that non-uniformly dispersed curved CNTs would experience a greater change in resistance compared with uniformly dispersed straight CNTs for the same volume fraction.

In the following, parametrical studies are carried out on the effect of different parameters on the theoretical predictions of piezoresistivity. Fig. 12(a) gives the resistance change of the nanocomposite under the

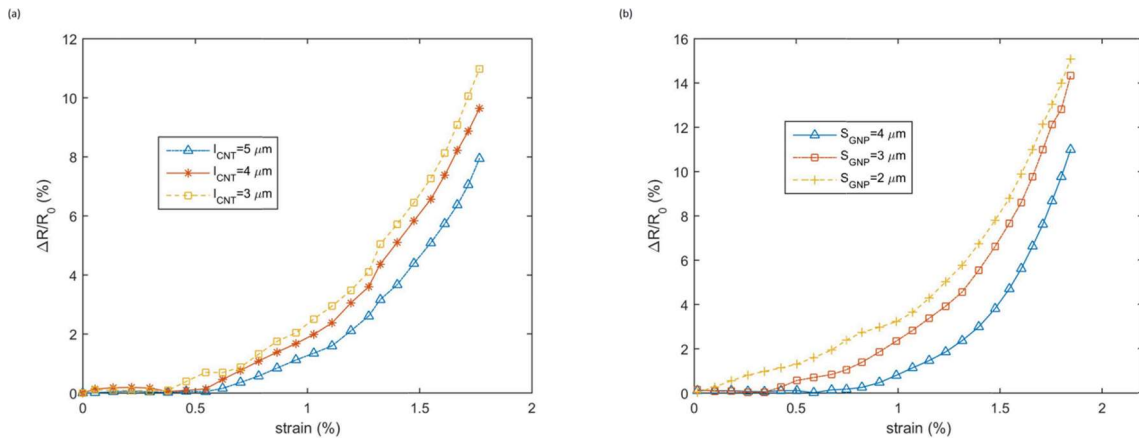


Fig. 12. Piezoresistivity of nanocomposite with different (a) CNT lengths and (b) GNP side lengths.

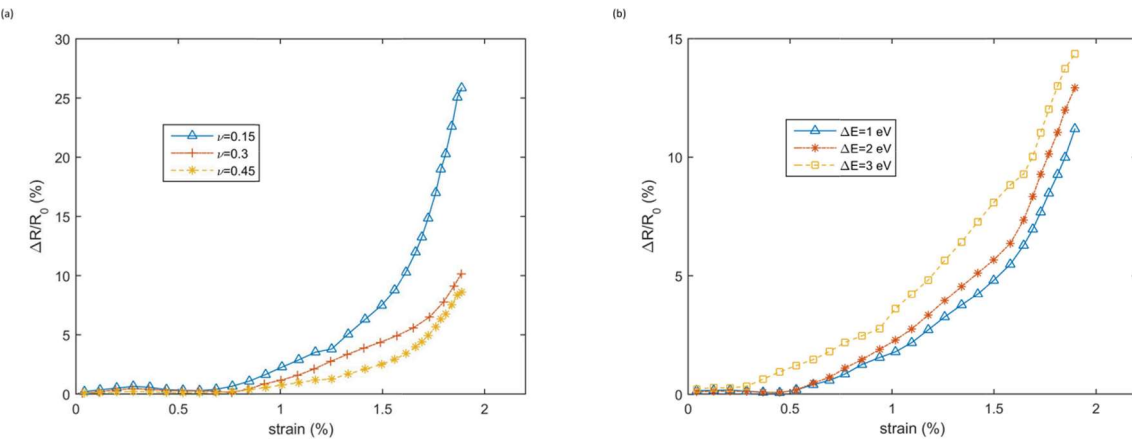


Fig. 13. Piezoresistivity of nanocomposite with different (a) Poisson's ratios and (b) heights of barrier potential.

applied strain for different CNT lengths while CNT diameter is kept constant at 10 nm. Considering a larger $\Delta R/R_0$ as higher sensitivity, Fig. 12(a) exhibits that the piezoresistivity is more sensitive with shorter CNTs. This reveals that nanocomposites with shorter CNTs are more susceptible to the breakdown of conductive networks. This is understandable as the increase in CNT length could increase the overlap ratio between CNTs which leads to longer network length affecting the electrical response of the nanocomposite coming from the exponential dependence of the resistance change ratio versus strain. Fig. 12(b) shows the influence of GNP side length on piezoresistivity. Fig. 12(b) demonstrates that resistance change ratio increased almost linearly with the strain at the beginning following by an exponential increase. As expected from theory, inter-particle distance increases extremely with further increment of the gap between fillers since a higher deformation span influences the network of fillers inside the polymer more widely. Fig. 12(b) also suggests that the resistivity of the nanocomposite with smaller GNP side length is more sensitive to stretching because GNPs with larger side length appear to have a permanent contribution by bridging and promoting electron tunneling. In this case, the average separation distance easily falls in the analytical range < 1.4 nm where the lower limit is imposed due to van der Waals interactions and upper limit is enforced by distance available for the electric conduction between two platelets. Also, the specific surface area of the GNP is much larger as a natural consequence of the larger side length which leads to physical contact between platelets to form conductive pathways and prohibit the breakdown of conductive networks. This again emphasizes the importance of the low average separation distance provided by large surface area for tunneling-type contact between adjacent platelets.

Fig. 13 plots the measured resistance change ΔR normalized by the

initial resistance R_0 , as a function of the tensile strain for different Poisson's ratios and heights of barrier potential. It is assumed that the effect of filler volume fraction and orientation on the Poisson's ratio is negligible. Fig. 13(a) shows that the piezoresistivity of the hybrid nanocomposite drastically changes with Poisson's ratio. This suggests the transverse motion effect that nullifies part of the strained CNTs transportation in displacement direction. The huge difference between the curves is attributed to the morphological structure of nanocomposites with different Poisson's ratios. Isotropic dispersion promotes inter-filler connection through contact, allowing the formation of continuous percolated pathways while anisotropic dispersion leads to desolating effects. As stated earlier, the condition for a charge to pass over an energy barrier with a given potential is to have the energy equal or greater than the barrier. Height of barrier potential indicates this dependency and affects the probability for a charge to pass through a potential barrier. Fig. 13(b) plots the resistance change ratio with strain for different heights of barrier potential. The decrease of sensitivity by increase in the height of barrier potential indicates the drawback of the insulating layer's potential barrier. This is quite interesting, since charge carriers choose the lowest resistance path possible through the nanocomposite and electrical conductivity network is mainly attributed to the electron hopping.

Fig. 14 shows the strain dependence of resistance change ratio for various volume fractions of CNTs and GNPs. Fig. 14(a) demonstrates that for a given level of strain, the resistance change ratios are lower when CNT volume fraction is higher. This result reflects that the previous consideration that network sparseness led to larger deformation of percolating network was true. Fig. 14(a) also demonstrates that the curves start to fluctuate from beginning due to updated fillers positions

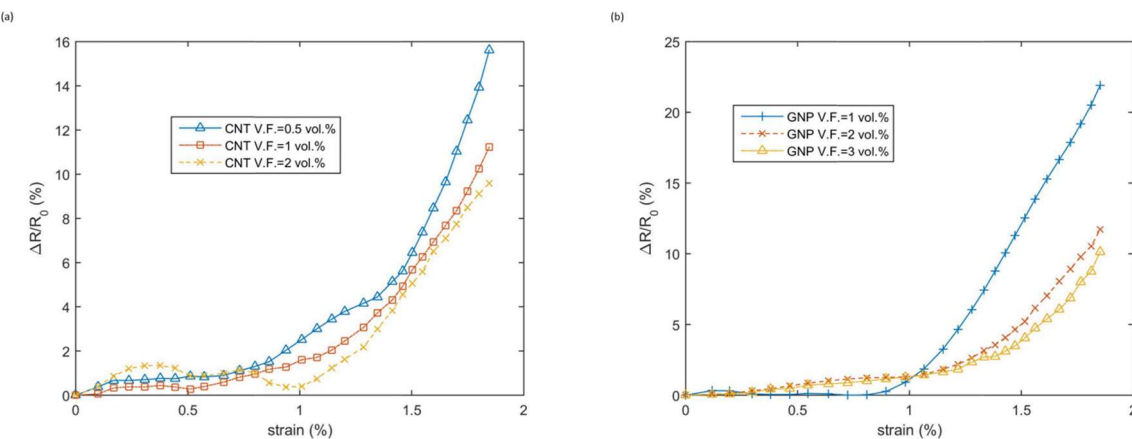


Fig. 14. Piezoresistivity of nanocomposite with different (a) CNT volume fractions and (b) GNP volume fractions.

and recalculated tunneling resistance between them. At percolation threshold, where fillers are separated with critical distances, strain has remarkable effect on the decrease or increase of the number of CNTs' contacts which creates high sensitivity related to the distortion or formation of percolation paths. This formation of conductive pathways in small strain is more specifically related to the straightening of individual disordered GNPs to evolved ordered aligned ones which decrease the efficacy of conducting pathways in primary increments of strain. Fig. 14(b) shows that the piezoresistivity substantially depends on GNP volume fraction and suggests that the resistivity of the composite with lower GNP volume fraction is more sensitive to stretching. This indicates that composite has higher sensitivity when a small number of conductive networks exist in nanocomposites. Fig. 14(b) also demonstrates a special tendency of the curve with lowest GNP volume fraction, which is related to the setup of the model and it seems that the number of distorted paths is equal to the number of paths created for the small strain. This is stemming from the fact that at small strains, the mean inter-particle distance may decrease due to the rotation of the fillers that are out of order, leading to better arrangement and reduced resistivity, whereas at higher strain, the in-plane inter-particle separation distance of aligned GNPs increases so the conductive paths are broken and the nanocomposite becomes more resistive. It seems that at earlier stage of strain range these two competing considerations are balanced.

4. Conclusion

The 3D Monte Carlo simulation was used to investigate the electrical conductivity and piezoresistivity of CNT/GNP polymer nanocomposite using percolation network model. The analytical model has been validated by experimental data published in the literature for both electrical conductivity and piezoresistivity of hybrid nanocomposite. The study results showed that the electrical conductivity is dominated by CNT/GNP quantum tunneling influenced by cutoff distance. The influences of height of barrier, CNT's orientation, volume fraction and dimensions and GNP side length on electrical conductivity and piezoresistivity were studied. Results showed that the conductivity of composite can be effectively enhanced by increasing CNT aspect ratio, orientation angle and GNP side length. Parametric studies revealed that the increase in height of barrier potential led to a decrease of electrical conductivity and more sensitive piezoresistivity. It was also indicated that the increase in Poisson's ratio, enabled CNTs to be more aligned along the stretching direction, which decreased the piezoresistive sensitivity while a higher CNT/GNP volume fraction led to less sensitivity. Although, this work has shown success in predicting the effect of different parameters on the electrical conductivity and piezoresistivity of CNT/GNP polymer nanocomposite, its applicability in a wider scenario, especially at a relatively high CNT volume fraction is limited because the current model does not take the agglomeration effects and distortion of CNT into account.

CRediT authorship contribution statement

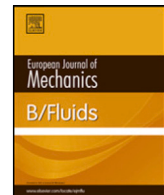
M. Haghgoor: Methodology, Software, Formal analysis, Investigation, Writing – original draft, Writing – review & editing. **R. Ansari:** Validation, Resources, Writing – review & editing, Supervision. **M.K. Hassanzadeh-Aghdam:** Conceptualization, Data curation, Writing – original draft, Visualization.

Declaration of Competing Interest

The authors declare that they have no known competing financial interests or personal relationships that could have appeared to influence the work reported in this paper.

References

- [1] Zhao H, Bai J. Highly sensitive piezo-resistive graphite nanoplatelet–carbon nanotube hybrids/polydimethylsiloxane composites with improved conductive network construction. *ACS Appl Mater Interfaces* 2015;7(18):9652–9.
- [2] Xiang D, Zhang X, Harkin-Jones E, Zhu W, Zhou Z, Shen Y, et al. Synergistic effects of hybrid conductive nanofillers on the performance of 3D printed highly elastic strain sensors. *Compos A Appl Sci Manuf* 2020;129:105730. <https://doi.org/10.1016/j.compositesa.2019.105730>.
- [3] Maiti S, Khatua BB. Graphene nanoplate and multiwall carbon nanotube–embedded polycarbonate hybrid composites: High electromagnetic interference shielding with low percolation threshold. *Polym Compos* 2016;37(7):2058–69.
- [4] Morales P, Moyanova S, Pavone I, Fazi L, Mirabile Gattia D, Rapone B, et al. Self-grafting carbon nanotubes on polymers for stretchable electronics. *The European Physical Journal Plus* 2018;133(6). <https://doi.org/10.1140/epjp/i2018-12040-0>.
- [5] Xiang D, Wang L, Zhang Q, Chen B, Li Y, Harkin-Jones E. Comparative study on the deformation behavior, structural evolution, and properties of biaxially stretched high-density polyethylene/carbon nanofiller (carbon nanotubes, graphene nanoplatelets, and carbon black) composites. *Polym Compos* 2018;39(S2):E909–23.
- [6] Rathi A, Kundalwal SI. Mechanical and fracture behavior of MWCNT/ZrO₂/epoxy nanocomposite systems: Experimental and numerical study. *Polym Compos* 2020;41(6):2491–507.
- [7] Xiang D, Wang L, Tang Y, Harkin-Jones E, Zhao C, Li Y. Processing-property relationships of biaxially stretched binary carbon nanofiller reinforced high density polyethylene nanocomposites. *Mater Lett* 2017;209:551–4.
- [8] Chen Q, Xiang D, Wang L, Tang Y, Harkin-Jones E, Zhao C, et al. Facile fabrication and performance of robust polymer/carbon nanotube coated spandex fibers for strain sensing. *Compos A Appl Sci Manuf* 2018;112:186–96.
- [9] Perets Y, Aleksandrovych L, Melnychenko M, Lazarenko O, Vovchenko L, Matzui L. The electrical properties of hybrid composites based on multiwall carbon nanotubes with graphite nanoplatelets. *Nanoscale Res Lett* 2017;12(1):1–10.
- [10] Du J, Zhao L, Zeng Y, Zhang L, Li F, Liu P, et al. Comparison of electrical properties between multi-walled carbon nanotube and graphene nanosheet/high density polyethylene composites with a segregated network structure. *Carbon* 2011;49(4):1094–100.
- [11] Li C, Thostenson ET, Chou T-W. Dominant role of tunneling resistance in the electrical conductivity of carbon nanotube–based composites. *Appl Phys Lett* 2007;91(22):223114. <https://doi.org/10.1063/1.2819690>.
- [12] Alig I, Skipa T, Lellingen D, Bierdel M, Meyer H. Dynamic percolation of carbon nanotube agglomerates in a polymer matrix: comparison of different model approaches. *physica status solidi (b)* 2008;245(10):2264–2267.
- [13] Xiang D, Wang L, Tang Y, Harkin-Jones E, Li Y. Effect of phase transitions on the electrical properties of polymer/carbon nanotube and polymer/graphene nanoplatelet composites with different conductive network structures. *Polym Int* 2018;67(2):227–35.
- [14] Kundalwal SI, Rathi A. Improved mechanical and viscoelastic properties of CNT-composites fabricated using an innovative ultrasonic dual mixing technique. *Journal of the Mechanical Behavior of Materials* 2020;29(1):77–85.
- [15] Kundalwal SI. Review on micromechanics of nano-and micro-fiber reinforced composites. *Polym Compos* 2018;39(12):4243–74.
- [16] Wang X, Meng Si, Tebyetekerwa M, Li Y, Pionteck J, Sun B, et al. Highly sensitive and stretchable piezoresistive strain sensor based on conductive poly(styrene-butadiene-styrene)/few layer graphene composite fiber. *Compos A Appl Sci Manuf* 2018;105:291–9.
- [17] Spinelli G, Lamberti P, Tucci V, Vertuccio L, Guadagno L. Experimental and theoretical study on piezoresistive properties of a structural resin reinforced with carbon nanotubes for strain sensing and damage monitoring. *Compos B Eng* 2018;145:90–9.
- [18] Oliva-Avilés AI, Avilés F, Seidel GD, Sosa V, Seidel Gt, Sosa V: On the contribution of carbon nanotube deformation to piezoresistivity of carbon nanotube/polymer composites. *Compos B Eng* 2013;47:200–6.
- [19] Lu S, Tian C, Wang X, Chen D, Ma K, Leng J, et al. Health monitoring for composite materials with high linear and sensitivity GnP/epoxy flexible strain sensors. *Sens Actuators, A* 2017;267:409–16.
- [20] Zhang X, Xiang D, Zhu W, Zheng Y, Harkin-Jones E, Wang P, et al. Flexible and high-performance piezoresistive strain sensors based on carbon nanoparticles@polyurethane sponges. *Compos Sci Technol* 2020;200:108437. <https://doi.org/10.1016/j.compscitech.2020.108437>.
- [21] Xiang D, Wang L, Tang Y, Harkin-Jones E, Zhao C, Wang P, et al. Damage self-sensing behavior of carbon nanofiller reinforced polymer composites with different conductive network structures. *Polymer* 2018;158:308–19.
- [22] Pech-Pisté R, Cen-Puc M, Balam A, May-Pat A, Avilés F. Multifunctional sensing properties of polymer nanocomposites based on hybrid carbon nanostructures. *Mater Today Commun* 2020;25:101472. <https://doi.org/10.1016/j.mtcomm.2020.101472>.
- [23] Namilae S, Li J, Chava S. Improved piezoresistivity and damage detection application of hybrid carbon nanotube sheet-graphite platelet nanocomposites. *Mech Adv Mater Struct* 2019;26(15):1333–41.
- [24] Ke K, Yue L, Shao H, Yang M-B, Yang W, Manas-Zloczower I. Boosting electrical and piezoresistive properties of polymer nanocomposites via hybrid carbon fillers: a review. *Carbon* 2021;173:1020–40.
- [25] Li J, Fang L, Sun B, Li X, Kang SH. Recent progress in flexible and stretchable piezoresistive sensors and their applications. *J Electrochem Soc* 2020;167(3):037561.



A class of exact solutions of the Navier–Stokes equations in three and four dimensions

R.K. Michael Thambbynayagam

Retired, Schlumberger, Houston, TX, USA



ARTICLE INFO

Article history:

Received 13 October 2022

Received in revised form 21 February 2023

Accepted 22 February 2023

Available online 8 March 2023

MSC:

35Q30

76D05

Keywords:

Navier–Stokes

Incompressible flow

Viscous flows

Euler flow

Partial differential equations

ABSTRACT

A few basic, intuitive, properties of the Navier–Stokes system of equations for incompressible fluid flows are discussed in this paper. We present a rephrased interpretation of the Navier–Stokes equation in a space having an arbitrary number of dimensions. We then derive spatially periodic solutions for the velocity and pressure fields that span an unbounded domain in three and four dimensions, given a smooth solenoidal initial velocity vector field. In these solutions all velocity components depend non-trivially on all coordinate directions.

© 2023 The Author(s). Published by Elsevier Masson SAS. This is an open access article under the CC BY-NC-ND license (<http://creativecommons.org/licenses/by-nc-nd/4.0/>).

1. Introduction

The Navier–Stokes equations are a set of partial differential equations that were developed by Claudio-Louis Navier [1] and George Gabriel Stokes [2] to describe the motion of a Newtonian fluid, which can be either liquid or gas. These equations are essential for modeling fluid behavior in fluid dynamics, and they are used in many mathematical physics applications. Unfortunately, the equations are nonlinear and thus difficult to solve analytically. To gain a better understanding of the nonlinearity of these equations, one can refer to [3]. For those who need background knowledge on the subject, [4–7]’s monographs provide useful information.

Analytical or exact solutions are invaluable in understanding physical phenomena, as they provide a simple explicit expression of the behavior in terms of well-defined functions. They are also essential for testing numerical solvers, ensuring accuracy and reliability of the solutions. Moreover, analytical solutions offer more insight into the problem than a numerical tabulation alone. [8] has provided an insightful assessment of the significance and importance of analytical solutions to partial differential equations.

A general overview of analytical solutions to the Navier–Stokes equations is given by [9–11]. In a broad sense, analytical solutions to the Navier–Stokes equations are divided into two classes. The first class involves solutions where the nonlinearity is weakened or completely removed from the solution structure [12].

Examples of this simplified analysis include [13,14] flows. The second class is the Beltrami class of solutions, which involve nonzero nonlinear terms; [15]. Two-dimensional solutions to the Navier–Stokes equation for incompressible flows were developed by [16], while unsteady analytical solutions involving all three Cartesian velocity components were presented by [17]. Recently, a triple-periodic fully three-dimensional analytical solution to the Navier–Stokes Equation for unsteady incompressible fluid flows was presented by [18], extending Ethier and Steinman’s work to a class of solutions for the velocity vector field in three dimensions.

Analytical solutions can be used to benchmark numerical Navier–Stokes solvers, as proposed in this paper. These solutions are extensible to higher dimensions, such as four or more, and can help identify and quantify discrepancies caused by numerical instabilities. Furthermore, they can provide insight into the underlying structure of physical systems, allowing for a deeper understanding of their behavior which can lead to further research and development in a variety of scientific disciplines. By exploring boundary conditions and turbulence, scientists can gain a better understanding of the physical world and develop solutions to complex problems. Additionally, higher dimensional analytical solutions are essential for developing robust numerical algorithms which can be used in a wide range of applications, such as those found in chemical engineering and biomedical engineering. Finally, these solutions can be used to stress-test Navier–Stokes solvers used to analyze the behavior of fluids in complex systems.

Antuono’s solution structure is essentially the same as that of [17], where the unsteady terms, $\frac{\partial \mathbf{v}}{\partial t}$, are equated to the viscous terms in the momentum equation. The velocity vector field \mathbf{v} and

E-mail address: michael.thambbynayagam@gmail.com.

the advective term $(\mathbf{v} \cdot \nabla) \mathbf{v}$ are represented through a stream function ψ ($\mathbf{v} = \nabla \times \psi$) and as the gradient of a scalar function respectively. These two equations are then decomposed into a linear equation for the stream function and a nonlinear equation for the pressure field. The linear equation for the stream function is solved analytically by separation of variables. Antuono describes the velocity vector field in a tours $\mathbb{T}^3 = [0, L]^3$ in two parts, characterized by positive and negative helicity respectively. The velocity components were normalized by a reference velocity v_r so that the average kinetic energy per unit of mass is $\left(\frac{v_r^2}{2}\right)$ at $t = 0$. Finally, the pressure field was obtained in terms of a reference pressure and reference density from the velocity field.

In a previous article [19], a method was presented to derive analytical solutions by rephrasing the Navier–Stokes equation into three distinct terms associated with linear viscous forces, inertial forces, and external forces applied to the fluid. This paper applies the method to derive a time evolution analytical solution for the velocity vector field and pressure that span the entire unbounded domain. The mathematical expressions, particularly equations (4.4)–(4.30) and (5.5)–(5.36), are tedious and exhaustively boring to derive, but they are straightforward once understood. The method presented in this paper is an effective way of deriving analytical solutions for velocity vector fields and pressure in unbounded domains.

2. The fundamental problem

In a space having an arbitrary number of dimensions, \mathbb{R}^n , the fundamental equations of momentum and mass conservation for incompressible viscous fluid flow fields are represented as follows:

$$\frac{\partial v_i}{\partial t} + g_i = \kappa \Delta v_i - \frac{1}{\rho} \frac{\partial p}{\partial x_i} + f_i \quad x \in \mathbb{R}^n, \quad t \geq 0 \quad (2.1)$$

where $v_i = v_i(x, t)$, $x \in \mathbb{R}^n$, $i = 1, 2, \dots, n$, is the solenoidal velocity vector field and $p = p(x, t)$ the pressure of the fluid.

$$g_i = g_i(x, t) = \sum_{j=1}^n v_j \frac{\partial v_i}{\partial x_j} \quad (2.2)$$

is the nonlinear inertial force, $f_i = f_i(x, t)$ are the components of an externally applied force, ρ is the constant density of the fluid, κ is the positive coefficient of kinematical viscosity and $\Delta = \sum_{i=1}^n \frac{\partial^2}{\partial x_i^2}$ is the Laplacian in the space variables.

The conservation of mass yields the solenoidal (incompressibility) condition

$$\operatorname{div} \mathbf{v} = \sum_{i=1}^n \frac{\partial v_i}{\partial x_i} = 0 \quad x \in \mathbb{R}^n, \quad t \geq 0 \quad (2.3)$$

Conservation law also implies that the energy dissipation of a viscous fluid is bounded by the initial kinetic energy. Therefore, if the externally applied force does no net work on the fluid, the kinetic energy of the solution should be finite. There exists a constant E such that

$$\int_{\mathbb{R}^n} |\mathbf{v}|^2 dx < E \quad t \geq 0 \quad (2.4)$$

The Navier–Stokes equation (2.1) must be solved forward in time $t \geq 0$, starting from an initial solenoidal velocity field

$$v_i(x, 0) = v_i^0 \quad x \in \mathbb{R}^n \quad (2.5)$$

with the pressure evolving in time to maintain the incompressibility constraint (2.3). The superscript 0 is used to denote the value of a function at time zero.

$$g_i(x, 0) = g_i^0 = \sum_{j=1}^n v_j^0 \frac{\partial v_i^0}{\partial x_j} \quad (2.6)$$

3. Rephrasing the Navier–Stokes equation:

$$\mathbb{R}^n = \{-\infty < x_i < \infty; i = 1, 2, \dots, n\}$$

In this section, in order to be perspicuous, we repeat the material from [19] relating to the rephrasing of the Navier–Stokes equation and the resulting *lemma*. Assuming that the divergence and the linear operator can be commuted, the pressure field may be formally obtained by taking the divergence of (2.1) as a solution of the Poisson equation, which is

$$\Delta p = \rho \sum_{i=1}^n \frac{\partial (f_i - g_i)}{\partial x_i} \quad (3.1)$$

Eq. (3.1) is called the pressure Poisson equation. In a paper by [20], the use of the pressure Poisson equation in solving the Navier–Stokes equation is discussed. It is important to note that while (2.1) and (2.3) lead to the pressure Poisson equation (3.1), the reverse does not always hold true; that is, (2.1) and (3.1) do not necessarily lead to (2.3). Therefore, when deriving solutions of the Navier–Stokes equations, it is essential to ensure that the velocity vector field remains solenoidal at all times, as defining pressure at the initial time independent of velocity would render the problem ill-posed.

The general solution of the Poisson equation (3.1) is given by

$$\begin{aligned} p(x, t) &= -\frac{\rho}{2\pi} \int_{\mathbb{R}^2} P(y, t) \ln \left(\frac{1}{\sqrt{P_n(x, y)}} \right) \prod_{j=1}^2 dy_j, \quad n = 2, \\ p(x, t) &= -\frac{\rho \Gamma(\frac{n}{2})}{2(n-2)\pi^{\frac{n}{2}}} \int_{\mathbb{R}^n} \frac{P(y, t)}{\{P_n(x, y)\}^{\frac{n-2}{2}}} \prod_{j=1}^n dy_j, \quad n \geq 3 \end{aligned} \quad (3.2)$$

where $\Gamma(z) = \int_0^\infty e^{-u} u^{z-1} du$ [$\Re z > 0$], is the Gamma function,

$$P(x, t) = \sum_{j=1}^n \frac{\partial (f_j - g_j)}{\partial x_j} \quad (3.3)$$

and

$$P_n(x, y) = \sum_{j=1}^n (x_j - y_j)^2 \quad (3.4)$$

Differentiating (3.2) with respect to x_i we obtain

$$\frac{\partial p}{\partial x_i} = \frac{\rho \Gamma(\frac{n}{2})}{2\pi^{\frac{n}{2}}} \int_{\mathbb{R}^n} \frac{(x_i - y_i) P(y, t)}{\{P_n(x, y)\}^{\frac{n}{2}}} \prod_{j=1}^n dy_j, \quad n \geq 2 \quad (3.5)$$

Substituting for $\frac{\partial p}{\partial x_i}$ in (2.1) the following can be formulated:

$$\begin{aligned} \frac{\partial v_i}{\partial t} &= \kappa \Delta v_i - \frac{\Gamma(\frac{n}{2})}{2\pi^{\frac{n}{2}}} \int_{\mathbb{R}^n} \frac{(x_i - y_i) P(y, t)}{\{P_n(x, y)\}^{\frac{n}{2}}} \prod_{j=1}^n dy_j + f_i - g_i, \\ n &\geq 2, \quad x \in \mathbb{R}^n, \quad t \geq 0 \end{aligned} \quad (3.6)$$

The difficulty in solving the system of equations (2.1)–(2.3) stems from the presence of the nonlinear term g_i . We therefore rephrase the Navier–Stokes equation (3.6) as:

$$\frac{\partial v_i}{\partial t} = \kappa \Delta v_i - \mathcal{U}_i + \mathcal{F}_i \quad x \in \mathbb{R}^n, \quad t \geq 0 \quad (3.7)$$

where

$$\begin{aligned} \mathcal{U}_i &= g_i - \frac{\Gamma(\frac{n}{2})}{2\pi^{\frac{n}{2}}} \int_{\mathbb{R}^n} \frac{(x_i - y_i) \sum_{k=1}^n \frac{\partial g_k(y, t)}{\partial y_k}}{\{P_n(x, y)\}^{\frac{n}{2}}} \prod_{j=1}^n dy_j, \\ x &\in \mathbb{R}^n, \quad t \geq 0 \end{aligned} \quad (3.8)$$

and

$$\mathcal{F}_i = f_i - \frac{\Gamma(\frac{n}{2})}{2\pi^{\frac{n}{2}}} \int_{\mathbb{R}^n} \frac{(x_i - w_i) \sum_{k=1}^n \frac{\partial f_k(w,t)}{\partial w_k}}{\{\mathcal{P}_n(x, w)\}^{\frac{n}{2}}} \prod_{j=1}^n dw_j, \\ x \in \mathbb{R}^n, t \geq 0 \quad (3.9)$$

$\mathcal{U}_i = \mathcal{U}_i(x, t)$ and $\mathcal{F}_i = \mathcal{F}_i(x, t)$. The three terms on the right hand side of (3.7), $\kappa \Delta v_i$, \mathcal{U}_i and \mathcal{F}_i are associated, respectively, with the linear viscous force, the nonlinear inertial force and the externally applied force acting on the fluid.

A posteriori we state the following lemma: If $\mathcal{U}_i \equiv 0$, that is

$$g_i = \frac{\Gamma(\frac{n}{2})}{2\pi^{\frac{n}{2}}} \int_{\mathbb{R}^n} \frac{(x_i - y_i) \sum_{k=1}^n \frac{\partial g_k(y,t)}{\partial y_k}}{\{\mathcal{P}_n(x, y)\}^{\frac{n}{2}}} \prod_{j=1}^n dy_j, \quad (3.10)$$

then the solution of the Navier–Stokes equation (2.1) is determined as a solution of the non-homogeneous diffusion equation [21,22]:

$$v_i(x, t) = \frac{1}{(2\sqrt{\pi\kappa t})^n} \int_{\mathbb{R}^n} v_i^0(y) e^{-\sum_{k=1}^n \frac{(x_k - y_k)^2}{4\kappa t}} \prod_{j=1}^n dy_j + \\ + \frac{1}{(2\sqrt{\pi\kappa})^n} \int_{\mathbb{R}^n} \int_0^t \frac{\mathcal{F}_i(y, \tau) e^{-\sum_{k=1}^n \frac{(x_k - y_k)^2}{4\kappa(t-\tau)}}}{(t-\tau)^{\frac{n}{2}}} d\tau \prod_{j=1}^n dy_j \quad (3.11)$$

belong to the class of Beltrami flows. If the externally applied force on the fluid f_i is set to zero, then, the second term on the right hand side of Eq. (3.11) vanishes and the solution of the Navier–Stokes equation (2.1) reduces to that of the Cauchy diffusion equation:

$$v_i(x, t) = \frac{1}{(2\sqrt{\pi\kappa t})^n} \int_{\mathbb{R}^n} v_i^0(y) e^{-\sum_{k=1}^n \frac{(x_k - y_k)^2}{4\kappa t}} \prod_{j=1}^n dy_j \quad (3.12)$$

We may express (3.5) as follows if (3.10) is satisfied for an n -tuple-periodic form of the solenoidal velocity vector field:

$$\frac{\partial p}{\partial x_i} = -\rho g_i = -\rho g_i^0 e^{-2n\alpha^2 \kappa t} \quad (3.13)$$

Where α is the wavelength. Pressure is obtained from straightforward integration of (3.13).

Appendix A provides two known solutions, the two-dimensional double-periodic solution of [16] and the unsteady unit periodic three-dimensional solution of [23] derived by [19], that satisfy the integral equation (3.10).

4. A solution in $\mathbb{R}^3 = \{-\infty < x_i < \infty; i = 1, 2, 3\}$

At time zero, we consider the solenoidal velocity vector field $v_i^0(x)$ of a triple-periodic form

$$\frac{v_1^0}{v_r} = \sin(\alpha x_1 + \xi_1) \cos(\alpha x_2 + \xi_2) \sin(\alpha x_3 + \xi_3) - \\ - \sin(\alpha x_1 + \xi_2) \cos(\alpha x_3 + \xi_1) \sin(\alpha x_2 + \xi_3) \quad (4.1)$$

$$\frac{v_2^0}{v_r} = \sin(\alpha x_2 + \xi_1) \cos(\alpha x_3 + \xi_2) \sin(\alpha x_1 + \xi_3) - \\ - \sin(\alpha x_2 + \xi_3) \cos(\alpha x_1 + \xi_1) \sin(\alpha x_3 + \xi_2) \quad (4.2)$$

$$\frac{v_3^0}{v_r} = \sin(\alpha x_3 + \xi_1) \cos(\alpha x_1 + \xi_2) \sin(\alpha x_2 + \xi_3) - \\ - \sin(\alpha x_3 + \xi_2) \cos(\alpha x_2 + \xi_1) \sin(\alpha x_1 + \xi_3) \quad (4.3)$$

where v_r is the reference velocity, ξ_1 , ξ_2 , and ξ_3 are phase angles. The externally applied force on the fluid f_i is set to zero. Eq. (3.10) may be written as follows at time zero in \mathbb{R}^3 :

$$g_i^0 = \frac{1}{4\pi} \int_{\mathbb{R}^3} \frac{(x_i - y_i) \mathcal{G}^0(y_1, y_2, y_3)}{\{\mathcal{P}_3(x, y)\}^{\frac{3}{2}}} \prod_{j=1}^3 dy_j \quad i = 1, 2, 3 \quad (4.4)$$

where $\mathcal{G}^0(y_1, y_2, y_3) = \sum_{k=1}^3 \frac{\partial g_k^0(y,t)}{\partial y_k}$. Changing the variable of integration, $u_i = x_i - y_i$, gives

$$g_i^0 = \frac{1}{4\pi} \int_{\mathbb{R}^3} \frac{u_i \mathcal{G}^0(x_1 - u_1, x_2 - u_2, x_3 - u_3)}{[u_1^2 + u_2^2 + u_3^2]^{\frac{3}{2}}} \prod_{j=1}^3 du_j \quad i = 1, 2, 3 \quad (4.5)$$

It becomes apparent on closer examination of (4.5) that any term in g_i^0 , derived from (2.6), that is not a function of x_i cannot be recovered by performing the integrals on the righthand side of (4.5); as a result of the integral identity $\int_{-\infty}^{\infty} \frac{u}{u^2 + \beta} du = 0$, β a constant, these terms vanish entirely. As a consequence, it is a prerequisite for the integral equation (4.5) to hold that all of the terms that are not functions of x_i on the righthand side of (2.6) must sum to zero. We therefore divide g_i^0 into two parts as follows:

$$g_i^0 = \mathcal{V}_i^0 + \mathcal{W}_i^0 \quad i = 1, 2, 3 \quad (4.6)$$

\mathcal{V}_i^0 is the sum of all terms that are not functions of x_i , and \mathcal{W}_i^0 is the sum of all remaining terms. For the integral equation (4.5) to hold all terms in \mathcal{V}_i^0 must sum to zero. By substituting v_1^0 , v_2^0 and v_3^0 into (2.6) and separating the terms into \mathcal{V}_i^0 and \mathcal{W}_i^0 we get the following expressions:

$$\begin{aligned} g_1^0(x_1, x_2, x_3; \xi_1, \xi_2, \xi_3) \\ = \mathcal{V}_1^0(x_2, x_3; \xi_1, \xi_2, \xi_3) + \mathcal{W}_1^0(x_1, x_2, x_3; \xi_1, \xi_2, \xi_3) \end{aligned} \quad (4.7)$$

$$\begin{aligned} g_2^0(x_2, x_3, x_1; \xi_1, \xi_2, \xi_3) \\ = \mathcal{V}_2^0(x_3, x_1; \xi_1, \xi_2, \xi_3) + \mathcal{W}_2(x_2, x_3, x_1; \xi_1, \xi_2, \xi_3) \end{aligned} \quad (4.8)$$

$$\begin{aligned} g_3^0(x_3, x_1, x_2; \xi_1, \xi_2, \xi_3) \\ = \mathcal{V}_3^0(x_1, x_2; \xi_1, \xi_2, \xi_3) + \mathcal{W}_3(x_3, x_1, x_2; \xi_1, \xi_2, \xi_3) \end{aligned} \quad (4.9)$$

where

$$\begin{aligned} \mathcal{V}_1^0(x_2, x_3; \xi_1, \xi_2, \xi_3) \\ = \frac{v_r^2}{\alpha} \cos(\xi_1 - \xi_3) \sin(\xi_2 - \xi_3) \cos(2\alpha x_2 + \xi_2 + \xi_1) - \\ - \frac{\alpha}{4} \cos(\xi_1 - \xi_3) \cos(\xi_1 - \xi_2) \sin(2\alpha x_3 + \xi_2 + \xi_3) - \\ - \frac{\alpha}{4} \cos(\xi_3 - \xi_2) \cos(\xi_1 - \xi_2) \sin(2\alpha x_2 + \xi_3 + \xi_1) - \\ - \frac{\alpha}{4} \cos(\xi_3 - \xi_2) \sin(\xi_1 - \xi_3) \cos(2\alpha x_3 + \xi_1 + \xi_2) + \\ + \frac{\alpha}{4} \sin(\xi_2 - \xi_1) \sin(\xi_3 - \xi_1) \sin(2\alpha x_2 + \xi_2 + \xi_3) + \\ + \frac{\alpha}{4} \sin(\xi_2 - \xi_1) \sin(\xi_2 - \xi_3) \sin(2\alpha x_3 + \xi_3 + \xi_1) \end{aligned} \quad (4.10)$$

$$\mathcal{V}_2^0(x_3, x_1; \xi_1, \xi_2, \xi_3) = v_r^2 \mathcal{V}_1^0(x_3, x_1; \xi_1, \xi_2, \xi_3) \quad (4.11)$$

$$\mathcal{V}_3^0(x_1, x_2; \xi_1, \xi_2, \xi_3) = v_r^2 \mathcal{V}_2^0(x_1, x_2; \xi_1, \xi_2, \xi_3) \quad (4.12)$$

$$\begin{aligned} \mathcal{W}_1^0(x_1, x_2, x_3; \xi_1, \xi_2, \xi_3) \\ = \frac{v_r^2}{\alpha} \mathcal{W}_1^0(x_1, x_2, x_3; \xi_1, \xi_2, \xi_3) \end{aligned}$$

$$\begin{aligned}
&= \frac{\alpha}{4} \sin(2\alpha x_1 + 2\xi_1) - \frac{\alpha}{4} \sin(2\alpha x_1 + 2\xi_1) \cos(2\alpha x_3 + 2\xi_3) + \\
&+ \frac{\alpha}{4} \sin(2\alpha x_1 + 2\xi_2) - \frac{\alpha}{4} \sin(2\alpha x_1 + 2\xi_2) \cos(2\alpha x_2 + 2\xi_3) - \\
&- \frac{\alpha}{2} \sin(\xi_3 - \xi_2) \sin(\xi_3 - \xi_1) \sin(2\alpha x_1 + \xi_1 + \xi_2) - \\
&- \frac{\alpha}{4} \sin(\xi_3 - \xi_1) \sin(2\alpha x_1 + \xi_1 + \xi_2) \sin(2\alpha x_2 + \xi_2 + \xi_3) - \\
&- \frac{\alpha}{4} \sin(\xi_3 - \xi_2) \sin(2\alpha x_1 + \xi_1 + \xi_2) \sin(2\alpha x_3 + \xi_3 + \xi_1) + \\
&+ \frac{\alpha}{4} \sin(\xi_2 - \xi_3) \cos(2\alpha x_1 + \xi_3 + \xi_1) \cos(2\alpha x_2 + \xi_1 + \xi_2) + \\
&+ \frac{\alpha}{4} \cos(\xi_1 - \xi_2) \cos(2\alpha x_1 + \xi_3 + \xi_1) \sin(2\alpha x_3 + \xi_2 + \xi_3) - \\
&+ \frac{\alpha}{4} \cos(\xi_1 - \xi_2) \cos(2\alpha x_1 + \xi_2 + \xi_3) \sin(2\alpha x_2 + \xi_3 + \xi_1) + \\
&+ \frac{\alpha}{4} \sin(\xi_1 - \xi_3) \cos(2\alpha x_1 + \xi_2 + \xi_3) \cos(2\alpha x_3 + \xi_1 + \xi_2)
\end{aligned} \tag{4.13}$$

$$\mathcal{W}_2^0(x_2, x_3, x_1; \xi_1, \xi_2, \xi_3) = v_r^2 \mathcal{W}_1^0(x_2, x_3, x_1; \xi_1, \xi_2, \xi_3) \tag{4.14}$$

$$\mathcal{W}_3^0(x_3, x_1, x_2; \xi_1, \xi_2, \xi_3) = v_r^2 \mathcal{W}_2^0(x_3, x_1, x_2; \xi_1, \xi_2, \xi_3) \tag{4.15}$$

If (4.5) is to hold, it is imperative that the following prerequisites are met:

$$\mathcal{V}_1^0(x_2, x_3; \xi_1, \xi_2, \xi_3) = 0 \quad \forall -\infty < x_2 < \infty \text{ and } -\infty < x_3 < \infty \tag{4.16}$$

$$\mathcal{V}_2^0(x_3, x_1; \xi_1, \xi_2, \xi_3) = 0 \quad \forall -\infty < x_3 < \infty \text{ and } -\infty < x_1 < \infty \tag{4.17}$$

$$\mathcal{V}_3^0(x_1, x_2; \xi_1, \xi_2, \xi_3) = 0 \quad \forall -\infty < x_1 < \infty \text{ and } -\infty < x_2 < \infty \tag{4.18}$$

It is therefore necessary to choose the phase angles ξ_1 , ξ_2 and ξ_3 such that they satisfy the prerequisites (4.16), (4.17) and (4.18). In this particular case, as can be seen by substituting into (4.10), (4.11) and (4.12), the phase angles $\xi_1 = -\frac{\pi}{3}$, $\xi_2 = \frac{\pi}{3}$, and $\xi_3 = \frac{\pi}{2}$ satisfy (4.16), (4.17) and (4.18).

$$\begin{aligned}
\frac{\mathcal{V}_1^0(x_2, x_3; -\frac{\pi}{3}, \frac{\pi}{3}, \frac{\pi}{2})}{v_r^2} &= -\frac{\alpha\sqrt{3}}{16} \cos(2\alpha x_2) + \frac{3\alpha}{32} \sin(2\alpha x_3) \\
&\quad - \frac{\alpha\sqrt{3}}{32} \cos(2\alpha x_3) + \\
&\quad + \frac{3\alpha}{32} \sin(2\alpha x_2) + \frac{\alpha\sqrt{3}}{32} \cos(2\alpha x_2) \\
&\quad + \frac{\alpha\sqrt{3}}{16} \cos(2\alpha x_3) + \\
&\quad - \frac{3\alpha}{32} \sin(2\alpha x_2) + \frac{\alpha\sqrt{3}}{32} \cos(2\alpha x_2) - \\
&\quad - \frac{3\alpha}{32} \sin(2\alpha x_3) - \frac{\alpha\sqrt{3}}{32} \cos(2\alpha x_3) \\
&= 0
\end{aligned} \tag{4.19}$$

$$\frac{\mathcal{V}_2^0(x_3, x_1; -\frac{\pi}{3}, \frac{\pi}{3}, \frac{\pi}{2})}{v_r^2} = 0 \tag{4.20}$$

$$\frac{\mathcal{V}_3^0(x_1, x_2; -\frac{\pi}{3}, \frac{\pi}{3}, \frac{\pi}{2})}{v_r^2} = 0 \tag{4.21}$$

In light of the fact that \mathcal{G}_i^0 equals \mathcal{W}_i^0 , the following expressions are derived for \mathcal{G}_i^0 and $\mathcal{G}^0(x_1, x_2, x_3) = \sum_{k=1}^3 \frac{\partial \mathcal{W}_k^0}{\partial x_k}$:

$$\begin{aligned}
\frac{\mathcal{G}_1^0(x_1, x_2, x_3)}{v_r^2} &= -\frac{3\alpha}{8} \sin(2\alpha x_1) - \frac{3\alpha}{32} \sin(2\alpha x_1) \cos(2\alpha x_2) \\
&\quad - \frac{3\alpha}{32} \sin(2\alpha x_1) \cos(2\alpha x_3) - \\
&\quad - \frac{3\sqrt{3}\alpha}{32} \cos(2\alpha x_1) \cos(2\alpha x_3) \\
&\quad + \frac{3\sqrt{3}\alpha}{32} \cos(2\alpha x_1) \cos(2\alpha x_2) + \\
&\quad + \frac{3\sqrt{3}\alpha}{32} \sin(2\alpha x_1) \sin(2\alpha x_2) \\
&\quad - \frac{3\sqrt{3}\alpha}{32} \sin(2\alpha x_1) \sin(2\alpha x_3) + \\
&\quad + \frac{3\alpha}{32} \cos(2\alpha x_1) \sin(2\alpha x_3) \\
&\quad + \frac{3\alpha}{32} \cos(2\alpha x_1) \sin(2\alpha x_2)
\end{aligned} \tag{4.22}$$

$$\mathcal{G}_2^0(x_2, x_3, x_1) = v_r^2 \mathcal{G}_1^0(x_2, x_3, x_1) \tag{4.23}$$

$$\mathcal{G}_3^0(x_3, x_1, x_2) = v_r^2 \mathcal{G}_2^0(x_3, x_1, x_2) \tag{4.24}$$

$$\begin{aligned}
\frac{\mathcal{G}^0(x_1, x_2, x_3)}{v_r^2} &= -\frac{3\alpha^2}{4} \cos(2\alpha x_1) - \frac{3\alpha^2}{4} \cos(2\alpha x_2) \\
&\quad - \frac{3\alpha^2}{4} \cos(2\alpha x_3) - \\
&\quad - \frac{3\alpha^2}{8} \cos(2\alpha x_1) \cos(2\alpha x_2) \\
&\quad - \frac{3\alpha^2}{8} \cos(2\alpha x_1) \cos(2\alpha x_3) + \\
&\quad + \frac{3\sqrt{3}\alpha^2}{8} \sin(2\alpha x_1) \cos(2\alpha x_3) \\
&\quad - \frac{3\sqrt{3}\alpha^2}{8} \sin(2\alpha x_1) \cos(2\alpha x_2) + \\
&\quad + \frac{3\sqrt{3}\alpha^2}{8} \cos(2\alpha x_1) \sin(2\alpha x_2) \\
&\quad - \frac{3\sqrt{3}\alpha^2}{8} \cos(2\alpha x_1) \sin(2\alpha x_3) - \\
&\quad - \frac{3\alpha^2}{8} \sin(2\alpha x_1) \sin(2\alpha x_3) \\
&\quad - \frac{3\alpha^2}{8} \sin(2\alpha x_1) \sin(2\alpha x_2) - \\
&\quad - \frac{3\alpha^2}{8} \cos(2\alpha x_2) \cos(2\alpha x_3) \\
&\quad - \frac{3\sqrt{3}\alpha^2}{8} \sin(2\alpha x_2) \cos(2\alpha x_3) + \\
&\quad + \frac{3\sqrt{3}\alpha^2}{8} \cos(2\alpha x_2) \sin(2\alpha x_3) \\
&\quad - \frac{3\alpha^2}{8} \sin(2\alpha x_2) \sin(2\alpha x_3)
\end{aligned} \tag{4.25}$$

By substituting $\mathcal{G}^0(x_1, x_2, x_3)$ from (4.25) into (4.5) and evaluating the definite integrals term by term, we can see that the results equal \mathcal{G}_i^0 derived from (2.6); that is, $\mathcal{U}_i^0 \equiv 0$, $i = 1, 2, 3$. We have used the integral identities (B.4)–(B.8) given in Appendix B to perform the integrations.

Substituting for the initial condition v_i^0 , $i = 1, 2, 3$ from (4.1), (4.2) and (4.3) into (3.12) with phase angles ξ_1 , ξ_2 and ξ_3 set,

respectively, to $-\frac{\pi}{3}$, $\frac{\pi}{3}$, and $\frac{\pi}{2}$ and performing the integrations, we arrive at the solution of the Navier–Stokes equation (2.1) in three dimensions:

$$\begin{aligned} v_1 &= v_r \left[\sin\left(\alpha x_1 - \frac{\pi}{3}\right) \cos\left(\alpha x_2 + \frac{\pi}{3}\right) \sin\left(\alpha x_3 + \frac{\pi}{2}\right) - \right. \\ &\quad \left. - \sin\left(\alpha x_1 + \frac{\pi}{3}\right) \cos\left(\alpha x_3 - \frac{\pi}{3}\right) \sin\left(\alpha x_2 + \frac{\pi}{2}\right) \right] e^{-3\alpha^2 kt} \end{aligned} \quad (4.26)$$

$$\begin{aligned} v_2 &= v_r \left[\sin\left(\alpha x_2 - \frac{\pi}{3}\right) \cos\left(\alpha x_3 + \frac{\pi}{3}\right) \sin\left(\alpha x_1 + \frac{\pi}{2}\right) - \right. \\ &\quad \left. - \sin\left(\alpha x_2 + \frac{\pi}{3}\right) \cos\left(\alpha x_1 - \frac{\pi}{3}\right) \sin\left(\alpha x_3 + \frac{\pi}{2}\right) \right] e^{-3\alpha^2 kt} \end{aligned} \quad (4.27)$$

$$\begin{aligned} v_3 &= v_r \left[\sin\left(\alpha x_3 - \frac{\pi}{3}\right) \cos\left(\alpha x_1 + \frac{\pi}{3}\right) \sin\left(\alpha x_2 + \frac{\pi}{2}\right) - \right. \\ &\quad \left. - \sin\left(\alpha x_3 + \frac{\pi}{3}\right) \cos\left(\alpha x_2 - \frac{\pi}{3}\right) \sin\left(\alpha x_1 + \frac{\pi}{2}\right) \right] e^{-3\alpha^2 kt} \end{aligned} \quad (4.28)$$

We have used the integral identities (B.1)–(B.3) given in Appendix B to perform the integrations.

Pressure is obtained from the solution of the Poisson equation (3.2). Because (3.10) is satisfied, we can express (3.5) as follows:

$$\frac{\partial p}{\partial x_i} = -\rho g_i = -\rho g_i^0 e^{-6\alpha^2 kt} \quad i = 1, 2, 3 \quad (4.29)$$

This leads to straightforward integration for pressure:

$$\begin{aligned} p &= -\frac{3\rho v_r^2}{16} [\cos(2\alpha x_1) + \cos(2\alpha x_2) + \cos(2\alpha x_3)] e^{-6\alpha^2 kt} - \\ &\quad - \frac{3\rho v_r^2}{64} [\cos(2\alpha x_1 - 2\alpha x_2) + \cos(2\alpha x_3 - 2\alpha x_1) \\ &\quad + \cos(2\alpha x_3 - 2\alpha x_2)] e^{-6\alpha^2 kt} - \\ &\quad - \frac{3\sqrt{3}\rho v_r^2}{64} [\sin(2\alpha x_1 - 2\alpha x_2) + \sin(2\alpha x_3 - 2\alpha x_1) \\ &\quad + \sin(2\alpha x_2 - 2\alpha x_3)] e^{-6\alpha^2 kt} \end{aligned} \quad (4.30)$$

5. A solution in $\mathbb{R}^4 = \{-\infty < x_i < \infty; i = 1, 2, 3, 4\}$

At time zero, we consider the solenoidal velocity vector field $v_i^0(x)$ of a quadruple-periodic form

$$\begin{aligned} \frac{v_1^0}{v_r} &= \sin(\alpha x_1 + \xi_1) \cos(\alpha x_2 + \xi_2) \sin(\alpha x_3 + \xi_3) \cos(\alpha x_4 + \xi_4) - \\ &\quad - \sin(\alpha x_1 + \xi_2) \sin(\alpha x_2 + \xi_3) \cos(\alpha x_3 + \xi_4) \cos(\alpha x_4 + \xi_1) \end{aligned} \quad (5.1)$$

$$\begin{aligned} \frac{v_2^0}{v_r} &= \sin(\alpha x_2 + \xi_1) \cos(\alpha x_3 + \xi_2) \sin(\alpha x_4 + \xi_3) \cos(\alpha x_1 + \xi_4) - \\ &\quad - \sin(\alpha x_2 + \xi_2) \sin(\alpha x_3 + \xi_3) \cos(\alpha x_4 + \xi_4) \cos(\alpha x_1 + \xi_1) \end{aligned} \quad (5.2)$$

$$\begin{aligned} \frac{v_3^0}{v_r} &= \sin(\alpha x_3 + \xi_1) \cos(\alpha x_4 + \xi_2) \sin(\alpha x_1 + \xi_3) \cos(\alpha x_2 + \xi_4) - \\ &\quad - \sin(\alpha x_3 + \xi_2) \sin(\alpha x_4 + \xi_3) \cos(\alpha x_1 + \xi_4) \cos(\alpha x_2 + \xi_1) \end{aligned} \quad (5.3)$$

$$\begin{aligned} \frac{v_4^0}{v_r} &= \sin(\alpha x_4 + \xi_1) \cos(\alpha x_1 + \xi_2) \sin(\alpha x_2 + \xi_3) \cos(\alpha x_3 + \xi_4) - \\ &\quad - \sin(\alpha x_4 + \xi_2) \sin(\alpha x_1 + \xi_3) \cos(\alpha x_3 + \xi_1) \cos(\alpha x_2 + \xi_4) \end{aligned} \quad (5.4)$$

where ξ_1, ξ_2, ξ_3 and ξ_4 are phase angles. The externally applied force on the fluid f_i is set to zero. Eq. (3.10) may be written as

follows at time zero in \mathbb{R}^4 :

$$g_i^0 = \frac{1}{2\pi^2} \int_{\mathbb{R}^4} \frac{(x_i - y_i) \mathcal{G}^0(y_1, y_2, y_3, y_4)}{\{\mathcal{P}_4(x, y)\}^2} \prod_{j=1}^4 dy_j \quad i = 1, 2, 3, 4 \quad (5.5)$$

where $\mathcal{G}^0(y_1, y_2, y_3, y_4) = \sum_{k=1}^4 \frac{\partial g_k^0(y, t)}{\partial y_k}$. Changing the variable of integration, $u_i = x_i - y_i$, gives

$$g_i^0 = \frac{1}{2\pi^2} \int_{\mathbb{R}^4} \frac{u_i \mathcal{G}^0(x_1 - u_1, x_2 - u_2, x_3 - u_3, x_4 - u_4)}{[u_1^2 + u_2^2 + u_3^2 + u_4^2]^2} \prod_{j=1}^4 du_j \quad i = 1, 2, 3, 4 \quad (5.6)$$

Following the method of the previous case, we divide g_i^0 into two parts:

$$g_i^0 = \mathcal{V}_i^0 + \mathcal{W}_i^0 \quad i = 1, 2, 3, 4 \quad (5.7)$$

By substituting v_1^0, v_2^0, v_3^0 and v_4^0 into (2.6) and separating the terms into \mathcal{V}_i^0 and \mathcal{W}_i^0 we get the following expressions:

$$\begin{aligned} \mathcal{G}_1^0(x_1, x_2, x_3, x_4; \xi_1, \xi_2, \xi_3, \xi_4) &= \mathcal{V}_1^0(x_2, x_3, x_4; \xi_1, \xi_2, \xi_3, \xi_4) + \\ &\quad + \mathcal{W}_1^0(x_1, x_2, x_3, x_4; \xi_1, \xi_2, \xi_3, \xi_4) \end{aligned} \quad (5.8)$$

$$\begin{aligned} \mathcal{G}_2^0(x_2, x_3, x_4, x_1; \xi_1, \xi_2, \xi_3, \xi_4) &= \mathcal{V}_2^0(x_3, x_4, x_1; \xi_1, \xi_2, \xi_3, \xi_4) + \\ &\quad + \mathcal{W}_2^0(x_2, x_3, x_4, x_1; \xi_1, \xi_2, \xi_3, \xi_4) \end{aligned} \quad (5.9)$$

$$\begin{aligned} \mathcal{G}_3^0(x_3, x_4, x_1, x_2; \xi_1, \xi_2, \xi_3, \xi_4) &= \mathcal{V}_3^0(x_4, x_1, x_2; \xi_1, \xi_2, \xi_3, \xi_4) + \\ &\quad + \mathcal{W}_3^0(x_3, x_4, x_1, x_2; \xi_1, \xi_2, \xi_3, \xi_4) \end{aligned} \quad (5.10)$$

$$\begin{aligned} \mathcal{G}_4^0(x_4, x_1, x_2, x_3; \xi_1, \xi_2, \xi_3, \xi_4) &= \mathcal{V}_4^0(x_1, x_2, x_3; \xi_1, \xi_2, \xi_3, \xi_4) + \\ &\quad + \mathcal{W}_4^0(x_4, x_1, x_2, x_3; \xi_1, \xi_2, \xi_3, \xi_4) \end{aligned} \quad (5.11)$$

The expressions for $\frac{\mathcal{V}_1^0(x_2, x_3, x_4; \xi_1, \xi_2, \xi_3, \xi_4)}{v_r^2}$ and $\frac{\mathcal{W}_1^0(x_1, x_2, x_3, x_4; \xi_1, \xi_2, \xi_3, \xi_4)}{v_r^2}$ are given by (C.1) and (C.2) respectively in Appendix C.

$$\mathcal{V}_2^0(x_3, x_4, x_1; \xi_1, \xi_2, \xi_3, \xi_4) = v_r^2 \mathcal{V}_1^0(x_3, x_4, x_1; \xi_1, \xi_2, \xi_3, \xi_4) \quad (5.12)$$

$$\mathcal{V}_3^0(x_4, x_1, x_2; \xi_1, \xi_2, \xi_3, \xi_4) = v_r^2 \mathcal{V}_2^0(x_4, x_1, x_2; \xi_1, \xi_2, \xi_3, \xi_4) \quad (5.13)$$

$$\mathcal{V}_4^0(x_1, x_2, x_3; \xi_1, \xi_2, \xi_3, \xi_4) = v_r^2 \mathcal{V}_3^0(x_1, x_2, x_3; \xi_1, \xi_2, \xi_3, \xi_4) \quad (5.14)$$

$$\mathcal{W}_2^0(x_2, x_3, x_4, x_1; \xi_1, \xi_2, \xi_3, \xi_4) = v_r^2 \mathcal{W}_1^0(x_2, x_3, x_4, x_1; \xi_1, \xi_2, \xi_3, \xi_4) \quad (5.15)$$

$$\mathcal{W}_3^0(x_3, x_4, x_1, x_2; \xi_1, \xi_2, \xi_3, \xi_4) = v_r^2 \mathcal{W}_2^0(x_3, x_4, x_1, x_2; \xi_1, \xi_2, \xi_3, \xi_4) \quad (5.16)$$

$$\mathcal{W}_4^0(x_4, x_1, x_2, x_3; \xi_1, \xi_2, \xi_3, \xi_4) = v_r^2 \mathcal{W}_3^0(x_4, x_1, x_2, x_3; \xi_1, \xi_2, \xi_3, \xi_4) \quad (5.17)$$

If (5.6) is to hold the following prerequisites must be met:

$$\mathcal{V}_1^0(x_2, x_3, x_4; \xi_1, \xi_2, \xi_3, \xi_4) = 0,$$

The technique presented in this paper is a straightforward and direct method to derive solutions of the velocity and pressure fields for the Navier–Stokes flow problem. We have demonstrated its efficacy by applying it to reproduce the double-periodic solution of [16], the unit-periodic solution of [23], and the triple-periodic solution of [18]. In addition, we have also derived a new quadruple-periodic form of the solution in four dimensions. The method is easy to master and can almost be reduced to a ‘drill’.

Declaration of competing interest

The authors declare that they have no known competing financial interests or personal relationships that could have appeared to influence the work reported in this paper.

Data availability

No data was used for the research described in the article.

Appendix A. Derivations of two known solutions [16,23] satisfying Eq. (3.10) presented from [19]

A.1. The Taylor solution in $\mathbb{R}^2 = \{-\infty < x_i < \infty; i = 1, 2\}$

A two-dimensional solenoidal velocity vector field of a double-periodic form $v_i^0(x)$ is considered at time zero:

$$v_1^0 = v_r \sin(\pi x_1) \cos(\pi x_2) \quad (\text{A.1})$$

$$v_2^0 = -v_r \cos(\pi x_1) \sin(\pi x_2) \quad (\text{A.2})$$

The externally applied force on the fluid f_i is set to zero. At time zero in \mathbb{R}^2 , (3.10) may be written as follows:

$$g_i^0 = \frac{1}{2\pi} \int_{\mathbb{R}^2} \frac{(x_i - y_i) \sum_{k=1}^2 \mathcal{G}^0(y_1, y_2)}{\mathcal{P}_2(x, y)} \prod_{j=1}^2 dy_j \quad i = 1, 2 \quad (\text{A.3})$$

Where $g_i^0 = \sum_{j=1}^2 v_j^0 \frac{\partial v_i^0}{\partial x_j}$ and $\mathcal{G}^0(y_1, y_2) = \sum_{k=1}^2 \frac{\partial g_k^0(y, t)}{\partial y_k}$. Changing the variable of integration, $u_i = x_i - y_i$ and performing the integrations we obtain

$$g_i^0 = \frac{1}{2\pi} \int_{\mathbb{R}^2} \frac{u_i \mathcal{G}^0(x_1 - u_1, x_2 - u_2)}{[u_1^2 + u_2^2]^{\frac{3}{2}}} \prod_{j=1}^2 du_j = \frac{\pi}{2} \sin(2\pi x_i) \quad i = 1, 2 \quad (\text{A.4})$$

resulting in $u_i(x, t) \equiv 0$. $v(x, t)$ is obtained from (3.12):

$$\frac{v_1}{v_r} = \sin(\pi x_1) \cos(\pi x_2) e^{-2\pi^2 \kappa t} \quad (\text{A.5})$$

$$\frac{v_2}{v_r} = -\cos(\pi x_1) \sin(\pi x_2) e^{-2\pi^2 \kappa t} \quad (\text{A.6})$$

We have used the integral identities (B.1)–(B.3) given in Appendix B to perform the integrations. The pressure $p(x, t)$ is obtained by integrating (3.13):

$$p = \frac{\rho v_r^2 e^{-4\pi^2 \kappa t}}{4} [\cos(2\pi x_1) + \cos(2\pi x_2)] \quad (\text{A.7})$$

A.2. Arnold–Beltrami–Childress (ABC) flows in $\mathbb{R}^3 = \{-\infty < x_i < \infty; i = 1, 2, 3\}$

A three-dimensional solenoidal velocity vector field of a unit-periodic form $v_i^0(x)$ is considered at time zero:

$$\frac{v_1^{(0)}}{v_r} = a \sin \pi x_3 - c \cos \pi x_2 \quad (\text{A.8})$$

$$\frac{v_2^{(0)}}{v_r} = b \sin \pi x_1 - a \cos \pi x_3 \quad (\text{A.9})$$

$$\frac{v_3^{(0)}}{v_r} = c \sin \pi x_2 - b \cos \pi x_1 \quad (\text{A.10})$$

Where a, b and c are real constants. The externally applied force on the fluid f_i is set to zero. At time zero in \mathbb{R}^3 , (3.10) may be written as follows

$$g_i^0 = \frac{1}{4\pi} \int_{\mathbb{R}^3} \frac{(x_i - y_i) \mathcal{G}^0(y_1, y_2, y_3)}{\{\mathcal{P}_3(x, y)\}^{\frac{3}{2}}} \prod_{j=1}^3 dy_j \quad i = 1, 2, 3 \quad (\text{A.11})$$

Where $g_i^0 = \sum_{j=1}^3 v_j^0 \frac{\partial v_i^0}{\partial x_j}$ and $\mathcal{G}^0(y_1, y_2, y_3) = \sum_{k=1}^3 \frac{\partial g_k^0(y, t)}{\partial y_k}$. Changing the variable of integration, $u_i = x_i - y_i$ and performing the integrations we obtain

$$\begin{aligned} g_1^{(0)} &= \frac{1}{4\pi} \int_{\mathbb{R}^3} \frac{u_1 \mathcal{G}^0(x_1 - u_1, x_2 - u_2, x_3 - u_3)}{[u_1^2 + u_2^2 + u_3^2]^{\frac{3}{2}}} \prod_{j=1}^3 du_j \\ &= \pi \{bc \sin(\pi x_1) \sin(\pi x_2) - ab \cos(\pi x_1) \cos(\pi x_3)\} \end{aligned} \quad (\text{A.12})$$

$$\begin{aligned} g_2^{(0)} &= \frac{1}{4\pi} \int_{\mathbb{R}^3} \frac{u_2 \mathcal{G}^0(x_1 - u_1, x_2 - u_2, x_3 - u_3)}{[u_1^2 + u_2^2 + u_3^2]^{\frac{3}{2}}} \prod_{j=1}^3 du_j \\ &= \pi \{ac \sin(\pi x_2) \sin(\pi x_3) - bc \cos(\pi x_1) \cos(\pi x_2)\} \end{aligned} \quad (\text{A.13})$$

$$\begin{aligned} g_3^{(0)} &= \frac{1}{4\pi} \int_{\mathbb{R}^3} \frac{u_3 \mathcal{G}^0(x_1 - u_1, x_2 - u_2, x_3 - u_3)}{[u_1^2 + u_2^2 + u_3^2]^{\frac{3}{2}}} \prod_{j=1}^3 du_j \\ &= \pi \{ab \sin(\pi x_1) \sin(\pi x_3) - ac \cos(\pi x_2) \cos(\pi x_3)\} \end{aligned} \quad (\text{A.14})$$

resulting in $u_i(x, t) \equiv 0$. $v(x, t)$ is obtained from (3.12):

$$\frac{v_1}{v_r} = \{a \sin(\pi x_3) - c \cos(\pi x_2)\} e^{-2\pi^2 \kappa t} \quad (\text{A.15})$$

$$\frac{v_2}{v_r} = \{b \sin(\pi x_1) - a \cos(\pi x_3)\} e^{-2\pi^2 \kappa t} \quad (\text{A.16})$$

$$\frac{v_3}{v_r} = \{c \sin(\pi x_2) - b \cos(\pi x_1)\} e^{-2\pi^2 \kappa t} \quad (\text{A.17})$$

A unit periodicity is observed for the solution according to the chosen initial conditions (A.8)–(A.10); no velocity component is dependent on all three spatial coordinates. The integrations were carried out using the integral identities (B.1)–(B.3) in Appendix B. Taking into account the unit periodicity of the velocity field ($m = 1$), integrating (3.13), we obtain the pressure $p(x, t)$:

$$\begin{aligned} p &= -\rho e^{-2\pi^2 \kappa t} [bc \cos(\pi x_1) \sin(\pi x_2) \\ &\quad + ab \cos(\pi x_3) \sin(\pi x_1) + ac \cos(\pi x_2) \sin(\pi x_3)] \end{aligned} \quad (\text{A.18})$$

Appendix B. Integral identities used in this paper

$$\int_{-\infty}^{\infty} e^{-\frac{(x-u)^2}{4\tau}} du = 2\sqrt{\pi\tau} \quad (\text{B.1})$$

$$\int_{-\infty}^{\infty} \sin(\beta u) e^{-\frac{(x-u)^2}{4\tau}} du = 2\sqrt{\pi\tau} e^{-\beta^2 \tau} \sin(\beta x) \quad (\text{B.2})$$

$$\int_{-\infty}^{\infty} \cos(\beta u) e^{-\frac{(x-u)^2}{4\tau}} du = 2\sqrt{\pi\tau} e^{-\beta^2 \tau} \cos(\beta x) \quad (\text{B.3})$$

$$\int_{-\infty}^{\infty} \int_{-\infty}^{\infty} \int_{-\infty}^{\infty} \frac{u_1 \cos\{\beta(x_1 - u_1)\}}{[u_1^2 + u_2^2 + u_3^2]^{\frac{3}{2}}} \prod_{j=1}^3 du_j = \frac{4\pi}{\beta} \sin(\beta x_1) \quad (\text{B.4})$$

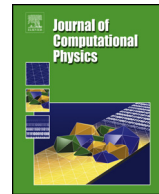
$$\int_{-\infty}^{\infty} \int_{-\infty}^{\infty} \int_{-\infty}^{\infty} \frac{u_1 \cos\{\beta(x_1 - u_1)\} \cos\{\beta(x_2 - u_2)\}}{[u_1^2 + u_2^2 + u_3^2]^{\frac{3}{2}}} \prod_{j=1}^3 du_j$$



Contents lists available at ScienceDirect

Journal of Computational Physics

journal homepage: www.elsevier.com/locate/jcp



A time-relaxed Monte Carlo method preserving the Navier-Stokes asymptotics



Fei Fei

School of Aerospace Engineering, Huazhong University of Science and Technology, 430074 Wuhan, China

ARTICLE INFO

Article history:

Received 1 November 2022

Received in revised form 9 March 2023

Accepted 3 April 2023

Available online 6 April 2023

Keywords:

Boltzmann equation

Monte Carlo method

Asymptotic preserving scheme

Multiscale flows

ABSTRACT

In this paper, a new time-relaxed Monte Carlo (TRMC) method is proposed for the inhomogeneous Boltzmann equation. Compared to the standard TRMC scheme, the proposed method performs the same convection operator; however, divides the collision operator by a micro-macro decomposition. The continuous part of the collision operator is constructed based on the first-order Chapman-Enskog expansion and solved by an explicit second-order scheme, while the numerical solution of the rest nonequilibrium part is still provided by the standard TRMC scheme. In this way, the new TRMC method demonstrates the same accuracy as the standard TRMC scheme in the kinetic limit, however, preserves Navier-Stokes asymptotics and the second-order accuracy in the fluid limit. Several numerical cases of inhomogeneous flows, such as the one-dimensional Poiseuille flow, Sod tube flow, the shock wave and two-dimensional hypersonic flow past a cylinder, are calculated and compared with direct simulation Monte Carlo (DSMC) or Navier-Stokes solutions. It is noted that the new TRMC scheme is more accurate and efficient than the standard TRMC and DSMC methods for simulations of multi-scale gas flows.

© 2023 Elsevier Inc. All rights reserved.

1. Introduction

Multi-scale gas flows, which include both continuum and rarefied flow regimes, widely exist in aerospace and micro-electro-mechanical systems. Different flow regimes are identified by the Knudsen (Kn) number, which is the ratio between the mean free path of the molecules and the characteristic length of the flow field. In a continuum flow regime, a gas flow near the equilibrium state can be simulated by a gas dynamic scheme, such as computational fluid dynamic (CFD) based on Euler or Navier-Stokes equations. Conversely, in a rarefied flow regime, a gas flow departs far from thermodynamical equilibrium, and a kinetic approach, which tracks molecular motions and collisions individually, is necessary. However, if the Kn number varies over several orders of magnitude in the flow field, neither the dynamic nor the kinetic treatment is appropriate. A pure gas dynamic method will lose physics where the Kn number is large, while a standard kinetic scheme, such as the direct simulation Monte Carlo (DSMC) method [1], is very expansive with a small Kn number due to the numerical stiffness. To reach a compromise between computational accuracy and efficiency, domain decomposition methods, such as the hybrid CFD-DSMC algorithms [2–5], were established. It divides the computational domain into a continuous region, which is solved by a CFD scheme, and a rarefied region, which is calculated by a kinetic one. The key point of this hybrid CFD-DSMC method is how to decompose the computational domain. However, finding a common

E-mail address: fei@hust.edu.cn.

continuum-breakdown criterion to position the interface between the continuous and rarefied regions is not easy [6–8]. Therefore, besides the hybrid CFD-DSMC method, several particle-particle hybrid schemes are also proposed recently, such as the BGK-DSMC [10], FP-DSMC [11] and USPBGK-DSMC [12] methods. They employ a stochastic particle method based on the Bhatnagar-Gross-Krook (BGK) or Fokker-Planck model to simulate the continuous region. Since kinetic models can be applied to a much wider range of the Kn number, the choice of the breakdown criterion is more flexible compared to the hybrid CFD-DSMC method [9]. However, extending these particle-particle hybrid schemes for complex gases, such as including multi-species or chemical reactions, is still problematic due to the lack of accurate kinetic models.

In addition to the idea of domain decomposition, another strategy, direct starting from a kinetic scheme, is to design a suitable time discretization of the Boltzmann equation for a wide range of Kn numbers. In consideration of Monte Carlo methods, this class of algorithms includes the time relaxed [13,14], exponential Runge-Kutta [15] and asymptotic-preserving Monte Carlo methods [16]. The main interest is that their time steps are not constrained by the mean collision time. Therefore, these multiscale Monte Carlo methods are much more efficient than the conventional DSMC method. In detail, if the time step is fixed, for a large Kn number, they are consistent with a standard kinetic scheme of the Boltzmann equation; and when the Kn number decreases, their numerical solutions tend to a local Maxwellian. This is the well-known property called asymptotic preservation (AP) [17] and a related algorithm is the AP scheme. To our knowledge, most of the existing Monte Carlo methods with AP property only preserve the Euler asymptotics. Therefore, they are struggling to accurately capture shear stress and heat flux in the fluid limit [16]. However, the viscous effect is important in several circumstances, such as the boundary layer and vortex flows. An exception is the Monte Carlo method [20] based on the micro-macro decomposition [18,19]. Since the micro-macro decomposition scheme treats a perturbation probability distribution function (PDF) deviated from the Maxwellian, an AP property of Navier-Stokes equations can be obtained. But the perturbation PDF will also introduce particles with negative weights, which are quite complicated to deal with in the collision process of DSMC [20].

The goal of this work is to develop a new asymptotic-preserving Monte Carlo method preserving the Navier-Stokes asymptotics and second-order accuracy. Starting from the standard time-relaxed Monte Carlo (TRMC) method [14,21], the collision operator of the proposed scheme is also derived from the Wild sum expansion of the homogeneous Boltzmann equation [22]. However, unlike a Maxwellian truncation in the standard TRMC method, a micro-macro decomposition to the collision operator, which is based on the Chapman-Enskog expansion [23,24], is employed to achieve an AP property of NS equations. Generally speaking, the proposed TRMC method is constructed by directly combining the DSMC and a continuous model, such as the Navier-Stokes solution in the present work. Therefore, it is independent of the special kinetic model in contrast to the existing particle-particle hybrid schemes.

The rest of the paper is organized as follows. In Section 2, we briefly review the DSMC and TRMC methods. After that, a new asymptotic-preserving Monte Carlo method, which is based on the standard TRMC method and preserves the Navier-Stokes asymptotics, is developed and analyzed in Section 3. In Section 4, the proposed method is validated by several inhomogeneous problems in various flow regimes. The numerical results show that the proposed method can achieve a higher order of accuracy and perform better than the standard TRMC and DSMC methods in the simulation of multiscale flows. The paper is concluded in Section 5.

2. Review of the time-relaxed Monte Carlo method

2.1. The Boltzmann equation

From the viewpoint of kinetic theory, a gas flow is governed by the Boltzmann equation, i.e.,

$$\frac{\partial f(\mathbf{V}; \mathbf{x}, t)}{\partial t} + V_i \frac{\partial f(\mathbf{V}; \mathbf{x}, t)}{\partial x_i} = \frac{1}{\varepsilon} Q(f, f), \quad (2.1)$$

where $f(\mathbf{V}; \mathbf{x}, t)$ is the probability density function (PDF) of gas molecules with velocity \mathbf{V} at position \mathbf{x} and time t . For simplicity, monoatomic gas is considered in the present work. The right-hand side of Eq. (2.1) refers to the Boltzmann collision term, in which $Q(f, f)$ describes the binary collisions of molecules and is given as

$$Q(f, f) = \int_{\mathbb{R}^3} \int_{\mathbb{S}^2} [f(\mathbf{V}') f(\mathbf{V}'_1) - f(\mathbf{V}) f(\mathbf{V}_1)] c_r \sigma d\Omega d\mathbf{V}_1, \quad (2.2)$$

where \mathbf{V} and \mathbf{V}_1 are pre-collisional velocities of collision pair and \mathbf{V}' and \mathbf{V}'_1 represent their post-collisional velocities. $c_r = |\mathbf{V} - \mathbf{V}_1|$ is the relative velocity of the colliding molecules. σ is the differential cross-section of the binary collision. Ω is the solid angle. Here, Eq. (2.1) is written in a dimensionless form and the parameter ε is related to the Kn number.

The Boltzmann collision term preserves mass, momentum and energy, i.e.,

$$\int_{\mathbb{R}^3} Q(f, f) \phi(\mathbf{V}) d\mathbf{V} = 0, \quad \phi(\mathbf{V}) = 1, \mathbf{V}, \mathbf{V}^2. \quad (2.3)$$

Therefore, taking the ensemble average of Eq. (2.1) with $\phi(\mathbf{V})$, the conservation equations are obtained as

$$\frac{\partial \rho}{\partial t} + \frac{\partial (\rho u_i)}{\partial x_i} = 0, \quad (2.4a)$$

$$\frac{\partial (\rho u_i)}{\partial t} + \frac{\partial (\rho u_i u_j)}{\partial x_j} + \frac{\partial P_{ij}}{\partial x_j} = 0, \quad (2.4b)$$

$$\frac{\partial (\rho e)}{\partial t} + \frac{\partial (\rho u_i e)}{\partial x_i} + P_{ij} \frac{\partial u_j}{\partial x_i} + \frac{\partial q_i}{\partial x_i} = 0, \quad (2.4c)$$

where ρ is the density; \mathbf{u} is the macroscopic velocity; $e = 3RT/2$ is the internal energy, T is the temperature and R is the gas constant.

$$P_{ij} = \int_{\mathbb{R}^3} C_i C_j f d\mathbf{V} \quad \text{and} \quad q_i = \int_{\mathbb{R}^3} \frac{1}{2} C_i C^2 f d\mathbf{V} \quad (2.5)$$

are the pressure tensor and heat flux, respectively. $\mathbf{C} = \mathbf{V} - \mathbf{u}$ denotes the peculiar velocity of molecules. In general, since the pressure tensor and heat flux are dependent on the details of the PDF, the conservation equations are not closed. However, the Euler and Navier-Stokes (NS) equations can be obtained from the Chapman-Enskog theory. Using Chapman-Enskog expansion [36], the PDF can be written as a series corresponding to the Kn number, i.e.,

$$f = f^{(0)} + f^{(1)} + f^{(2)} + \dots, \quad (2.6)$$

where $f^{(0)} = f_M$ is the Maxwellian distribution,

$$f_M = \rho \left(\frac{1}{2\pi T} \right)^{3/2} \exp \left(-\frac{C^2}{2T} \right). \quad (2.7)$$

$f^{(1)}$ and $f^{(2)}$ refer to the first and second-order Chapman-Enskog expansions, and $f^{(1)}$ is given as

$$f^{(1)} = f_M \left[\frac{1}{2pT} \left(\mathbf{C} \otimes \mathbf{C} - \frac{1}{3} C^2 \mathbf{I} \right) : \boldsymbol{\sigma}^{(1)} + \frac{2}{5} \frac{1}{pT} \mathbf{C} \cdot \mathbf{q}^{(1)} \left(\frac{C^2}{2T} - \frac{5}{2} \right) \right], \quad (2.8)$$

where p is the pressure.

$$\boldsymbol{\sigma}^{(1)} = -\frac{1}{Re} \left(\nabla \mathbf{u} + (\nabla \mathbf{u})^T - \frac{2}{3} \nabla \cdot \mathbf{u} \mathbf{I} \right) \quad \text{and} \quad \mathbf{q}^{(1)} = -\frac{5}{2} \frac{Pr}{Re} \nabla T \quad (2.9)$$

are the first-order expansion of stress and heat flux, respectively. Pr is the Prandtl number and the Reynolds number is defined as $Re = (\rho^* x^* \sqrt{RT^*}) / \mu \cdot x^*$. ρ^* and T^* are characteristic length, density and temperature, respectively. μ refers to the gas viscosity.

In the equilibrium state $f = f_M$, $P_{ij} = \rho RT \delta_{ij}$ and $q_i = 0$, then Eq. (2.4) reduces to the Euler equations. Here δ_{ij} is the Kronecker delta function. Otherwise, if the PDF is assumed as the first-order of Chapman-Enskog expansion, i.e., $f = f_M + f^{(1)}$, Navier-Stokes equations can be obtained from Eq. (2.4).

2.2. The DSMC method

As the Knudsen number increases, the gas flow departs far away from equilibrium and the Navier-Stokes equations become inappropriate. Therefore, in the rarefied flow regime, the Boltzmann equation should be calculated instead. To solve the Boltzmann equation, one can either represent PDF using discrete velocity points or stochastic particles [25]. Because of the high dimensionality of the Boltzmann equation, the former one is usually computationally expensive, especially for hypersonic gas flows. In contrast, the memory consumption of the stochastic particle method is much smaller, which is only dependent on the particle number. The most prominent stochastic particle algorithm is the direct simulation Monte Carlo (DSMC) method [1]. Using a simple operator splitting scheme, DSMC calculates the particle convection and collision processes successively, as it were, the Boltzmann equation (2.1) is solved with two steps:

$$\text{Convection: } \frac{\partial f}{\partial t} + V_i \frac{\partial f}{\partial x_i} = 0 \quad \text{and} \quad (2.10a)$$

$$\text{Collision: } \frac{\partial f}{\partial t} = \frac{1}{\varepsilon} Q(f, f). \quad (2.10b)$$

During the convection step, particles' velocities are unchanged and their positions are updated like in free molecular motion. Therefore, the numerical solution of PDF is evolved as

$$f^*(\mathbf{V}; \mathbf{x}) = \mathcal{T}_{\Delta t}(f^n) = f^n(\mathbf{V}; \mathbf{x} - \mathbf{V} \Delta t). \quad (2.11)$$

$f^n(\mathbf{V}; \mathbf{x})$ denotes the initial PDF at time $n\Delta t$, Δt is the time step; $f^*(\mathbf{V}; \mathbf{x})$ refers to the PDF solution after the convection step. $\mathcal{T}_{\Delta t}(f)$ is defined as the convection operator.

During the collision step, particles' positions keep constant while their velocities are calculated based on the dynamics of binary collisions. To reproduce the actual mean collision rate, collision pairs should be carefully selected. Bird's no time counter (NTC) scheme [1] and Nanbu-Babovsky's scheme [26] are the most used two sampling algorithms. For example, in the framework of Nanbu-Babovsky's scheme, the governing equation of the collision step, i.e., Eq. (2.10b), is rewritten as

$$\frac{\partial f}{\partial t} = \frac{1}{\varepsilon} [P(f, f) - \beta f]. \quad (2.12)$$

If Maxwellian molecules are employed, we can set $P(f, f) = Q^+(f, f)$ and $\beta = Q^-(f)$, therefore $Q^+(f, f)$ and $Q^-(f)$ are given as

$$Q^+(f, f) = \int_{\mathbb{R}^3} \int_{\mathbb{S}^2} f(\mathbf{V}') f(\mathbf{V}'_1) c_r \sigma d\Omega d\mathbf{V}_1 \quad \text{and} \quad (2.13a)$$

$$Q^-(f) = \int_{\mathbb{R}^3} \int_{\mathbb{S}^2} f(\mathbf{V}_1) c_r \sigma d\Omega d\mathbf{V}_1, \quad (2.13b)$$

which denote the gain and loss terms of the Boltzmann collision term, respectively. Considering $f^*(\mathbf{V}; \mathbf{x})$ as the initial condition and solving Eq. (2.12) using the forward Euler scheme, we have

$$f^{n+1}(\mathbf{V}; \mathbf{x}) = \mathcal{C}_{\Delta t}^{DSMC}(f^*) = \left(1 - \frac{\beta \Delta t}{\varepsilon}\right) f^* + \frac{\beta \Delta t}{\varepsilon} \frac{P(f^*, f^*)}{\beta}, \quad (2.14)$$

where $\mathcal{C}_{\Delta t}^{DSMC}(f)$ is defined as the collision operator of DSMC. The probabilistic interpretation of Eq. (2.14) is that, in DSMC simulation a particle will not collide with probability $(1 - \beta \Delta t / \varepsilon)$, and collide following the collision operator $P(f^*, f^*)$ with probability $\beta \Delta t / \varepsilon$. From Eq. (2.14), it is also observed that the time step of DSMC is restricted by ε / β . Otherwise, too large time step will lead the coefficient of the first term of Eq. (2.14) negative and the assumption of the decoupling of particle motion and collision invalid. Therefore, if applied to the continuum flow regime, i.e., $\varepsilon \rightarrow 0$, the conventional DSMC method will show strong numerical stiffness and become quite inefficient. To overcome this defect, several Monte Carlo methods with the asymptotic preserving (AP) property have been proposed, such as the time-relaxed Monte Carlo (TRMC) method [14]. The AP property allows the TRMC method to recover the Euler solution as $\varepsilon \rightarrow 0$.

2.3. The TRMC method

2.3.1. The numerical scheme of TRMC

Starting from the homogeneous Boltzmann equation, the TRMC method replaces the time variable t and PDF f with the expressions

$$t' = 1 - e^{-\beta t / \varepsilon} \quad \text{and} \quad F(\mathbf{V}; \mathbf{x}, t') = f(\mathbf{V}; \mathbf{x}, t) e^{\beta t / \varepsilon}. \quad (2.15)$$

Then, Eq. (2.12) is rewritten as

$$\frac{\partial F}{\partial t'} = \frac{1}{\beta} P(F, F). \quad (2.16)$$

Its numerical solution after the time step Δt is constructed using the first $m + 1$ terms of Wild Sum [22], and given as

$$f^{n+1} = \mathcal{C}_{\Delta t}^{TRMC}(f^*) = \sum_{k=0}^m A_k f_k + A_{m+1} f_M. \quad (2.17)$$

Similarly, $\mathcal{C}_{\Delta t}^{TRMC}(f)$ is defined as the collision operator of TRMC, and m denotes the order of the TRMC method. The functions f_k are given by the recurrence formula

$$f_{k+1}(\mathbf{V}) = \frac{1}{k+1} \sum_{h=0}^k \frac{1}{\beta} P(f_h, f_{k-h}), \quad k = 0, 1, \dots \quad \text{and} \quad (2.18a)$$

$$f_0(\mathbf{V}) = f^*(\mathbf{V}; \mathbf{x}). \quad (2.18b)$$

A_k are nonnegative weight functions. In the standard TRMC method [14], a choice of these functions is given by

$$A_k = e^{-\beta \Delta t / \varepsilon} (1 - e^{-\beta \Delta t / \varepsilon})^k, \quad k = 0, \dots, m-1, \quad A_m = 1 - \sum_{k=0}^{m-1} A_k - A_{m+1}, \quad A_{m+1} = (1 - e^{-\beta \Delta t / \varepsilon})^{m+2}. \quad (2.19)$$

However, other choices of these parameters are also possible [27]. The probabilistic interpretation of Eq. (2.17) is that simulated particles are unchanged with probability A_0 , performed multiple collision processes with probability A_k ($k \in [1, m]$), and sampled from the Maxwellian distribution with probability A_{m+1} . In addition, Gabetta et al. [13] have proved that for any $m \geq 1$, $\lim_{\beta \Delta t/\varepsilon \rightarrow \infty} f^{n+1} = f_M$, therefore, the standard TRMC method satisfied the AP property of Euler equations.

Besides Maxwellian molecules, the TRMC method can also be applied to other molecule models. Pareschi and Russo [14] have given a general expression of $P(f, f)$, i.e.,

$$P(f, f) = Q(f, f) + \beta f = Q^+(f, f) + f(\beta - Q^-(f)), \quad (2.20)$$

and the constant β should satisfy

$$\beta \geq Q^-(f). \quad (2.21)$$

The details of the TRMC method with the variable hard sphere (VHS) molecules are referred to the reference [14].

2.3.2. The accuracy of the TRMC method

In the kinetic limit ($\beta \Delta t/\varepsilon \ll 1$), Gabetta et.al. [13] have shown that the time relaxed scheme can obtain m^{th} order of accuracy with numerical solution (2.17) for the homogeneous Boltzmann equation. However, in practice, the accuracy of the TRMC method will also be influenced by the choice of β [28].

For the inhomogeneous Boltzmann equation, the simple splitting scheme as DSMC is usually employed in TRMC, i.e., $f^{n+1} = C_{\Delta t}^{\text{TRMC}} [\mathcal{T}_{\Delta t}(f^n)]$. The simple splitting scheme only has first order accuracy even though we solve both particle motion and collision steps with great accuracy. To improve the accuracy in time, another choice is the Strang splitting scheme [29], i.e.,

$$f^{n+1} = \mathcal{T}_{\Delta t/2} \left\{ C_{\Delta t}^{\text{TRMC}} [\mathcal{T}_{\Delta t/2}(f^n)] \right\}. \quad (2.22)$$

Using the Strang splitting scheme, TRMC can achieve second order of accuracy in the kinetic limit, if both the convection and collision steps are at least second order.

In the fluid limit ($\beta \Delta t/\varepsilon \gg 1$), however, the Strang splitting scheme of the standard TRMC method cannot preserve accuracy. We demonstrate it in the following. As $\beta \Delta t/\varepsilon \gg 1$, the numerical solution of the TRMC collision operator approaches the equilibrium state as shown in Eq. (2.17). Therefore, according to Eq. (2.22), at the half time step its PDF solution can be assumed as Maxwellian $f_M^{n+1/2}$. Correspondingly, macroscopic variables are calculated as $U^{n+1/2} = \langle \phi(\mathbf{V}) f_M^{n+1/2} \rangle$, where $\langle \dots \rangle$ denotes the ensemble average. In addition, according to the Strang splitting scheme as shown in Eq. (2.22), $f_M^{n+1/2}$ is calculated from the convection of the PDF at time $(n - 1/2)\Delta t$; thus, the numerical solution of $U^{n+1/2}$ is also written as

$$U_{\text{TRMC}}^{n+1/2} = \langle \phi(\mathbf{V}) f_M^{n-1/2}(\mathbf{V}; \mathbf{x} - \mathbf{V}\Delta t) \rangle. \quad (2.23)$$

Then, taking Taylor expansion at time $(n - 1/2)\Delta t$ and position \mathbf{x} , Eq. (2.23) can be rewritten as

$$\begin{aligned} U_{\text{TRMC}}^{n+1/2} &= \langle \phi(\mathbf{V}) f_M^{n-1/2}(\mathbf{V}; \mathbf{x}) \rangle - \Delta t \frac{\partial}{\partial \mathbf{x}} \langle \mathbf{V} \phi(\mathbf{V}) f_M^{n-1/2}(\mathbf{V}; \mathbf{x}) \rangle \\ &\quad + \frac{1}{2} \Delta t^2 \frac{\partial^2}{\partial \mathbf{x}^2} \langle \mathbf{V}^2 \phi(\mathbf{V}) f_M^{n-1/2}(\mathbf{V}; \mathbf{x}) \rangle + O(\Delta t^3). \end{aligned} \quad (2.24)$$

Conversely, from the viewpoint of gas dynamics, macroscopic variables also satisfy Euler equations in the equilibrium state, i.e.,

$$\frac{\partial U}{\partial t} = \mathcal{T}(U), \quad \text{and} \quad (2.25)$$

$$\mathcal{T}(U) = -\frac{\partial}{\partial \mathbf{x}} \langle \mathbf{V} f_M(\mathbf{V}; \mathbf{x}, t) \phi(\mathbf{V}) \rangle. \quad (2.26)$$

Based on Eqs. (2.25) and (2.26), Taylor expansion of the solution $U^{n+1/2}$ at time step $(n - 1/2)\Delta t$ and position \mathbf{x} can be calculated as

$$U^{n+1/2} = U^{n-1/2} + \Delta t \mathcal{T}(U^{n-1/2}) + \frac{\Delta t^2}{2} \frac{\partial \mathcal{T}(U^{n-1/2})}{\partial t} + O(\Delta t^3), \quad \text{and} \quad (2.27)$$

$$\frac{\partial \mathcal{T}(U^{n-1/2})}{\partial t} = -\frac{\partial}{\partial \mathbf{x}} \left\langle \mathbf{V} \frac{\partial f_M^{n-1/2}(\mathbf{V}; \mathbf{x})}{\partial U} \phi(\mathbf{V}) \mathcal{T}(U^{n-1/2}) \right\rangle. \quad (2.28)$$

Comparing Eqs. (2.24) and (2.27), their difference is obtained as

$$\begin{aligned} U_{TRMC}^{n+1/2} - U^{n+1/2} &= \frac{1}{2} \Delta t^2 \frac{\partial}{\partial x} \left\langle \mathbf{V} \frac{\partial f_M^{n-1/2}(\mathbf{V}; \mathbf{x})}{\partial U} \phi(\mathbf{V}) \frac{\partial (\mathbf{V} U^{n-1/2})}{\partial x} \right\rangle \\ &+ \frac{1}{2} \Delta t^2 \frac{\partial}{\partial x} \left\langle \mathbf{V} \frac{\partial f_M^{n-1/2}(\mathbf{V}; x)}{\partial U} \phi(\mathbf{V}) \mathcal{T}(U^{n-1/2}) \right\rangle + O(\Delta t^3). \end{aligned} \quad (2.29)$$

Since $\mathbf{V} U^{n-1/2} = \mathbf{V} \langle f_M^{n-1/2}(\mathbf{V}; x) \phi(\mathbf{V}) \rangle \neq \langle \mathbf{V} f_M^{n-1/2}(\mathbf{V}; x, t) \phi(\mathbf{V}) \rangle$ in general [30], therefore,

$$U_{TRMC}^{n+1/2} = U^{n+1/2} + O(\Delta t^2). \quad (2.30)$$

It indicates that the Strang splitting scheme of the standard TRMC method is only first order accurate in the fluid limit. This order reduction of the Strang splitting scheme has also been discussed by Jin [31] for hyperbolic systems with stiff relaxation terms.

3. A TRMC method preserving the Navier-Stokes asymptotics

As discussed in Section 2, the existing TRMC method preserves the Euler asymptotics and only has first order of accuracy in the fluid limit. To improve its performance in the continuum flow regime, a new TRMC method is proposed in this work. To summarize, the main features of this proposed scheme would be:

- Asymptotic preserving property of NS equations;
- Asymptotic preserving second-order accurate in the fluid limit and the same order accurate as the standard TRMC method in the kinetic limit;
- Implemented with stochastic particles like DSMC.

In addition, we call this proposed method as the AAP-TRMC (asymptotic accurate and preserving TRMC) method for short in the present work.

3.1. The numerical scheme

In the proposed TRMC method, to reach a high order accuracy for the inhomogeneous Boltzmann equation, the Strang splitting scheme as shown in Eq. (2.22) is also employed, therefore, its numerical solution during a time step can be written as

$$f^{n+1} = \mathcal{T}_{\Delta t/2} \left\{ \mathcal{C}_{\Delta t}^{AAP-TRMC} [\mathcal{T}_{\Delta t/2} (f^n)] \right\}. \quad (3.1)$$

The convection operator is as same as that of the standard TRMC scheme, however, its collision operator $\mathcal{C}_{\Delta t}^{AAP-TRMC}$ is constructed based a micro-macro decomposition [23,24] as follows:

First, using the Chapman-Enskog expansion (2.6), the Boltzmann collision term can also be expanded as

$$Q(f, f) = Q^{(0)}(f) + Q^{(1)}(f) + Q^{(2)}(f) + \dots, \quad (3.2)$$

where $Q^{(0)}(f) = 0$; $Q^{(1)}(f) = 2Q(f^{(0)}, f^{(1)})$ and $Q^{(2)}(f)$ represent the first and second order expansions, respectively. Note that $Q^{(1)}$ is a linear operator. Therefore, the first order expansion of the standard TRMC collision operator, i.e., Eq. (2.17), can be written as

$$\mathcal{C}_{\Delta t}^{TRMC,(1)}(f^*) = \sum_{k=0}^m A_k f_k^{(1)}. \quad (3.3)$$

According to Eq. (2.18),

$$f_{k+1}^{(1)}(\mathbf{V}) = \frac{1}{k+1} \sum_{h=0}^k \frac{1}{\beta} P^{(1)}(f_h, f_{k-h}), \quad k = 0, 1, \dots \quad \text{and} \quad (3.4a)$$

$$f_0^{(1)}(\mathbf{V}) = f^{*,(1)}(\mathbf{V}; \mathbf{x}), \quad (3.4b)$$

where $f^*(\mathbf{V}; \mathbf{x}) = \mathcal{T}_{\Delta t/2}(f^n)$ denotes the numerical solution after particle convection for half time step, and $P^{(1)}(f, f) = Q^{(1)}(f) + \beta f^{(1)}$.

Second, we keep the high order expansions of the standard TRMC collision operator unchanged, however, replace the first order one, i.e., Eq. (3.3), by the numerical solution of a second order scheme, which is

$$\mathcal{C}_{\Delta t}^{AAP-TRMC,(1)}(f^*) = f^{*,(1)} + \frac{\Delta t}{\varepsilon} Q^{(1)}(f^*) + \frac{1}{2} \left(\frac{\Delta t}{\varepsilon} \right)^2 Q^{(1)}(Q^{(1)}(f^*)). \quad (3.5)$$

It is noted that $\partial [Q^{(1)}(f^*)]/\partial t = Q^{(1)}(Q^{(1)}(f^*))$ as $Q^{(1)}$ is a linear operator. Therefore, combining Eqs. (2.17), (3.3) and (3.5), the collision operator of the proposed method is reconstructed as

$$\begin{aligned} \mathcal{C}_{\Delta t}^{AAP-TRMC}(f^*) &= \mathcal{C}_{\Delta t}^{TRMC}(f^*) - \mathcal{C}_{\Delta t}^{TRMC,(1)}(f^*) + \mathcal{C}_{\Delta t}^{AAP-TRMC,(1)}(f^*) \\ &= \sum_{k=0}^m A_k f_k + A_{m+1} \left(f_M^{n+1/2} + f_\alpha \right), \end{aligned} \quad (3.6)$$

where $f_\alpha = \frac{1}{A_{m+1}} \left\{ f^{*,(1)} + \frac{\Delta t}{\varepsilon} Q^{(1)}(f^*) + \frac{1}{2} \left(\frac{\Delta t}{\varepsilon} \right)^2 Q^{(1)}[Q^{(1)}(f^*)] - \sum_{k=0}^m A_k f_k^{(1)} \right\}$, and $f_M^{n+1/2}$ is defined as the Maxwellian corresponding to f^* . Compared to the standard TRMC method, an additional PDF f_α is introduced in the last term of right-hand side of Eq. (3.6).

Third, according to the convection operator, we assume that f^* is approximated as

$$f^{*,(1)}(\mathbf{V}; \mathbf{x}) \approx f_M^{n+1/2} + f^{n+1/2,(1)} - \frac{\Delta t}{2\varepsilon} Q^{(1)}(f^{n+1/2}), \quad (3.7)$$

and

$$f^{n+1/2,(1)} = f_M^{n+1/2} \left[\frac{1}{2pT} \left(\mathbf{C} \otimes \mathbf{C} - \frac{1}{3} C^2 \mathbf{I} \right) : \boldsymbol{\sigma}^{(1)} + \frac{2}{5} \frac{1}{pT} \mathbf{C} \cdot \mathbf{q}^{(1)} \left(\frac{C^2}{2T} - \frac{5}{2} \right) \right] \quad \text{and} \quad (3.8a)$$

$$\begin{aligned} Q^{(1)}(f^{n+1/2}) &= \varepsilon \left(\frac{\partial_0 f_M^{n+1/2}}{\partial t} + V_i \frac{\partial f_M^{n+1/2}}{\partial x_i} \right) \\ &= - \frac{f_M^{n+1/2}}{\mu/(p\varepsilon)} \left[\frac{1}{2pT} \left(\mathbf{C} \otimes \mathbf{C} - \frac{1}{3} C^2 \mathbf{I} \right) : \boldsymbol{\sigma}^{(1)} + \frac{2}{5} \frac{1}{pT} \text{Pr} \mathbf{C} \cdot \mathbf{q}^{(1)} \left(\frac{C^2}{2T} - \frac{5}{2} \right) \right]. \end{aligned} \quad (3.8b)$$

$\boldsymbol{\sigma}^{(1)}$ and $\mathbf{q}^{(1)}$, which represent the first order expansion of stress and heat flux, are given by Eq. (2.9). Then, using the approximations of $f^{*,(1)}$, f_α can be derived as

$$f_\alpha = \frac{1}{A_{m+1}} f_M^{n+1/2} \left\{ \begin{aligned} &\left[1 - \frac{\Delta t}{2\mu/p} - \left(1 + \frac{\Delta t}{2\mu/p} \right) \Phi_1 \right] \frac{1}{2pT} \left(\mathbf{C} \otimes \mathbf{C} - \frac{1}{3} C^2 \mathbf{I} \right) : \boldsymbol{\sigma}^{(1)} \\ &+ \left[1 - \frac{\Delta t}{2\mu/p} \text{Pr} - \left(1 + \frac{\Delta t}{2\mu/p} \text{Pr} \right) \Phi_2 \right] \frac{2}{5} \frac{1}{pT} \mathbf{C} \cdot \mathbf{q}^{(1)} \left(\frac{C^2}{2T} - \frac{5}{2} \right) \end{aligned} \right\}, \quad (3.9)$$

where higher order terms, such as $O(\Delta t)^3$, are omitted. Φ_1 and Φ_2 are coefficient functions dependent on the time step size and distinct for the TRMC method with different orders. In detail, the collision operator for first order AAP-TRMC method (AAP-TRMC1) is written as

$$\mathcal{C}_{\Delta t}^{AAP-TRMC1}(f^*) = A_0 f^* + A_1 \frac{P(f^*, f^*)}{\beta} + A_2 \left(f_M^{n+1/2} + f_\alpha \right), \quad (3.10)$$

and

$$\Phi_1 = A_0 + A_1 (1 - \chi^{-1}) \quad \text{and} \quad \Phi_2 = A_0 + A_1 (1 - \text{Pr} \chi^{-1}), \quad (3.11)$$

where $\chi = \mu\beta/(p\varepsilon)$. For the second order AAP-TRMC method (AAP-TRMC2), the collision operator is given as

$$\mathcal{C}_{\Delta t}^{AAP-TRMC2}(f^*) = A_0 f^* + A_1 \frac{P(f^*, f^*)}{\beta} + A_2 \frac{P(f^*, f_1)}{\beta} + A_3 \left(f_M^{n+1/2} + f_\alpha \right), \quad (3.12)$$

and

$$\Phi_1 = A_0 + \left(A_1 + \frac{1}{2} A_2 \right) (1 - \chi^{-1}) + \frac{1}{2} A_2 (1 - \chi^{-1})^2 \quad \text{and} \quad (3.13a)$$

$$\Phi_2 = A_0 + \left(A_1 + \frac{1}{2} A_2 \right) (1 - \text{Pr} \chi^{-1}) + \frac{1}{2} A_2 (1 - \text{Pr} \chi^{-1})^2. \quad (3.13b)$$

3.2. Properties of the AAP-TRMC method

3.2.1. Positivity

Following the Strang splitting scheme, the AAP-TRMC method calculates the particle convection and collision operators separately. As a stochastic particle method, the particle convection operator is positivity preserving in any time. For the collision operator, the coefficients A_k of the AAP-TRMC method are as same as those from the standard TRMC method,

which always keep positive [14]. However, it should be mentioned that in the AAP-TRMC collision operator, the velocities of computational particles, which belong to the last term of Eq. (3.6), are resampled from the PDF $(f_M^{n+1/2} + f_\alpha)$. Since f_α is constructed based on the Chapman-Enskog expansion as shown in Eq. (3.9), the PDF $(f_M^{n+1/2} + f_\alpha)$ may include negative part as the Kn number increases. To avoid this situation, we introduce a scaling factor θ before f_α to ensure the positivity in the simulation, as it were, $(f_M^{n+1/2} + f_\alpha)$ is replaced by $(f_M^{n+1/2} + \theta f_\alpha)$ and

$$\theta = \begin{cases} 1 & \beta \Delta t / \varepsilon \geq 1 \\ \min\left\{1, \frac{\varepsilon}{\beta \Delta t} A_{m+1}\right\} & \beta \Delta t / \varepsilon < 1 \end{cases}. \quad (3.14)$$

In the fluid limit, as $\beta \Delta t / \varepsilon \gg 1$, $A_{m+1} \rightarrow 1$, Φ_1 and $\Phi_2 \rightarrow 0$, we obtain

$$f_M^{n+1/2} + \theta f_\alpha \approx f_M^{n+1/2} \left\{ 1 + \left[1 - \frac{\Delta t}{2\mu/p} \right] \frac{1}{2pT} \boldsymbol{\sigma}^{(1)} : \left(\mathbf{C} \otimes \mathbf{C} - \frac{1}{3} C^2 \mathbf{I} \right) \right. \\ \left. + \left[1 - \frac{\Delta t}{2\mu/p} \text{Pr} \right] \frac{2}{5} \frac{1}{pT} \mathbf{C} \cdot \mathbf{q}^{(1)} \left(\frac{C^2}{2T} - \frac{5}{2} \right) \right\}. \quad (3.15)$$

According to Ref. [32], the positivity of above PDF can be estimated by the coefficients before the second and third terms on the right-hand side of Eq. (3.15). Similarly, a parameter B refers to the maximum of these coefficients is defined as

$$B = \max \left(\left| \left[1 - \frac{\Delta t}{2\mu/p} \right] \frac{\boldsymbol{\sigma}^{(1)}}{p} \right|, \left| \left[1 - \frac{\Delta t}{2\mu/p} \text{Pr} \right] \frac{\mathbf{q}^{(1)}}{pT^{1/2}} \right| \right). \quad (3.16)$$

If $B < 0.1$, the PDF given by Eq. (3.15) is negative about 0.05% of the time [32]. Using Eq. (2.9), the range of parameter B satisfies

$$B < \left| 1 - \frac{\Delta t}{2\mu/p} \right| \frac{\mu}{p} (Ma + 1) \approx \frac{\Delta t}{2} (Ma + 1). \quad (3.17)$$

Applying the CFL condition, $\Delta t (Ma + 1)/2 = \text{CFL} \cdot \Delta h/2$. It is noted that, if setting the CFL number with $\text{CFL} \leq 1$ and the dimensionless cell size Δh much smaller than 1, the condition $B < 0.1$ can be achieved in most situations.

In the kinetic limit, as $\beta \Delta t / \varepsilon \ll 1$, the Taylor expansion of $(f_M^{n+1/2} + \theta f_\alpha)$ is given as

$$f_M^{n+1/2} + \theta f_\alpha \approx f_M^{n+1/2} \left\{ 1 + O\left(\frac{\Delta t}{\mu/p}\right) \frac{1}{2pT} \boldsymbol{\sigma}^{(1)} : \left(\mathbf{C} \otimes \mathbf{C} - \frac{1}{3} C^2 \mathbf{I} \right) \right. \\ \left. + O\left(\frac{\Delta t}{\mu/p}\right) \frac{2}{5} \frac{1}{pT} \text{Pr} \mathbf{C} \cdot \mathbf{q}^{(1)} \left(\frac{C^2}{2T} - \frac{5}{2} \right) \right\}. \quad (3.18)$$

Similar to Eq. (3.17), the estimation of parameter B is $B < \Delta t (Ma + 1)$, which also assures the positivity of $(f_M^{n+1/2} + \theta f_\alpha)$. In addition, the scaling factor θ will not affect the other properties of the AAP-TRMC method, such as the preserving and accurate asymptotics, as discussed below.

3.2.2. Accuracy

In the fluid limit as $\beta \Delta t / \varepsilon \gg 1$, using Eqs. (3.5)–(3.9), the numerical solution of the AAP-TRMC collision operator approaches

$$\mathcal{C}_{\Delta t}^{AAP-TRMC} (f^*) = f_M^{n+1/2} + f^{n+1/2,(1)} + \frac{\Delta t}{2\varepsilon} Q^{(1)} (f^{n+1/2}). \quad (3.19)$$

Since the Strang splitting scheme (3.1) can also be written as $\mathcal{T}_{\Delta t/2} (f^n) = \mathcal{T}_{\Delta t} \left\{ \mathcal{C}_{\Delta t}^{AAP-TRMC} [\mathcal{T}_{\Delta t/2} (f^{n-1})] \right\}$, then combining Eqs. (3.7) and (3.19), we obtain

$$\left[f_M^{n+1/2} + f^{n+1/2,(1)} \right] (\mathbf{V}; \mathbf{x}) - \left[f_M^{n-1/2} + f^{n-1/2,(1)} \right] (\mathbf{V}; \mathbf{x} - \mathbf{V} \Delta t) \\ = \frac{\Delta t}{2\varepsilon} Q^{(1)} (f^{n+1/2}) (\mathbf{V}; \mathbf{x}) + \frac{\Delta t}{2\varepsilon} Q^{(1)} (f^{n-1/2}) (\mathbf{V}; \mathbf{x} - \mathbf{V} \Delta t), \quad (3.20)$$

which is just the Crank-Nicolson scheme, therefore second order of accuracy can be achieved. The proof below is derived following the accuracy analysis of the standard TRMC method in Section 2.3, i.e., Eqs. (2.23)–(2.30). First, using Eq. (3.20), the solution of the macroscopic variables at the middle of the time step is calculated as

$$\begin{aligned} U_{AAP-TRMC}^{n+1/2} &= \left\langle \phi(\mathbf{V}) \left\{ \left[f_M^{n+1/2} + f^{n+1/2,(1)} \right] (\mathbf{V}; \mathbf{x}) - \frac{\Delta t}{2\varepsilon} Q^{(1)} \left(f^{n+1/2} \right) (\mathbf{V}; \mathbf{x}) \right\} \right\rangle \\ &= \left\langle \phi(\mathbf{V}) \left\{ \left[f_M^{n-1/2} + f^{n-1/2,(1)} \right] (\mathbf{V}; \mathbf{x} - \mathbf{V}\Delta t) + \frac{\Delta t}{2\varepsilon} Q^{(1)} \left(f^{n-1/2} \right) (\mathbf{V}; \mathbf{x} - \mathbf{V}\Delta t) \right\} \right\rangle. \end{aligned} \quad (3.21)$$

Taking Taylor expansion of Eq. (3.21) at time $(n - 1/2)\Delta t$ and position \mathbf{x} and using Chapman-Enskog theory, we have

$$\begin{aligned} U_{AAP-TRMC}^{n+1/2} &= \left\langle \phi(\mathbf{V}) f_M^{n-1/2} (\mathbf{V}; \mathbf{x}) \right\rangle - \Delta t \frac{\partial}{\partial x} \left\langle \mathbf{V} \phi(\mathbf{V}) f_M^{n-1/2} (\mathbf{V}; \mathbf{x}) \right\rangle \\ &\quad + \frac{\Delta t^2}{2} \frac{\partial^2}{\partial x^2} \left\langle \mathbf{V}^2 \phi(\mathbf{V}) f_M^{n-1/2} (\mathbf{V}; \mathbf{x}) \right\rangle - \frac{\Delta t^2}{2\varepsilon} \frac{\partial}{\partial x} \left\langle \mathbf{V} \phi(\mathbf{V}) Q^{(1)} \left(f^{n-1/2} \right) (\mathbf{V}; \mathbf{x}) \right\rangle + O(Kn) + O(\Delta t^3). \end{aligned} \quad (3.22)$$

Then, assuming the macroscopic variables also satisfy Euler equations, Taylor expansion of the solution $U^{n+1/2}$ at time step $(n - 1/2)\Delta t$ and position \mathbf{x} is given by Eq. (2.27). Comparing Eqs. (3.22) and (2.27), the numerical solution of the AAP-TRMC method yields

$$U_{AAP-TRMC}^{n+1/2} = U^{n+1/2} + O(Kn) + O(\Delta t^3). \quad (3.23)$$

Therefore, the AAP-TRMC method has second order of accuracy in time in the fluid limit.

In the kinetic limit, as shown in Eq. (3.18), the additional PDF θf_α approaches to $A_{m+1}O(\beta\Delta t/\varepsilon)$, which is negligible compared to the other terms in the standard TRMC method. Therefore, the AAP-TRMC scheme reduces to standard TRMC method and shares the same accuracy in the kinetic limit.

3.2.3. Asymptotic preserving property

In the fluid limit, as $\beta\Delta t/\varepsilon \gg 1$, the approximate solution of the AAP-TRMC collision operator is given by Eq. (3.19). Then, applying the convection operator for another half of time step, the numerical solution at time $(n + 1)\Delta t$ can be written as

$$\begin{aligned} f^{n+1} &= \mathcal{T}_{\Delta t/2} \left\{ \mathcal{C}_{\Delta t}^{AAP-TRMC} (f^*) \right\} = \left[f_M^{n+1/2} + f^{n+1/2,(1)} + \frac{\Delta t}{2\varepsilon} Q^{(1)} \left(f^{n+1/2} \right) \right] (\mathbf{V}; \mathbf{x} - \mathbf{V}\Delta t/2) \\ &= f_M^{n+1/2} (\mathbf{V}; \mathbf{x}) + f^{n+1/2,(1)} (\mathbf{V}; \mathbf{x}) + \frac{\Delta t}{2} \frac{\partial f_M^{n+1/2} (\mathbf{V}; \mathbf{x})}{\partial t} + O(\Delta t^2). \end{aligned} \quad (3.24)$$

Obviously, the AAP-TRMC method preserves the Navier-Stokes asymptotics.

3.3. The numerical implementation

In summary, the AAP-TRMC method employs the Strang splitting scheme as shown Eq. (3.1), with a newly proposed collision operator as

$$\mathcal{C}_{\Delta t}^{AAP-TRMC} (f^*) = \sum_{k=0}^m A_k f_k + A_{m+1} \left(f_M^{n+1/2} + \theta f_\alpha \right). \quad (3.25)$$

Similar to the standard TRMC method, its computational procedure includes following five steps:

1. **Initialization.** Assign simulated particles in the computational domain;
2. **Convection.** Compute particle motions for the first half time step;
3. **Collision.** Compute particle collisions for a whole time step;
4. **Convection.** Compute particle motions for another half time step;
5. **Sampling.** Compute the macroscopic quantities.

We give details of above numerical implementations below.

3.3.1. Initialization

Similar to DSMC, the AAP-TRMC method employs stochastic particles to simulate the PDF of gas molecules. In each compactional cell, the number of initial particles N_c is determined as

$$N_c = Iround \left(\frac{nV_c}{F_N} \right), \quad (3.26)$$

and

$$Iround(z) = \begin{cases} [z] & \text{with probability } [z] + 1 - z, \\ [z] + 1 & \text{with probability } z - [z], \end{cases} \quad (3.27)$$

where $[z]$ refers to the integer part of z . n is the number density; V_c is the cell volume; and F_N refers to the number of real molecules represented by one computational particle.

For each computational particle with index α , its velocity $\mathbf{M}^{(\alpha)}$ is sampled from the local equilibrium distribution, i.e., the Maxwellian distribution as shown in Eq. (2.7), and its position $\mathbf{X}^{(\alpha)}$ is randomly distributed in the computational cell.

3.3.2. Convection

Particle's position is updated according to its velocity for half time step $\Delta t/2$, e.g., for the convection of the first half time step, we obtain

$$\mathbf{X}^{(\alpha),n+1/2} = \mathbf{X}^{(\alpha),n} + \mathbf{M}^{(\alpha),n} \Delta t/2. \quad (3.28)$$

The boundary condition of the AAP-TRMC method is as same as DSMC, and also implemented in the convection process.

3.3.3. Collision

In general, the collision operator of the AAP-TRMC method is implemented similarly to the standard TRMC scheme. To emphasizing the difference between these two methods, only a brief procedure of the second order AAP-TRMC method with VHS molecules is presented below. However, the details of the collision algorithm for the TRMC method are referred to Ref. [14].

Algorithm 3.1 (*Collision operator of AAP-TRMC2 for VHS molecules*). For each computational cell:

- 1) Determining the parameter β . Compute an upper bound of $(\sigma_T c_r)_{\max}$, $\sigma_T = \int_{S^2} \sigma d\Omega$ is the total collision cross-section. The parameter β in the AAP-TRMC method is chosen as $\rho (\sigma_T c_r)_{\max}$ [14];
- 2) Computing A_0 , A_1 , A_2 and A_3 according to Eq. (2.19), and Φ_1 and Φ_2 according to Eq. (3.13);
- 3) Randomly selecting three groups of particles from the computational cell corresponding to the last three terms in the right-hand side of Eq. (3.12), respectively. Setting $N_1 = Iround(A_1 N_c)$, $N_2 = Iround(A_2 N_c)$ and $N_3 = Iround(A_3 N_c)$, which are the number of particles in each group;
- 4) The first group of particles performs the collision process according to the collision term $P(f^*, f^*)/\beta$;
- 5) The second group of particles performs the collision process according to the collision term $P(f^*, f_1)/\beta$. The algorithm of computing these two collision terms for VHS molecules is as same as Ref. [14];
- 6) Resampling the velocities of the third group of particles according to $(f_M^{n+1/2} + \theta f_\alpha)$, where $f_M^{n+1/2}$ and f_α are given as Eq. (2.7) and Eq. (3.9), respectively. It is noted that both $f_M^{n+1/2}$ and f_α are determined by the macroscopic quantities, such as ρ , \mathbf{u} and T , after the convection step of the first half time step. Its sampling method is introduced in section 3.3.4.

The implementations of the other AAP-TRMC schemes, such as the first order one, i.e., AAP-TRMC1, can be performed similarly.

3.3.4. Sampling

Like DSMC, the macroscopic quantities are averaged from the velocities of the computational particles as

$$\rho = m N_c / V_c, \quad u_i = \sum_{k=1}^{N_c} M_i^{(k)} / N_c \quad \text{and} \quad T = \sum_{k=1}^{N_c} (M_i^{(k)} - u_i)^2 / 3R(N_c - 1), \quad (3.29)$$

where the factor $1/(N_c - 1)$ in the temperature occurs to produce unbiasedness of T . To reduce statistical noise, the exponentially weighted moving time averaging [33] is employed for the simulation of steady flows. In addition, as the AAP-TRMC method has a second-order of accuracy in time in the fluid limit, a same order accuracy should be achieved in space. Therefore, at least a second order interpolation is requested in the AAP-TRMC method. Then, the Maxwellian distribution $f_M(\mathbf{V}; \mathbf{X}^{(\alpha)}, t)$ and the additional PDF $f_\alpha(\mathbf{V}; \mathbf{X}^{(\alpha)}, t)$ related to the resampled computational particles are computed based on the macroscopic quantities and their derivatives at the particle location $\mathbf{X}^{(\alpha)}$.

The molecular velocities satisfied PDF $(f_M^{n+1/2} + \theta f_\alpha)$ can be sampled using either the acceptance-rejection algorithm [32] or the Metropolis-Hastings (MH) method [34].

3.3.5. Conservation

As well Known, if the molecular velocities are sampled by the acceptance-rejection algorithm or the MH method, the momentum and energy conservation can only be obtained in a statistical sense. Therefore, like other stochastic particle

methods [38,39], to conserve the momentum and energy in each cell, a correction step for the velocities of individual particle is implemented after the collision step, i.e.,

$$\mathbf{M}^{(k)} = \alpha \left(\mathbf{M}^{(k)'} - \sum_{k=1}^{N_c} \mathbf{M}^{(k)'} / N_c \right) + \sum_{k=1}^{N_c} \mathbf{M}^{(k)*} / N_c, \quad (3.30)$$

where $\mathbf{M}^{(k)*}$ and $\mathbf{M}^{(k)'}$ are the velocities of the k^{th} particle before and after the collision step, respectively. The coefficient α is given by

$$\alpha = \sqrt{\sum_{k=1}^{N_c} \left(M_i^{(k)*} - \sum_{k=1}^{N_c} M_i^{(k)*} / N_c \right)^2 / \sum_{k=1}^{N_c} \left(M_i^{(k)'} - \sum_{k=1}^{N_c} M_i^{(k)'} / N_c \right)^2}. \quad (3.31)$$

4. Numerical results

4.1. Poiseuille flow

The Poiseuille flow is first calculated. The argon gas, initially in the standard condition ($T_0 = 273$ K and $p_0 = 1$ atm), is simulated with three Knudsen numbers varied from the rarefied to the continuum flow regimes, such as 0.1, 0.01 and 0.001. The distance H between parallel walls is calculated based on the Kn number, i.e., $H = \lambda/\text{Kn}$, where $\lambda = 6.36 \times 10^{-8}$ m. The wall temperature keeps 273 K and fully diffusive boundary condition is employed. For three Kn numbers, corresponding pressure gradients are chosen as 4.0×10^{10} Pa m $^{-1}$, 4.0×10^8 Pa m $^{-1}$ and 4.0×10^6 Pa m $^{-1}$, respectively.

The VHS molecules are employed and the molecular diameter is set as 4.17×10^{-10} m with a reference temperature $T_{\text{ref}} = 273$ K and viscosity $\mu_{\text{ref}} = 2.117 \times 10^{-5}$ Pas. With the exponent $\omega = 0.81$, the viscosity of argon is calculated as $\mu = \mu_{\text{ref}} (T/T_{\text{ref}})^{\omega}$. In this case, computational cells are uniformly distributed with a cell width Δh . The time step is determined by the CFL condition with $CFL = 1.0$.

Fig. 1 shows the mean velocity and temperature distributions calculated by the AAP-TRMC2 method. From Fig. (1a) to (1f), 100, 60, and 140 computational cells are employed for $\text{Kn} = 0.1$, 0.01, and 0.001, respectively. 500 computational particles are assigned in each cell initially. For large Knudsen numbers, i.e., 0.1 and 0.01, the results of AAP-TRMC2 agree well with the DSMC data. However, larger cell and time size can be used in AAP-TRMC2. For the smaller Kn number of 0.001, the gas flow belongs to the continuum regime and DSMC is computationally expansive. The AAP-TRMC2 method is compared with the analytical NS solution [37], and consistent results are also obtained.

To investigate the accuracy of the AAP-TRMC method in different flow regions, we calculate the L_2 -norm of error for the mean velocity as shown in Fig. 2, in which u_x^{ref} denotes the finest DSMC results for $\text{Kn} = 0.1$ and 0.01 and the analytical NS solutions for $\text{Kn} = 0.001$. In the kinetic limit, such as $\text{Kn} = 0.1$, AAP-TRMC reduces to the standard TRMC method. Therefore, the curves of TRMC2, which refers to the second order standard TRMC method, and AAP-TRMC2 overlap with each other. However, the first order AAP-TRMC method shows less accurate than AAP-TRMC2. In the fluid limit, such as $\text{Kn} = 0.001$, both of the AAP-TRMC1 and AAP-TRMC2 methods turn to the Crank-Nicolson scheme and achieve the second order of accuracy. Conversely, larger numerical dissipation is observed for the standard TRMC scheme in the fluid limit, and its accuracy approaches to the first order as shown in Sec. 2.3.2. For the moderate Knudsen number, such as $\text{Kn} = 0.01$, the AAP-TRMC method can be considered as a mixture of the standard TRMC and Crank-Nicolson schemes. Therefore, due to the competition of these two schemes, a flat error curve is observed in this range. Even so, it is still noted that the AAP-TRMC method is more accurate than the standard TRMC method with the moderate Knudsen number.

In addition, the computational efficiency of the AAP-TRMC2 method is compared with DSMC [1] for the case of $\text{Kn} = 0.001$. Since the accuracy of the stochastic particle method is also dependent on the number of computational particles, three particle numbers are tested for the AAP-TRMC2 method, i.e., 50, 200 and 500 particles per cell. In DSMC, we initially assigned 50 particles in each cell. In Fig. 3, different levels of error are achieved by changing mesh size, and the CFL number is also set as 1.0 for all simulations. The computational time refers to the cost CPU time to simulate the Poiseuille flow for a certain physical period. It is normalized by T_0 , which is the longest computational time among the DSMC cases. We note that, to obtain the same level of accuracy for this one-dimensional flow, the AAP-TRMC2 method can save at least 10 times the CPU time compared to DSMC. It is also noted that the accuracy of the AAP-TRMC2 method decreases as fewer computational particles are employed. However, even if 50 particle per cell is used, the AAP-TRMC2 still demonstrates better performance than DSMC.

4.2. Sod tube flow

The Sod tube flow is a typical multiscale one-dimensional gas flow. In this test, the computational domain is set as one meter and a density discontinuity is initially assigned in the middle of the tube. Argon gas is simulated and the VHS molecule model as same as Sec. 4.1 is employed. At the beginning, the mean velocity is zero and the gaseous temperature is 273 K in the whole tube. However, the densities in the left and right sides of the tube are different. Three Knudsen numbers,